Unstart Phenomenology of a Dual-Mode Scramjet Subject to Time-Varying Fuel Input

Dissertation

Presented in Partial Fulfillment of the Requirements for
the Degree Doctor of Philosophy in the
Graduate School of The Ohio State University

By

Logan P. Riley, B.S. Mechanical Engineering (Minor Applied Mathematics)

Graduate Program in Aeronautical and Astronautical Engineering

The Ohio State University

2019

Dissertation Committee:

Datta Gaitonde, PhD, Advisor

Jen-Ping Chen, PhD

Jeffrey Donbar, PhD (AFRL)

Seung Hyun Kim, PhD

Mo Samimy, PhD

Abstract

Scramjet-based, air-breathing propulsion systems are poised to enable development of hypersonic defense, high speed transport, and access-to-space aerospace vehicles. A particular variant of scramjet engine, the dual-mode scramjet, is capable of operating in subsonic- and supersonic-burning modes and is attractive for flight at or above Mach 5. Despite the relative geometric simplicity of such scramjet engines, the intense hypersonic flight environment presents challenges to routine, long-duration hypersonic flight in the form of shock-turbulence interactions, heat-transfer, and turbulent-combustion.

A critical component of dual-mode scramjets, the isolator, conditions the flow before it reaches the combustion zone and contains the Pre-Combustion Shock-Train (PCST) which forms in response to the pressure rise due to chemical heat release. When subjected to sufficiently large mechanically- or chemically-induced back-pressures, the isolator may unstart, resulting in the rapid ejection of the shock-train from the isolator, adversely affecting controllability and survivability of high-speed air-breathing vehicles.

To better anticipate and control for isolator unstart events, detailed understanding of the combustor dynamics is required. In particular, the selection and placement of measurement sensors for ground and flight experiments is predicated on

quantifying the dynamic response of the scramjet engine system. This dissertation computationally studies the isolator dynamics during a fuel-staging-induced unstart event. In this process, fuel flow rates are varied in time between two reference fueling states studied experimentally and characterized as aft-fueled and forward-fueled biased, respectively.

The dynamics of a rectangular cross-section scramjet combustor, in the presence of simulated inflow-distortion, are described and quantified with respect to combustion-induced unstart. Because of the high Reynolds number and multi-physics effects of mixing and combustion, a model-based, Unsteady Reynolds-Averaged Navier-Stokes (URANS) approach is employed to study the turbulent reacting flowfield. Before characterizing unstart phenomenology, solution sensitivities to model parameters and assumptions are quantified.

The primary analysis considers the dynamics of the PCST during the imposed fuel-staging transient. A wall-pressure-based shock sensor employed in experiments is used to track the response of the PCST to the heat release-induced back-pressure gradients. From this sensor, an incipient unstart condition is identified which delineates between slowly-varying, pre-unstart PCST motion and more rapid PCST *unstart* motion. Extending this one-dimensional sensor to the predicted two-dimensional wall field reveals strong spanwise gradients associated with side wall separation.

Rectangular combustors are particularly sensitive to corner flow, including shock-induced separation and secondary flow. Commensurately, side wall separation is identified as a principal component of the unstart dynamics in this rectangular combustor. Viscous effects associated with these separation zones are characterized in terms of the isolator confinement parameter employed in the literature, which suggests a shift from an oblique to normal shock-train structure. Secondary flow is also quantified in terms of streamwise vorticity variations along the combustor. A separation bubble on the upper wall of the isolator is also identified which modulates the shock-train structure near the isolator entrance. A bias in mixing and heat release zones near the side wall of the combustor is identified as the primary driver of the side wall separation dynamics which precede unstart, consistent with experimental measurements of steady-state combustor operation.

A secondary component of the analysis leverages Model Order Reduction (MOR) techniques to filter the high-dimensional flowfield into a low-dimensional basis of features called modes. Two popular MOR methods, namely, snapshot-based Proper Orthogonal Decomposition (POD) and Dynamic Mode Decomposition (DMD), are employed to isolate spatially coherent flow structures from the computational dataset via the extracted modes. These methods, which are typically applied to statistically stationary flowfields, require careful extension to the statistically unsteady unstart event. To anchor the MOR-based analysis, the Total Variation metric is adapted to quantify spatially-localized flowfield dynamics and provide a basis to verify that the extracted modes are representative of the non-stationary dynamics. From the dominant POD and DMD modes, as applied to selected analysis planes (spatial windows), flow structures related to upper and side wall separation zones are captured. Time-windowing the dataset provides an additional filter to isolate PCST structures at different phases of the fuel-staging transient.

The efficiency of the MOR-based representations of the combustor dynamics are evaluated in terms of the reconstruction error for a given level of data compression (order reduction). Importantly, two methods are proposed from which to infer higher-order dynamics using the reconstruction errors. The first method, relies directly on the reduced-order reconstruction to identify large-magnitude error regions indicative of higher-order dynamics. A second approach is presented in which the MOR-based filters are applied to the entire three-dimensional domain for which brute force computation of reconstruction error is computationally infeasible. DMD, in particular, is shown to encode information of the time-mean and higher-order dynamics within the dominant mode. Consequently, the difference between the time-mean field and DMD mode is shown to identify regions which feature non-linear temporal flowfield variations. The three-dimensional MOR analysis isolates spanwise gradients associated with isolator corner flow and shear layers developing downstream of the cavity and the backward-facing steps.

To facilitate MOR analysis of the full, three-dimensional simulation data, variables are partitioned into separate decompositions to mitigate computation cost. For DMD, it is shown that partitioning the observables of interest into separate MOR decompositions produces similar but not identical dynamics, as inferred from the DMD eigenspectra. This suggests caution when applying these techniques to high-dimensional three-dimensional datasets if the goal is to compare the low-order representations of different variables.

Finally, a time-local variant of the DMD method is applied to filter the statistically unsteady scramjet flowfield. The method shows improved reconstruction performance over standard DMD while still capturing the primary dynamic structure associated with upper wall separation. Such MOR decompositions are thus shown to provide a reasonable filter to the leading dynamics of the statistically unsteady combustor which may further facilitate control system development and optimal sensor selection and placement.

Dedication

With Love to Mom and Dad. Meanit.

Acknowledgments

I owe, especially, a great deal of gratitude to Professor Datta Gaitonde for his guidance, patience, and perspective during the course of my PhD studies. I am thankful for his emphasis on the importance of developing the depth of my research but also the communication thereof. For the latter, I am particularly appreciative of the opportunities he facilitated to engage with professional researchers across industry, academia, and government laboratories.

There are several researchers at the Air Force Research Lab (AFRL) to whom I am also indebted. First, my thanks go to Dr. Jeff Donbar for sponsoring the Dayton Area Graduate Studies Institute (DAGSI) Fellowship project that supported much of my research. Moreover, his guidance on the experiments at AFRL which form the basis of my research was most helpful. I also wish to thank Dr. Mark Hagenmaier for many valuable discussions regarding my computations during the course of my studies. My thanks also to Drs. Nick Bisek, Dean Eklund, Ez Hassan, Jiwen Liu, Susan Cox-Stouffer, and Charlie Tyler for their insights during numerous discussions.

My thanks also go to my committee members: Professors Jen-Ping Chen, Seung Hyun Kim, and Mo Samimy, for their instruction and guidance during my graduate studies. Additional thanks go to Professors Jeffrey Bons, Jack McNamara, Sundip Mazumder, and Jeffrey Sutton for their instruction and support. To Janeen Sands and

Nick Breckenridge, my appreciation for their tireless efforts in making sure all the T's are crossed and all the I's dotted in addition to their guidance and support throughout my graduate program. I am likewise thankful to my undergraduate advisors and instructors Drs. Jerry Drummond, Alex Povitsky, and Richard Gross who started me on the path towards fluid dynamics, thermodynamics, heat-transfer, and the computational modeling and simulation there-of.

A myriad thanks go to my friends and colleagues in the High-Fidelity Computational Multi-Physics Lab (HFCMPL). To Robert Yentsch, I am thankful for his assistance in getting acclimated to the lab and for helping jump-start my research in the realm of hypersonics. Thanks are also due to Rachelle Speth, David González, Mbu Waindim, Unni Krishnan, Lionel Agostini, Arvind Mohan, Vilas Shinde, Rajesh Ranjan, and Michael Adler for many edifying discussions spanning turbulence, combustion, reduced-order modeling, and hypersonics. For the latter, an additional thanks go to Michael for such insights as "fire is hard when you go fast!" My thanks also to Rajesh Ranjan for allowing me to use (and modify!) his numerically optimized Dynamic Mode Decomposition code for portions of my work.

This research would not have been completed without financial support from several programs. Much of this project was conducted through a DAGSI Fellowship, project RQ-14-11, with thanks due to Dr. Elizabeth Downie at the DAGSI program office. Additional support was provided by AFRL and the Collaborative Center for Aeronautical Sciences (CCAS). I'm also grateful for a Presidential Fellowship from The Ohio State University Graduate School which provided support during my final year of studies.

This work would not have been possible without many computing resources. Computational resources used in this work were provided through The U.S. Department of Defense (DoD) High-Performance Computing Modernization Program (HPCMP) DSRCs at AFRL, ARL, ERDC, and NAVO. Additional computing resources were provided by the Ohio Supercomputer Center (OSC).[1] Special thanks are also due to Dr. Jim Giuliani for his assistance in troubleshooting OSU networking issues, in particular, and computing problems, more generally. Several figures within the manuscript were generated using Intelligent Light's visualization software FieldView™ whose licenses are provided under a University Partnership Agreement. Lastly, honorable mentions include a variety of computational tools without which this work would not have been completed: GNU Parallel,[2] Python,[3] IPython,[4] NumPy,[5] Matplotlib,[6] and the kdtree 2[7] library.

Vita

8 July 1989	Born Cleveland, Ohio, USA
June 2007	Avon High School Avon, OH
August 2007	Began undergraduate studies, The University of Akron Akron, OH
July 2008-August 2008 December 2008-January 2009	Lewis' Educational and Research Collaborative Internship Program (LERCIP) Army Research Labs (ARL) Vehicle Technology Directory (VTD) Intern NASA Glenn Research Center Cleveland, OH
May 2012	B.S. Mechanical Engineering, The University of Akron Akron, OH
July 2013	Began Graduate studies, The Ohio State University Columbus, OH
August 2014-February 2017	Dayton Area Graduate Research Studies Institute (DAGSI) Fellowship
June 2015-August 2015	DAGSI Intern at the Air Force Research Laboratory (AFRL) Dayton, OH
May 2018-Present	Ohio State Graduate School Presidential Fellow

Publications

ORCiD

orcid.org/0000-0003-0808-7705

Journal Articles

L. P. Riley, M. A. Hagenmaier, J. M. Donbar, D. V. Gaitonde, "Isolator Dynamics during Unstart of a Dual-Mode Scramjet," *Journal of Propulsion and Power, Vol. 34 N. 6, 1409-1427 2018, doi:10.2514/1.B36888*.

Conference Papers

L. P. Riley, R. Ranjan, D. V. Gaitonde, "Unsteady scales of a supersonic backward-facing step flow via perturbation analysis," In *46th AIAA Aerospace Sciences Meeting Conference*, San Diego, California. January 2019, AIAA Paper 2019-1910. doi:10.2514/6.2019-1910.

L. P. Riley, M. A. Hagenmaier, J. M. Donbar, D. V. Gaitonde, "Transient Feature Extraction in Simulated Scramjet Unstart via Model Order Reduction Methods," In *54th AIAA/SAE/ASEE Joint Propulsion Conference*, Cincinnatti, Ohio. July 2018, AIAA Paper 2018-4535. doi:10.2514/6.2018-4535.

L. P. Riley, M. A. Hagenmaier, J. M. Donbar, D. V. Gaitonde, "Model Order Reduction and Transient Identification In Scramjet Unstart Simulations," In *36th Joint Army Navy NASA Air Force Air-breathing Propulsion Subcommittee Meeting*, Newport News, Virginia. December 2017, JANNAF/APS 2017-5575.

L. P. Riley, M. A. Hagenmaier, J. M. Donbar, D. V. Gaitonde, "Isolator Dynamics and Heat Release during Unstart of a Dual-Mode Scramjet" In *55th Aerospace Sciences Meeting*, Grapevine, Texas, January 2017, AIAA Paper 2017-0544, doi:10.2514/6.2017-0554.

L. P. Riley, M. A. Hagenmaier, J. M. Donbar, D. V. Gaitonde, "A Computational Investigation of Unstart in a Dual-Mode Scramjet," In *54th Aerospace Sciences Meeting* San Diego, California, January 2016, AIAA Paper 2016-1901, doi:10.2514/6.2016-1901.

L. P. Riley, D. V. Gaitonde, J. M. Donbar "Preliminary Investigation of Unstart-Related Transients in a Dual-Mode Scramjet," In *51st AIAA/SAE/ASEE Joint Propulsion Conference* Orlando, Florida, July 2015, AIAA Paper 2015-4206, doi:10.2514/6.2015-4206.

Conference Proceedings

L. P. Riley, M. A. Hagenmaier, J. M. Donbar, D. V. Gaitonde, "Analysis of Simulated Scramjet Unstart Dynamics using Model Order Reduction Methods," In *43rd Dayton-Cincinnati Aerospace Sciences Symposium (DCASS)*, Dayton, Ohio. February 2018, 43DCASS-025.

L. P. Riley, M. A. Hagenmaier, J. M. Donbar, D. V. Gaitonde, "Unsteadiness and Modal Decomposition of Scramjet Unstart Computations," In *13th Dayton Engineering Sciences Symposium*, Wright State University. October 2017, DESS2017-057.

Invited Seminars

L. P. Riley, D. V. Gaitonde, "Unsteady Multi-Physics Computations of High-Speed Air-Breathing Propulsion Systems," *Air Force Research Lab DoD Supercomputing Resource Center*, Wright-Patterson AFB, Ohio, October 2018.

L. P. Riley, D. V. Gaitonde, "CFD Simulations of Scramjet Flow Path Transients," *Boeing Research & Technology*, St. Louis, MO, July 2018.

L. P. Riley, D. V. Gaitonde, J. M. Donbar, "Time-Accurate CFD Simulations of Scramjet Engines for Control System Development," In *Dayton Area Graduate Studies Institute Annual Review*, Wright-Patterson AFB, Ohio, November 2017.

L. P. Riley, D. V. Gaitonde, "CFD Simulations of Scramjet Flow Path Transients," *NAVAIR Propulsion and Power, Patuxent River NAS*, Patuxent River, MD, May 2017.

L. P. Riley, D. V. Gaitonde, J. M. Donbar, "Time-Accurate CFD Simulations of Scramjet Engines for Control System Development," In *Dayton Area Graduate Studies Institute Annual Review*, Wright-Patterson AFB, Ohio, December 2016.

L. P. Riley, D. V. Gaitonde, J. M. Donbar, "Time-Accurate CFD Simulations of Scramjet Engines for Control System Development," In *Dayton Area Graduate Studies Institute Annual Review*, Wright-Patterson AFB, Ohio, December 2015.

Technical Research Reports

L. P. Riley, R. J. Yentsch, D. V. Gaitonde, in "Assessment of Predictive Capabilites for Aerodynamic Heating of Hypersonic Systems," O. Chazot, D. Knight eds. *NATO Research and Technology Organization*, November 2015, STO-TR-AVT-205.

Fields of Study

Major Field: Aeronautical and Astronautical Engineering

Table of Contents

List of Tables

List of Figures

Nomenclature

Constants

$\mathcal{H}$	Isolator entrance height	$[m]$
$\mathcal{L}$	Isolator length	$[m]$
$\mathcal{R}_u$	Universal gas constant	$[J\ kmol^{-1}\ K^{-1}]$
$\mathcal{S}_\lambda$	Sutherland's constant for thermal conductivity	$[K]$
$\mathcal{S}_\mu$	Sutherland's constant for dynamic viscosity	$[K]$
$\mathcal{T}$	Time scale	$[sec]$
$\mathcal{W}$	Isolator width	$[m]$
W_s	Molecular weight of s-th species	$[kg\ kmol^{-1}]$

State Variables

ω	Frequency	$[rad\ s^{-1}]$
ρ	Density	$[kg\ m^{-3}]$
σ	Growth rate	$[sec^{-1}]$
E	Total energy	$[J\ kg^{-1}]$
f	Frequency	$[Hz]$
m	Mass	$[kg]$
p	Static pressure	$[Pa]$
Q	Solution vector	[arb.]
R	Specific gas constant	$[J\ kg^{-1}\ K^{-1}]$
T	Static temperature	$[K]$

t	Time	$[sec]$
u	Streamwise velocity component	$[m\ s^{-1}]$
v	Vertical velocity component	$[m\ s^{-1}]$
w	Spanwise velocity component	$[m\ s^{-1}]$
x	Streamwise distance from isolator entrance	$[m]$
y	Vertical distance from isolator body-side wall	$[m]$
z	Spanwise distance from isolator centerline	$[m]$

Thermo-physical Quantities

Δh^o	Enthalphy of formation	$[J\ kg^{-1}]$
γ	Ratio of specific heats	
λ_s	Thermal conductivity of s-th species	$[Wm^{-1}\ K^{-1}]$
$\mathcal{D}$	Binary diffusion coefficient	$[m^2 s^{-1}]$
μ	Dynamic viscosity	$[kg\ m^{-1}\ s^{-1}]$
ν	Kinematic viscosity	$[m^2\ s^{-1}]$
c_p	Specific heat at constant pressure	$[J\ kg^{-1}\ K^{-1}]$
c_v	Specific heat at constant volume	$[J\ kg^{-1}\ K^{-1}]$
g	Gibbs free energy	$[J\ kg^{-1}]$
H	Total enthalpy	$[J\ kg^{-1}]$
h	Static enthalpy	$[J\ kg^{-1}]$
s	Entropy	$[J\ kg^{-1}\ K^{-1}]$

Turbulence Quantities

δ	Boundary-layer thickness	$[m]$
ϵ	Turbulent Eddy Dissipation rate	$[m^2\ s^{-3}]$
$\mathcal{P}_k$	Turbulent Kinetic Energy production	$[m^2\ s^{-3}]$
θ	Momentum thickness	$[m]$

I_t	Turbulence intensity	
k	Turbulent Kinetic Energy	$[m^2\ s^{-2}]$
u_τ	Inner boundary-layer scaling, velocity	$[m\ s^{-1}]$
y^+	Inner boundary-layer scaling, distance based on u_τ	
$y^\star$	Inner boundary-layer scaling, distance based on k	
y_v	Boundary-layer viscous sublayer distance	$[m]$

Chemistry Quantities

χ	Scalar dissipation rate	$[sec^{-1}]$
$\Delta \bar{G}^o$	Standard Gibbs function change	$[J\ kmol^{-1}]$
$\dot{\omega}_s$	generation rate of s-th species	$[kg\ m^{-3}\ s^{-1}]$
$\dot{H}R$	Volumetric heat release rate	$[W\ m^{-3}]$
Λ_T	Takeno flame index	
ν'	Stoichiometric coefficient of reactant	
ν''	Stoichiometric coefficient of product	
ϕ	Fuel-air equivalence ratio	
A_k	Frequency Factor for k-th reaction	$[kmol\ m^{-3}\ s^{-1} K^{-b_k}]$
b_k	Temperature exponent for k-th reaction	
C_s	Molar concentration of s-th species	$[kmol\ m^{-3}]$
E_{a_k}	Activation Energy for k-th reaction	$[J\ kmol^{-1}]$
k_b	Backward reaction rate	$[kmol\ m^{-3}\ s^{-1}]$
k_f	Forward reaction rate	$[kmol\ m^{-3}\ s^{-1}]$
K_p	Equilibrium constant based on partial pressures	
l_F	Laminar flame thickness	$[m]$
M_s	Chemical symbol of s-th species	
s_L	Laminar flame speed	$[m\ s^{-1}]$

X_s	Mole Fraction of s-th species	
Y_s	Mass Fraction of s-th species	
Z	Mixture fraction	

Tensor Quantities

δ_{ij}	Kronecker delta	
$\mathbf{\Omega}$	Nondimensional vorticity magnitude	
$\mathbf{S}$	Nondimensional strain-rate magnitude	
Ω_{ij}	Vorticity tensor, indicial notation	$[sec^{-1}]$
τ_{ij}	Stress tensor, indicial notation	$[N\ m^{-2}]$
q_i	Heat flux vector, indicial notation	$[W\ m^{-2}]$
$S^{\star}_{ij}$	Deviatoric strain rate tensor, indicial notation	$[sec^{-1}]$
S_{ij}	Strain rate tensor, indicial notation	$[sec^{-1}]$
u_i	Velocity vector, indicial notation	$[m\ s^{-1}]$

Non-dimensional Parameters

C_δ	Shock train confinement parameter	
Da	Damkölher number	
Ma	Mach number	
Pr	Prandtl number	
Re	Reynolds number	
Sc	Schmidt number	

Superscripts

$\dot{\{.\}}$	Rate	$[arb.\ sec^{-1}]$
$\{.\}'$	Reynolds-Averaged fluctuating quantity	
$\{.\}''$	Favre-Averaged fluctuating quantity	
$\overline{\{.\}}$	Reynolds-Averaged quantity	

$\widehat{\{.\}}$	Scaled quantity
$\widetilde{\{.\}}$	Favre-Averaged quantity

Subscripts

0	Stagnation condition
∞	Free stream
$comb$	Combustion state quantity
e	Isolator entrance
f	Fuel
m	Mode number
mix	Gas mixture quantity
n	Iteration number
ox	Oxidizer
s	Shock quantity
st	Stoichiometric condition
t	Turbulence quantity
$tare$	Tare state quantity
TV	Total Variation of quantity
uns	Unstart
w	Wall boundary
wm	Wall model quantity

Abbreviations

1-D	One-dimensional
2-D	Two-dimensional
3-D	Three-dimensional
AFR	Air-fuel ratio

AFRL	Air Force Research Laboratory
AMG	Algebraic Multi-Grid
AR	Aspect Ratio
BSW	Body-side wall
CFD	Computational Fluid Dynamics
CFL	Courant-Friedrichs-Lewy
CPU	Central Processing Unit
CSW	Cowl-side wall
DBD	Di-electric Barrier Discharge
DES	Detached-Eddy Simulation
DG	Distortion Generator
DLR	Deutsches Zentrum für Luft- und Raumfahrt (German Aerospace Center)
DMD	Dynamic Mode Decomposition
DNS	Direct Numerical Simulation
DOF	Degree(s) of Freedom
DSRC	DoD Supercomputer Resource Center
EASM	Explicit Algebraic Reynolds Stress Model
FAR	Fuel-air ratio
FLOPS	Floating Point Operation per Second
GCI	Grid Convergence Index
HIFiRE	Hypersonic International Flight Research Experiment
LES	Large-Eddy Simulation
MOR	Model Order Reduction
mrDMD	Multi-Resolution Dynamic Mode Decomposition
NACA	National Advisory Committee for Aeronautics

NASA	National Aeronautics and Space Administration
PCA	Principal Component Analysis
PCST	Pre-Combustion Shock-Train
PDF	Probability Density Function
PIV	Particle Image Velocimetry
PLIF	Planar Laser-Induced Flouresence
POD	Proper Orthogonal Decomposition
RANS	Reynolds-Averaged Navier-Stokes
RBCC	Rocket-Based Combined Cycle
ROM	Reduced-Order Model
SBLI	Shock/Boundary-Layer Interaction
SSW	South-side wall
SVD	Singular Value Decomposition
TBC	Thermal Barrier Coating
TBCC	Turbine-Based Combined Cycle
TDLAS	Tunable-Diode Laser Absorption Spectroscopy
TDLAT	Tunable-Diode Laser Absorption Tomography
TED	Turbulent Eddy Dissipation
TKE	Turbulent Kinetic Energy
TP2	Taitech-Princeton 2
TV	Total Variation
TVD	Total Variation Diminishing
URANS	Unsteady Reynolds-Averaged Navier-Stokes
WMLES	Wall-Modeled Large-Eddy Simulation

Chapter 1

Introduction

Air-breathing propulsion is attractive for hypersonic flight at or above 5 times the speed of sound (Mach 5 and above) since it obviates the need to carry oxidizer, leading to relatively higher efficiency in terms of specific impulse (thrust per fuel flow rate) compared to rocket engines.[14–16] A particular variant of hypersonic air-breathing engine is the *dual-mode* **s**upersonic **c**ombustion **r**amjet – **scr**amjet – system[14,17–19] which is designed to operate across both ramjet (subsonic burning) and scramjet (supersonic or mixed supersonic/subsonic burning) regimes. The engine flowpath for a notional scramjet-powered vehicle at Mach 5 flight ($Ma_\infty \approx 5$),[†] shown schematically in Figure 1.1, comprises the inlet, isolator duct, combustion zone, and nozzle. The engine system may also feature external compression from shock waves (denoted in red) generated by the vehicle body in a mixed-compression type inlet prior to flow entering the inlet.[20] Following the inlet, an isolator duct conditions the flow entering the combustion zone. Critically, this duct balances the pressure rise between the inlet and combustion zone. The system of compression waves in the isolator, known as the

[†]For a freestream temperature of $T_\infty \approx 300\ K$, the corresponding fluid velocity scale is $u_\infty \approx 1700\ m/s$. Assuming a one meter long $L = 1\ m$ combustor, the representative flow timescale is $t \approx 0.6\ ms$.

Pre-Combustion Shock-Train (PCST), forms in response to pressure rise due to heat release.[10,18] The PCST compresses the incoming flow within the pseudo-shock[9,21,22] region which may feature additional mixing processes downstream of the shock-train before reaching the combustion region. A schematic of a pseudo-shock at $Ma_e \approx 2$ is shown for a rectangular duct in Figure 1.2. In this schematic, the pseudo-shock is characterized as normal because of the normal-like, rather than oblique, compression waves. The pseudo-shock or shock-train takes on an oblique character for higher isolator Mach numbers with increasingly oblique compression waves.[9] Combustion is typically anchored by one or more flame-holder cavities[23–25] which encourage mixing and reaction by increasing fluid residence time. Subsequently, a nozzle expands the flow to extract thrust. Although the engine geometry is relatively simple compared to conventional turbine-based engines, the hypersonic flight environment presents complicated flow physics.

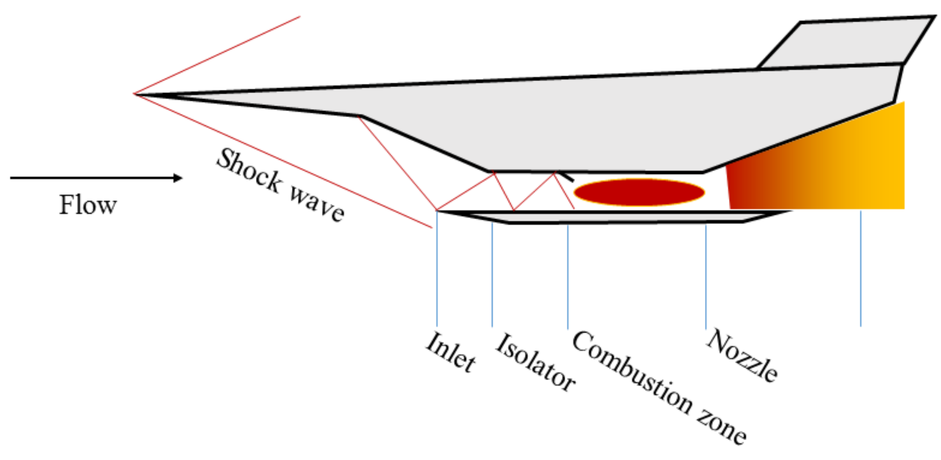

Figure 1.1: Notional scramjet schematic including inlet, isolator, combustion zone, and nozzle.

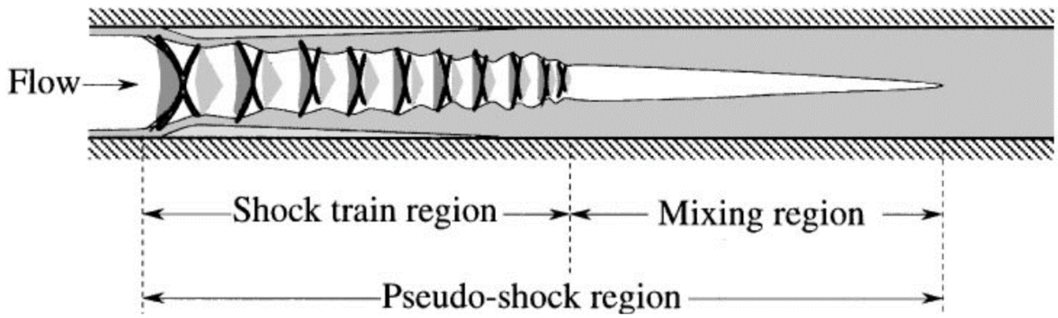

Figure 1.2: Schematic of a normal shock-train and pseudo-shock. Adapted from Matsuo *et al.*[9]

1.1 The Challenges of Hypersonic Flight

Intense research over the preceding decades[26,27] has sought to enable hypersonic air-breathing propulsion technologies for defense,[28–30] high-speed transport,[31,32] and access-to-space.[20,33–35] In particular, fundamental research on supersonic inlets[36–38] and supersonic combustion flows[18,26,39–42] laid the groundwork for modern flight demonstrators. Recent efforts have yielded successful flight tests for the hydrogen-fueled X-43 (Hyper-X)[43–45] and HyShot II[46] programs as well as the hydrocarbon-fueled HIFiRE-2[47] and X-51[48–51] programs. Ongoing work with Rocket-Based (RBCC) and Turbine-Based Combined-Cycle (TBCC) integrated scramjet engines[52,53] is driving development of commercial space-plane[54,55] and high-speed reconnaissance vehicles.[56,57]

Despite the success of recent flight tests, routine hypersonic flight is still not reliably achieved because of the harsh flight environment.[58–60] Hypersonic flight is characterized by intense drag and heat transfer loads to the vehicle,[19,34,60,61] where each is augmented by hypersonic boundary-layer transition.[62] Both externally and internally, viscous/inviscid interactions in the form of Shock/Boundary-Layer Interactions (SBLIs)[63] with inherent unsteadiness[64,65] affect boundary-layer transition and separation.[14] In turn, SBLIs may adversely affect vehicle control surfaces and engine performance. Hypersonic air-breathing propulsion systems are further complicated by short, sub-millisecond timescales in which to mix and burn fuel. Flame-holder cavities used to enhance fuel-oxidizer mixing have residence times for combustion on the order of several milliseconds.[24,25] Thermo-acoustic oscillations can also exist within flame-holder cavities which may adversely affect propulsion performance.[66] Thermal[67,68] and chemical[14,18] non-equilibrium within the combustor can also strongly affect ignition behavior and combustion efficiency. Ignition transients are particularly challenging in terms of modeling and control because of the short, microsecond timescales.[19,69–71]

1.2 The Problem of Isolator Unstart

One particular challenge to routine operation of scramjet-powered vehicles is isolator unstart, whereby the shock-train is ejected out of the inlet leading to loss of engine mass capture and intense, unsteady aerodynamic loads[72] which may take the form of strong pressure oscillations in the inlet known as 'Buzz'.[73–75] The adverse effects of unstart on combustor performance was acutely demonstrated during the second flight[76] of the X-51 program where loss of the vehicle is attributable to unstart of the engine system. Hence, understanding of isolator flow dynamics is necessary to develop unstart detection[77] and control[78] schemes to mitigate the deleterious effects of unstart events.

The severity of unstart events motivates analysis of isolator performance to identify operational boundaries of the engine system. This includes understanding the threshold or margin for unstart which serves as a measure of the allowable back pressure of the isolator.[79] Fundamental work has characterized steady performance of inlets and isolators by way of analytical methods and empiricial correlations including the analyses of Kantrowitz,[80] and Waltrup and Billig,[42,81] respectively. As reviewed by Smart,[82] many integral approaches are popular[32,41,42,83,84] for scramjet propulsion modeling and analysis. While modifications to these approaches have been developed via statistical methods,[85,86] for example, their generalization to complex geometries[87] and large-scale dynamics such as mode-transition,[88] is non-trivial. Consequently, such models do not capture all of the critical three-dimensional (3-D) flow features common to scramjet isolators.[85]

Experimental and computational studies have also targeted steady-state performance mapping to determine the isolator operational boundaries for ramjet, scramjet, and unstart states. Sullins and McLafferty[89] examined several fixed back-pressure ratios for entrance Mach numbers (Ma_e) of 2 and 2.85 comparing changes in observed shock-train length to empirical correlations. Sullins[90] studied a hydrogen-fueled combustor at $Ma_e = 3.3$ and measured steady-state isolator pressure distributions in ramjet and scramjet combustion modes. Bachchan and Hillier[91] tested an axisymmetric inlet at off-design conditions over the range of $4 \leq Ma_\infty \leq 6$ to qualitatively describe inlet SBLIs and boundary-layer separation using two-dimensional Reynolds-Averaged Navier-Stokes (RANS) computations. Unsteady RANS (URANS) computations in two[92] and three[93] dimensions for a $Ma_e = 1.8$ square-duct identified back-pressure limits sufficient for isolator unstart. Fotia and Driscoll[94] experimentally mapped isolator-cavity performance for a hydrogen-fueled scramjet in terms of mechanical and chemical effects by comparing the influence of fuel injector momentum flux ratio for jets-in-crossflow and their corresponding fuel-air equivalence ratio in $Ma_e = 2.2$ flow. Similarly, Aguilera *et al.*[95] studied steady-state scramjet and ramjet operation in a direct-connect combustor at $Ma_e = 1.9$ to determine time-mean isolator pressure distributions and unsteady pressure oscillations in the combustor cavity. These experiments provide understanding of fuel-air equivalence ratios at which mode-transition between ramjet and scramjet states occurs. Despite the insight provided, these studies are often limited to steady-state analysis which may overlook short-time flowfield transients.

1.3 State of the Art in the Study of Isolator Dynamics

Statistically steady-state studies previously described help define isolator operational boundaries. However, fine-scale combustor dynamics, particularly in the isolator, must be quantified in order to minimize the risk of unstart. Isolator dynamics are characterized by both large and fine-scale unsteadiness which are influenced by geometry, back pressure forcing, boundary-layer state, fuel-injection, and turbulent-combustion interactions.

As a model for more complex isolator physics, fine-scale, statistically steady dynamics of an isolated normal shock in a duct, with and without the presence of forcing, have been studied. In the simplest case, a single normal shock in a rectangular duct was subjected to acoustic disturbances as modeled by Culick *et al.*[96] to identify the effect of pressure perturbations on shock-induced separation. Bruce and Babinsky[97] studied a normal shock subject to periodic forcing over range

$8 \leq f \leq 45\ Hz$ to characterize the relationship between forcing frequency and shock oscillation amplitude in a $Ma_e = 1.5$ flow. Consistent with an analytic model, they identified a critical frequency below which the oscillation amplitude is insensitive to duct divergence angle. Carroll and Dutton[98–100] measured the unsteadiness of a normal shock-train in a constant area duct at $Ma_e = 1.6$ and $Ma_e = 2.45$ and identified the influence of shock boundary-layer interactions on flow separation. Turbulent statistics such as turbulent kinetic energy and the Reynolds stresses were also quantified. Morgan *et al.*[101] compared Large-Eddy Simulation (LES) predictions with the Laser Doppler Velocimetry (LDV) measurements of Carroll and Dutton at $Ma_e = 1.61$ to capture interactions between the shocks and turbulent boundary-layers and the resultant separated shear layer unsteadiness. However, the reduced Reynolds number applied in the simulation, as a consequence of LES grid-scaling requirements, resulted in a mismatch between the predicted and measured shock-train locations.

In ducts more representative of conventional scramjet isolators, multiple shock structures manifest as part of a shock-train. Sugiyama *et al.*[102] quantified flow separation behavior for a pseudo-shock in a square duct at Mach 2 and 4 using unsteady wall pressure spectra and time-resolved Schlieren imaging. Unsteady pressure and Schlieren imaging by Klomparens *et al.*[103] characterized constant area duct flow subject to cyclic back-pressure forcing at $Ma_e = 2.75$ to quantify shock sensitivity to the imposed back-pressures. Shock structures were found to oscillate in the streamwise direction by $0.08 - 0.12\mathcal{H}$ where $\mathcal{H}$ is the isolator duct height. Additional work on this isolator[104] at $Ma_e = 2$ also quantified shock train motion hysteresis effects from cycle to cycle of the dominant low frequency motion. Stereo Particle Image Velocimetry (PIV) and time-resolved wall pressure measurements captured corner flow features in terms of the viscous confinement parameter[105] (C_δ), a measure of the boundary layer (δ) to duct height ratio, $C_\delta \propto \delta/\mathcal{H}$. Shocks were observed to oscillate up to $\pm 0.2\mathcal{H}$ about the time-mean position.[106] Additionally, Hunt *et al.*[107] observed a linear relationship between shock displacement and back-pressure consistent with other works. The study also characterized the transition between normal and oblique shock-train states[108] and statistically quantified disturbance propagation in terms of a phase lag between shock structures within the isolator.[109] Time-resolved Tunable-Diode Laser Absorption Spectroscopy (TDLAS) measurements identified shock-train oscillation distances of the order of the duct diameter for a dominant low frequency $\mathcal{O}(100)$ Hz unsteadiness.[110,111] Unsteady pressure measurements in a rectangular isolator at $Ma_e = 2$ for forcing frequencies of $105 \leq f \leq 225$ Hz indicated that oscillations amplitudes decrease with increasing excitation frequency.[112]

The influence of back-pressure forcing was also captured in several numerical studies. Computational studies of shock-train response to imposed back-pressure forcing for a single normal shock[113] and an inlet/isolator model[114] quantified the effects of forcing frequency and amplitude on shock-train motion. Numerical studies[115] of an axisymmetric supersonic inlet at $Ma_\infty = 2.1$ for forcing frequencies $250 \leq f \leq 4000$ Hz showed that disturbance amplitudes of five percent introduce non-linear behavior such that shock oscillations become less sinuous. Increasing the forcing amplitude to 10 percent of the nominal back pressure lead to non-linearities sufficient to unstart the inlet.

Ultimately, many works are interested in quantifying isolator flowfield dynamics *during* unstart events. Although such events also contain fine-scale unsteady features such as boundary-layer turbulence and shock-turbulence interaction, large-scale dynamics (such as shock-induced flow separation) are also observed over the length of the engine flowpath, $\mathcal{O}(1)$ m. Often, un-fueled (*tare*), mechanically forced, back-pressure-induced unstart is used as a surrogate for the pressure rise due to combustion. Early work by Wieting,[116] for example, examined time-resolved wall pressure levels in a inlet/isolator model at $Ma_\infty = 5.3$. Larger pressure magnitudes were observed during the unstart process than at the statistically steady unstart state. Experiments and computations of a similar model by Sato *et al.*[117] observed sensitivity of the unstart shock speed to disturbance amplitude at $Ma_\infty = 3$. Unsteady wall pressure signals were similarly leveraged,[118] to track inlet shock structure motion at $Ma_e = 3$. Fundamental work by Rodi *et al.*[119] studied both cowl- and back-pressure-induced unstart events in an inlet/isolator model[120] in the NASA Langley Mach 4 Blowdown facility (M4BDF). Three-dimensional URANS computations of this configuration by Neaves *et al.*[121] characterized dynamics of oblique shock reflections in the inlet during back-pressure-induced unstart and the influence on flow separation. Deng *et al.*[122] similarly identified the formation of shock-induced separation zones during the unstart process of the M4BDF configuration. Benson and McRae[123] employed an adaptive grid approach in a URANS framework to study 2-D and 3-D geometries at $Ma_\infty = 3$ with inflow bleed. These computations of back-pressure-induced unstart events indicate the importance of 3-D flow features, particularly those related to shock-induced separation. URANS computations by Hoeger,[93] based on experimental work[124] of a rectangular isolator at $Ma_e = 1.8$, identified transient pressure loads as a result of imposed back-pressures. Zhang *et al.*[125,126] separated a back-pressure-induced unstart process at $Ma_\infty = 5$ into distinct phases which include the formation of a separation bubble prior to unstart and the presence of buzz post unstart.

Fine-scale turbulent features have been connected to large-scale isolator dynamics in terms of unstart sensitivity to boundary-layer state. Separation was observed on both the upper and lower isolator walls of a $Ma_\infty = 5$ rectangular inlet-isolator undergoing unstart using time-resolved wall pressures, Schlieren, and Particle Image Velocimetry (PIV) by Wagner *et al.*[127–129] Shock-train length dependence on boundary-layer state has also been identified. Numerical studies of a constant area isolator at fixed back pressure for $Ma_e = 1.8$[130] and $Ma_e = 3$[131] flow showed that the shock-train length is more sensitive to boundary-layer thickness at relatively higher back pressures. Unstart initiated by a transverse jet in a $Ma_\infty = 5$ tunnel by Do *et al.*[132,133] indicated symmetric boundary-layers delay unstart initiation compared to asymmetric boundary-layer thicknesses on the upper and lower walls of a 2-D rectangular model. Fiévet *et al.*[134] examined normal shock-train response to unsteady inflow boundary-layer thickness (δ) to assess confinement effects in $Ma_\infty = 2$ flow of a rectangular duct using Direct Numerical Simulation (DNS). Forcing frequencies of $20 - 1000$ Hz and variations in boundary-layer momentum thickness (θ) amplitude of ± 0.3 cm were shown to affect shock-train length. Decreasing the boundary-layer thickness decreased the shock-train length while the pressure gradient across the leading shock increased and vice versa. Additionally, when the boundary-layer thickened, the oblique portion of shock train also became more prominent.

The dependence of shock-train structure on inlet/isolator geometry is evident from several studies. Smith *et al.*[135] studied an axisymmetric combustor configuration for shock-holding and pressure distribution for both constant and diverging isolator ducts across a range Mach numbers $3 \leq Ma \leq 5$. From RANS computations and experiments,[136] an axisymmetric combustor was found to support higher back-pressures than rectangular configurations for the same isolator areas at $Ma = 1.8$ and $Ma = 2.2$ conditions.

Rectangular isolators, like that addressed in this work, bring additional challenges to modeling by introducing 3-D, unsteady features by way of corner[137,138] flow separation and shock/boundary-layer interactions which are sensitive to isolator aspect ratio, defined as the duct width to height ($AR \equiv \mathcal{W}/\mathcal{H}$). A $Ma = 2.75$ tunnel at low $AR = 0.8$ was observed[139–141] to contain prominent corner vortices and flow separation. Experimental study of corner flow separation in a square inlet model, attributable to oblique shock waves, was considered by Funderburk and Narayanaswamy[142] in a 2-D configuration at $Ma = 2.5$. While the primary separation present in two-dimensional SBLIs contains a range of frequencies, the corner separation energy content was localized to higher-frequency bands. The amplitude of the viscous corner flow wall-pressure fluctuations was also smaller than for the primary separation. A computational study[143] of isolators with aspect ratios of 1, 6, and 9 indicated that shock-train length increases for higher aspect ratios at $Ma_e = 3.2$; however, the opposite trend was observed at lower $Ma_e = 2$. A rectangular isolator with chamfered corners was studied numerically by Grendell[144] who observed that chamfered corners shifted the shock-train downstream, compared to square corners. Geerts and Yu[145] characterized shock trains in various aspect ratio $3 \leq AR \leq 6$ isolators using time-resolved wall pressures, shadowgraph, and surface oil flows. Higher-aspect ratio ducts were observed to yield flows that were more closely two-dimensional. However, a numerical study[146] based on experiments of a normal shock in a high aspect ratio duct with $AR = 4.3$ at $Ma_e = 1.6$ identified the formation of corner shocks which affected the centerline flowfield for a relatively large aspect ratio ($AR > 1$) duct.

Analysis of three-dimensional inlets, like 3-D isolators, reveals geometrical influence on scramjet start and unstart limits. Efforts to compute multiple shock-fin interactions representative of inlets with side wall compression highlight open and closed separation patterns.[147] Recently, Hohn and Gülhan[148] characterized the effect of sidewall compression on inlet starting behavior at the German Aerospace Center (DLR) facility for Mach 7 flow. Corner flow effects on SBLIs and boundary layer transition were observed from heat flux measurements indicating the formation of corner vorticies, induced by side wall compression waves which limited starting ability. Stephen *et al.*[149] experimentally studied starting limits at off-design conditions for different side-slip angles and angles-of-attack for a stream-traced, inward-turning inlet of the HIFiRE 6[150] model between Mach 3 and 4.6. The results compared favorably with classic Kantrowitz[80] starting analysis, but the complex geometry introduced hysteresis effects between started and unstarted inlet states.

Like un-fueled studies, flow separation and viscous/inviscid interactions are dominant features in turbulent, *reacting* flowfields. Experiments[151] in a hydrogen-fueled combustor at $Ma_e = 2$ quantified the variation of shock-train oscillation with changes in fuel-air equivalence ratio, *i.e.* the ratio of fuel and air mass flow rates. An experimental study[152] of an $Ma_e = 3.6$, axisymmetric, hydrogen-fueled combustor identified flow separation at higher fuel-air equivalence ratios ($\phi > 1$). Time-resolved pressure loads were also measured[153] during statistically steady operation and unstart for a $Ma_\infty = 3.5$, hydrogen-fueled combustor model which showed boundary-layer combustion noise was greater in amplitude than a standard turbulent flat plate boundary-layer. Shimura *et al.*[72] measured peak aerodynamics loads in a hydrogen-fueled scramjet over the range $4 \leq Ma_\infty \leq 6$ and attributed unstable inlet oscillations to separation bubble formation. URANS computations of another rectangular, hydrogen-fueled configuration by McDaniel and Edwards[154,155] also identified shock-induced separation emphasizing the importance of the side wall region during unstart.

Thermal conditions, which include combustor wall temperature and chemical heat release, affect isolator performance characteristics. Lin *et al.*[156] numerically studied the influence of wall temperature on pseudo-shock pressure rise in rectangular and axisymmetric configurations. The results indicate that cool walls delay choking of the flow for $Ma_e = 1.8$ and $Ma_e = 2.2$ conditions. Fischer and Olivier[157] also identified variation in shock-train pressure rise with combustor wall temperatures at $Ma_\infty = 7.7$ where higher wall temperatures were found to increase the pressure gradient and reduced the shock-train length. Experimental and 1-D numerical analysis of a hydrogen-fueled geometry by Yoon *et al.*[158] identified thermal-choking limits, whereby heat release slows the flow to subsonic conditions, at $Ma_e = 2.2$. Mashio *et al.*[159] quantified thermal choking limits for different fuel-air equivalence ratios in hydrogen-fueled $Ma_\infty = 2$ flow. Time-resolved shadowgraph and wall pressure measurements by O'Byrne *et al.*[160] in a constant area duct with gaseous hydrogen for entrance Mach numbers of 2.5 and 3.8 suggest shock-train unstart speeds are more strongly dependent on heat release at the lower Mach number condition.

Fine-scale turbulence-combustion interactions also contribute to isolator dynamics. In ramjet-like (subsonic-combustion) operation, combustors are susceptible to thermo-acoustic instabilities[161–164] Acoustic disturbances in a simple hydrogen-fueled ramjet were studied experimentally[165] to identify multiple resonant frequencies. In ramjet mode, acoustic-vortical interactions have also been observed computationally.[166,167] For example, the LES[168] of an axisymmetric ramjet also resolved combustion oscillations comprising both small-amplitude, high-frequency and large-amplitude, low-frequency components.

Several efforts have also characterized turbulent combustion interactions for the hydrogen-fueled HyShot II scramjet. Experiments[169] and LES computations[170] of the rectangular HyShot combustor identified 'localized' thermal choking regions where heat release fluctuations lead to locally subsonic flow. Wall-Modeled LES[171] also identified a critical fuel equivalence ratio threshold sufficient to generate a 'combustor shock train' which formed further downstream of the primary isolator section. Larsson *et al.*[170] also identified a dependence on unstart shock propagation speed on fuel equivalence ratio from LES. However, a separate LES[172] study by Nordin-Bates and Fureby observed turbulence-limited reacting flow where the ratio of fluid to chemical timescales, the Damköhler number, is small ($Da < 1$) during incipient unstart conditions.

Although numerous efforts have characterized hydrogen-fueled combustors, more practical, hydrocarbon (HC)-fueled combustors have also gained considerable research attention. Ethylene, or ethylene-based mixtures, serve as surrogates for heavier HC fuels like JP-7, as in the HIFiRE 2 program,[173,174] for example. Experiments[175] in an ethylene-fueled combustor measured the influence of an impinging shock on cavity-based flame-holding and mixing behavior. Ma *et al.*[176] also computed the unsteady response of an ethylene-fueled rectangular combustor to acoustic forcing identifying a coupling between acoustic interactions and chemical mixing and heat release.

Ethylene-fueled, cavity-based combustor experiments[10] revealed a strong correlation between statistically steady shock position and the fuel flow rate to injectors upstream of the cavity flameholder. Planar Laser-Induced Flouresence (PLIF) measurements of ethylene- and JP-7-based combustion indicate strong spanwise gradients in the reaction zones.[177] A similar ethylene-fueled combustor was studied by Lin *et al.*[178] which characterized frequency response for thermal-acoustic interactions at $Ma_e = 1.8$ and 2.2. Unsteady flame dynamics measured[179–181] with time-resolved surface pressures and heat-flux indicated a sudden drop in signal during unstart in an ethylene-fueled combustor at $Ma_\infty = 3, 4.5, 9$, corresponding to upstream flame propagation. Follow-on experiments[182] at $Ma_\infty = 4.5$ identified the influence of free-stream turbulence and inlet geometry[183] on stable flame structures. PLIF measurements indicated higher freestream turbulence increased combustion intensity which altered flame stability. Fotia and Driscoll[94,184,185] studied ramjet-scramjet transition and identified the combined effects of momentum transport and chemical heat release on separation as a result of fuel injector jet-in-crossflow interaction.

1.4 Research Scope and Objectives

Isolator dynamics, featuring both fine and large scales, are strongly influenced by geometry and heat release. Rectangular combustors, in particular, are sensitive to corner interactions attributable to shock-induced separated flow. Despite efforts to predict large-scale transients during inlet start,[186–188] few computational works have been leveraged to study large-scale unstart phenomena for fully three-dimensional scramjet geometries in the presence of inflow distortion and heat release at representative flight conditions. Inflow distortion is especially crucial as it affects ignition-behavior of scramjet systems[189–191] and has been shown[192] to lead to differences between direct-connect ground-test (non-distorted) flows and flight test (distorted) configurations during the HIFiRE 2 program.

A central goal of the present work is to address a major gap in the state-of-the-art by computationally examining unstart dynamics for a high-aspect ratio ($AR = 5.4$) rectangular combustor in the presence of inflow distortion. To ensure confidence in the approach, simulations are extensively validated with the experiments of Donbar *et al.*[10] Critically, the work investigates unstart induced by time-varying fuel flow rates within the combustor. Particular emphasis is placed on describing and quantifying isolator dynamics during transient fuel-staging; namely, the role of unsteady shock motion and corner flow interactions such as flow separation and the mechanisms leading to unstart initiation.

The spatial and temporal scales in the combustor, ranging from fine-scale boundary-layer unsteadiness (mm and μs) to large-scale events like mode-transition (m and ms), pose significant challenges to scale-resolving simulations such as LES and DNS.[†] Flight Reynolds numbers are typically on the order of $\mathcal{O}(10^6)$. The correspondingly stringent grid-scaling requirements[193] for LES and DNS make scale-resolving simulation of complex geometries at flight conditions computationally intensive (*e.g.* Bisek[194]). Therefore, in order to efficiently capture dynamics on the length-scale of combustor ($\mathcal{O}(1)$ m), a model-based approach using Unsteady Reynolds-Averaged Navier-Stokes is adopted for the study. Carefully calibrated URANS approaches have been successfully employed for mode-transition[195,196] and

[†]Representative boundary length and time scales are $\delta \approx \mathcal{O}(10^{-3})$ m and $u \approx \mathcal{O}(10^3)$ m/s which yield a timescale $\tau_\delta \approx \mathcal{O}(10^{-6})$ sec. Similarly, combustor scales comprise length $L \approx \mathcal{O}(1)$ m and velocity scale u to give $\tau_L \approx \mathcal{O}(10^{-3})$ sec.

transient aero-throttle[197] problems, indicating such an approach is suitable to capture *large*-scale flowfield dynamics.

From the primary objective, related research questions arise in the context of sensing and control. Numerous shock-train detection and tracking methods based on wall pressure measurements have been studied[77,112,198–204] as a first step to anticipate or control for unstart events. Linear arrays of high-frequency pressure transducers have been used to gauge shock motion, *e.g.* the experiments[10] of the rectangular combustor to be studied in this work. However, scramjet flowfields are inherently three-dimensional and wall-based measurements may not fully characterize 3-D features such as secondary corner flow. This computational study therefore seeks to connect predicted wall-pressure unsteadiness to 3-D shock-train dynamics.

Recent advances in non-intrusive laser-based diagnostics, such as Tunable-Diode Laser Absorption Spectroscopy (TDLAS)[110,111,205] and Tomography (TDLAT), in addition to high-resolution OH-PLIF,[206] may provide more detailed 3-D measurements into the core of the flow for velocity, temperature, and species concentration.Of particular interest are the effects of localized heat release on unstart which have been shown[169,170] to affect isolator dynamics. Another question addressed in this research is: how do the combined effects of mechanical and heat release blockage (observed in other jet-in-crossflow-based fuel injection schemes[94,184,185]) manifest in the present scramjet combustor?

Coupled with the definition of shock-train tracking methods are the development of control systems to detect and avoid unstart.[79] Multiple passive[207–209] and active[203,208,210–217] control schemes have been studied to manage shock-train displacements in response to back pressure. A fundamental challenge of control system development is the optimal selection and placement of sensors to capture global system response from sparse measurements.[218] However, such optimization is difficult for high-dimensional problems such as those from computations and advanced optical measurements. Consequently, dimensionality or model order reduction (MOR) algorithms such as Proper Orthogonal Decomposition (POD)[219] and Dynamic Mode Decomposition (DMD)[220,221] are attractive to find underlying energetic or coherent structures in turbulent flowfields[222] and to develop Reduced Order Models (ROMS) by splitting snapshots of the temporally evolving flowfield into a reduced mathematical basis. These methods, which rely on linearity and/or statistical stationarity assumptions, pose a challenge in their application to non-stationary, non-linear unstart dynamics. The final thrust of this work is to adapt these methods to extract coherent flow structures and quantify system response to fuel flow rate transients so as to inform sensor selection and placement with respect to pre-unstart and unstart flowfield dynamics. The main research thrusts are thus enumerated:

1. Employ URANS to model unstart initiated by time-varying fuel flow rates:
    - Compute dynamics of an ethylene-fueled, high aspect-ratio $AR = 5.4$ combustor in the presence of isolator distortion.
    - Validate the model approach with an experimental database.
2. Characterize isolator dynamics with respect to shock motion, corner flow, and separation:
    - Connect wall pressures, typically measured in experiment, to *three-dimensional* unsteady shock structures.

    - Identify the role of spatially localized heat release on isolator dynamics and unstart initiation.

3. Quantify dynamics to identify regions of the combustor sensitive to the fuel-staging transient which may facilitate sensor and actuator placement:

    - Use Model Order Reduction methods of Proper Orthogonal Decomposition and Dynamic Mode Decomposition to filter high-dimensional dataset into lower-dimensional mode bases.

    - Extend Model Order Reduction methods to filter pre-unstart and unstart isolator dynamics from non-stationary dataset.

1.5 Overview of Dissertation

To initiate the main discussion, the combustor geometry and operating conditions are first introduced by reviewing the experiments which form the basis of this work (Ch. 2). The rectangular scramjet combustor, including the combustor cavity, fuel injectors, and inflow distortion generator are described. Two reference operating conditions from the experimental database are selected to represent aft-fuel- and forward-fuel-biased fuel-staging. A wall-pressure based metric used for estimating shock-train location in the experiments is defined for subsequent application and extension in the analysis of the dynamics predicted from the computations.

In Ch. 3, the methods used to model the turbulent, reacting flowfield are introduced. Governing equations for the flowfield of an unsteady, thermally perfect gas mixture, as well as the finite-rate kinetics method used to model combustion, are described. Thereafter, closure models and assumptions are discussed. Lastly, the computational domain, boundary-conditions, and solution initialization approach are provided.

Because of the approximations inherent to the numerical approach, a sensitivity study is conducted to understand the influence of numerical parameters and assumptions on the predicted flowfield with respect to experimental measurements (Ch. 4). In particular, numerical predictions are compared to statistically steady-state wall pressure measurements to assess the effects of boundary conditions, spatial resolution, and model coefficients such as turbulent Schmidt number. This last parameter is shown to have a strong effect on the numerical predictions, consistent with other computational studies. Analysis of the relevant fluid and chemical timescales is used to evaluate the suitability of the chemistry model assumption. The sensitivity of the predicted transient fuel-staging event is also examined in the context of the time integration parameters.

In Ch. 5, the flow topologies of the two steady-fueling states are first used to provide context for the observations of unstart phenomenology. The importance of 3-D flow features such as distortion-induced flow curvature and isolator side wall separation are described. Importantly, a wall-pressure-based metric, adapted from experiments, is used to identify an incipient unstart condition. Distinct phases of shock-train motion are also identified. In the pre-unstart phase, relatively slow upstream shock motion is observed together with a shift from an oblique to normal shock-train is identified. The unstart phase is characterized by much higher shock-train speeds.

In the context of facilitating control system development, particularly sensor placement and selection, Ch. 6 explores the application of a Total Variation (TV)-based metric to characterize key transient signatures in the flowfield. The TV metric complements qualitative descriptions of the dynamics and the quantitative shock sensor predictions. In conjunction with this metric, data-driven Model Order Reduction methods Proper Orthogonal Decomposition and Dynamic Mode Decomposition are applied to address the 'curse of dimensionality' of the high-dimensional computations to extract underlying flow features. From the MOR-generated modes, the signature of upper-wall flow separation and shock-train structures are identified. For potential application to reduced-order modeling suitable for control system development, the level of compression (order reduction) of POD and DMD are compared in terms of reconstruction error for reduced-order representations of flowfield. POD is observed to produce minimal reconstruction error for a given level of order-reduction despite the statistically unsteady nature of scramjet unstart. The strongly non-stationary flowfield introduces errors in the compressed DMD representation as a result of the linearity assumption. However, methods are proposed to leverage these errors in order to infer dynamically significant flowfield regions. Time-windowing of the flowfield snapshots is shown to reduce reconstruction errors of both POD and DMD methods and isolate the dynamics within specific phases of shock-train motion. However, manual selection of time windows to capture time-local transients is not possible *a priori*. Consequently, the data-driven multi-resolution DMD (mrDMD) is leveraged to capture time-local dynamics suitable for data-compression of the statistically unsteady flowfield.

Final conclusions are summarized in Ch. 7 and recommendations for future research activities are presented.

Chapter 2

Experimental Background

This computational work is based on experiments of Donbar *et al.*[10] in a rectangular, ethylene-fueled combustor facility.[223] The experiments characterized the combustor operating limits for different steady-state fuel-staging conditions. In particular, the Pre-Combustion Shock-Train (PCST) response to different fuel-staging conditions, as well as unstart margin, was explored. Details of the flowpath are first described (§ 2.1) before discussing the two operating conditions selected from the experimental database (§ 2.2).

2.1 Direct Connect Facility

The direct-connect experimental facility, shown schematically in Figure 2.1 comprises the nozzle, distortion generator, isolator, cavity, and expansion duct. The geometry is characterized in terms of the the isolator entrance height $\mathcal{H} = 42.3\ mm$ (1.664 $in.$). The isolator entrance serves as the streamwise reference datum $x = x_e = 0$. Flame-holding is provided by a cavity with backward-facing step of depth 22 mm and ramp with 22.5 degree close-out angle. The cavity step is located $12\mathcal{H}$ from the isolator entrance and spans 78 percent of the isolator width $\mathcal{W} = 228.6\ mm$ (9 $in.$).

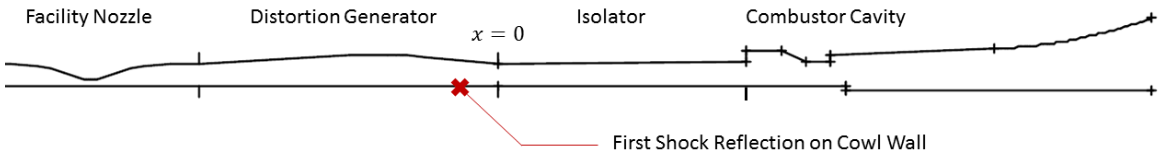

Figure 2.1: Experimental flowpath schematic. Adapted from Donbar *et al.*[10]

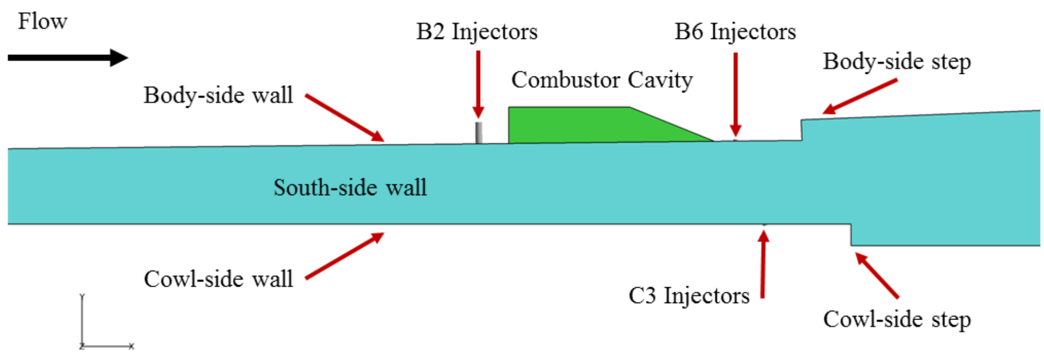

Figure 2.2: Combustor geometry details: cavity and fuel injectors.

A detailed view of the cavity is shown in Figure 2.2. Two backward-facing steps located downstream of the cavity provide additional flame-holding and span the full combustor width.

A crucial feature of the facility is the Distortion Generator (DG) which emulates[11,224] distortion present in flight for a mixed (external and internal) compression inlet. The DG introduces flow non-uniformity by initiating an oblique shock wave upstream of the isolator entrance which impinges on the cowl-side wall at the non-dimensional streamwise distance $\hat{x} \equiv x/\mathcal{H} = -2$. Distortion is characterized in terms of the computed non-dimensional pressure profiles across across the duct

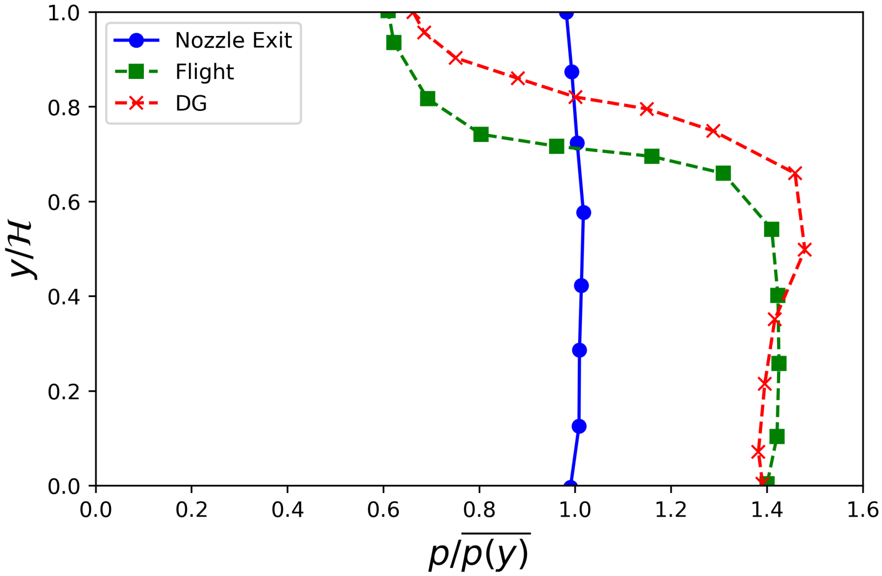

Figure 2.3: Predicted isolator inflow distortion profiles as a function of isolator duct height. Profiles are normalized by their respective spatial averages. Adapted from Gruber *et al.*[11]

with height above the cowl (lower) wall ($\hat{y} \equiv y/\mathcal{H}$) shown in Figure 2.3. The nearly uniform nozzle exit profile (blue) serves as a reference for the design $Ma_\infty = 6.5$ flight distortion curve (green) and the actual facility nozzle ($Ma_{nozz} = 2.84$) curve (red), representative of $Ma_\infty \approx 5$ flight Mach number.

Although the facility contains numerous sets of fuel injectors, only three injector sets are considered in the present study for the selected fuel-staging conditions described in the subsequent discussion (§ 2.2). The injectors labeled $B2$, $B6$, and $C3$ (Figure 2.2) are described in terms of their diameter d, streamwise location $\hat{x}$, and spanwise spacing $\Delta\hat{z} \equiv \Delta z/\mathcal{H}$ in Table 2.1. Injectors labeled Bn and Cn are located on the body-side (upper) and cowl-side (lower) walls, respectively. Each of the injectors are oriented normal to their respective walls.

Table 2.1: Fuel injector configuration.

Injector	*Quantity* [–]	*Diameter* d $[mm]$	*Location* $x/\mathcal{H}$ [–]	*Spacing* $\Delta z/\mathcal{H}$ [–]
B2	5	3.96	11.57	0.9
B6	4	2.36	15.15	0.9
C3	9	2.36	15.56	0.45

Pressure transducers on the body, cowl, and side walls were used to characterize steady-state and transient PCST position with the isolator. Time-resolved wall pressures were captured using eight, 3-kHz wall pressure transducers located on the isolator cowl-side wall. Additional 1-Hz wall pressure taps provided time-mean pressure profiles on the body, cowl, and side walls. In total, the facility contained over 200 pressure sensors whose locations are shown in Figure 2.4.

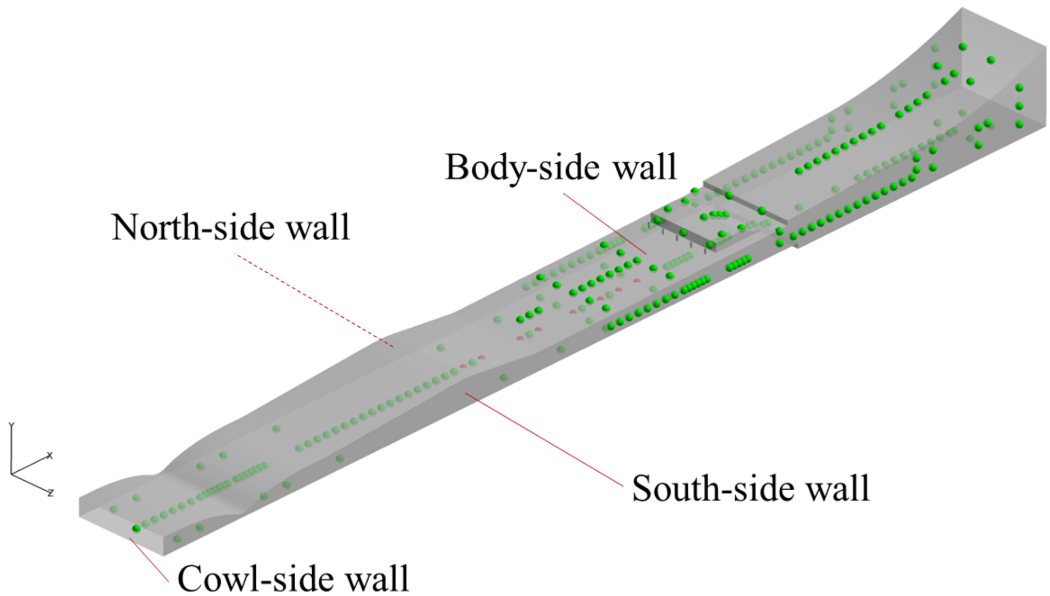

Figure 2.4: Experimental pressure transducer locations: *red* - 3 kHz response, *green* - 1 Hz response.

2.2 Combustor Operating Conditions

The facility nozzle stagnation conditions $p_0 = 1.72 \pm 0.007\ MPa$ ($250 \pm 1\ psia$) and $T_0 = 1390 \pm 5\ K$ (2500 ± 10^oR), with design Mach number $Ma_{nozz} = 2.84$, provide a Mach 5 flight environment with corresponding unit Reynolds number $Re' \approx 18.4 \times 10^6\ m^{-1}$. The nozzle stagnation temperature is set using an in-stream, methane-fueled combustion heater. PCST response to combustion-induced pressure rise was explored by varying the fuel-staging (distribution) by adjusting the local fuel-air equivalence ratio ϕ of each injector set which compares the ratio of mass flow rate of the fuel and oxidizer to the stoichiometric condition (eqn. 2.1). For reasons provided below, two operating conditions are selected from the experimental database comprising aft-fueled and forward-fueled operating states with fixed total equivalence

Table 2.2: Reference experimental steady-state fuel-staging conditions in terms of local fuel-injector fuel-air equivalence ratios.

Staging	*Exp.*	ϕ_{tot}	ϕ_{B2}	ϕ_{B6}	ϕ_{C3}	$x_s/\mathcal{H}$
Aft-fueled	07074AD	0.90	0.20	0.33	0.37	7.81
Forward-fueled	07074AG	0.90	0.40	0.24	0.26	UNS

ratio of $\phi_{tot} = 0.9$ where ϕ_{tot} is sum of local fuel injector conditions (eqn. 2.2). The aft-fueled condition represents a reference on-design condition with relatively lower ϕ_{B2}. In contrast, the forward-fueled condition induces an unstarted isolator with an increased ϕ_{B2}. The isolator is considered unstarted when the PCST or pressure-rise due to combustion, moves upstream of the isolator entrance $\hat{x} = 0$. The local fuel-air equivalence ratios for each of the three injector sets are described in Table 2.2.

$$\phi = \frac{\dot{m}_f/\dot{m}_{ox}}{\dot{m}_f/\dot{m}_{ox}|_{st}} \tag{2.1}$$

$$\phi_{tot} = \sum_i \phi_i \tag{2.2}$$

In each experiment, the isolator was allowed to reach steady-state tare (un-fueled) operation before fuel injector manifolds were allowed to pressurize and reach a final steady-state combustion condition. Sample time-histories for time-resolved pressures at the aft-fueled condition are shown in Figure 2.5. Here, the fuel valves were opened around $t = 15$ seconds and the reacting flow established a new steady-state around $t = 40$ seconds. From the steady-state tare and reacting states, the shock-train position was computed from the centerline cowl-side wall pressure measurements. The PCST streamwise location (x_s) is defined where the non-dimensional pressure, denoted here as $\hat{p}$, exceeds a defined threshold. The non-dimensional pressure is

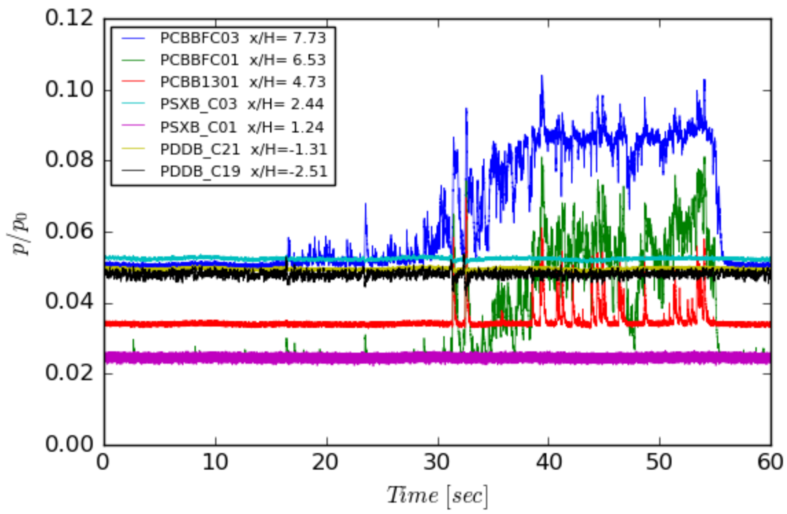

Figure 2.5: Cowl-side wall pressure histories for aft-fueled case. Adapted from Donbar *et al.*[10]

the ratio of the time-mean combustion $p_{comb}(x)$ and tare $p_{tare}(x)$ pressures. For these experiments, the threshold was set to ten percent above the tare condition. The time-mean PCST location for the two reference fuel-staging conditions are also summarized in Table 2.2.

The experiments found a strong correlation between upstream $B2$ injector fuel flow rate and the time-mean PCST position as shown in Figure 2.6. This trend is consistent with observations in the literature. Hunt *et al.*,[108] for example, show a linear relation between shock-train position and back pressure ratio for an unfueled rectangular isolator. Consequently, these two reference experimental cases are selected to bound the extremes of PCST positions upstream and downstream of the isolator entrance for the computational study.

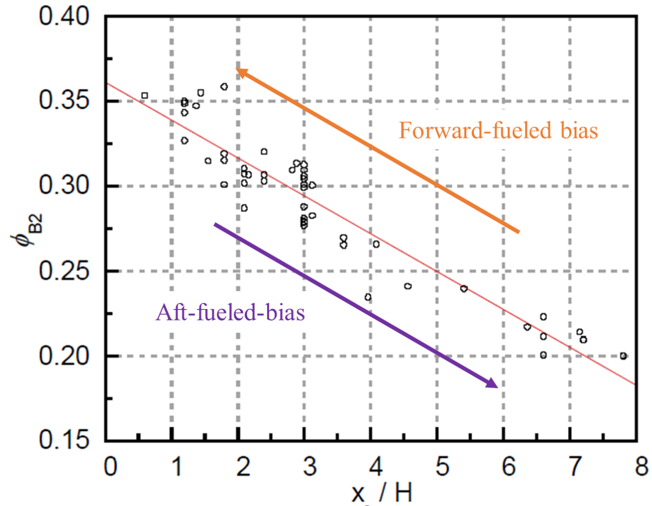

Figure 2.6: Experimentally measured, steady-state PCST streamwise locations. Adapted from Donbar *et al.*[10]

Chapter 3

Computational Approach

The current model-based approach utilizes the Unsteady Reynolds-Averaged Navier-Stokes, finite-volume framework within the CFD++[225] solver.† The system of governing equations are first introduced (§ 3.1). Since turbulence modeling introduces additional model terms, the closure methods are then described (§ 3.2). Numerical flux and temporal integration schemes are discussed in § 3.3. The computational domain and domain-decomposition approach are described (§ 3.4). The boundary and initial conditions are summarized in sections § 3.5 and § 3.6, respectively.

3.1 Governing Equations

The governing system of conservation equations include energy (eqn. 3.1), mass (eqn. 3.2), momentum (eqn. 3.3), and multi-species (eqn. 3.4) transport and are written using indicial (Einstein) notation.‡ The energy equation is written in terms of total energy (eqn. 3.5) and total enthalpy (eqn. 3.6). Species transport is defined in terms of mass fraction Y_s and the equations are written for $ns-1$ species where ns

---

† Versions 14.1.1 to 16.1.4 were used.

‡ The principal coordinates corresponding to indices $i = 1, 2, 3$ are equivalent to the streamwise (x), vertical (y), and spanwise (z) directions, respectively.

is the total number of species. The ns-th species is computed from continuity. The momentum equations employ Stokes' assumption for the shear stress (eqn. 3.7). The heat flux vector contains contributions from from conduction, written from Fourier's law (eqn. 3.8), and interspecies diffusion. Fickian diffusion is assumed with a single binary diffusion coefficient $\mathcal{D}$ for all species. The system is closed for pressure with the state relation for a thermally perfect gas (eqn. 3.9) based on the mixture gas constant (eqn. 3.10) computed from the species mass fractions Y_s, molecular weights W_s, and universal gas constant $\mathcal{R}_u$.

$$\frac{\partial(\rho E)}{\partial t} = \frac{\partial}{\partial x_j}\left(\rho H u_j\right) = \frac{\partial}{\partial x_j}\left(-q_j - u_j \tau_{ij}\right) \tag{3.1}$$

$$\frac{\partial \rho}{\partial t} + \frac{\partial}{\partial x_j}\left(\rho u_j\right) = 0 \tag{3.2}$$

$$\frac{\partial(\rho u_i)}{\partial t} + \frac{\partial}{\partial x_j}\left(\rho u_i u_j\right) = \frac{\partial}{\partial x_j}\left(-\delta_{ij} p + \tau_{ij}\right) \tag{3.3}$$

$$\frac{\partial(\rho Y_s)}{\partial t} + \frac{\partial}{\partial x_j}\left(\rho Y_s u_j\right) = \frac{\partial}{\partial x_j}\left(\rho \mathcal{D} \frac{\partial Y_s}{\partial x_j}\right) + \dot{\omega}_s \tag{3.4}$$

$$E = h_{mix} - \frac{p}{\rho} + \frac{1}{2} u_i u_i \tag{3.5}$$

$$H = h_{mix} + \frac{1}{2} u_i u_i \tag{3.6}$$

$$\tau_{ij} = \mu_{mix}\left(\frac{\partial u_i}{\partial x_j} + \frac{\partial u_j}{\partial x_i}\right) - \frac{2}{3}\delta_{ij}\mu_{mix}\frac{\partial u_k}{\partial x_k} \tag{3.7}$$

$$q_j = -\lambda_{mix}\frac{\partial T}{\partial x_j} - \sum_s \rho \mathcal{D} \frac{\partial Y_s}{\partial x_j} h_s(T) \tag{3.8}$$

$$p = \rho R_{mix} T \tag{3.9}$$

$$R_{mix} = \mathcal{R}_u \sum_s \frac{Y_s}{W_s} \tag{3.10}$$

3.1.1 Mixture Properties

For the multi-species flow considered, the effective mixture properties are computed for thermal conductivity λ, dynamic viscosity μ, and enthalpy h. The flow is assumed to behave as a mixture of thermally perfect gases whose individual thermodynamic properties are computed using NASA[226] curve fits (eqns. 3.11-3.12) defined over the temperature ranges $300 \leq T \leq 1000$ and $1000 \leq T \leq 5000$.† The enthalpy of the mixture is subsequently computed from eqn. 3.13 where Δh_s^o is the enthalpy of formation.

$$\frac{c_{p_s}}{R_s} = a_{1,s} + a_{2,s}T + a_{3,s}T^2 + a_{4,s}T^3 + a_{5,s}T^4 \tag{3.11}$$

$$\frac{g_s}{R_s} = a_{1,s}(T - T\ln T) - \frac{a_{2,s}}{2}T^2 - \frac{a_{3,s}}{6}T^3 - \frac{a_{4,s}}{12}T^4 - \frac{a_{5,s}}{20}T^5 + \frac{\Delta h_s^o}{R_s} - a_{7,s}T \tag{3.12}$$

$$h_{mix} = \sum_s Y_s \int c_{p_s} dT + \sum_s Y_s \Delta h_s^o \tag{3.13}$$

The constituent species' viscosities and thermal conductivities are computed by Sutherland's relations (eqns. 3.14-3.15). Wilke's[227] mixing rule is employed to compute the mixture viscosity‡ (eqns. 3.16-3.17) which is reasonable (*cf* Palmer *et al.*[228]) for the modest total temperature ($T_0 < 2000$) of the approximately Mach 5 flow of present work. Similarly, although thermal non-equilibrium can affect[229,230] ignition behavior in hypersonic vehicles, thermal non-equilibrium effects are assumed to be negligible for the *relatively* low total temperature.

†The solver however modifies the lower bound of these fits such that the lower range is $100 \leq T \leq 1000$.[225]

‡Mixture thermal conductivity is computed in the same manner and is not shown for brevity.

$$\frac{\mu_s}{\mu_{s,ref}} = \left(\frac{T}{T_{ref,s}}\right)^{3/2} \frac{T_{ref,s} + \mathcal{S}_{\mu,s}}{T + \mathcal{S}_{\mu,s}} \tag{3.14}$$

$$\frac{\lambda_s}{\lambda_{s,ref}} = \left(\frac{T}{T_{ref,s}}\right)^{3/2} \frac{T_{ref,s} + \mathcal{S}_{\lambda,s}}{T + \mathcal{S}_{\lambda,s}} \tag{3.15}$$

$$\mu_{mix} = \sum_s \left(\frac{X_s \mu_s}{\Sigma_j X_j \phi_{sj}}\right) \tag{3.16}$$

$$\phi_{sj} = \frac{\left[1 + \left(\frac{\mu_s}{\mu_j}\right)^{1/2} \left(\frac{W_s}{W_j}\right)^{1/4}\right]^2}{\left[8\left(1 + \frac{W_s}{W_j}\right)\right]^{1/2}} \tag{3.17}$$

3.1.2 Chemistry

There are many popular approaches to chemistry modeling in high-speed flows. The Eddy Dissipation Concept-based models[231] are applied for mixing-limited conditions where reaction timescales are small relative to the turbulent timescales (Damköhler number ($Da > 1$)). These methods are attractive for their computationally efficiency, *i.e.* they typically utilize one-step (global) chemistry. While some efforts[232,233] have successfully used mixing-limited methods in the study of the ethylene-fueled HIFiRE 2 combustor, the range of fluid scales in scramjet combustors may vary and be less than or on the same order as the chemical time scales, such that the fast chemistry assumption is not appropriate.[58,234] In contrast, finite-rate kinetics approaches, which compute chemical reaction rates as a function of thermodynamic state and mixture composition, may be more physical between extremes of chemical equilibrium and frozen flow. The range of flow and chemical scales is assessed in § 4.3.3.

For this work a finite-rate chemistry approach is adopted because of the wide range of turbulent and chemical scales observed[235] in scramjet combustors. This assumption is assessed in terms of the fluid and chemical scales of the present combustor which are analyzed in the subsequent chapter (§ 4.3.3). This method relies on a set of chemical reaction equations which constitute a reaction mechanism. A general chemical reaction step is written in terms of the stoichiometric coefficients of the reactants ν' and products ν'' given in eqn. 3.18 where M_s is symbol of the s-th species. The forward reaction rate of the k-th step is written in Arrhenius form (eqn. 3.19) as a function of frequency factor (A_k), temperature exponent (b_k), and activation energy (E_{a_k}). The backwards reaction rate k_b is computed (eqn. 3.20) from the equilibrium constant based on partial pressures K_p (eqn. 3.21). The latter is a function of the change in Gibbs energy defined in eqn. 3.22. Consequently, the production rate of the s-th species in each reaction k is written in eqn. 3.23 as a function of the forward and backward reaction rates and species molar concentration C_s. Summing over all reaction steps k yields the net production rate of the s-th species (eqn. 3.24).

$$\Sigma\nu'_s M_s \leftrightarrows \Sigma\nu''_s M_s \tag{3.18}$$

$$k_{f_k} = A_k T^{b_k} \exp\left(\frac{-E_{a_k}}{\mathcal{R}_u T}\right) \tag{3.19}$$

$$\frac{k_f}{k_b} = K_p \left(\frac{p}{\mathcal{R}_u T}\right)^{\Sigma\nu'' - \Sigma\nu'} \tag{3.20}$$

$$K_p = \exp \frac{-\Delta \bar{G}^o}{\mathcal{R}_u T} \tag{3.21}$$

$$\Delta \bar{G}^o_k = \sum_l \nu''_{lk} W_l g_l - \sum_l \nu'_{lk} W_l g_l \tag{3.22}$$

$$\dot{\omega}_{sk} = W_s(\nu''_{sk} - \nu'_{sk}) \left[\sum_{k=1}^{nr} k_{f,k} \Pi_l C_l^{\nu'_{ik}} - \sum_{k=1}^{nr} k_{b,k} \Pi_l C_l^{\nu''_{ik}} \right] \tag{3.23}$$

$$\dot{\omega}_s = \sum_k \dot{\omega}_{sk} \tag{3.24}$$

Chemical kinetics pose an additional modeling challenge since the selection of a kinetics mechanism can profoundly affect solution accuracy. However, the selection of a kinetics mechanism requires balancing mechanism detail with computational cost.[236] Moreover, the kinetics are assumed to follow laminar rates, which may not be generalizable to supersonic turbulent combustion.[237] As part of the sensitivity study (§ 4.3.1), two kinetics mechanisms are considered, each tailored to supersonic ethylene-air combustion. The first, a 'quasi-global' mechanism,[8] contains 3-steps and 6 species (Table 3.1) and is chosen for computational efficiency. However, its simplicity limits the ability to capture ignition delay in comparison with other ethylene mechanisms.[236] The mechanism is also expected to overpredict heat release. As shown in the Appendix (§ A.1), for example, the quasi-global mechanism is shown to predict higher adiabatic flame temperatures compared to a reference detailed mechanism. A second, reduced mechanism,[238,239] the Taitech-Princeton (TP2) reaction set, contains 22 species and over 200 reaction steps.† Its inclusion for consideration follows its successful application in simulation of an axisymmetric research combustor,[240] the University of Virginia Scramjet Combustor Facility (UVaSCF),[241] and the HIFiRE 2[196] combustor.

†The TP2 mechanism also employs the quasi-steady-state (QSS) assumption for some intermediate reactions whose timescales are relatively small.

Table 3.1: Arrhenius rate coefficients for three-step, ethylene mechanism: Frequency factor A, temperature exponent b and activation temperature T_a. Reproduced from Baurle *et al.*[8]

Reaction	A_k $[cm^3\ mol^{-1}\ s^{-1}]$	b	T_a $[K]$
$C_2H_4 + O_2 \rightleftharpoons 2CO + 2H_2$	2.10×10^{14}	0.0	18015.3
$2CO + O_2 \rightleftharpoons 2CO_2$	3.48×10^{11}	2.0	10134.9
$2H_2 + O_2 \rightleftharpoons 2H_2O$	3.00×10^{20}	-1.0	0.0

3.2 Turbulence Modeling

Applying the Reynolds- (eqns. 3.25-3.26) and Fávre-averaging (eqns.3.27-3.28) operators to the primitive variables (eqns. 3.29- 3.34) yields the set of modeled governing equations (eqns. 3.35-3.39). The averaged shear-stress (eqn. 3.40), heat-flux (eqn. 3.41), mixture enthalpy (eqn. 3.42), reaction rate (eqn. 3.43) and mixture properties μ_{mix} are written in terms of the averaged state variables. Averaging yields several new un-closed correlation terms. The gradient diffusion[242,243] assumption is used to close these terms (eqns. 3.44-3.46). A variable Schmidt number ($Sc \equiv \nu/\mathcal{D}$) model for the $\widetilde{Y_s''u_j''}$ term is also considered (§ 3.2.1). A non-linear turbulence closure is applied for the Reynolds stresses $\widetilde{u_i''u_j''}$ as described in § 3.2.2.

$$\bar{f} = \lim_{\mathcal{T}\to\infty} \frac{1}{\mathcal{T}} \int_0^{\mathcal{T}} f(t)dt \tag{3.25}$$

$$f' = f(t) - \bar{f} \tag{3.26}$$

$$\tilde{f} = \frac{\overline{\rho f}}{\bar{\rho}} \tag{3.27}$$

$$f'' = f(t) - \tilde{f} \tag{3.28}$$

$$\rho = \bar{\rho} + \rho' \tag{3.29}$$

$$p = \bar{p} + p' \tag{3.30}$$

$$u_i = \tilde{u}_i + u_i'' \tag{3.31}$$

$$T = \tilde{T} + T'' \tag{3.32}$$

$$h = \tilde{h} + h'' \tag{3.33}$$

$$Y_s = \tilde{Y}_s + Y'' \tag{3.34}$$

$$\frac{\partial(\bar{\rho}\tilde{E})}{\partial t} + \frac{\partial}{\partial x_j}\left(\bar{\rho}\tilde{H}\tilde{u}_j\right) = \frac{\partial}{\partial x_j}\left(-\tilde{q}_j + \tilde{u}_j\tilde{\tau}_{ij} - \bar{\rho}\widetilde{h''u_j''} - \bar{\rho}\tilde{u}_i\widetilde{u_i''u_j''} - \bar{\rho}\widetilde{k''u_j''}\right) \tag{3.35}$$

$$\frac{\partial\bar{\rho}}{\partial t} + \frac{\partial}{\partial x_j}\left(\bar{\rho}\tilde{u}_j\right) = 0 \tag{3.36}$$

$$\frac{\partial(\bar{\rho}\tilde{u}_i)}{\partial t} + \frac{\partial}{\partial x_j}\left(\bar{\rho}\tilde{u}_i\tilde{u}_j\right) = \frac{\partial}{\partial x_j}\left(-\delta_{ij}\bar{p} + \tilde{\tau}_{ij} - \bar{\rho}\widetilde{u_i''u_j''}\right) \tag{3.37}$$

$$\frac{\partial\left(\bar{\rho}\tilde{Y}_s\right)}{\partial t} + \frac{\partial}{\partial x_j}\left(\bar{\rho}\tilde{Y}_s\tilde{u}_j\right) = \frac{\partial}{\partial x_j}\left(\frac{\mu}{Sc}\frac{\partial\tilde{Y}_s}{\partial x_j} - \bar{\rho}\widetilde{Y_s''u_j''}\right) + \tilde{\dot{\omega}}_s \tag{3.38}$$

$$\bar{p} = \tilde{\rho}R_{mix}(\tilde{Y})\tilde{T} \tag{3.39}$$

$$\tilde{\tau}_{ij} = \mu_{mix}\left(\frac{\partial\tilde{u}_i}{\partial x_j} + \frac{\partial\tilde{u}_j}{\partial x_i}\right) - \frac{2}{3}\delta_{ij}\mu_{mix}\frac{\partial\tilde{u}_k}{\partial x_k} \tag{3.40}$$

$$\tilde{q}_j = -\lambda_{mix}\frac{\partial\tilde{T}}{\partial x_j} - \sum_s \frac{\mu}{Sc}\frac{\partial\tilde{Y}_s}{\partial x_j}\tilde{h}_s(T) \tag{3.41}$$

$$\tilde{h} = h(\tilde{T}, \tilde{Y}) \tag{3.42}$$

$$\tilde{\dot{\omega}}_s = \dot{\omega}_s(\tilde{T}, \tilde{Y}) \tag{3.43}$$

$$\bar{\rho}\widetilde{h''u_j''} = -\frac{\mu_t}{Pr_t}\frac{\partial\tilde{h}}{\partial x_j} \tag{3.44}$$

$$\bar{\rho}\widetilde{Y_s''u_j''} = -\frac{\mu_t}{Sc_t}\frac{\partial\tilde{Y}_s}{\partial x_j} \tag{3.45}$$

$$\bar{\rho}\widetilde{k''u_j''} = -\frac{\mu_t}{\sigma_k}\frac{\partial\tilde{k}}{\partial x_j} \tag{3.46}$$

3.2.1 Variable Schmidt Model

While a constant turbulent Schmidt number (Sc_t) is primarily employed for the computations in this study, a variable Schmidt number model is also considered. The model by Goldberg *et al.*[244] has been validated[245] for several supersonic mixing flows, including the hydrogen-fueled scramjet experiments of Burrows and Kurkov.[246] The variable Sc_t correlation is defined, in incompressible form, from eqns. 3.47-3.48 where Re_t is the turbulent Reynolds number (eqn. 3.49). In compressible form, $u'u'$ terms are replaced with $u''u''$; commensurately, the mean scalar gradients are replaced with gradients of their Fávre averages. The hatted index ($\hat{i}$), by the convention of Goldberg *et al.*, indicates that summation is not to be performed on that index. The diffusivity $\mathcal{D}$ (eqns. 3.50-3.53) is computed from the species s with maximum gradient of Y in conjunction with the mean strain-rate magnitude $|S| = \sqrt{S_{ij}S_{ij}}$. The final expression for Sc_t is given by eqns. 3.54-3.55. Closure coefficients for this approach are summarized in Table 3.2.

$$\overline{u_i'Y_s'} = \frac{T_t}{C_{\theta_1} + \frac{1}{2}(\mathcal{P}_k/\epsilon - 1)} \left[\overline{u_i'u_j'} \frac{\partial \bar{Y}}{\partial x_j} - \frac{C_{\theta_2}}{6R_\theta} f_\theta \sqrt{\left(\overline{u_{\hat{i}}'u_j'}\ \overline{u_{\hat{i}}'u_j'} \right) \left(\frac{\partial \bar{Y}}{\partial x_k} \frac{\partial \bar{Y}}{\partial x_k} \right)} \right] \tag{3.47}$$

$$f_\theta = \beta_\theta \frac{tanh(\alpha_\theta Re_t^{3/2})}{tanh(\beta_\theta Re_t^{3/2})} \tag{3.48}$$

$$Re_t = \frac{\bar{k}^2}{\nu\bar{\epsilon}} \tag{3.49}$$

Table 3.2: Variable Schmidt model closure coefficients.

Correlation	$R_\theta = 0.8$	$C_{\theta_1} = 3$	$C_{\theta_2} = 0.6$
Damping	$\alpha_\theta = 0.1$	$\beta_\theta = 5$	
Schmidt	$Sc_{t,const} = 0.7$	$\phi_\theta = 2$	$\lambda_\theta = 10^{-5}$

$$\mathcal{D}^{-1} = \sqrt{\frac{\frac{\partial \bar{Y}}{\partial x_j}\frac{\partial \bar{Y}}{\partial x_j}}{\overline{u_i'Y'}\;\;\overline{u_i'Y'}}} \tag{3.50}$$

$$\sigma_{t_1} = \nu_t \mathcal{D}^{-1} \tag{3.51}$$

$$\sigma_{t_2} = \frac{\sqrt{\overline{u_i'u_j'}\;\overline{u_i'u_j'}}}{|S|}\mathcal{D}^{-1} \tag{3.52}$$

$$\sigma_t = max\left\{\sigma_{t_1}, \sigma_{t_2}\right\} \tag{3.53}$$

$$Sc_t = \begin{cases} Sc_{t,const} & \zeta^2 < \lambda_\theta \\ max\left\{0.1, min\left[Sc_{t,const}, \phi_\theta \sigma_t\right]\right\} & \zeta^2 \geq \lambda_\theta \end{cases} \tag{3.54}$$

$$\zeta^2 = \frac{\partial \bar{Y}}{\partial x_j}\frac{\partial \bar{Y}}{\partial x_j} \tag{3.55}$$

3.2.2 Reynolds Stresses

As explored in several numerical studies of supersonic and hypersonic flows,[247–249] the choice of turbulence model plays a critical role in the predictions of RANS computations. The selection of a non-linear k-ϵ model (which falls in the family of Explicit Algebraic Reynolds Stress Models) for the present work is motivated by previous successes in computations of the HIFiRE Flight 2 configuration.[196,233] Crucially, the cubic k-ϵ model allows for anisotropy of the normal Reynolds stresses and permits[250] capture of streamline curvature making it an attractive model for the 3-D flowfields typical of scramjet combustors. The non-linear turbulence closure is also attractive since EASM type models have been shown to capture secondary flows in channels[251] which are important[252] for modeling SBLIs in rectangular ducts. Following the work of Yentsch,[196] the compressibility correction in the solver is employed. The compressibility correction[253] accounts for the pressure strain which appears in the complete Turbulent Kinetic Energy transport equation.[254]†

The non-linear turbulence model employs a realizable k-ϵ formulation[256] (eqns. 3.56-3.57) where turbulent production and dissipation terms are described by eqns. 3.58-3.64. Reynolds stresses are subsequently closed[250] using eqn. 3.65 with symmetric (eqn. 3.66) and anti-symmetric (eqn. 3.67) components of the velocity gradient tensor. The deviatoric part of S_{ij} is denoted as a starred quantity (eqn. 3.68) and non-dimensional strain and vorticity, used by the closure coefficients (Table 3.3), are given by eqns. 3.61-3.70. The turbulent viscosity is defined using eqns. 3.71-3.72. Realizability, which enforces physical (realizable) limits on quantities such as eddy-viscosity μ_t and Reynolds stresses, can help improve model predictions. Here, realizability is enforced by implementation of the Bradshaw limiter,[257,258] recommended[225] for hypersonic flows, which limits eddy viscosity in conjunction with the damping function (f_μ) and adjusts the C_μ coefficient. Additionally, the model is formed such that turbulent timescale τ_t does not fall below the Kolmogorov scale ($\tau_k = \sqrt{\nu/\epsilon} = 1$) near walls.

† As noted by Wilcox,[255] there exist several proposed corrections for the pressure dilatation term, $\overline{p' \frac{\partial u_i''}{\partial x_i}}$. These corrections are typically written in terms of a local turbulent Mach number ($Ma_t \propto u'/c$), *e.g.* Sarkar.[254]

$$\frac{\partial(\bar{\rho}\tilde{k})}{\partial t} + \frac{\partial}{\partial x_j}(\bar{\rho}\tilde{u}_j\tilde{k}) = \frac{\partial}{\partial x_j}\left[\left(\mu + \frac{\mu_t}{\sigma_k}\right)\frac{\partial \tilde{k}}{\partial x_j}\right] + \mathcal{P}_k - \bar{\rho}\tilde{\epsilon} \tag{3.56}$$

$$\frac{\partial(\bar{\rho}\tilde{\epsilon})}{\partial t} + \frac{\partial}{\partial x_j}(\bar{\rho}\tilde{u}_j\tilde{\epsilon}) = \frac{\partial}{\partial x_j}\left[\left(\mu + \frac{\mu_t}{\sigma_\epsilon}\right)\frac{\partial \tilde{\epsilon}}{\partial x_j}\right] + \left(C_{\epsilon_1}\mathcal{P}_k - C_{\epsilon_2}\bar{\rho}\tilde{\epsilon} + E_\epsilon\right)\mathbf{T}_t^{-1} \tag{3.57}$$

$$\mathcal{P}_k = -\bar{\rho}\widetilde{u_i''u_j''}\frac{\partial \tilde{u}_i}{\partial x_j} \tag{3.58}$$

$$E_\epsilon = \bar{\rho}A_E V\sqrt{\tilde{\epsilon}\mathbf{T}_t}\Psi \tag{3.59}$$

$$\mathbf{T}_t = \tau_t \ max\{1, \xi^{-1}\} \tag{3.60}$$

$$\tau_t = \frac{\tilde{k}}{\tilde{\epsilon}} \tag{3.61}$$

$$\xi = \frac{\sqrt{Re_t}}{C_\tau} \tag{3.62}$$

$$\Psi = max\left\{\frac{\partial \tilde{k}}{\partial x_j}\frac{\partial \tau_t}{\partial x_j}, 0\right\} \tag{3.63}$$

$$V = max\{\tilde{k}^{\frac{1}{2}}, (\nu\tilde{\epsilon})^{\frac{1}{4}}\} \tag{3.64}$$

$$\begin{aligned}
\bar{\rho}\widetilde{u_i''u_j''} = {} & \bar{\rho}\tilde{k}\delta_{ij} - \mu_t S_{ij} \\
& + C_1\mu_t\tau_t\left(S^\star_{ik}S^\star_{kj} - \frac{1}{3}S^\star_{kl}S^\star_{kl}\delta_{ij}\right) \\
& + C_2\mu_t\tau_t\left(\Omega_{ik}S^\star_{kj} + \Omega_{jk}S^\star_{ki}\right) \\
& + C_3\mu_t\tau_t\left(\Omega_{ik}\Omega_{jk} - \frac{1}{3}\Omega_{lk}\Omega_{lk}\delta_{ij}\right) \\
& + C_4\mu_t\tau_t^2\left(S^\star_{ki}\Omega_{lj} + S^\star_{kj}\Omega_{li}\right)S^\star_{kl} \\
& + C_5\mu_t\tau_t^2\left(\Omega_{il}\Omega_{lm}S^\star_{mj} + S^\star_{il}\Omega_{lm}\Omega_{mj} - \frac{2}{3}S^\star_{lm}\Omega_{mn}\Omega_{nl}\delta_{ij}\right) \\
& + C_6\mu_t\tau_t^2\left(S^\star_{ij}S^\star_{kl}S^\star_{kl}\right) \\
& + C_7\mu_t\tau_t^2\left(S^\star_{ij}\Omega_{kl}\Omega_{kl}\right)
\end{aligned} \tag{3.65}$$

Table 3.3: Cubic k-ϵ turbulence model closure coefficients.

TKE/TED	$\sigma_k = 1.0$ $A_E = 0.15$	$\sigma_\epsilon = 1.3$ $C_\tau = \sqrt{2}$	$C_{\epsilon_1} = 1.44$ $A_\mu = 0.0085$	$C_{\epsilon_2} = 1.92$
Re-stresses	$C_\mu = \frac{2/3}{A_1+\mathbf{S}+0.9\mathbf{\Omega}}$ $C_1 = \frac{3/4}{(1000+\mathbf{S}^3)C_\mu}$ $C_5 = 0$	$A_1 = 1.25$ $C_2 = \frac{15/4}{(1000+\mathbf{S}^3)C_\mu}$ $C_6 = -2C_\mu^2$	$C_3 = \frac{-19/4}{(1000+\mathbf{S}^3)C_\mu}$ $C_7 = -C_6$	$C_4 = -10C_\mu^2$

$$S_{ij} = \left(\frac{\partial \tilde{u}_i}{\partial x_j} + \frac{\partial \tilde{u}_j}{\partial x_i}\right) \tag{3.66}$$

$$\Omega_{ij} = \left(\frac{\partial \tilde{u}_i}{\partial x_j} - \frac{\partial \tilde{u}_j}{\partial x_i}\right) \tag{3.67}$$

$$S^\star_{ij} = S_{ij} - \frac{2}{3}\frac{\partial \tilde{u}_k}{\partial x_k}\delta_{ij} \tag{3.68}$$

$$\mathbf{S} = \tau_t\sqrt{\frac{1}{2}S^\star_{ij}S^\star_{ij}} \tag{3.69}$$

$$\mathbf{\Omega} = \tau_t\sqrt{\frac{1}{2}\Omega_{ij}\Omega_{ij}} \tag{3.70}$$

$$\mu_t = C_\mu f_\mu \bar{\rho}\frac{\tilde{k}^2}{\tilde{\epsilon}} \tag{3.71}$$

$$f_\mu = \frac{1-e^{A_\mu Re_t}}{1-e^{-\sqrt{Re_t}}} max\{1, \xi^{-1}\} \tag{3.72}$$

3.3 Numerics

3.3.1 Fluxes and Reconstruction

Inviscid fluxes are computed using the positivity-preserving[259] variant of the Harten-Lax-van-Lear[260] with Contact discontinuity (HLLC) scheme based on the work of Toro.[261] Reconstruction for inviscid flux evaluation is achieved by a multi-dimensional, nodal-based method where Total Variation Diminishing (TVD)[262,263] is enforced by either a minmod or Van-Leer-like slope limiter. The Van-Leer limiter is used, as it was found to reduce residuals by one order of magnitude in fewer iterations compared to the minmod approach. Second-order differencing is applied for the viscous fluxes.

3.3.2 Time Integration

The solution is advanced in time using an implicit, dual-time-stepping approach. Writing the governing system of equations (eqn. 3.73) and linearizing the right-hand-side (RHS) yields eqn. 3.75. A sub- (inner) time-step ($\Delta\tau$) is introduced (eqn. 3.76-3.77) to solve for $\delta Q^{\star}$ (eqn. 3.78). At the start of each global step (Δt), $Q^{\star}$ is set to Q^{n} in order to sub-iterate for $\delta Q^{\star}$. At convergence of the sub-iteration $Q^{\star\star} = Q^{\star}$, such that the solution at the next timestep is $Q^{n+1} = Q^{\star\star}$.

To converge the inner-iterations, an Algebraic Multi-Grid (AMG) scheme using a W-cycle is applied. Generally, 20 levels per cycle and 5 cycles per global step are employed.[†] Agglomeration is stopped at 10 or fewer groups. Although the W-cycle is double the memory cost of V-cycle, the method is more efficient per cycle in driving down the residual.[225] The inner iteration convergence criterion is specified as one order-of-magnitude reduction of the residuals. The inner timestep varies locally in space and is computed from the specified CFL number, $CFL \propto c\Delta\tau/\Delta x = 20$.

[†]Varying the number of levels or cycles was found to have negligible effect in user wall time for steady-fueling computations.

$$\frac{\partial Q}{\partial t} = RHS \tag{3.73}$$

$$\frac{Q^{n+1} - Q^n}{\Delta t} = RHS^{n+1} \tag{3.74}$$

$$\frac{\delta Q}{\Delta t} = RHS^n + \left(\frac{\partial RHS}{\partial Q}\right)^n \delta Q \tag{3.75}$$

$$\frac{\delta Q}{\Delta \tau} + \frac{\delta Q}{\Delta t} = RHS^n + \left(\frac{\partial RHS}{\partial Q}\right)^n \delta Q \tag{3.76}$$

$$\left[\frac{I}{\Delta \tau} + \frac{I}{\Delta t} - \left(\frac{\partial RHS}{\partial Q}\right)^\star\right] \delta Q^\star = RHS^\star - \frac{Q^\star - Q^n}{\Delta t} \tag{3.77}$$

$$\delta Q^\star = Q^{\star\star} - Q^\star \tag{3.78}$$

3.4 Computational Domain and Domain Decomposition

As shown in Figure 3.1, the computational domain includes the facility nozzle, distortion generator, isolator, cavity, and expansion duct. Boundaries are color-coded with symmetry at the combustor midspan ($\hat{z} = 0$) (yellow), nozzle inlet (red), expansion duct outflow (blue), fuel injector inflows (pink), and walls (grey). Although RANS solutions can be affected by symmetry assumptions,[264] the present computations at steady-fueling conditions do not appear sensitive to this geometry simplification. Therefore, symmetry at the mid-span of the combustor is assumed to limit the cost of discretizing the $L \approx 1\ m$ domain.

To efficiently compute the flowfield, the code is parallelized which requires partitioning the domain into multiple sub-domains.† A grid resolution study is considered in the next chapter (§ 4.1). However, solutions are typically executed with $256 - 512$ processors because of the limited improvements in user wall time

†Domain decomposition is computed using the ParMETIS library.[265]

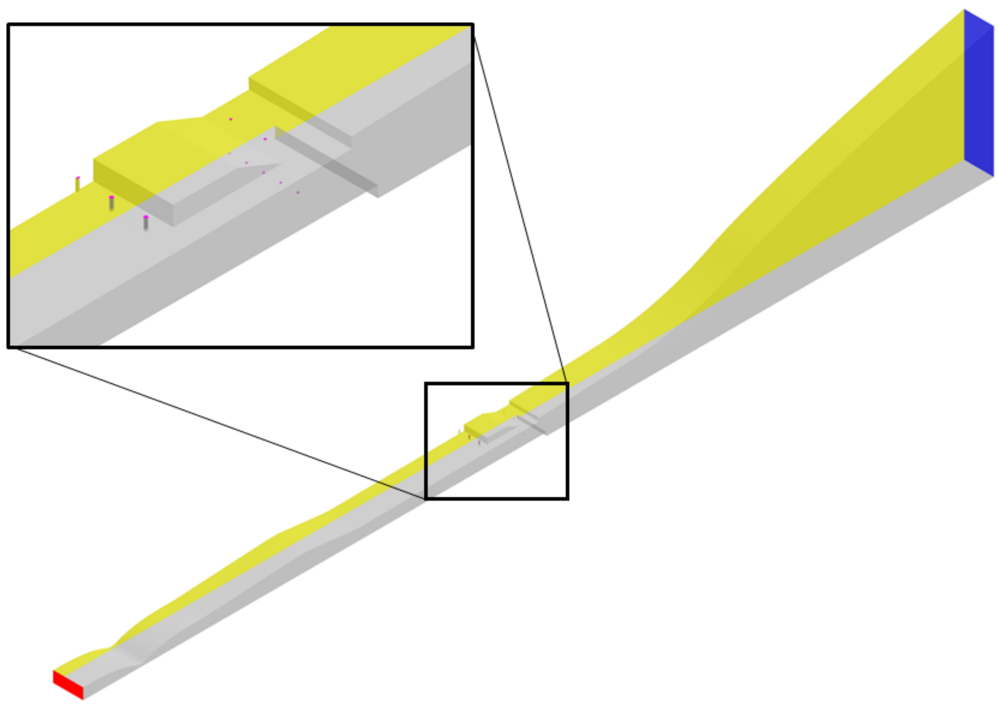

Figure 3.1: Computational domain and boundaries: *red* - nozzle inlet, *blue* - expansion outflow, *yellow* - symmetry, *pink* - fuel injector inflows, and *grey* - walls.

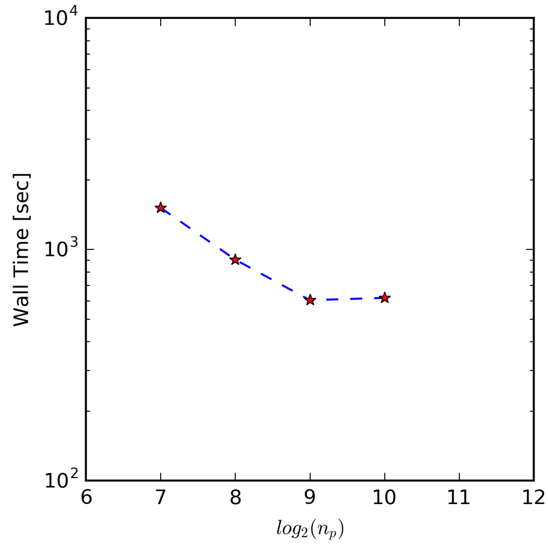

Figure 3.2: Code scaling with domain partitions for 10^3 iterations of tare solution on 6-million cell grid.

with increasing processor count, attributable to communication overhead. This code-scaling behavior is shown in Figure 3.2. These data points represent 1000 iterations computed for steady, un-fueled combustor operation on a 6 million cell grid. The computational cost for steady-state un-fueled, steady-state fueled, and transient fueling cases are of $\mathcal{O}(10)K$, $\mathcal{O}(25)K$, $\mathcal{O}(90)K$ CPU-hours, respectively, on a SGI ICE X machine.†

3.5 Boundary Conditions

Besides the symmetry assumption to limit domain descrization cost, a turbulence wall model is applied to further limit the computational cost for discretizing the near wall region over the domain length of 1.5 m. The wall model enables much coarser wall-normal grid spacing at wall boundaries such that the first grid point away from

†The 1.5 PFLOPS Spirit is based on the Intel Xeon E5 2600 CPU architecture.[266]

the wall is greater than $y^+ \gg 1$ in inner wall units (eqn. 3.79-3.80). Careful attention is given to modeling the heat-flux boundary conditions in addition to the nozzle inflow, fuel-injector inflows, and outflow boundaries is described below.

$$u_\tau = \sqrt{\frac{\tau_w}{\rho}} \tag{3.79}$$

$$y^+ = \frac{y u_\tau}{\nu} \tag{3.80}$$

3.5.1 Wall Model

A turbulence wall model, based on the work of Launder,[267] is applied where $\sqrt{k}$ is used as the scaling parameter, rather than the friction velocity (u_τ), resulting in $y^\star$ (eqn. 3.82) as the local, non-dimensional wall distance. Closure coefficients for the approach are shown in Table 3.4. As part of the closure coefficients, the logarithmic overlap region is assumed to start at $y_v^\star = 11.2$. The modification of Grotjans and Menter[268] is also applied where $y^\star$ at the first cell off wall ($y_1^\star$) is defined by eqn. 3.83.† Wall shear stress (eqn. 3.84) is computed from the local velocity component tangential to the wall (U_t) and the Van-Driest velocity (U_c) (eqns. 3.85-3.88), which further depends on the local tangential velocity sensitized to the local pressure gradient $\tilde{U}_t$ (eqn. 3.89). Heat flux at the wall is computed for specified wall temperatures using eqns. 3.90-3.91. Alternatively, the wall temperature is determined for an imposed heat flux boundary condition from eqn. 3.92.

$$\kappa^\star = c_\mu^{1/4} \kappa \tag{3.81}$$

$$y^\star = \frac{c_\mu^{1/4} \rho_w y \sqrt{k}}{\mu_w} \tag{3.82}$$

†The modification is equivalent to shifting the wall function solution by Δy_0 (first cell height at the wall). This ignores the viscous sublayer which is assumed thin ($y^+ \lesssim 10$), avoiding the singularity in the log-law, $u^+ = \frac{1}{\kappa} ln\ y^+ + C$, as $y^+ \to 0$.[268]

Table 3.4: Wall model closure coefficients.

van Driest	$\kappa = 0.41$	$c_\mu = 0.09$
Log layer	$y_v^\star = 11.2$	
Heat flux	$\mathbf{E} = 8.8$	

$$y_1^\star = max\{y^\star(y_1), y_v^\star\} \tag{3.83}$$

$$\tau_{w,wm} = \begin{cases} \frac{\mu_w(U_{c_1}-U_t)}{y_1} & y_1^\star \leq y_v^\star \\ \frac{\kappa^\star \rho_w \sqrt{k}_1(U_{c_1}-U_t)}{ln(\mathbf{E}\ y_1^\star)} & y_1^\star > y_v^\star \end{cases} \tag{3.84}$$

$$U_{c_1} = \sqrt{B}\left[arcsin\left(\frac{A_{vD}+\tilde{U}_t}{D}\right) - arcsin\left(\frac{A_{vD}}{D}\right)\right] \tag{3.85}$$

$$A_{vD} = \frac{U_t}{2} - \frac{\gamma R_{mix}\Delta T}{(\gamma-1)PrU_t} \tag{3.86}$$

$$B = \frac{2c_p}{Pr_t}T_w \tag{3.87}$$

$$D = \sqrt{A_{vD}^2 + B} \tag{3.88}$$

$$\tilde{U}_t = \begin{cases} U_t & y_1^\star \leq y_v^\star \\ U_t - \frac{1}{2}\frac{dp}{dx}\left[\frac{y_v}{\kappa^\star \rho\sqrt{k}}ln\left(\frac{y_1}{y_v}\right) + \frac{y_1-y_v}{\mu}\right] & y_1^\star > y_v^\star \end{cases} \tag{3.89}$$

$$q_{w,wm} = \begin{cases} -\tau_w\left[\frac{c_p(T_1-T_w)}{Pr(U_{c_1}-U_t)} + \frac{U_{c_1}-U_t}{2}\right] & y_1^\star \leq y_v^\star \\ -\tau_w\frac{ln(\mathbf{E}\ y_1^\star)}{ln(\mathbf{E}_T y_1^\star)}\left[\frac{c_p(T_1-T_w)}{Pr_t(U_{c_1}-U_t)} + \frac{U_{c_1}-U_t}{2}\right] & y_1^\star > y_v^\star \end{cases} \tag{3.90}$$

$$ln(\mathbf{E}_T) = \kappa(12.8Pr^{0.68} - 7.3) \qquad 0.7 < Pr < 7.5 \tag{3.91}$$

$$q_{w,wm} = -\lambda\frac{T_1 - T_w}{y_1} \tag{3.92}$$

A non-equilibrium approach is employed to set the boundary values for ϵ_w and k_w, as defined using eqns. 3.93-3.96. Turbulence production (eqn. 3.97) and dissipation rate (eqn. 3.98) are defined by the average boundary-layer value when the first point off the wall is located in the log layer ($y_1^\star > y_v^\star$).

$$
\begin{aligned}
k_w &= 0 && (3.93)\\
\epsilon_w &= \frac{2A_\epsilon k_1^2}{\nu Re_y \left(1 - e^{-A_\epsilon Re_y}\right)} && (3.94)\\
Re_y &= max\{\sqrt{2Re_t}, 2A_\epsilon Re_t\} && (3.95)\\
A_\epsilon &= \frac{c_\mu^{3/4}}{2\kappa} && (3.96)
\end{aligned}
$$

$$
\mathcal{P}_k = \begin{cases} 0 & y_1^\star \leq y_v^\star \\ \frac{(\tau_w/\rho_w)^2}{2\kappa^\star \sqrt{k_1} y_1} ln\left(\frac{2y_1}{y_v}\right) & y_1^\star > y_v^\star \end{cases} \quad (3.97)
$$

$$
\epsilon = \begin{cases} \frac{2\mu_1 k_1}{\rho_1 y_1^2} & y_1^\star \leq y_v^\star \\ \frac{k_1}{2y_1}\left[\frac{2\mu_1}{\rho_1 y_v} + \frac{c_\mu^{3/4}\sqrt{k_1}}{\kappa} ln\left(\frac{2y_1}{y_v}\right)\right] & y_1^\star > y_v^\star \end{cases} \quad (3.98)
$$

3.5.2 Wall Heat Flux

Radiative heat flux is estimated to be on order of $\mathcal{O}(10)$ percent of convective heat flux for the geometrically similar HIFiRE 2 combustor.[269–271] Radiation is neglected in the computations because of limited experimental measurements. However, to emulate the wall cooling present in experiments, a local 1-D resistive layer boundary condition is applied to capture the effect of combustor wall material and Thermal Barrier Coating (TBC). The 1-D resistive heat-flux boundary condition is described by eqn. 3.99. Here L_{eff} and λ_{eff} are the effective conductivity and length scale in the resistive layer, and $\Delta_{cell,w}$ is the distance from the wall to the adjacent cell centroid.

$$
\begin{aligned}
-\frac{\lambda_{eff}}{L_{eff}}\left(T_w - T_{amb}\right) &= -\lambda_{mix}\left.\frac{\partial T}{\partial y}\right|_{wall} \\
&= -\lambda_{mix}\frac{T_{cell} - T_w}{\Delta_{cell,w}}
\end{aligned} \quad (3.99)
$$

To specify the 1-D heat flux boundary, an effective thermal conductivity and length scale are required. Estimated thermal conductivity for the nozzle and DG (copper) and isolator and cavity (steel) are taken from tabulated[272] properties at 300 K (Table 3.5) where $T_{amb} = 300\ K$ serves as the approximate temperature of the cooling channel water. The assumed reference temperature of the cooling channels is based on available calorimeter data which indicates a maximum 20 degree change along each cooling loop.[273] The effective length scale (L_{eff}) is computed using the wall-normal depth to the water cooling channels plus the TBC thickness. TBC is only applied in the isolator and cavity regions. The depth to the cooling channels is taken as 2.54 mm (0.1 in) and the TBC coating thickness is estimated to be 0.508 mm (0.02 in).[274] From a circuit analogy, the steel and TBC layers in series yields $\lambda_{eff} \approx 5.8\ Wm^{-1}K^{-1}$ in the isolator and cavity (Figure 3.3).

Injector walls are set at a fixed isothermal temperature taking the average of the aft-fueled and forward-fueled static temperatures estimated from the choked condition and the measured stagnation temperature in the fuel injector plenums. Part of the isolator duct ($0 \leq \hat{x} \leq 5$) is an extension of the DG (copper) section of the tunnel whose thermal properties were not accounted for initially. However, including the slight change ($\leq$ 10 percent) in effective thermal conductivity does not affect predictions. A summary of all thermal wall boundaries is given in Table 3.6.

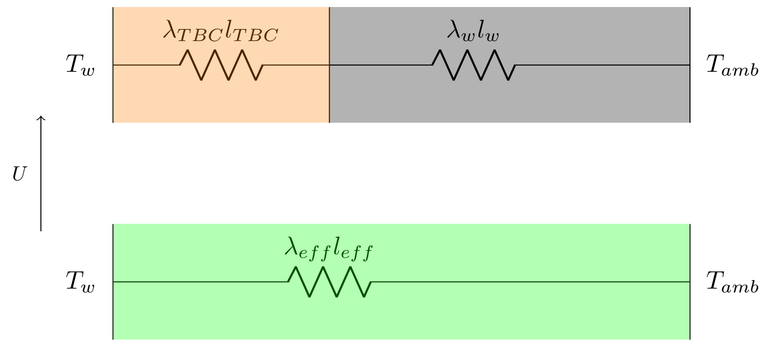

Figure 3.3: Combustor wall heat-flux resistive layer sketch: (*above*) assumed resistances, (*below*) modeled equivalent resistance.

Table 3.5: Estimated thermal conductivity properties for experimental test rig evaluated at 300 K.

Material $[-]$	Thermal Conductivity λ $[Wm^{-1}K^{-1}]$
Copper[272]	401
Steel[272]	41
TBC[274]	1.1

Table 3.6: Modeled wall heat flux boundary conditions.

Boundary	Type	Thickness	Conductivity	Ref. Temperature
$[-]$	$[-]$	L_{eff} $[mm]$	λ_{eff} $[Wm^{-1}K^{-1}]$	T_{ref} $[K]$
Nozzle wall	1-D	0.2540	401	300
DG wall	1-D	0.2540	401	300
Isolator	1-D	0.3048	5.819	300
Cavity	1-D	0.3048	5.819	300
Expansion	1-D	0.3048	5.819	300
B2 inj wall	isothermal	–	–	222.7
B6 inj wall	isothermal	–	–	233.5
C3 inj wall	isothermal	–	–	224.5

3.5.3 Inflow and Outflow

The nozzle inflow boundary is specified from the nominal stagnation temperature and pressure described in § 2.2. The sensitivity study (§ 4.3.1) examines the influence of vitiated and non-vitiated nozzle inflow as a result of the combustion heater. Mass fractions of the constituent species derived from measurements are shown in Table 3.7.[275] Note, for the $(ns-1)$ species transport equations, the small component of non-reactive Argon is lumped into diatomic nitrogen such that the any mass imbalance is absorbed by the last, non-reactive species.[276]

Individual fuel injector flow rates are derived from the as-computed tare (unfueled) solution air massflow and the nominal fuel-air ratio (FAR) splits of the three injector sets (Table 2.2). The computed nozzle flow rate is within five percent of experimental values. From a chemical balance of ethylene-air combustion (eqn. 3.100), the stoichiometric FAR condition is determined from eqn. 3.101. Employing the local fuel-air equivalance ratio ϕ_i, the mass-flow rates of each injector are specified as shown in Table 3.8. Fuel flow is assumed to be uniformly distributed between each injector within a particular set.

Table 3.7: Measured and modeled nozzle conditions for clean and vitiated inflow.

	Clean	Vitiated	
Species	$Y_{s,c}$	$Y_{s,v}$ (expt)	$Y_{s,v}$ (modeled)
N_2	0.767	0.63	0.64
O_2	0.233	0.24	0.24
CO_2	–	0.07	0.07
H_2O	–	0.05	0.05
Ar	–	0.01	–

Table 3.8: Fuel injector boundary conditions.

	Temperature [K]			Flow rate [kg/s]		
Staging Condition	B2	B6	C3	B2	B6	C3
Aft-fueled	222.7	233.5	224.5	0.055	0.091	0.248
Forward-fueled	222.7	233.5	224.5	0.110	0.066	0.072

$$C_2H_4 + 3(O_2 + 3.76N_2) \rightarrow 2CO_2 + 2H_2O + 3 \cdot 3.76N_2 \tag{3.100}$$

$$\begin{aligned} FAR_{st} &= \frac{1\ mol\ C_2H_4}{3\ mol\ (O_2 + 3.76N_2)} \\ &= \frac{1\ mol\ (2 \cdot 12.011\ g/mol + 4 \cdot 1.008\ g/mol)}{3\ mol\ (2 \cdot 15.999\ g/mol + 2 \cdot 14.007\ g/mol)} \\ &= 0.0681 \end{aligned} \tag{3.101}$$

Lastly, the inflow turbulent kinetic energy (TKE) and turbulent eddy dissipation rate (TED) values of $k = k_2$ and $\epsilon = \epsilon_2$ are initialized from eqns. 3.102-3.106 using a specified viscosity ratio $\mu_{t,1}/\mu$, turbulence intensity I_t, and free stream velocity. These are dependent on the damping function f_μ near the wall and the c_μ coefficient assumed for an equilibrium turbulent boundary-layer. U_{ref} is taken as either the nominal fuel injector flow velocity ($\mathcal{O}(300\ m/s)$) or nozzle stagnation velocity ($\approx 1\ m/s$). Although a relatively large viscosity ratio $\mu_t/\mu = 50$ was initially applied, computations are found to be insensitive (§ 4.2) to the imposed value consistent with the work of Yentsch *et al.*[196] 'Noisy' wind-tunnels are known[277] to have higher free stream turbulence intensities ($I_t \gtrsim \mathcal{O}(10^{-2})$) than flight ($I_t \lesssim \mathcal{O}(10^{-3})$). A conservative free stream intensity $I_t = 0.03$ is therefore selected for the computations of the ground-based facility.

$$k = \frac{3}{2}\left(I_t U_{ref}\right)^2 \tag{3.102}$$

$$\epsilon_1 = \frac{c_\mu \rho k^2}{\mu_{t,1}} \tag{3.103}$$

$$c_\mu = 0.09 \tag{3.104}$$

$$\frac{\mu_{t,2}}{\mu} = \frac{1}{f_\mu}\frac{\mu_{t,1}}{\mu} \tag{3.105}$$

$$\epsilon_2 = \frac{c_\mu \rho k^2}{\mu_{t,2}} \tag{3.106}$$

3.6 Solution Initialization

Tare computations are initialized to the approximate nozzle exit conditions, assuming isentropic nozzle expansion, which are summarized in Table 3.9. Subsequent reacting flows are initialized from the converged un-fueled solution. However, to initiate reactions in the cavity, the activation energy of the first step in the 3-step mechanism is artificially reduced by a factor of 10^3. Reaction zones typically establish within 2000 iterations as inferred from the increase in fluid temperature in the cavity and backward-facing step regions. After ignition is achieved, the nominal 3-step or TP2 reaction sets are re-enabled and the computation is iterated to convergence.

Table 3.9: Tare flow initial condition from estimated freestream nozzle exit conditions.

Parameter	*Value*	*Units*
U_∞	1312.96	$[m/s]$
p_∞	59.63	$[kPa]$
T_∞	531.93	$[K]$
Re'	18.16×10^6	$[m^{-1}]$

Chapter 4

Model Sensitivity to Numerical Parameters and Comparison with Experiment

Before proceeding to the time-dependent fuel-staging analysis, it is necessary to carefully calibrate numerical parameters to the experiments. Solution sensitivity to turbulence and chemistry-related modeling assumptions are particularly critical to understand as shown by the model parameter studies of Milligan *et al.*[240] at steady-state combustor operation. As a basis for the sensitivity study, wall pressure measurements from the simulations are compared with experimental time-mean static pressures for steady-state tare-mode (un-fueled) and combustion-mode operation. Numerical sensitivity to several key modeling parameters are studied, namely, the effects of grid resolution (§ 4.1), inflow and thermal boundary conditions (§ 4.2), chemical and mixing effects (§ 4.3), and temporal-scaling (§ 4.4). For the initial discussion, a turbulent Schmidt number $Sc_t = 0.7$ is used. In all cases, a fixed ratio of $Pr/Pr_t = 0.8$ applies. Steady-state operation computations are considered converged when the residual levels drop by at least 3 orders of magnitude and become asymptotic.

4.1 Grid Resolution

A hybrid grid approach is used wherein structured cells (hexahedra) are employed to control near-wall spacing suitable for the wall functions used in the solver, whereas unstructured cells (prisms and tetrahedra) are applied to address the geometrical complexity of the scramjet combustor near the fuel injectors. Structured (blue) and unstructured (red) cell zones are delineated in Figure 4.1 for the symmetry ($\hat{z} = 0$) plane. A representative view of the grid topology is shown for the cavity flameholder region in Figure 4.2.

Mesh quality is assessed by the cell quality metrics of edge length stretching ratio and cell equiangular skewness. Equiangle skewness measures the maximum ratio the included angles of the cell to the angle of an equilateral element.[278] Lower skewness (higher-quality) cells have a skewness of zero. Structured regions of the mesh are limited in stretching ratio (ratio of consecutive edge lengths) to below 15 percent. Mesh equiangle skewness is limited to below 0.80 with an average skewness of 0.12. The most highly skewed (lowest quality) cells are found in the unstructured regions.

A grid convergence study considers spatial discretizations ranging in size from 4-10 million cells. The grid cell heights at the wall (Δn_0) are selected to achieve an average n^+ (*i.e.* y^+) in the isolator and combustor suitable for the wall model. Grid cell-counts, initial cell height at the wall (Δn_0), and average streamwise spacing in the isolator (Δx) are summarized in Table 4.1. The n^+ values are computed from a surface average on the isolator walls for un-fueled operation. The grid labels C, M, F represent coarse, medium, and fine levels of grid refinement, respectively.

Steady-state tare pressure predictions for cowl-side, body-side, and south-side walls (Figure 2.4) at tare-mode and aft-fueled-combustion-mode operation are

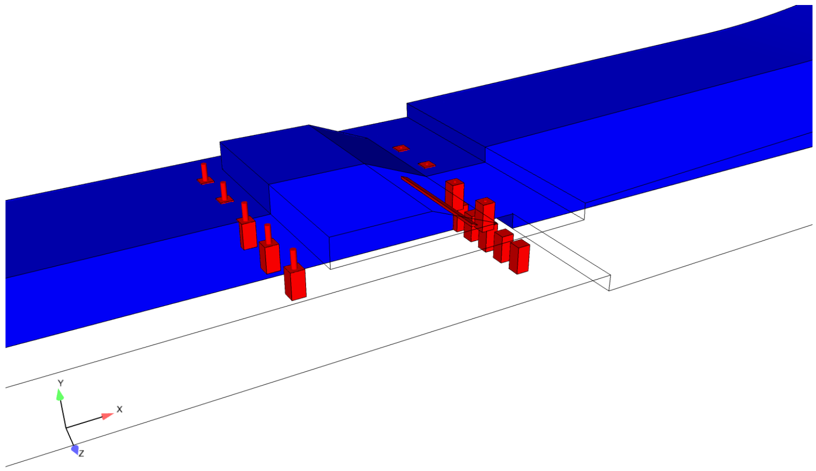

Figure 4.1: Domain cell types (domain symmetry shown): *blue* - structured cells, *red* - unstructured cells.

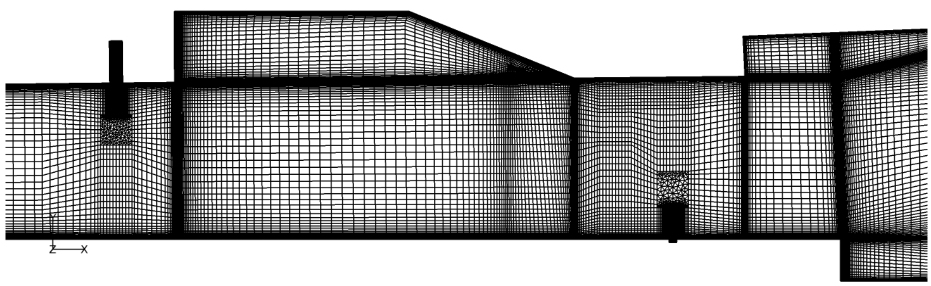

Figure 4.2: Combustor cavity grid detail on symmetry ($z/\mathcal{H} = 0$) plane.

Table 4.1: Summary of grid resolution study parameters.

	Cells $[\times 10^{-6}]$	$H/\Delta n_0$ $[-]$	Δn_0^+ $[-]$	$H/\Delta x$ $[-]$
C	3.8	555	36	4.3
M	6.3	832	23	5.0
F	10.7	1189	16	6.2

shown in Figure 4.3 The plotted pressures are normalized by the nozzle stagnation pressure for both experimental (symbols) and computational (lines) data. The Grid Convergence Index[279] (GCI), based on Richardson extrapolation, is computed to estimate the discretization error as defined in eqn. 4.1. The GCI is computed with refinement ratio $r \approx 1.5$, nominal scheme-order $p = 2$, safety-factor $F_s = 1.25$, and pressure distributions on the medium and fine grids as the observables of interest f_1 and f_2, respectively. Typically, $F_s = 3$ is assumed for a strict doubling or halving of the grid with second-order-accurate schemes such that the GCI approaches the discretization error in the limit of grid convergence. The selection of $F_s = 1.25$ for the subsequent discussion follows in a similar manner for the values of $r = 1.5$ and $p = 2$ of the present work.

$$GCI = F_s \frac{|f_1 - f_2|}{r^p - 1} \tag{4.1}$$

Although strict grid independence is not obtained, the results suggest the discretization error is minimal from the limited change between results on the medium and fine resolution grids. In particular, the computed GCI for the tare solutions indicates relatively large errors near the strongest gradients associated with the isolator oblique shock waves. The tare operation predictions (Figure 4.3 (a)) qualitatively agree with the time-averaged experimental measurements on the cowl- and body-side walls. In particular, computations capture locations and amplitudes of the sharp rises and gradual falls associated with the reflected oblique shock waves of the shock-train. Differences in the peak cavity pressure are observed for the body-side wall although the pressure rise along the aft wall of the cavity ($13.5 \leq \hat{x} \leq 14.9$) is qualitatively captured. The maximum pressure predicted downstream of the isolator entrance is consistent with the experimental measurements and is attributable to the

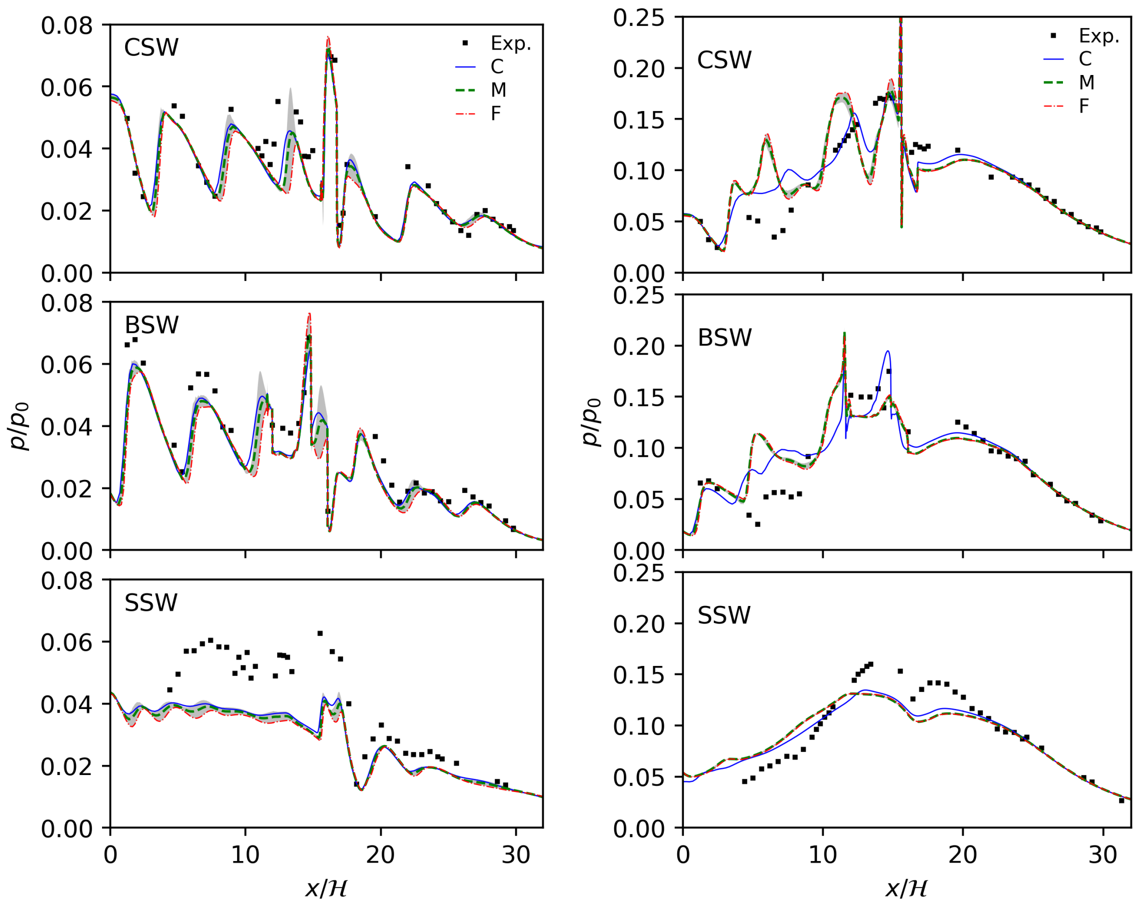

(a) Tare

(b) Aft-fueled

Figure 4.3: Isolator wall pressure prediction sensitivity to grid resolution: *CSW* - cowl-side, *BSW* - body-side, *SSW* south-side wall pressure distributions; and *GCI* - greyscale.

pressure rise on the cowl-side wall near $\hat{x} \approx 16$ as a result of the shock reflected off the cavity shear layer. Downstream of the body-side and cowl-side steps ($\hat{x} \geq 20$), the results are insensitive to grid refinement and agree well with experimental trends for all fuel-staging conditions.

Despite agreement on body- and cowl-side walls, notable qualitative disagreement with the experimental results are observed for the south-side wall. This difference may be associated with the simplicity of the wall heat-flux treatment, *e.g.* differences between material properties for the modeled wall thermal-resistance (*i.e.* the 1-D resistive model) versus the experimental test rig or specified turbulent Prandtl number. Sensitivity to imposed wall heat flux boundary condition is considered in § 4.2.3. The pressure rise on the side wall in experiments may be associated with flow separation which may be attributable to oscillations in the cavity that, in turn, interact with the side wall boundary-layer. This behavior would not be captured in the present model-based approach but would be amenable to scale-resolving computations.

Qualitative agreement in the reacting solution of the steady aft-fueled state is also observed in terms of the peak pressure levels (Figure 4.3 (b)). The peak cavity pressure on the cowl-side wall, for example, is captured near $\hat{x} \approx 14$. Interestingly, the GCI is also relatively smaller for the fueled condition with errors that are barely visible compared to the un-fueled results. However, the wall pressures are over-predicted in the isolator region $3 \leq \hat{x} \leq 7$ as indicated by the cowl- and body-side wall distributions. This is partly attributable to the choice of turbulent Schmidt number which is explored in § 4.3.2. Unlike the medium and fine mesh solutions, the coarse grid solution exhibits oscillatory behavior and is therefore time-averaged over approximately 10 cycles of the oscillation for comparison purposes. Since the simulation results change little between the two finest-resolution grids, the remaining combustion results are shown for the medium-resolution grid.

4.2 Boundary Conditions

The effects of variations in inflow boundary conditions are now assessed. Variations in combustor wall pressure distributions with freestream Reynolds number (via nozzle stagnation pressure) and inflow turbulence (via eddy viscosity ratio (μ_t/μ)) are examined. The latter eddy viscosity variation is applied to both nozzle and fuel injector inflow boundaries. The imposed wall heat-flux boundary is also varied to asses the effects on shock/boundary-layer interactions.

4.2.1 Nozzle Reynolds Number

With respect to the inflow Reynolds number Re, two additional cases are evaluated at 10 percent above (Re_+) and below (Re_-) the baseline unit Reynolds number ($Re' \approx 18 \times 10^6\ m^{-1}$), respectively. The Reynolds number is adjusted by changing the specified nozzle stagnation pressure. The computed wall pressure distributions (normalized by their respective stagnation conditions) are provided in Figure 4.4 for cowl, body, and side walls. The curves collapse indicating that the turbulent flow is insensitive to the small change in inflow Reynolds number for tare operation.

4.2.2 Inflow Turbulence

The initial simulations considered relatively high (turbulent) inflow values for the eddy viscosity ratio ($\mu_t/\mu = 50$). As observed[195] in computations of the geometrically similar HIFiRE 2 combustor, the effect of inflow turbulence on predicted

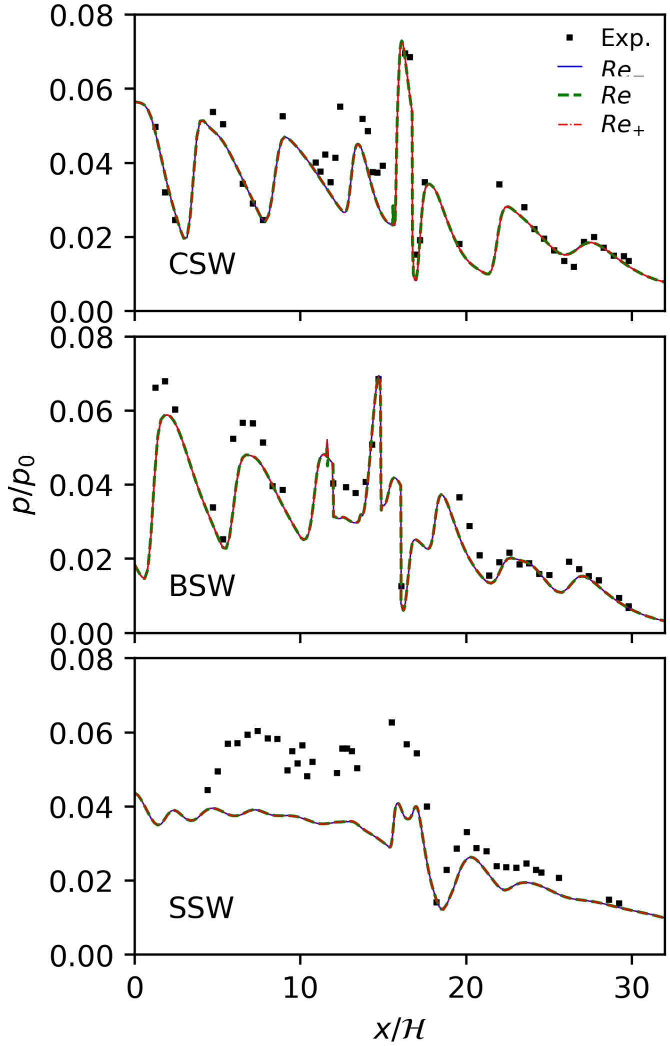

Figure 4.4: Isolator wall pressure prediction sensitivity to inflow Reynolds number.

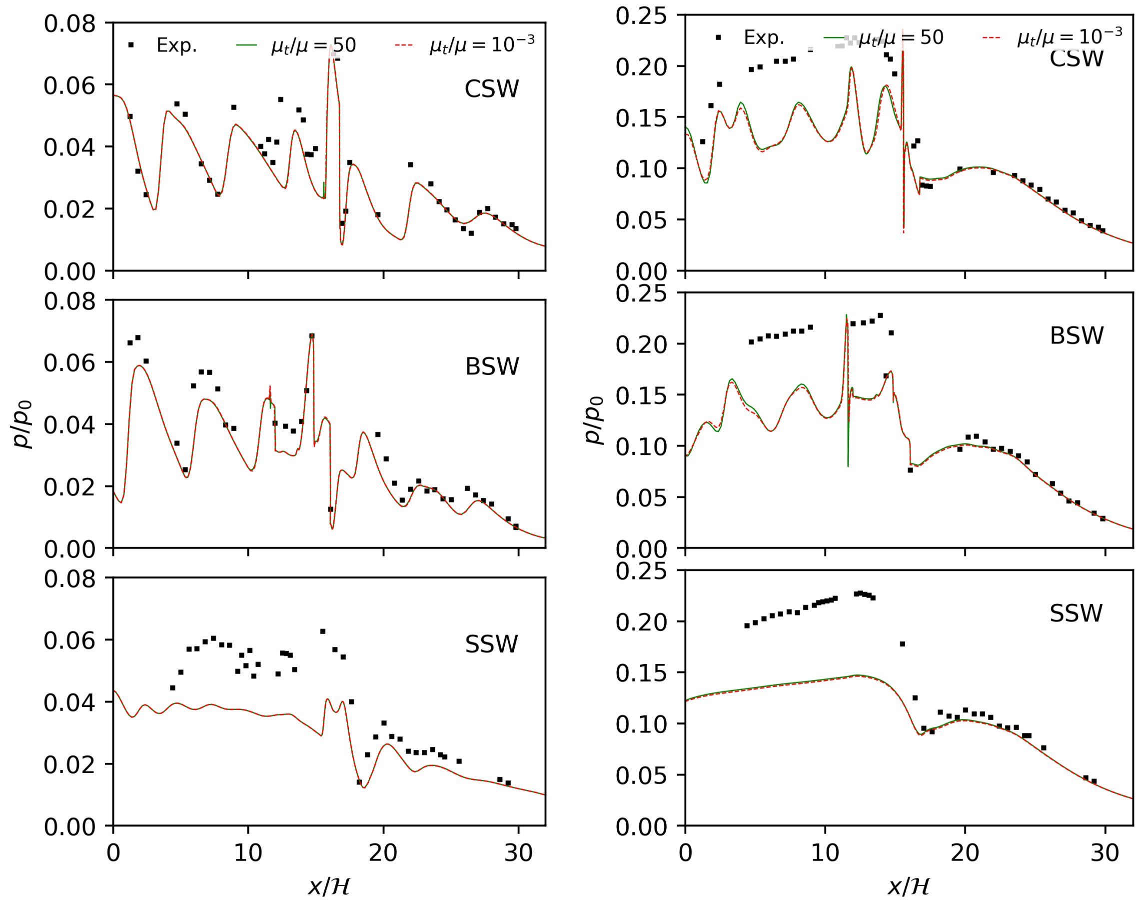

(a) Tare

(b) Forward-fueled

Figure 4.5: Isolator wall pressure prediction sensitivity to varying inflow turbulence: (a) tare, (b) forward-fueled.

wall pressures was limited. To validate that the assumed eddy viscosity boundary condition did not adversely affect the predictions, a lower viscosity ratio $\mu_t/\mu = 10^{-3}$ case was also computed. The same viscosity ratio was applied to all inflow boundaries, *i.e.* nozzle and fuel injectors. For tare (Figure 4.5 (a)) and aft-fueled (not shown) conditions, no appreciable change is observed in the predicted pressure profiles. A marginally larger effect is observed for forward-fueled condition (Figure 4.5 (b)) but the inflow eddy viscosity is negligible, consistent with the initial assumption.

4.2.3 Wall Thermal Condition

A numerical study by Lin *et al.*[156] of rectangular and axisymmetric scramjets quantified the change in isolator pressure rise with respect to the wall heat flux condition. High temperatures reduced the shock-train length and increased the pressure gradient. To understand the sensitivity of the present combustor to wall heat flux, an adiabatic wall case is compared with the more representative 1-D resistive layer approximation. The wall pressure distributions for each case are shown in Figure 4.6. Stagnation zones in the cavity $\hat{x} = 12$ show higher pressure levels for the body-side wall. However, the peak pressure corresponding to the reflected shock at $\hat{x} = 16$ (discussed in § 5.1) is lower. Predictions on the body-side wall in the cavity region $12 \leq \hat{x} \leq 14$ are closer to experiment but upstream pressure levels are under-predicted. Side wall pressure profiles are shifted slightly higher but are qualitatively unchanged from 1-D approximation results. Heat flux boundary sensitivity is also evident from the change in shock structures as shown by the divergence of the velocity ($\nabla \cdot \mathbf{U}$) field (dilatation), shown for adiabatic and 1-D resistive conditions in Figure 4.7 (a) and (b), respectively. Dark contours are indicative of compression regions, whereas lighter contours represent expansion zones. The largest difference between the two thermal conditions is shown for the DG-generated shock reflected from the cowl wall at $\hat{x} = -2$ and is attributable to shock-induced separation.

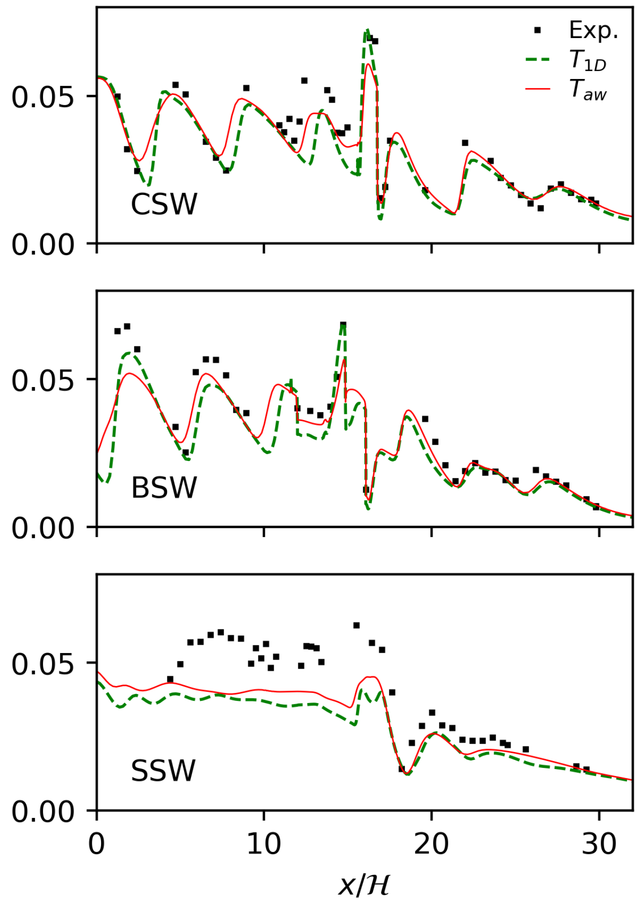

Figure 4.6: Isolator wall pressure prediction sensitivity to wall heat flux condition: T_{aw} - adiabatic, T_{1D} - 1-D resistive model.

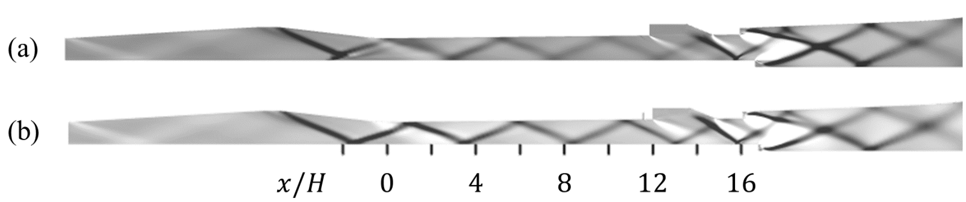

Figure 4.7: Symmetry plane ($\hat{z} = 0$) dilatation ($\nabla \cdot \mathbf{U}$) flowfield structure comparison at different wall thermal conditions: (a) adiabatic wall and (b) 1-D resistive model (Table 3.6).

4.3 Chemistry and Mixing

4.3.1 Kinetics Mechanism and Vitiation Effects

Next, predictions with the computationally expedient 3-step (Mawid) and reduced TP2 ethylene mechanisms are compared. Pressure distributions for the two kinetics mechanisms are shown in Figure 4.8 (a) which indicate that the TP2 mechanism produces slightly lower magnitude cowl-side wall pressures in the cavity region ($12 \leq \hat{x} \leq 15$) but somewhat higher magnitudes in the isolator ($2 \leq \hat{x} \leq 12$) compared to the 3-step mechanism. The pressure distributions on the south-side and body-side wall display similar trends. Lower pressures in the cavity may be attributable to the ability of the TP2 mechanism to more accurately capture ignition and extinction behavior which tend to reduce heat release compared to simpler mechanisms.[236] Given that the TP2 solution is approximately two-and-a-half times more computationally intensive per iteration than the 3-step mechanism, the remaining discussion on unstart considers computations using the 3-step mechanism.

At the time the initial steady-fueling simulations discussed above were computed, estimates for the vitiate species were not available. However, several studies, both measured[280–282] and predicted,[283] have observed sensitivity of vitiate species on combustor performance based on the presence of vitiate species. Therefore, as a *post facto* check, the impact of nozzle vitiate species on combustor predictions is evaluated. From the experiments of the present configuration, vitiates CO_2 and H_2O (Table 3.7) constitute 12 percent of the experimental isolator inflow by mass. Vitiated flow solutions are computed assuming spatially uniform mass fractions. Figure 4.8 (b) shows the predicted wall pressures for the cowl-side wall with and without vitiate species. Predicted wall pressures suggest minimal sensitivity to the inclusion of vitiate

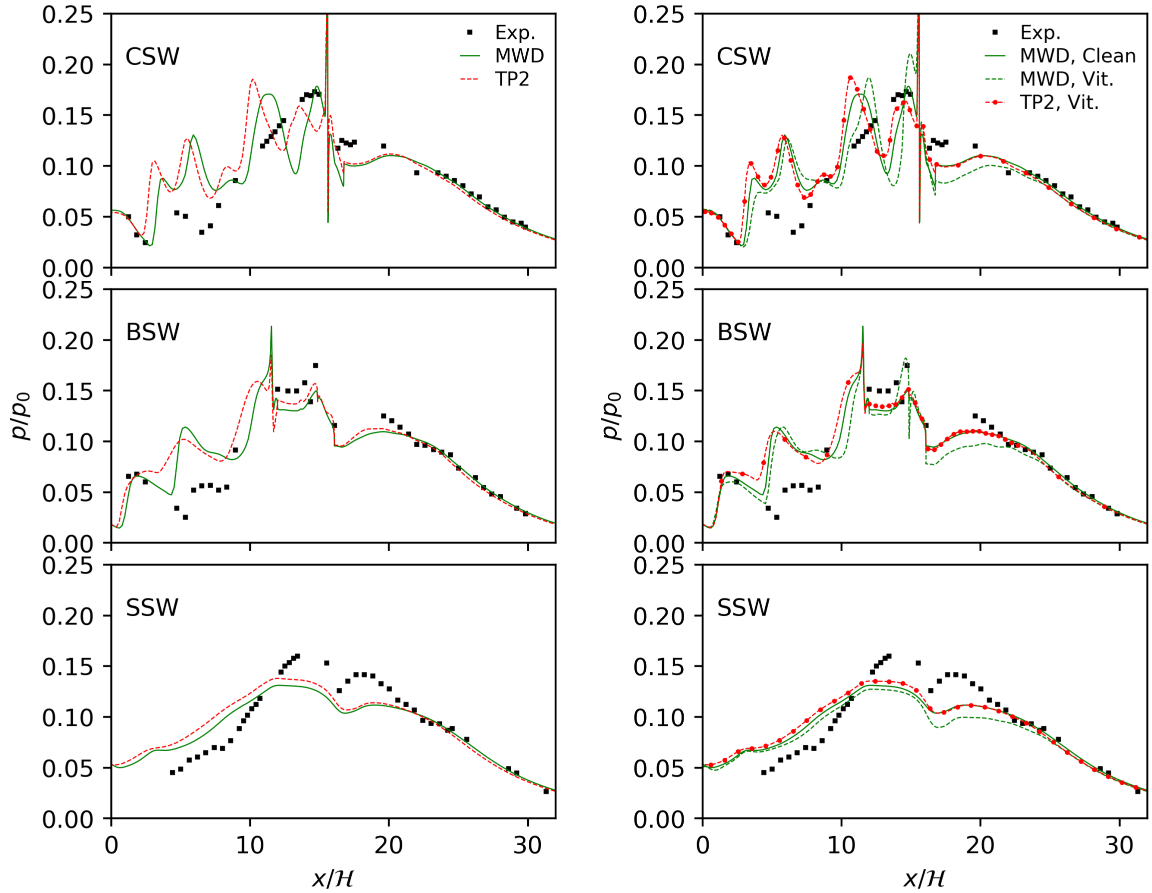

(a) Kinetics

(b) Vitiation

Figure 4.8: Isolator wall pressure prediction sensitivity to (a) kinetics mechanism and (b) vitiate species for steady aft-fueled condition.

species as reflected in a slight reduction in the pressure magnitudes. Thus, for this configuration, uniform vitiates at the nozzle inflow do not have a first-order effect on predictions.

4.3.2 Turbulent Schmidt Number

Mixing layers exhibit varying ratios of viscous and molecular diffusion, *i.e.* Schmidt number $Sc \equiv \nu/\mathcal{D}$. An experimental study[284] of a compressible plane mixing layer, for example, estimates a turbulent Schmidt number $Sc_t \equiv \nu_t/\mathcal{D}_t < 1$ with gas-phase shear layer mixing typically $Sc \approx \mathcal{O}(1)$.[285] Computations for mixing applications,[286] particularly for scramjets, are also sensitive to modeled turbulent Schmidt number. Constant values of Sc_t in the literature range from $0.5 \lesssim Sc_t \lesssim 0.9$ for supersonic mixing applications.[8,248,287] Given this sensitivity, validation efforts for the present scramjet configuration consider the effects of constant Schmidt number selection for both the aft-fueled and forward-fueled fueling conditions. Schmidt numbers in the range $0.5 \leq Sc_t \leq 1.2$, comparable to those in the literature, are tested. Although computationally convenient, constant Sc_t is not physical and modeling efforts[288,289] have sought to develop suitable variable Schmidt number models for turbulence applications. In this work, the variable turbulent Schmidt number approach evaluated (§ 3.2.1) is an algebraic model[244] which connects Sc_t to the ratio of turbulent kinetic energy production ($\mathcal{P}_k$) to turbulent eddy dissipation (ϵ).

Comparison of the time-mean wall pressures with different Schmidt number values for both the aft-fueled and forward-fueled fuel-staging conditions are shown in Figure 4.9. The initial baseline solution with $Sc_t = 0.7$ was previously shown to

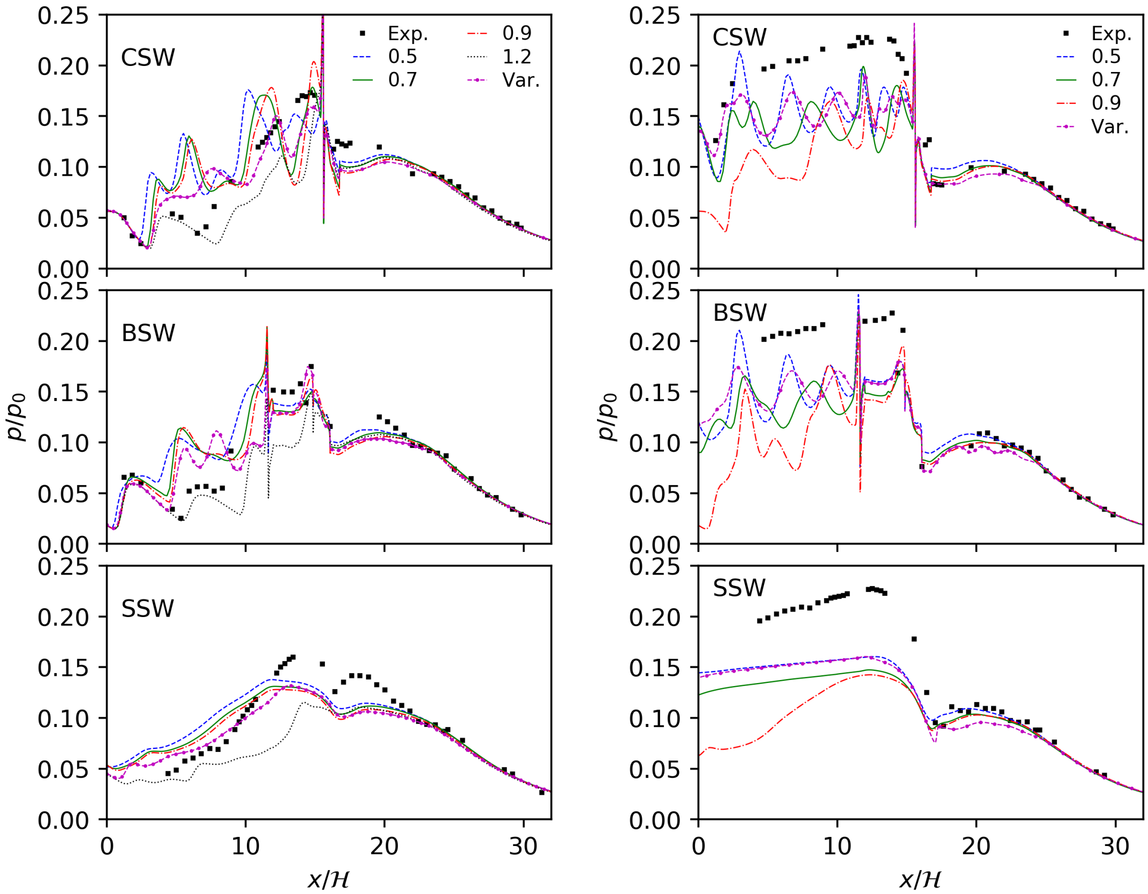

(a) Aft-fueled

(b) Forward-fueled

Figure 4.9: Isolator wall pressure prediction sensitivity to turbulent Schmidt number (Sc_t): (a) aft-fueled condition, (b) forward-fueled condition.

overpredict the pressure in the isolator (Figure 4.3). For this fueling condition, the variable Sc_t model produces pressure distributions bounded, approximately, by the constant turbulent Schmidt number cases of $Sc_t = 0.9$ and $Sc_t = 1.2$.

Increasing Sc_t, and thereby reducing the relative influence of turbulent mass diffusivity, improves agreement between predicted aft-fueled wall pressures and experiment upstream of the cavity. Specifically, a turbulent Schmidt number $Sc_t = 1.2$ yields reasonable agreement for the baseline fuel-staging condition

Table 4.2: Influence of Sc_t on PCST location for baseline (aft-fueled) condition ($\hat{x}_s|_{exp} = 7.81 \pm 0.3$).

Mechanism	Sc_t	$\hat{x}_s$	$\Delta\hat{x}_s$
Mawid	0.5	2.40	-5.41
Mawid	0.7	2.91	-4.90
Mawid	0.9	3.07	-4.74
Mawid	1.2	8.95	$+1.14$
Mawid	$Var.$	3.03	-4.78
TP2	0.7	2.25	-5.56
TP2	0.9	2.68	-5.13
TP2	1.2	3.08	-4.73

in terms of predicted PCST location (x_s) as compared against the experiments (Table 4.2). The experimentally determined shock-train position for baseline operation is $\hat{x}_s \equiv x_s/\mathcal{H} = 7.81 \pm 0.3$. Except for the $Sc_t = 1.2$ case, all Schmidt numbers underpredict the shock-train position by overpredicting the pressure levels on the isolator cowl-side wall. This difference in predicted shock location ($\Delta\hat{x}_s = \hat{x}_{s,cfd} - \hat{x}_{s,exp}$) suggests a non-linear relation between fixed values of Sc_t and x_s for the 3-step mechanism solutions. The TP2-predicted shock locations, which lie just upstream of the Mawid-predicted locations for each turbulent Schmidt number, are also shown in Table 4.2.

Results for the forward-fueled condition, in contrast to the aft-fueled solution, underpredict the isolator wall pressures compared to experiment for $Sc_t = 0.7$. Lowering the value of Sc_t improves agreement with experiment. Even with a lower $Sc_t = 0.5$, the solution shows qualitative differences in the pressure distribution within the isolator. The peak pressure predicted in the isolator is, however, in reasonable agreement with the magnitude of the experimental values. The cowl-side and body-side wall pressure predictions also highlight variations attributable to weak, reflecting oblique waves in the isolator. Consistent with the modeling study of Yoder *et al.*,[287] reducing Sc_t increases species diffusion leading to more favorable mixing for combustion to occur.

Solution sensitivity to Sc_t thus highlights a challenge in using a fixed global parameter to calibrate solutions to localized flow phenomena. Discussion of the steady fuel-staging flowfields consider the best prediction for the aft-fueled and forward-fueled case using the $Sc_t = 1.2$- and $Sc_t = 0.5$-computed results, respectively (§ 5.1). However, since the Sc_t value required to calibrate the steady aft-fueled and forward-fueled simulation pressure predictions differ, $Sc_t = 0.9$ was selected as a compromise between the two conditions to obtain a fixed set of model parameters for the transient-fueling computations (§ 4.4).

The largest deviations in predicted pressures are found near the cavity for the forward-fueled case. Physically, unsteadiness of the mixing layers in these zones may be more important in the predominantly subsonic, unstarted flow. Such unsteadiness would not be well captured with a URANS approach but might be targeted with scale-resolving turbulent simulations. However, the observed difference in optimal Sc_t for the computations may also be attributable to the different physical mixing modes between the aft-fueled and the forward-fueled states. That is, the range of chemical and fluid time scales may be different in each fuel-staging case.

4.3.3 Fluid and Chemical Scales

The analysis approach of Quinlan *et al.*[235] is adopted to evaluate the range of turbulence and chemical scales in this combustor. The method compares the fluid and chemical timescales by way of the Damköhler number $Da \equiv \tau_f/\tau_c$. Quinlan *et al.* observe that dual-mode operation of the HIFiRE 2 combustor is characterized by relatively higher Da (downstream of the cavity) compared to scramjet mode operation. A similar trend is expected for the aft-fueled and forward-fueled states, respectively, as a result of the increasing characteristic flow timescale. In the former case, turbulent fluctuations from SBLIs in the presence of the supersonic flow are expected to dominate with fluid time scales leading to relatively smaller Da. The forward-fueled case, however, features predominantly subsonic or weakly supersonic flow in the combustor region where increased fluid timescales (lower fluid velocities) may lead to relatively larger Da.

In this analysis of fluid and chemical scales, the quantities of interest are the Damköhler (Da) and turbulent Reynolds number (Re_t). The former parameter, which compares fluid and chemical timescales, is determined using the Takeno[290] flame index (Λ_T) (eqn. 4.5) which differentiates between premixed and non-premixed combustion as estimated from the spatial gradients of fuel (C_2H_4) and oxidizer (O_2). When spatial gradients are aligned $\Lambda_T \to 1$ the fluid is assumed to be premixed. Conversely, the flow is characterized as non-premixed when the gradients are opposed ($\Lambda_T \to -1$). From this metric, the local Damköhler number can be computed for non-premixed and premixed conditions (eqn. 4.10). The turbulent Reynolds number (eqn. 4.4) is based on the turbulent velocity and length scale computed from the turbulent kinetic energy (TKE) and turbulent eddy dissipation rate (TED) as in eqns. 4.2-4.3.

The non-premixed Damköhler number (Da_{NPM}) is determined using the time scale of water formation (τ_{H_2O}) (eqn. 4.6) and the scalar dissipation rate (χ) (eqn. 4.7). From Poinsot,*et al.*[291] the scalar dissipation rate is written as a function of the mixture fraction variance ($\widetilde{Z''Z''}$) (eqn. 4.8). Following, Quinlan[292] the upper limit approximation (eqn. 4.9) is employed for the mixture fraction variance, given in terms of $\tilde{Z}$, based on an assumed beta probability density function (PDF) for $\tilde{Z}$.[293]

For premixed combustion, the relevant Damköhler number Da_{PM} is determined from the fluid timescale, assumed to be τ_t, and from the estimated laminar flame timescale ($\tau_F \equiv l_F/s_L$). The latter is a function of the laminar flame thickness (l_F) and flame speed (s_L). The laminar flame scales are computed† at the average combustor pressure ($p/p_0 \approx 0.1 = 1.66\ atm$) and nozzle exit temperature ($T/T_0 \approx 0.36$) for the aft-fueled condition using a one-dimensional model of a freely propagating, laminar, premixed flame at fuel equivalence ratio ($\phi = 0.9$) from the 1-D conservation of mass, momentum, and energy equations. The computed laminar flame properties for ethylene-air are $s_L = 161\ cm/s$ and $l_F = 0.2\ mm$. This approximate flame time scale is $\tau_F = 9.7 \times 10^{-5}\ sec$. Additional details of this computation are provided in the Appendix (§ A.2).

$$u_t = \sqrt{2k} \tag{4.2}$$

$$l_t = \frac{k^{3/2}}{\epsilon} \tag{4.3}$$

$$Re_t = \frac{u_t l_t}{\nu} \tag{4.4}$$

$$\Lambda_T = \frac{\nabla\tilde{Y}_f \cdot \nabla\tilde{Y}_{ox}}{||\nabla\tilde{Y}_f \cdot \nabla\tilde{Y}_{ox}||} \tag{4.5}$$

†Laminar flame scales are computed with the Cantera[294] library.

$$\tau_{H_2O} = \frac{\bar{\rho}\tilde{Y}_{H_2O}}{\dot{\omega}_{H_2O}} \tag{4.6}$$

$$\chi = 2\mathcal{D}\frac{\partial Z}{\partial x_j}\frac{\partial Z}{\partial x_j} \tag{4.7}$$

$$\chi_{rans} = C\frac{\tilde{\epsilon}}{\tilde{k}}\widetilde{Z''Z''} \tag{4.8}$$

$$\approx \frac{\tilde{\epsilon}}{\tilde{k}}\tilde{Z}(1-\tilde{Z}) \tag{4.9}$$

$$Da = \begin{cases} Da_{NPM} = \frac{1}{\chi_{rans}\tau_{H_2O}} & \Lambda_T < 0 \\ Da_{PM} = \frac{\tau_t}{\tau_{flame,L}} \approx \frac{k/\epsilon}{l_F/s_L} & \Lambda_T > 0 \end{cases} \tag{4.10}$$

This analysis approach is further augmented by adapting the perspective of Fureby[295] as employed in the analysis of turbulence combustion scales in the hydrogen-fueled HyShot II scramjet. This approach, like that of Quinlan *et al.*, considers scaling of Re_t and Da as well the turbulent Mach number Ma_t. The turbulent Mach number is defined (eqn. 4.11) as the ratio of the turbulent velocity scale u_t and the local speed of sound c which provide a measure of compressibility.

$$Ma_t = \frac{u_t}{c} \tag{4.11}$$

The probes from the computational domain are mapped along the dimensions of turbulent Mach number Ma_t, turbulent Reynolds number Re_t, and Damköhler number Da in Figure 4.10 for the aft-fueled condition. Points are colored by the normalized chemical heat release rate $(\widehat{\dot{H}R})$ (eqn. 4.12) where the scaling factor is the spatially averaged heat release rate at the aft-fueled condition. Two-dimensional histograms in the $Ma_t - Re_t$, $Re_t - Da$, and $Ma_t - Da$ planes show the distribution of probes projected into each of the three pairs of dimensions. A wide range of scales is observed: $0 \leq Ma_t \leq 0.6$, $10^0 \leq Re_t \leq 10^6$, and $10^{-8} \leq Da \leq 10^6$. Higher histogram density is identified at relatively lower Ma_t and Da. Higher turbulent Mach numbers ($Ma_t \approx 0.6$) are seen for the aft-fueled condition which reduce to $Ma_t \leq 0.3$ at the forward-fueled condition (Figure 4.11) consistent with the reduced combustor velocity. DNS analysis[296] of isotropic turbulence suggests $Ma_t \geq 0.3$ as the transition point where compressibility effects become important. This indicates that, despite the reduction in velocity scale at forward-fueled condition, compressibility effects are non-negligible.

$$\dot{HR}(\mathbf{x}) = \sum \dot{\omega}_s \Delta h^o_{f,s} \tag{4.12}$$

As will be discussed in (§ 5.2.5), the sidewall region is important for mixing and heat release. To compare the change in scales within this region, points within one duct height $\mathcal{H}$ of the sidewall ($\hat{z} \geq \frac{1}{2}\frac{\mathcal{W}}{\mathcal{H}} - 1$) are isolated. The near wall scales are shown for the aft-fueled condition in Figure 4.12. The normalized heat release rate suggests the near wall region is more reactive than near the combustor centerline. Changing from aft-fueled to forward-fueled operation shifts the maximum Da from $Da \approx 10^{-6}$ to $Da \approx 10^{-5}$ consistent with the hypothesis of increasing fluid time scale and the observations of Quinlan *et al.*[235] Since relatively lower $Da \ll 1$ is observed in the reactive side wall region, mixing-limited or infinitely fast chemistry methods† are not suitable for this problem. However, mixing downstream of the cavity $\hat{x} \geq 16$ indicate a larger range of chemical time scales as shown for the aft-fueled condition in Figure 4.13.

†Infinitely fast chemistry is suitable for $Re \gg 1$ and $Da \gg 1$.[291]

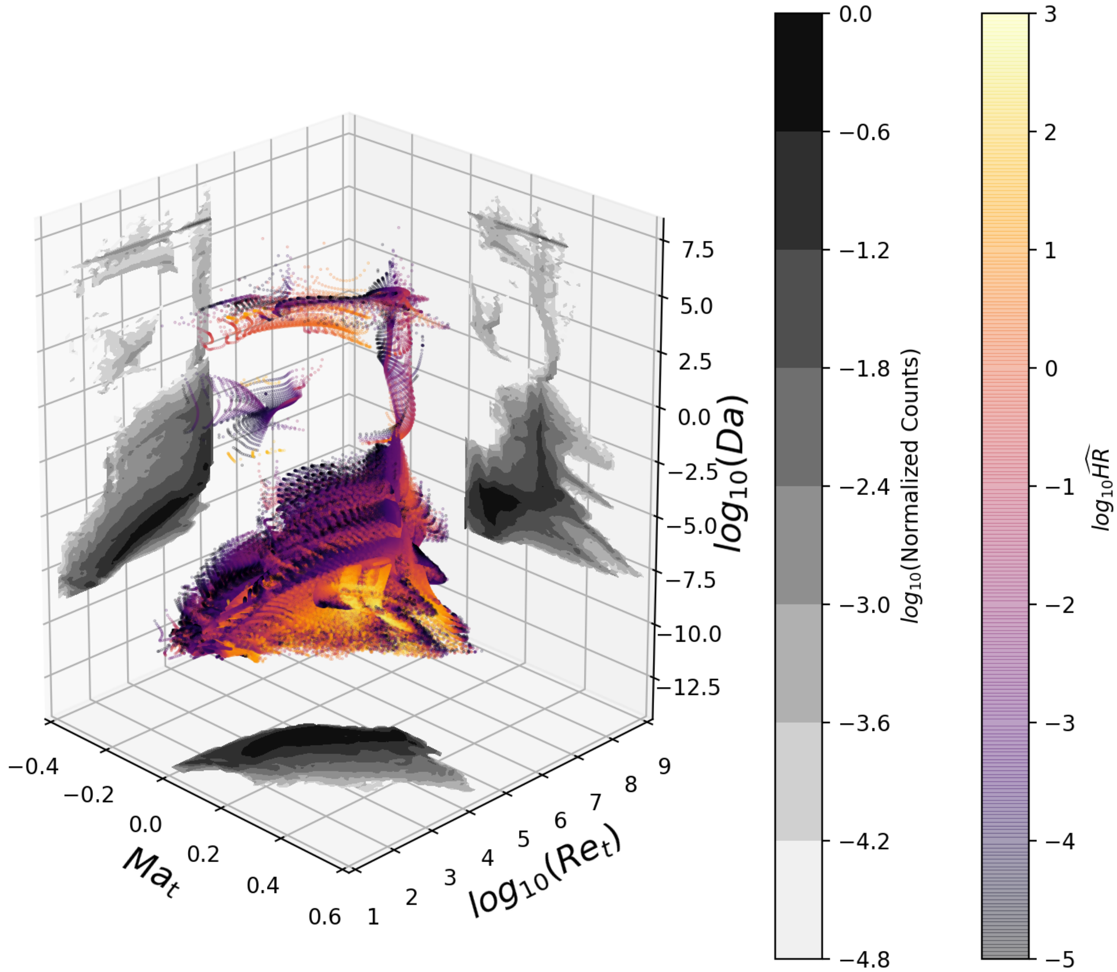

Figure 4.10: Comparison of fluid and chemistry scales Ma_t, Re_t, and Da at *aft-fueled* state. Points sampled in range $10 \leq x/\mathcal{H} \leq 26$.

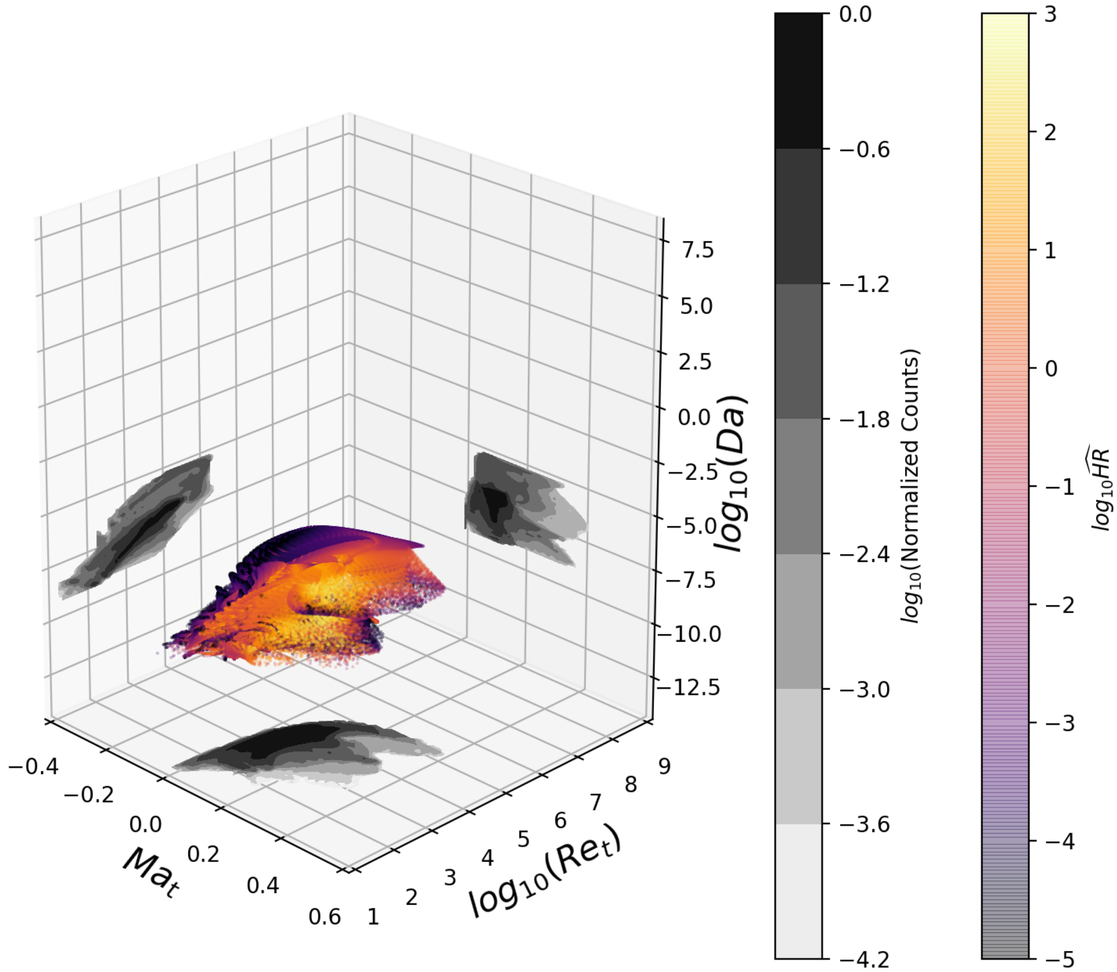

Figure 4.11: Comparison of fluid and chemistry scales Ma_t, Re_t, and Da at *forward-fueled* condition in sidewall region $\hat{z} \geq \frac{1}{2}\frac{\mathcal{W}}{\mathcal{H}} - 1$. Points sampled in range $10 \leq x/\mathcal{H} \leq 26$.

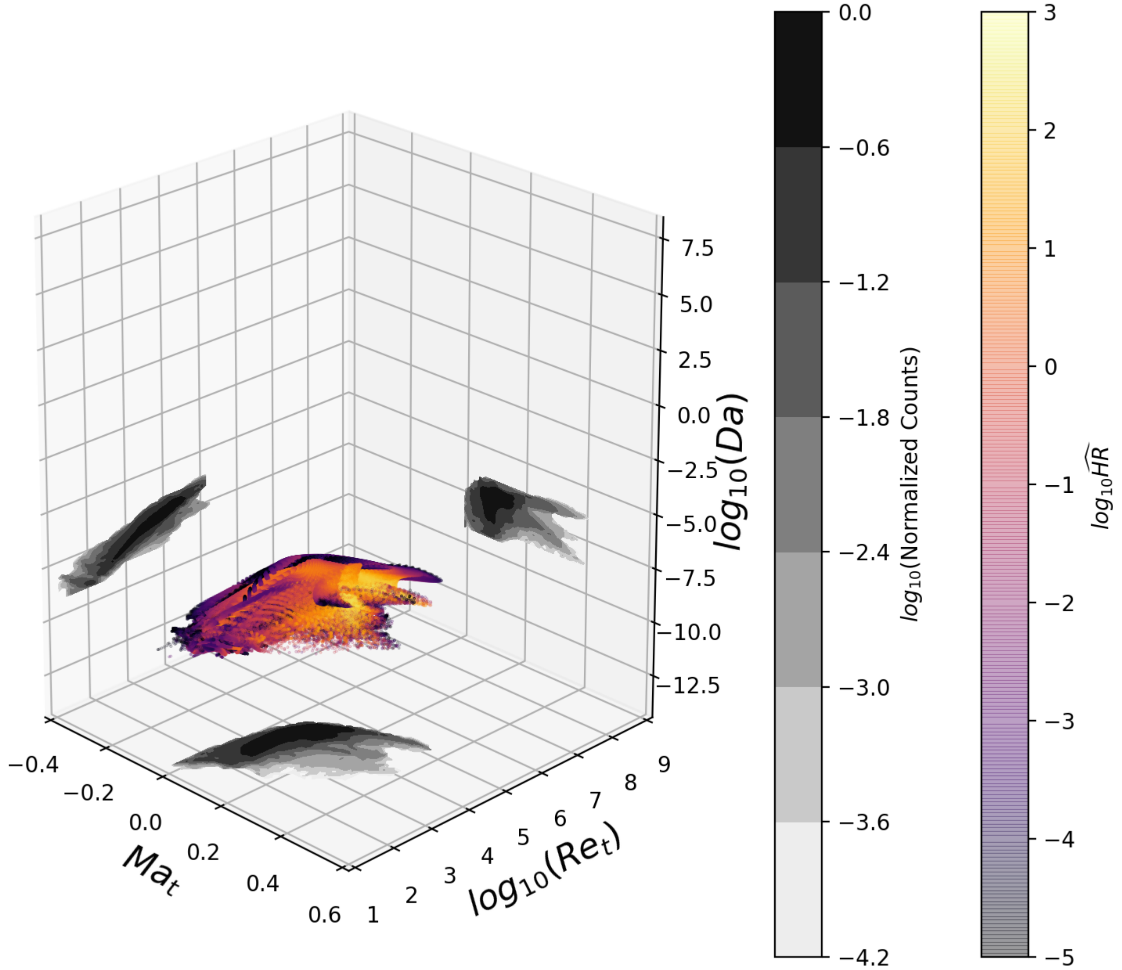

Figure 4.12: Comparison of fluid and chemistry scales Ma_t, Re_t, and Da at *aft-fueled* condition in sidewall region $\hat{z} \geq \frac{1}{2}\frac{\mathcal{W}}{\mathcal{H}} - 1$. Points sampled in range $10 \leq x/\mathcal{H} \leq 26$.

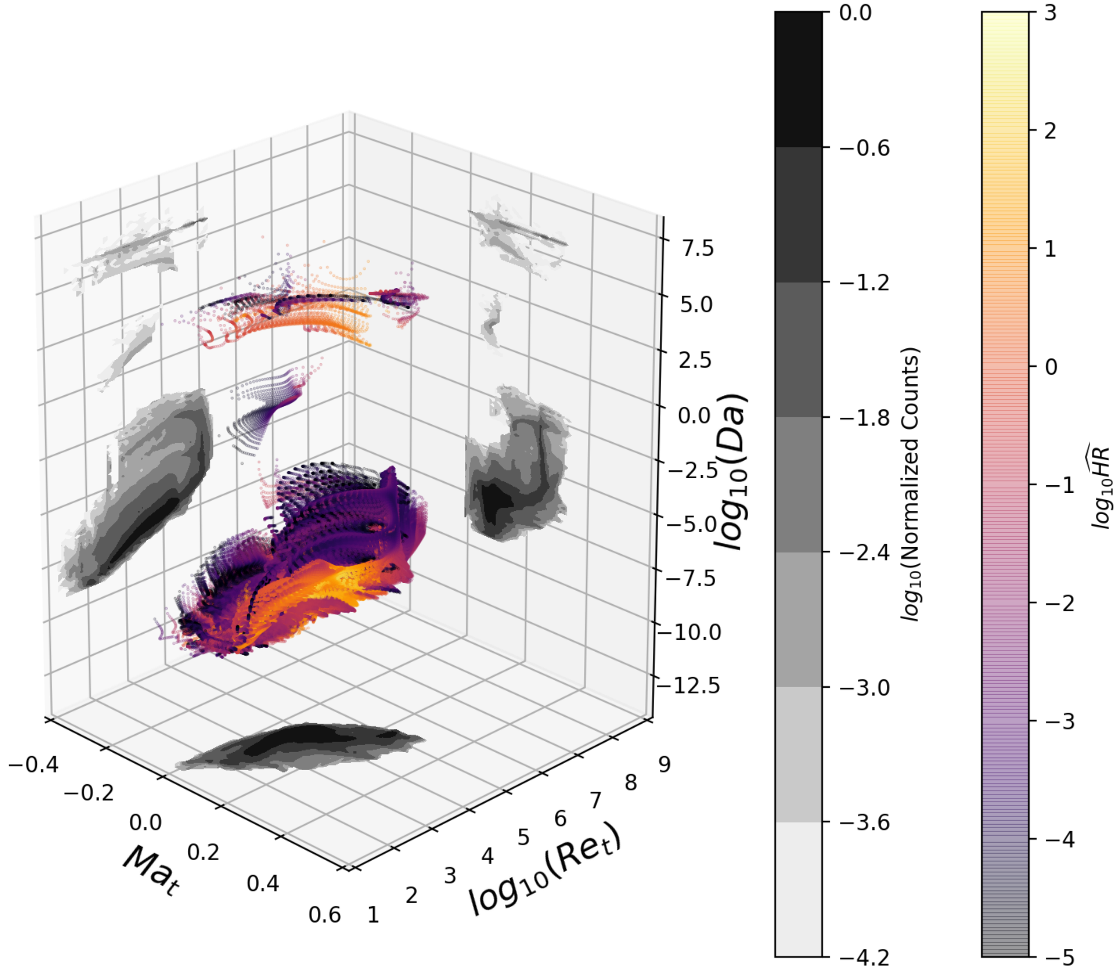

Figure 4.13: Comparison of fluid and chemistry scales Ma_t, Re_t, and Da at *aft-fueled* condition in downstream region $16 \leq \hat{x} \leq 26$.

4.4 Temporal Resolution and Fueling Timescale

This work considers a fuel-staging transient wherein unstart is induced by linearly varying the fuel injector flow rates between the aft-fueled and forward-fueled conditions. As noted in Ch 2, increasing the fuel flow rate at the B2 injectors correlates with steady-state PCST location moving upstream. If the local equivalence ratio split for these injectors exceeds $\phi_{B2} \geq 0.36$, the isolator is expected to unstart. The variation of local fuel injector equivalence ratio split (ϕ_i) versus non-dimensional simulation time, $\hat{t} \equiv t/\tau_{ramp}$, is shown in Figure 4.14. During an imposed fuel-transient period τ_{ramp}, the fuel flow rate is increased at the upstream B2 injectors and decreased at the injectors (B6 and C3) downstream of the cavity to maintain a fixed $\phi_{tot} = 0.9$. Note that, in contrast, the experiments only observed the fuel-ignition and transient process to steady-state for a fixed fuel-staging condition. The fuel-staging transient in this computational work is selected for two reasons. First, the ignition transient is not the primary concern. Rather, the intent is to study the unstart process for an already operative scramjet flowfield. Second, it is assumed that, by calibrating model parameters to the initial and final fuel-staging states, the fuel-transient can be approximated in a quasi-static-like process bounded by the extreme fueling states.

As part of the sensitivity study, the influence of global timestep size Δt and timescale τ_{ramp} on PCST motion is explored. The influence of these temporal parameters on unstart shock speeds and time-to-unstart are quantified. The selected cases for timescale and timestep are summarized in Table 4.3. For the reference solution ($TS0$), a global timestep $\Delta t = 10\ \mu s$ (corresponding to an effective Courant-Friedrich-Lewy ($CFL \equiv \frac{c\Delta t}{\Delta x}$) number of order unity based on fuel injection velocity

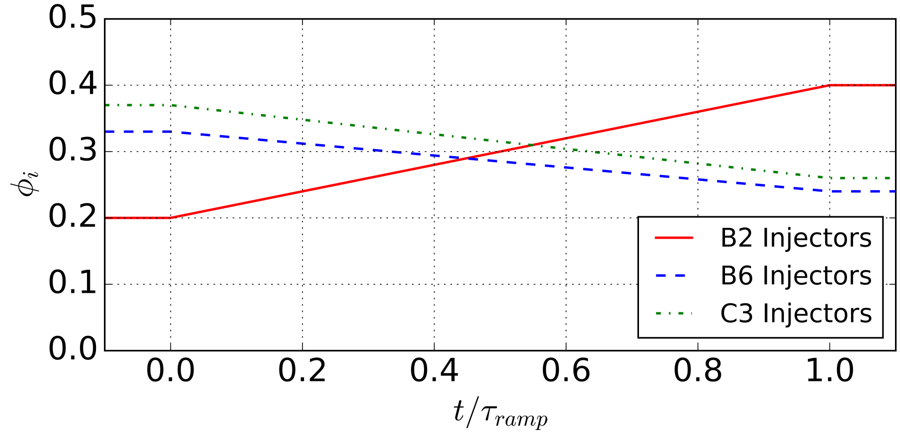

Figure 4.14: Imposed fuel-staging transient to induce unstart of the combustor.

Table 4.3: Summary of temporal scaling study parameters.

Case	Δt $[\mu s]$	τ_{ramp} $[ms]$	$\hat{t}_{uns}$ $--$	u_{uns} $[m/s]$	τ_{uns} $[ms]$
TS0	10	48	1.066	29.6	1.4
TS1	5	48	0.870	33.5	1.3
TS2	20	48	2.177	14.7	2.9
TS3	10	24	1.343	26.6	1.6
TS4	10	96	0.941	24.8	1.8

($\mathcal{O}(300)$ m/s) and near wall spacing) is applied to adequately resolve the dynamics over the fuel transient timescale. Solution results are typically sampled at least five times per core flow convective time ($\tau_{flow} \approx 1$ ms) yielding 289 snapshots during the reference simulation.

The specification of the fuel-staging timescale is constrained by computational expense and physical considerations. Adopting a fuel-staging timescale similar to the fuel transient of the experiments $\tau_{fuel,exp} \approx \mathcal{O}(10)$ sec is not computationally tractable. As mentioned in § 3.4, the transient fuel-staging requires $\mathcal{O}(100)K$ CPU-hours. Consequently, a reduced timescale is imposed for the computations. However, the solution further assumes a separation of scales. The computed solution is viewed as a quasi-static process as sketched in Figure 4.15, where the solver computes a steady-state solution within each global timestep Δt. The smallest physically limiting timescales within the combustor are likely associated with shock-separated or cavity[25,66,297] recirculation regions with estimated frequencies of $\mathcal{O}(1000)$ Hz. The range of relevant scales of the experiments and CFD fuel-transient are sketched in Figure 4.16. Since the RANS-based modeling approach adopted here does not resolve oscillatory turbulence features associated with these frequencies, a less stringent reference timescale $\tau_{ramp} = \tau_{fuel,cfd} = 48$ ms is selected for the computations such that $\tau_{flow} < \tau_{ramp} < \tau_{fuel,exp}$ where the overall simulation period is $\tau_{sim} = 1.2 \cdot \tau_{ramp}$. This reduction in simulation timescale (relative to experiment) is consistent with the study on mode-transition by Yenstch *et al.*[196] who showed that such a scaling does not qualitatively affect the large-scale dynamics of interest. However, to understand how varying τ_{ramp} may affect the predicted shock motion, several fuel-transient timescales over the range 24 $ms \leq \tau_{ramp} \leq 96$ ms are investigated.

Analogous to experimental measurements, the pressure-based metric defined in § 2.2 is used to track shock-train motion during the fuel-staging transient and quantify solution sensitivity to the predicted flow-field with respect to the time integration parameters. Figure 4.17 shows the predicted PCST motion at the isolator centerline ($\hat{z} = 0$) on the cowl-side wall ($\hat{y} = 0$) for the reference timescale case (TS0). During the fuel-staging event, the PCST speed (u_s) is relatively constant for $1 \lesssim \hat{x}_s \lesssim 3$ with $u_s \approx 2$ m/s. This speed is comparable to the average PCST upstream speed

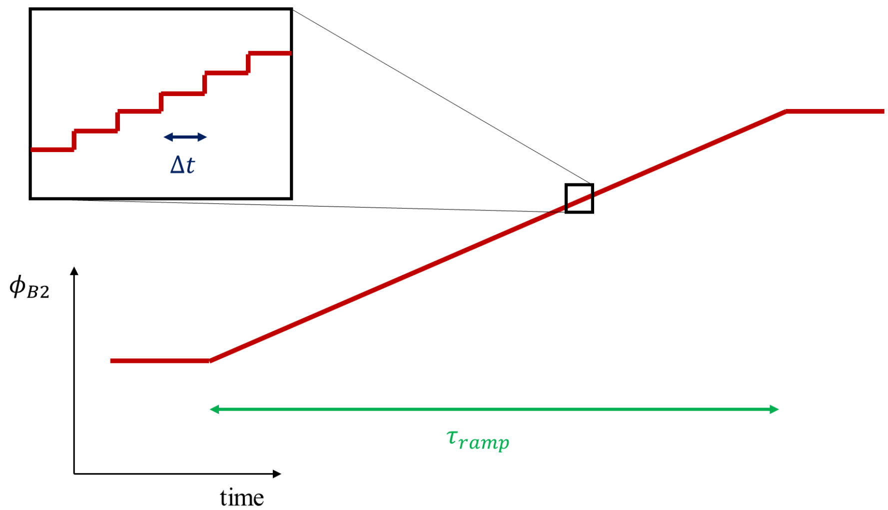

Figure 4.15: Sketch of quasi-static fueling process.

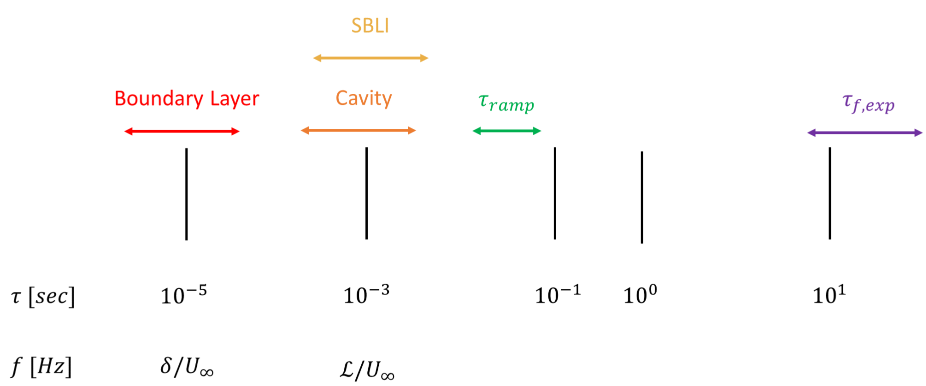

Figure 4.16: Comparison of estimated timescales in combustor.

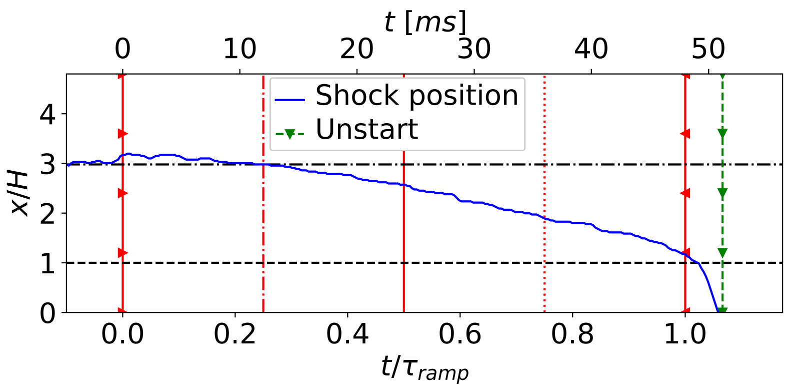

Figure 4.17: Predicted PCST position $\hat{x}_s$ versus simulation time of reference case (TS0).

estimated from the forward-fueled experiments. When $\hat{x}_s \approx 1$, however, an incipient unstart condition is identified corresponding to a change in the slope of the $\hat{x}_s$-$\hat{t}$ curve. Following this constant velocity period, the unstart PCST speed is estimated to be 29.6 m/s or $|u_s/u_\infty| \approx 0.023$. The unstart speed u_s is defined as the slope of the linear fit of the $\hat{x}_s - \hat{t}$ curve found in the range $0 \leq \hat{x}_s \leq 0.8$ prior to isolator unstart ($x_s = 0$). The shock-train travels approximately one duct height during the unstart phase, a corresponding timescale is computed $\tau_{uns} \equiv \mathcal{H}/u_s = 1.4\ ms$ with a predicted time-to-unstart of $\hat{t}_{uns} \equiv t_{uns}/\tau_{ramp} = 1.066$.

In comparison to the reference simulation, differing sensitivities to the time integration parameters are identified for variations in Δt and τ_{ramp} as shown in Figure 4.18. Here the $\hat{x}_s - \hat{t}$ curves are normalized by their respective fuel ramp timescales. Each simulation commences from the same initial condition and runs for $0.1 \cdot \tau_{ramp}$ at the aft-fueled state prior to initiating the imposed change in fuel-staging. As noted in § 3.6, the initial condition is taken from the converged steady-fueling solution at the aft-fueled condition. The extra constant-fueling period imposed prior to the linearly-varying phrase is intended to wash-out any numerical effects attributable to changes in timestep. Despite this extra period at the aft-fueled condition, greater sensitivity is observed from the predicted unstart PCST speed for changes in global time-step (Figure 4.18 (a)) than for to timescale (Figure 4.18 (b)). The unstart shock speed is selected as a quantity of interest since scale-resolving[298–300] and model-based[301] analyses of a $Ma_\infty = 5$ isolator[129] revealed variations in predicted shock speed with respect to model assumptions. Unstart speeds u_s and unstart timescales τ_{uns} are summarized in Table 4.3. As the time-step size is reduced, time-to-unstart $\hat{t}_{uns}$ is reduced and unstart shock speed increases slightly. Doubling the timestep relative to the reference case shows a much more significant change, with $\hat{t}_{uns}$ more than double that of the reference case. Changes in fuel-staging timescale, *i.e.* rate of change in fuel flow rate $\frac{d\dot{m}}{dt}$, reveal that τ_{ramp} and time-to-unstart $\hat{t}_{uns}$ are inversely related. However, the computed PCST unstart speed is relatively unchanged for doubling or halving of the timescale consistent with the proposition that the fueling process is much slower (larger timescale) than the unstart process. Despite these differences, the incipient unstart condition ($\hat{x}_s \approx 1$) is unchanged between these cases occuring for $x_s/\mathcal{H} \approx 1$. Careful characterization of the incipient unstart state is explored in § 5.2.3.

To understand the cause of the above scaling behavior, the computed differences in solution time-to-unstart are examined using spatially integrated chemical heat release rate in the combustor. Here, the heat release rate, $\dot{HR}(x,t)$, is normalized (eqn. 4.13) by the integrated heat release rate along the combustor streamwise axis $\underline{HR}_x$ (eqn. 4.14) at the start of the fueling transient $\hat{t} = 0$. Figure 4.19 compares the change in heat release in the combustor with time-step and fuel-ramp scale.

Figure 4.19 (a,d) shows the heat release rate integrated over the $\hat{x} = 11.57$ (B2 injectors) plane; whereas, Figure 4.19 (b,e) provides heat release at the $\hat{x} = 13.42$ plane (middle of the cavity flameholder). Interestingly, the heat release at the plane of the upstream injectors decreases over time despite the increase in fuel flow rate at this location. However, heat release does increase in the flame-holder cavity as upstream injector fuel flow rates are increased. In contrast, Figure 4.19 (c,f) shows the streamwise integrated heat release rate for each time instant ($\underline{\dot{HR}}_x(t)$).

$$\widehat{\dot{HR}}(\mathbf{x}, t) = \frac{\dot{HR}(x, t)}{\underline{\dot{HR}}_x(t = 0)} \tag{4.13}$$

$$\underline{\dot{HR}}_x(t) = \frac{1}{L} \int \dot{HR}(x, t) dx \tag{4.14}$$

The initial heat release at the start of the ramp period, critically, slightly increases as the time-step is reduced (Figure 4.19 (c)). Although the magnitudes of heat release (Figure 4.19 (c)) at $\hat{t} = 0$ are within two percent of one another, greater heat release in the cavity prior to the increase in fuel flow rate at the upstream injectors correlates with a shorter time-to-unstart. As addressed later (§ 5.2.5), increased heat release affects side wall separation contributing to unstart. The observed differences in unstart timescales is attributable, in part, to errors introduced by changing the time-step when restarting from converged steady aft-fueled solution. A sensitivity to initial condition was also observed by Yentsch *et al.*[302] in computations of mode-transition for the HIFiRE 2 scramjet. Although solution variations attributable to initial heat release are essentially washed out during the included $0.1 \cdot \tau_{ramp}$ prior ($\hat{t} < 0$) to the fuel transient phase, increasing the duration of the pre-fuel-ramp period of the computations may help to further minimize these effects. For changes in τ_{ramp}, curves

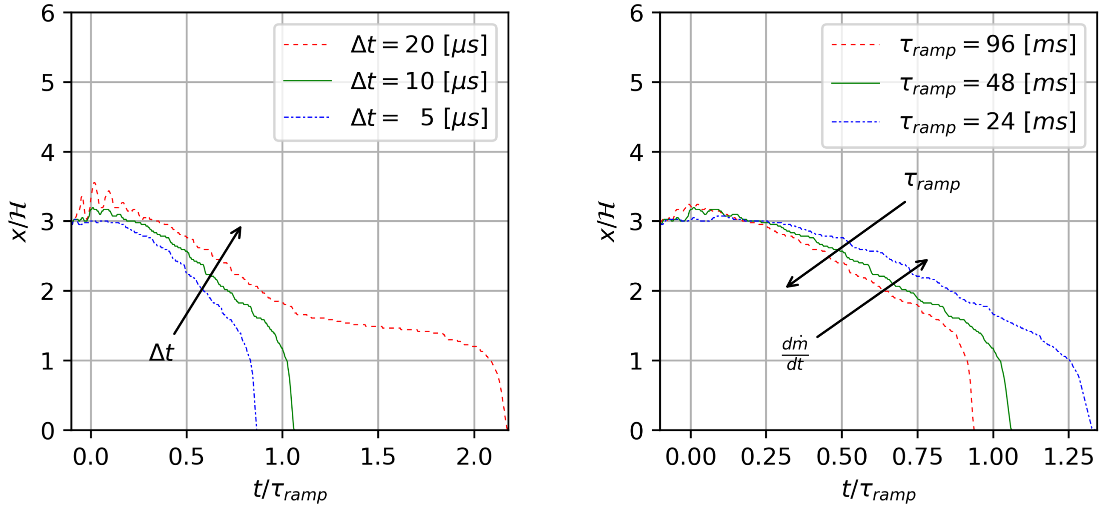

(a) Δt scaling

(b) τ_{ramp} scaling

Figure 4.18: Comparison of predicted PCST position $\hat{x}_s(\hat{t})$ for time-scaling study: (a) variation with global timestep Δt and (b) variation with fuel-staging time scale τ_{ramp}.

of heat release at the B2 injectors (Figure 4.19 (d)) and cavity (Figure 4.19 (e)) planes are in closer agreement (the curves collapse) than for the varying Δt cases.

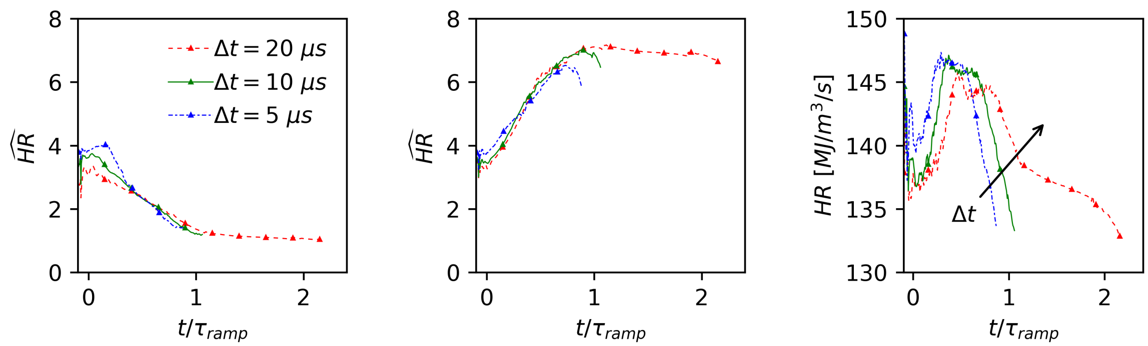

(a) B2 injectors, $\hat{x} = 11.57$ (b) Cavity, $\hat{x} = 13.42$ (c) Streamwise integrated

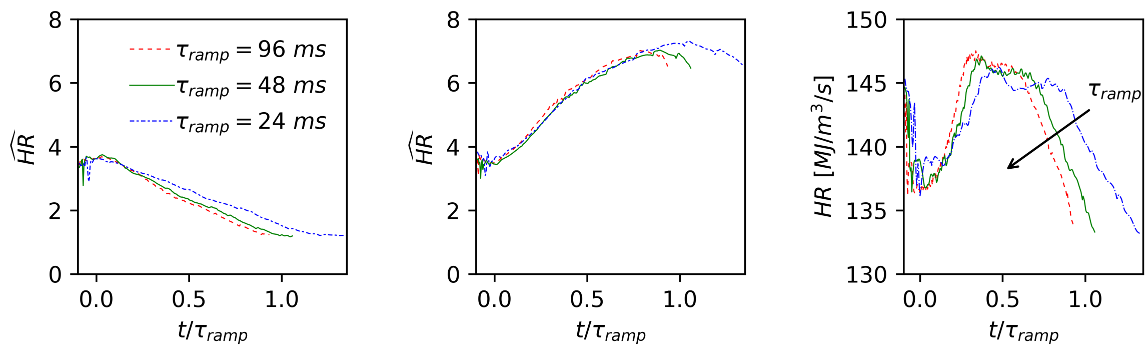

(d) B2 injectors, $\hat{x} = 11.57$ (e) Cavity, $\hat{x} = 13.42$ (f) Streamwise integrated

Figure 4.19: Normalized heat release comparison for Δt (*above*) and τ_{ramp} (*below*) scaling.

4.5 Summary

- Steady-state computations of un-fueled and fueled combustor operation are compared against the time-mean wall pressure measurements of experiment to assess model agreement and parameter sensitivities.
  - Un-fueled pressure profiles capture quantitative and qualitative trends of experiments
  - Solution sensitivity to grid resolution is quantified using the Grid Convergence Index. The largest errors for predicted steady-state, wall pressure profiles are associated with gradients corresponding to reflected shock waves.
- Boundary condition effects on predicted wall pressures are characterized as follows:
  - The un-fueled solution is insensitive to variation in inflow Reynolds number.
  - The inflow eddy viscosity ratio has negligible effect on predicted wall pressures.
  - The wall temperature condition affects SBLI reflection regions. An adiabatic wall assumption improves pressure predictions in the cavity, but decreases agreement with the upstream, isolator wall pressures.
- Steady-state fueled computations reveal greater sensitivity to model parameters. Peak pressures are correctly captured by the model but some local wall pressure variations are not well-captured.

- Model sensitivity to chemistry and mixing effects are carefully characterized:
  - Two laminar kinetics mechanisms are tested: a quasi-global and a reduced skeletal mechanism. The kinetics mechanisms are observed to have limited influence on the predicted wall pressure distributions, relative to other model uncertainties.
  - The presence of vitiate species at the nozzle inflow slightly decreases peak pressures but has limited effect overall.
  - Consistent with other works in the literature, the turbulent Schmidt number is observed to have largest influence on predicted isolator pressure distribution and presents the largest parameter uncertainty.
  - A single Sc_t does not capture both aft-fueled and forward-fueled combustion states. Decreasing Sc_t improves agreement at the forward-fueled condition, increasing turbulent diffusion effects. Conversely, increasing Sc_t improves agreement at the aft-fueled condition by increasing turbulent viscosity effects.
  - Discrepancies between measured and predicted side wall and cavity pressure profiles may be attributable to fine-scale turbulence-combustion interactions not captured by model-based approach.
  - Analysis of the turbulent and chemical scales reveals a wide range of scales suggesting the finite-rate kinetics approach is appropriate for the analysis.
  - Heat release primarily occurs near the side wall region at relatively lower Da.

  - An increase in fluid timescales between aft- and forward-fueled conditions indicates a modest upward shift in Da.

- Transient fuel-staging model sensitivities are assessed in terms of predicted unstart time and velocity scales:

  - The global timestep has the largest influence on predicted shock motion. As Δt is reduced, time-to-unstart reduces. This is attributable to numerical errors due to calculation of the non-linear chemical source terms. However, the shape of the shock motion curve is qualitatively unchanged.

  - The timescale of the fueling transient affects time-to-unstart but does not qualitatively affect the shock motion curve or shock speed.

- Overall, the model-based approach captures the global trends with respect to wall pressure profiles despite model uncertainties.

Chapter 5

Unstart Phenomenology

The flow structure of the two, steady-fuel-staging states are first explored before considering the dynamics of the fuel-staging transient. Specifically, the principal shock structures, vortical features, and three-dimensional separation regions near the side wall for both the aft-fueled and forward-fueled conditions provide context for observations of the unstart process. Three-dimensional observations are complemented by one-dimensional property analysis. The two cases considered employ the optimal turbulent Schmidt numbers selected for the aft- and forward-fueled conditions, respectively, as determined from the discussion in § 4.3.1.

5.1 Reference Fueling States

5.1.1 Flow Topology

Comparison of steady-state un-fueled and fueled conditions reveal strong flow-structure variations. Contours of Mach number highlight a supersonic core within the combustor as shown on the symmetry plane ($\hat{z} = 0$) in Figure 5.1. The static temperature field, also provided, indicates post-shock regions and reaction zones with higher contour magnitudes. For the tare condition (Figure 5.1 (a)), the supersonic core persists throughout the combustor. However, a smaller region of the isolator remains supersonic in the aft- and forward-fueled states (Figure 5.1 (b)–(c)). Relatively higher magnitude contours of static temperature indicate heat-release regions in the cavity shear layer and downstream of the backward-facing steps. A reduced, one-dimensional view of static pressure, static temperature, and Mach number is shown in Figure 5.2 which quantifies these trends. The static temperature and pressure are normalized by the respective nozzle stagnation conditions. In particular, reduction of the Mach number for the fueled conditions corresponds to increased pressure in the cavity as a result of combustion.

The divergence of the velocity field reveals complex shock/boundar-layer interactions within the scramjet as shown in Figure 5.1. For tare-mode operation, oblique shock reflections initiated by the Distortion Generator (DG) continue throughout the cavity region. The reacting cases, however, feature oblique waves that dissipate by $\hat{x} \approx 8$. In particular, a bow shock emanates from the body-side wall, upstream of the combustor cavity, as a result of injection from the centerline B2 fuel injector, as shown by the inset with the solid outline. Additional compression and expansion waves are evident downstream of back-facing steps, where flow leaving the cavity region acts like an under-expanded jet, with a series of alternating expansion and compression waves. These waves further interact with the shear layers anchored downstream of the body- and cowl-side wall steps, as shown in the inset with the dashed outline. At the forward-fueled condition, the isolator duct contains a series of planar-like waves interspersed between weakly supersonic regions. These views show a transition from an oblique- to a normal-mode shock-train[9] for decreasing Mach number in the isolator. Increased fuel flow rates at the upstream (B2) injectors at the forward-fueled condition generates a stronger compression wave upstream of the cavity which extends across the isolator duct. Similar to the aft-fueled condition, a shock diamond pattern is observed in the expansion duct for the forward-fueled case. Jet-like flow downstream of the backward-facing steps appears asymmetric. This is attributable to the streamwise offset between the backward-facing steps on the upper and lower wall. This feature might be leveraged for thrust-vectoring by modifying the streamwise distance between the body-side and cowl-side wall steps.

Like the symmetry plane, a horizontal plane located at half a duct height above the cowl-side wall ($\hat{y} = 0.5$) provides additional details of the structure of the reference flowfields. Dilatation and temperature contours for this horizontal slice (and symmetry plane) are shown in Figure 5.3. Side wall flow separation and the interaction of shock waves inside the supersonic core are observed for the aft-fueled condition. Shock structures, (Figure 5.3 (i) and (ii)), particularly on the horizontal plane, show curvature near the side wall as a result of shock-induced separation. In addition to contours of dilatation and temperature, examination of the TKE and TED fields complement observations of the separated zones. The TKE and TED fields (Figure 5.3 (iii)–(v)) are qualitatively similar for both aft- and forward-fueled conditions. The largest magnitudes of each are found in regions of high shear such as the cavity and backward-facing step shear layers with a turbulent timescale: $\tau_t \equiv \tilde{k}/\tilde{\epsilon} \approx 0.2\ ms$. In addition to the mixing regions, higher TKE and TED levels are identified near the inception of side wall separation as shown in the $\hat{y} = 0.5$ plane. Figure 5.4 shows the forward-fueled condition, which is structurally similar to the aft-fueled condition with respect to peak cavity TKE levels. However, the forward-fueled condition has lower velocity flow near the duct core relative to the aft-fueled state, with diminished TKE magnitudes. Higher temperatures on the horizontal plane (Figure 5.3 and Figure 5.4 (vii)) suggest greater heat release near the side walls; this behavior is detailed in the subsequent section (§ 5.1.2).

5.1.2 Mixing and Heat Release

The combustion and propulsive performance of scramjets is strongly coupled to the fuel injection and mixing strategies.[303] For example, fuel introduced by a jet-in-crossflow[297,304–306] can affect mixing and propulsion efficiency depending on fuel injector orientation relative to the main flow. To characterize the mixing behavior of the injected fuel, streamlines originating from each of the fuel injectors are shown for the steady aft- and forward-fueled states in Figure 5.5. Also depicted are Mach-number iso-surfaces at the sonic condition ($Ma = 1$) which are colored by the non-dimensional distance above the cowl wall ($\hat{y}$). These surfaces demarcate the supersonic core from the near-wall, subsonic, separated zones. Subsonic regions are particularly prevalent near the combustor side walls.

The strong contrast in mixing behavior for each fuel-staging condition also affects the heat-release behavior. Streamline curvature, suggests greater interaction near the combustor cavity, cowl/body-side wall steps, and isolator corners for the aft-fueled condition (Figure 5.5 (a)) than the forward-fueled condition (Figure 5.5 (b)). Streamlines from the outboard B2 injectors (yellow) at the forward-fueled condition are biased toward the side wall regions, similar to the aft-fueled condition. However, streamlines near the inboard injectors do not interact as significantly in the cavity region. This can be partly explained by the iso-surface, which indicates that fuel

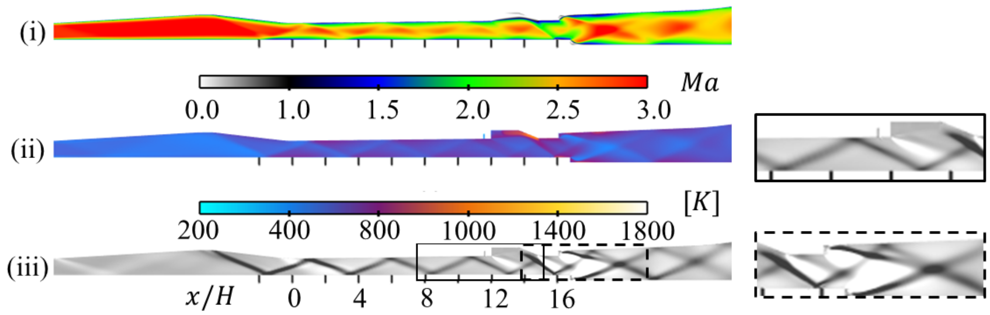

(a) Tare condition

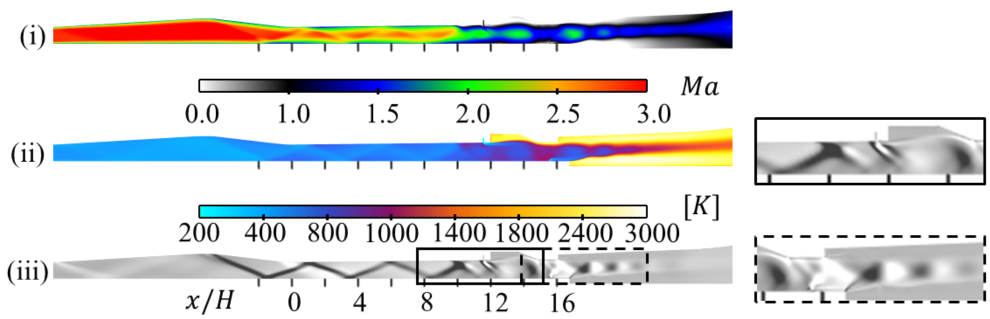

(b) Aft-fueled condition, $Sc_t = 1.2$

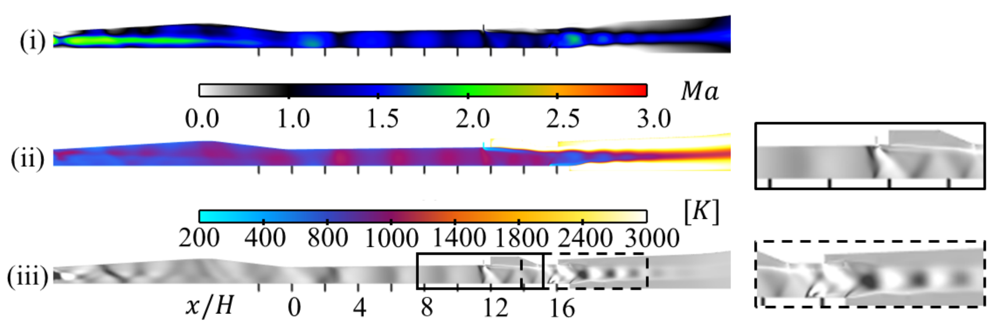

(c) Forward-fueled condition, $Sc_t = 0.5$

Figure 5.1: Flowfield comparison for contours of (i) Mach number, (ii) static temperature, and (iii) dilatation fields on the $\hat{z} = 0$ (symmetry) plane: (a) tare condition, (b) aft-fueled condition, (c) forward-fueled.

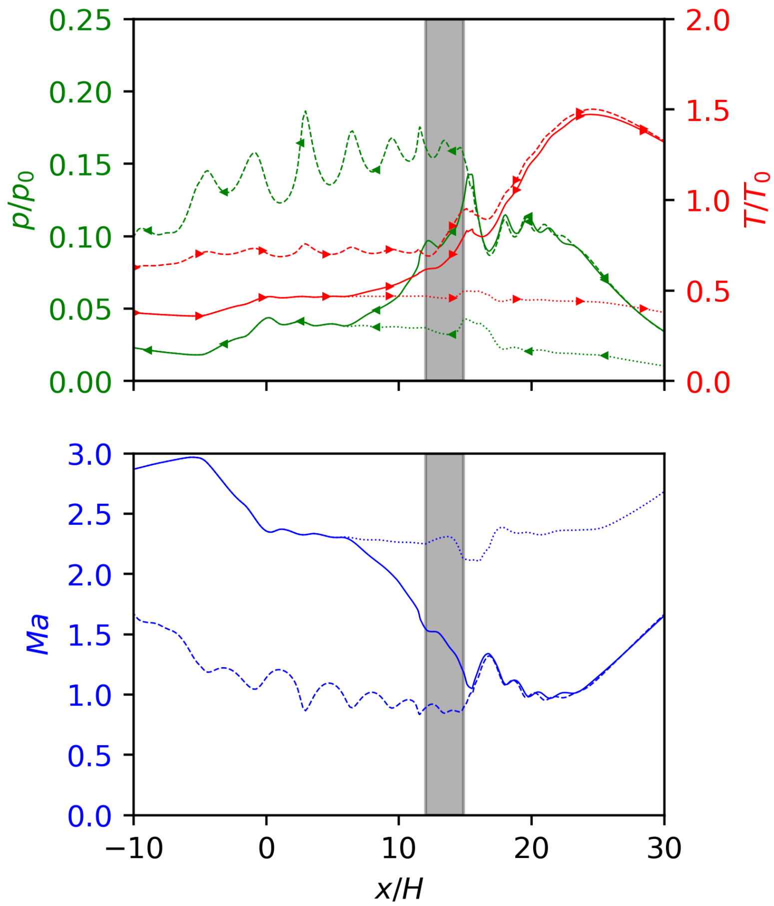

Figure 5.2: One-dimensional analysis of mass-flux-weighted Ma, static pressure, and static temperature: *tare* condition - dotted curves, *aft-fueled* condition - solid curves, *forward-fueled* condition - dashed curves, and *grey* - cavity.

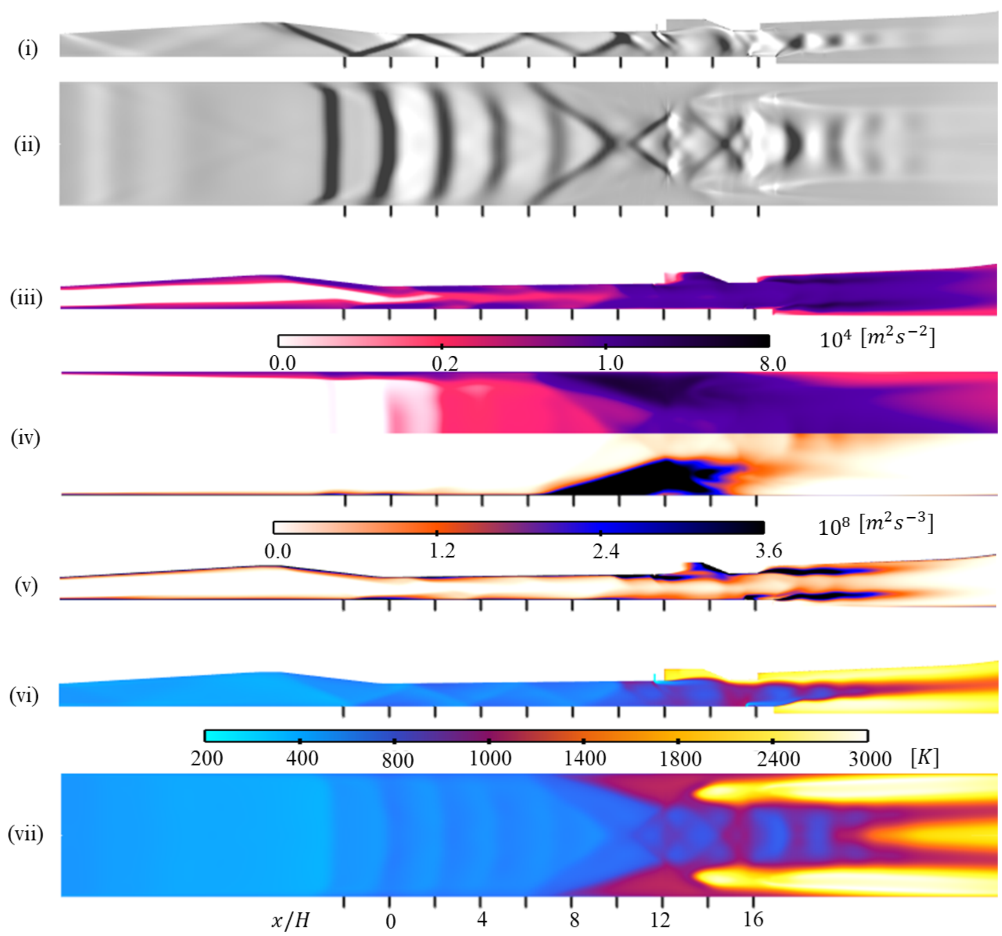

Figure 5.3: Aft-fueled flowfield: contour fields of dilatation on $\hat{z} = 0$ (i) and $\hat{y} = 0.5$ (ii); TKE on $\hat{z} = 0$ (iii); TKE (above), TED (below) on $\hat{y} = 0.5$ (iv); TED on $\hat{y} = 0.5$ (v); temperature on $\hat{z} = 0$ (vi) and $\hat{y} = 0.5$ (vii).

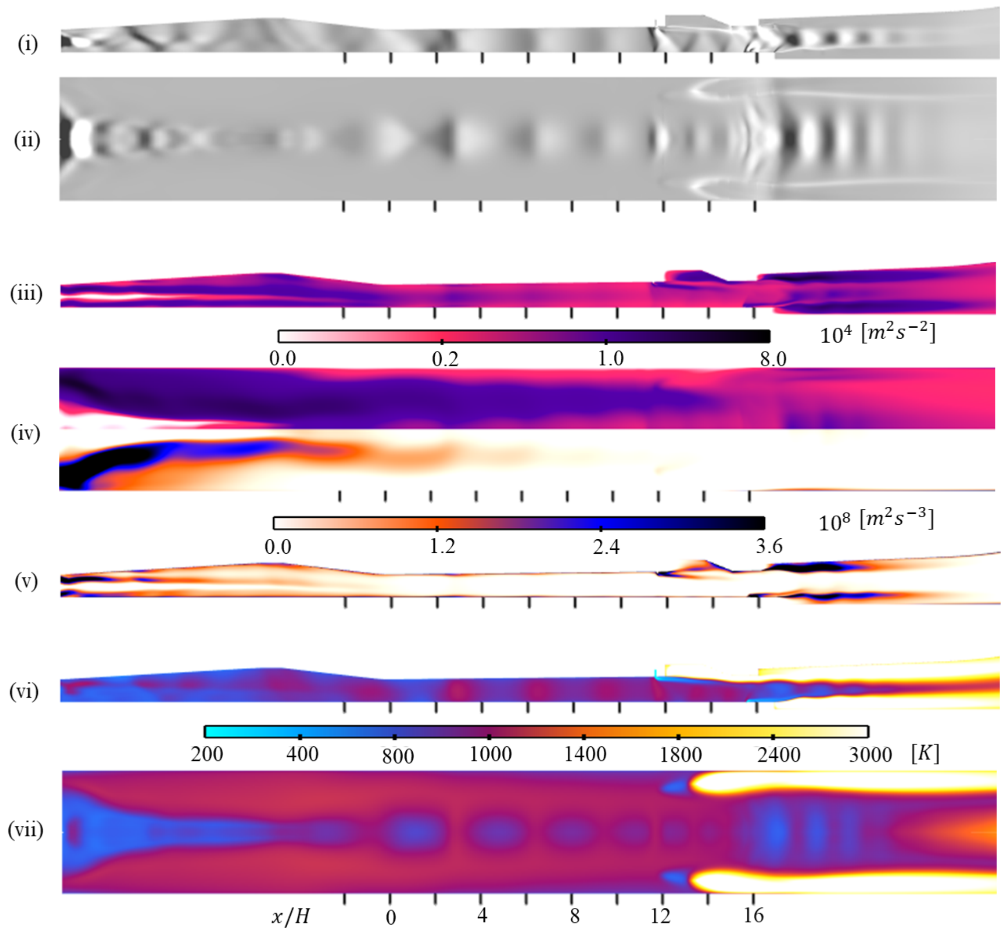

Figure 5.4: Forward-fueled flowfield: Contour fields of dilatation on $\hat{z} = 0$ (i) and $\hat{y} = 0.5$ (ii); TKE on $\hat{z} = 0$ (iii); TKE (above), TED (below) on $\hat{y} = 0.5$ (iv); TED on $\hat{y} = 0.5$ (v); temperature on $\hat{z} = 0$ (vi) and $\hat{y} = 0.5$ (vii).

from the B2 injectors penetrates deeper into the isolator duct for the forward-fueled operation compared to the aft-fueled case, consistent with the increased fuel flow rate.

In both cases, fuel injected from the outboard B2 injectors enters into the near-wall subsonic region where relatively strong mixing and reaction occurs. Contours of the normalized heat-release rate $\widehat{\dot{H}R}$, shown on the $\hat{z} = 0$ and $\hat{y} = 0.5$ planes in Figure 5.6, highlight prominent reaction zones near shear layers anchored to the cavity and backward-facing steps, consistent with the streamlines of Figure 5.5. At the aft-fueled condition, upstream fuel penetration leads to the cavity shear layer impinging on the aft-wall of the cavity. The deeper penetration of the B2 injectors at the forward-fueled condition, however, results in a shear layer reaction zone offset from the cavity aft-wall. The behavior of near-wall mixing plays an important role during the unstart dynamics as explored in § 5.2.5.

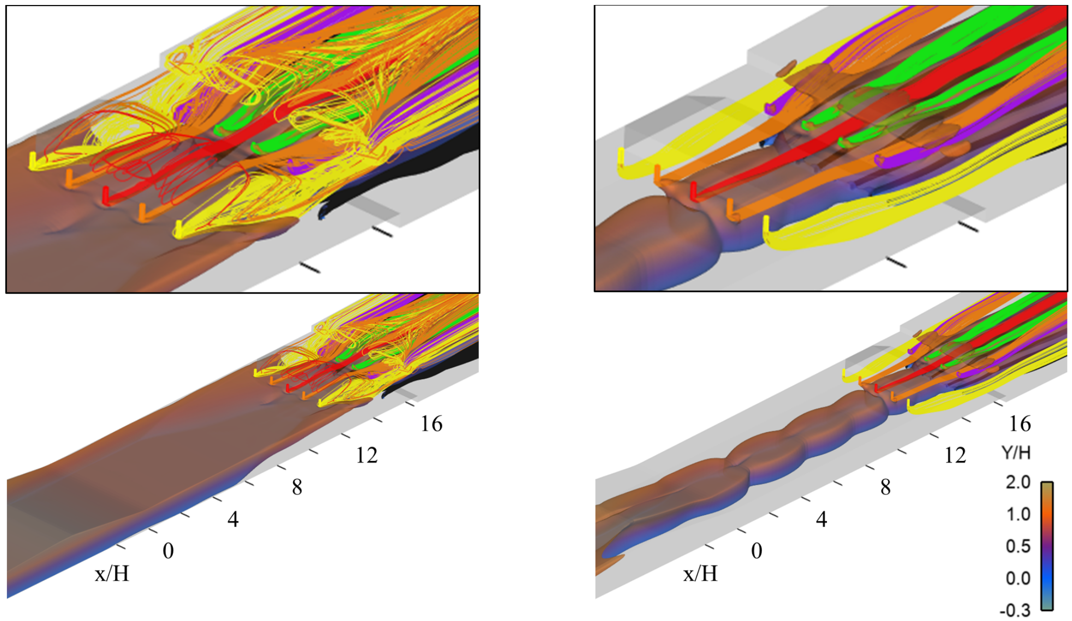

(a) Aft-fueled condition, $Sc_t = 1.2$ (b) Forward-fueled condition, $Sc_t = 0.5$

Figure 5.5: Comparison of fuel mixing: (a) aft-fueled, (b) forward-fueled condition. Iso-surface of sonic condition colored by height above cowl wall. Streamlines emitted from injectors: *red* - Centerline B2; *orange* - Inboard B2, *yellow* - Outboard B2; *green* - Inboard B6; *purple* - Outboard B6; *black* - C3 injectors.

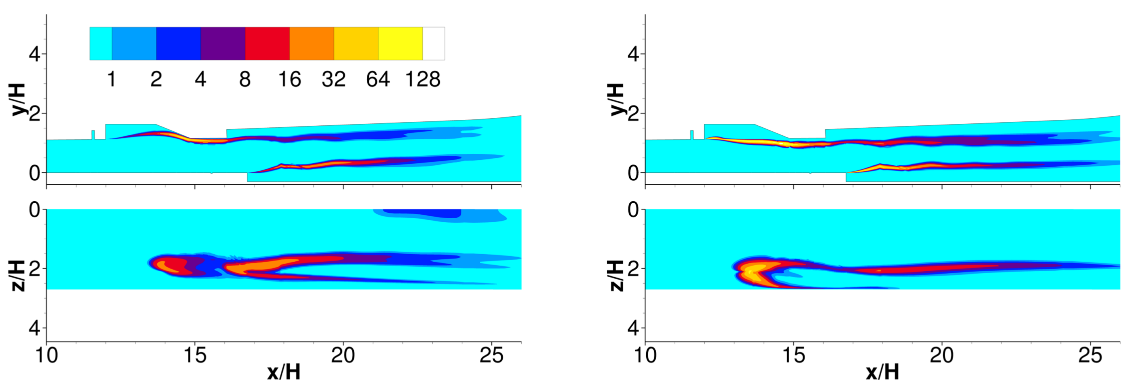

(a) Aft-fueled condition, $Sc_t = 1.2$ (b) Forward-fueled condition, $Sc_t = 0.5$

Figure 5.6: Comparison of non-dimensional heat-release rate $\widehat{\dot{H}R}$ on $\hat{z} = 0$ and $\hat{y} = 0.5$ planes: (a) aft-fueled, (b) forward-fueled.

5.2 Transient Fuel-Staging

Although quantitative sensitivities to timestep and timescale are identified in § 4.4, the dynamic unstart features are qualitatively independent of the selected timescale. For convenience, discussion of the unstart process is described with respect to the reference solution (TS0), with $\tau_{ramp} = 48\ ms$, as a representative instance of the relevant transients.

Corner effects present prior to the fuel-staging are initially described (§ 5.2.1) before exploring the two primary phases of PCST motion. The first, slowly varying or pre-unstart phase is characterized (§ 5.2.2) followed by the rapid upstream motion of the shock-train during the unstart phase (§ 5.2.4). An incipient unstart condition, which marks the transition between these two phases as previously noted in Figure 4.17, is then explored (§ 5.2.3). In particular, corner-flow behavior is described in terms of viscous confinement. After the PCST reaches the isolator entrance, a brief shock-train transient is also observed in which the PCST moves upstream of the 'inlet' shock generated by the DG (§ 5.2.4). Lastly, mixing behavior is used to explain strong spanwise flow gradients and the unstart mechanism involving chemical heat release (§ 5.2.5).

5.2.1 Initial State and Inflow Distortion

The influence of the distortion generator on the evolution of the isolator shock structures for the aft-fueled fueling condition is analyzed by considering select planes of instantaneous, simulated, surface oil flows. Surface oil flows on the body-side, south-side, and cowl-side walls are shown in Figure 5.7 at the start of the imposed fuel transient ($\hat{t} = 0$). The coalescence of surface flow lines on the cowl-side wall indicate the separated region near the side wall which is denoted by S_{csw}. The vortical signatures of the separated flow are featured prominently on the body-side wall, $v_{bsw,pri}$ (Figure 5.7 (a)). A related feature is the curved separation (S_{bsw}) indicated by the lines of coalescence on the upper wall. The curvature of the body-side wall separation underscores a complex interplay of the vortical structures and the incident shock created by the DG. A connected vortical feature, $v_{ssw,pri}$, is inferred from the side wall (Figure 5.7 (b)), along with another separation line, S_{ssw} (Figure 5.7 (c)). A vortical signature ($v_{ssw,sec}$) persists in the corner flow region downstream of the isolator entrance and merges with $v_{ssw,pri}$ as the fuel-staging transient progresses (§ 5.2.3).

The influence of streamline curvature and corner flow separation is also evident from examination of surface-constrained streamlines shown in Figure 5.8. On the upper (body-side wall) shown in red (Figure 5.8 (a)), streamlines constrict toward the midspan before passing through the cavity recirculation region. Bifurcation in the corner indicates a separated recirculation region along the side wall. Separation from the side wall is also evident on the lower (cowl-side) wall, as illustrated by orange streamlines (Figure 5.8 (b)) which similarly constrict toward the centerline. Complex side wall separation along the DG-generated shock is identifed by seeding two distinct sets of streamlines (Figure 5.8 (c)). A yellow, near-wall (inner layer) turns along the DG shock and follows the lower duct corner. A second (outer) layer in black also turns along the shock and fills the separation region delineated by the cowl-wall streamlines (red).

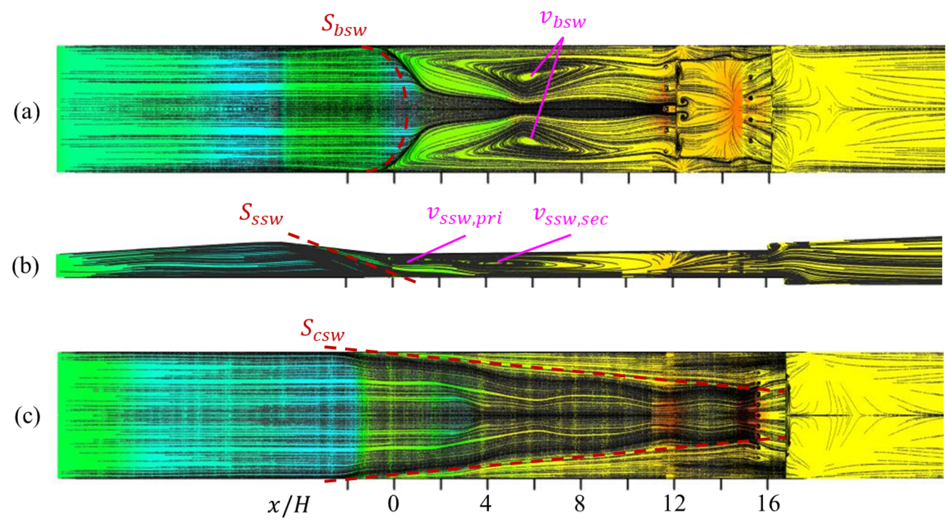

Figure 5.7: Flowfield state at aft-fueled condition ($\hat{t} = 0$): Instantaneous streamlines with contours of log pressure for (a) body-, (b) south-, and (c) cowl-side walls.

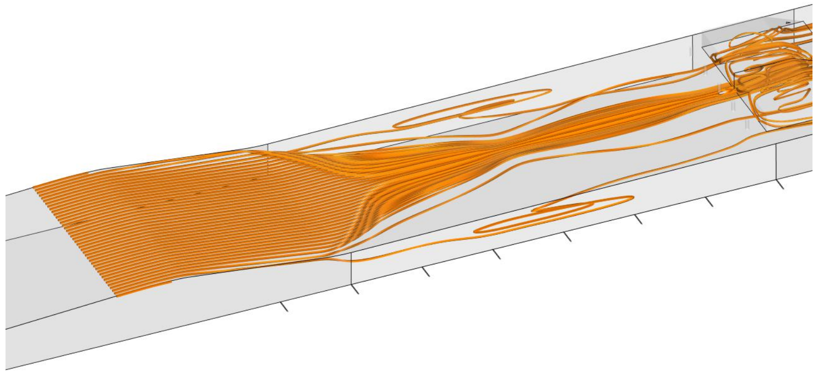

(a) Body-side wall (BSW)

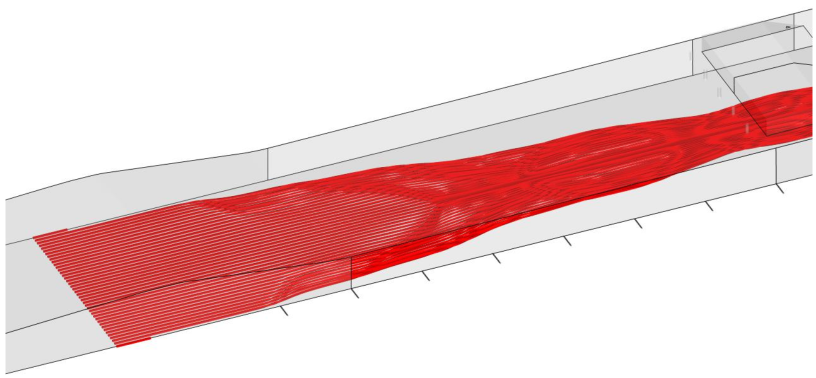

(b) Cowl-side wall (CSW)

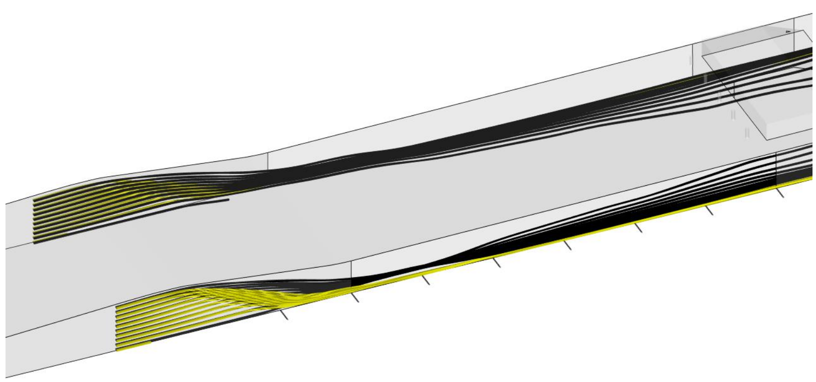

(c) Side-wall (SW)

Figure 5.8: Isolator entrance flow curvature and separation topology. Streamlines seeded near: (*a*) Body-side wall (orange), (*b*) cowl-side wall (red), (*c*) side walls: yellow (inner) black (outer) boundary-layer.

5.2.2 Pre-Unstart Phase

As fuel flow to the upstream injectors is increased, a period of constant-velocity motion of the shock-train is observed for $1 \lesssim \hat{x}_s \lesssim 3$ ($0 \lesssim \hat{t} \lesssim 1$) with an approximate PCST speed of $u_s \approx 2\ m/s$. During this period, the subsonic region near the body-side wall enlarges, propagates upstream, and ultimately distorts the isolator entrance shock as shown by the dilatation field in Figure 5.9. In Figure 5.9 (a), two oblique reflections (solid purple arrows) at the tail of the first and third reflected shocks are visible along the sonic line (red contour). As the subsonic zone advances upstream, the second interaction begins to break into two wave-like structures (Figure 5.9 (b)). The subsonic zone continues to grow until the shock-train terminates after the third reflected shock (Figure 5.9 (c)) which subsequently decays (Figure 5.9 (d)). This upper wall separation bubble is attributed to the adverse pressure gradient downstream of the isolator entrance plane. Consider the idealized case of quasi 1-D, inviscid flow. As flow downstream of the oblique DG-generated nears the isolator entrance, the flow is turned (expanded) through the isolator entrance plane the static pressure decreases. After expanding through this region, the incoming flow encounters an adverse pressure gradient due to the reflected oblique shock which impinges on the upper wall. This region is therefore likely more sensitive to the increasing combustion-induced back-pressure due to the pre-existing unfavorable pressure gradient near $\hat{x} \approx 2$ at the start of the fuel-staging transient.

The subsonic zone on the upper wall continues to modulate the now weaker ($Ma \approx 1$) core while increasing the deflection of the shock at the isolator entrance on the body-side wall until just prior to the unstart event (Figure 5.9 (e)). The resulting reflected shock at the body-side wall (solid arrow) takes on a lambda-like structure

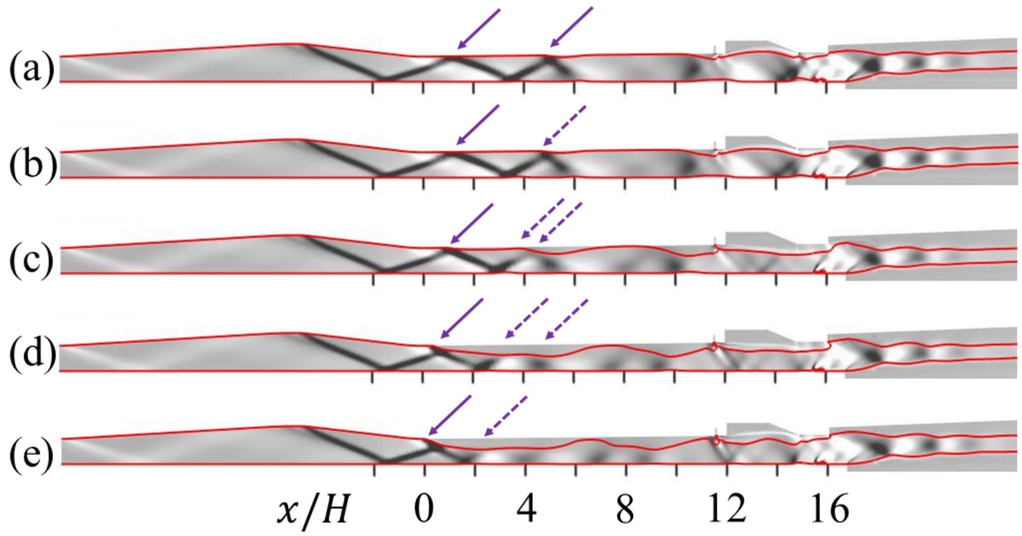

Figure 5.9: Body- and cowl-side wall shock modulation over quasi-steady period for time instances: (a) $\hat{t} = 0.00$, (b) $\hat{t} = 0.25$, (c) $\hat{t} = 0.5$, (d) $\hat{t} = 0.75$, (e) $\hat{t} = 1.00$. *Greyscale* - dilatation contours on symmetry ($\hat{z} = 0$) plane and *red* - $Ma = 1$ contour lines.

with the growth of subsonic fluid on the body-side wall acting like a compression ramp to the oncoming flow. Interestingly, the upstream PCST motion inferred from wall pressures may be re-interpreted as the modulation of the extant oblique shock waves near the isolator entrance, resulting in a shift from an oblique to a normal mode shock-train prior to unstart.

5.2.3 Incipient Condition and Initiation of Unstart

In the temporal parameters scaling study, the predicted shock motion indicates an incipient unstart condition when the PCST is approximately one duct height downstream of the isolator entrance ($x_s/\mathcal{H} = 1$). This incipient state, which functions as a reasonable indicator for the initiation of the unstart phase, is independent of the rate of change in fuel input to the combustor, as shown in § 4.4. To explore the physics contributing to the incipient unstart state at $\hat{x}_s = 1$, the non-dimensional PCST detector, which is applied in 1-D form along the isolator centerline ($\hat{z} = 0$), is extended to its 2-D analog on the cowl-side wall ($\hat{y} = 0$). The non-dimensional pressure distribution on the cowl-side wall is shown in Figure 5.10 for several snapshots during the simulation. A red contour line marking the PCST leading edge (determined by $\hat{p}$) is mapped onto the field. From the snapshots, the modified shock detector shows that the leading-edge of the PCST, (indicative of pressure rise due to combustion) advances upstream along the corner approximately three isolator duct heights in advance of the centerline location. At the instant of unstart ($\hat{t} = 1.066$), the PCST has advanced upstream to $\hat{x} = -2$ along the side wall. Taking the instant the PCST reaches $\hat{x} = 0$ at the side wall ($\hat{z} = 2.70$), may therefore provide a more conservative measure for unstart margin using similar wall-pressure-based shock-detection methods.

To better characterize the viscous 3-D behavior in the context of the literature, the confinement parameter (eqn. 5.1) of Merkli[105] is adopted. The shock-train oblique or normal character may be described in terms of the confinement parameter (C_δ) for rectangular ducts. Hunt *et al.*,[108] for example, use a shock-train regime diagram to compare relative viscous effects (boundary layer thickness) versus duct height at a given isolator Mach number (Ma_e).

In the present work, the confinement parameter is defined in terms of the ratio of the viscous area (A_δ) to the cross-section area (A_{iso}) as shown in Figure 5.11. The viscous area is computed from the difference in duct cross-section area and the

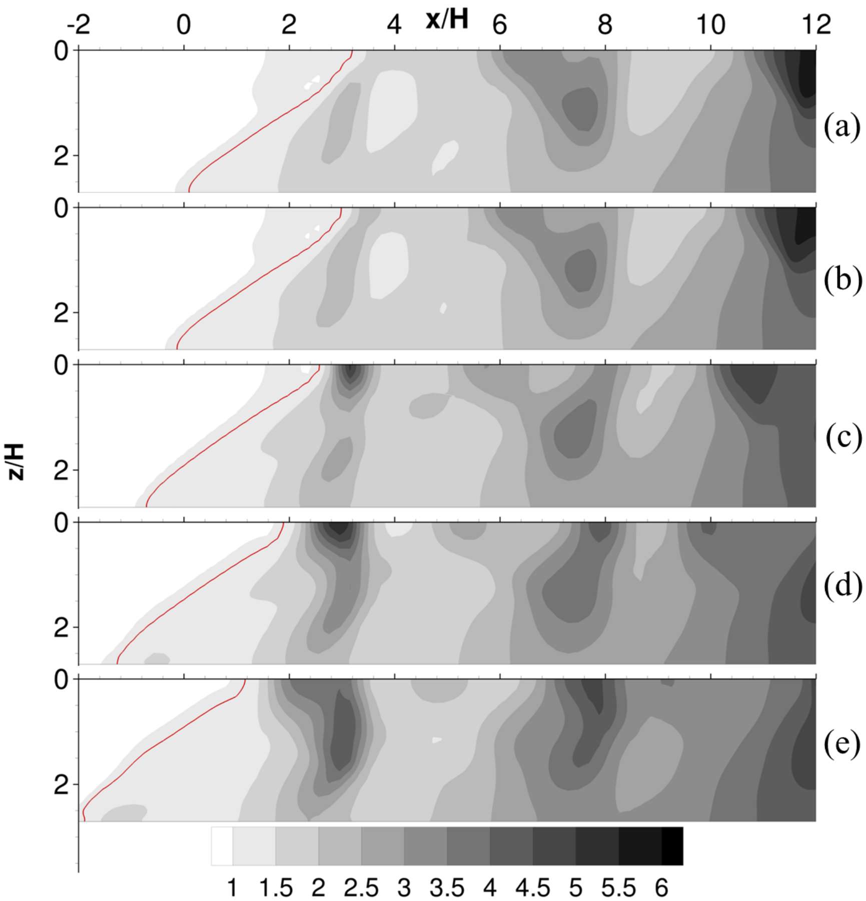

Figure 5.10: Non-dimensional pressure $\hat{p}(\hat{x}, \hat{z})$ on cowl-side wall ($\hat{y} = 0$) at time instances: (a) $\hat{t} = 0.00$, (b) $\hat{t} = 0.25$, (c) $\hat{t} = 0.50$, (d) $\hat{t} = 0.75$, (e) $\hat{t} = 1.00$. *Red* - contour of computed PCST leading-edge.

primarily inviscid supersonic core.† The current approach parallels the Axial Velocity Threshold approach used in the SBLI studies of Morajkar *et al.*[139,140,311] in which a fixed velocity threshold is selected to define the cut-off for boundary-layer separation. Here, the sonic condition is selected as the velocity threshold because the axial velocity varies along the streamwise extent of the isolator duct. Additionally, the $Ma = 1$ iso-surface delineates the supersonic core flow from the side wall separated region (*e.g.* Figure 5.5).

Spatiotemporal variations, as quantified by the confinement parameter, are shown in Figure 5.12 (a). Near the cavity ($\hat{x} = 12$), viscous effects are more prominent, consistent with the blockage induced by the near-wall fuel injectors. As the fuel-staging transient progresses, confinement levels increase in the isolator upstream of the cavity. As an alternative representation of these trends, the minimum, maximum, and average confinement levels (averaged over $0 \leq \hat{x} \leq 12$) are shown as functions of entrance Mach number ($Ma_e(t)$) in Figure 5.12 (b). The normal and oblique shock-train regions in the confinement domain are denoted using the comparison of Hunt *et al.*[108] A transitional region is shown in magenta. The maximum confinement corresponds to the near-cavity region and is consistent with the maximum values found in the review of Hunt *et al.*[108] The minimum and average confinement levels both increase linearly with increasing forward-fuel bias, which is attributable to the side wall separation zones. For each curve, the entrance Mach number decreases with time, highlighting a shift from the oblique to normal shock-train condition, as previously observed from Figure 5.9

†The supersonic core area is approximated using a convex hull using the SciPy implementation[307] of the qhull library[308] with accompanying Python libraries.[3–6,309,310]

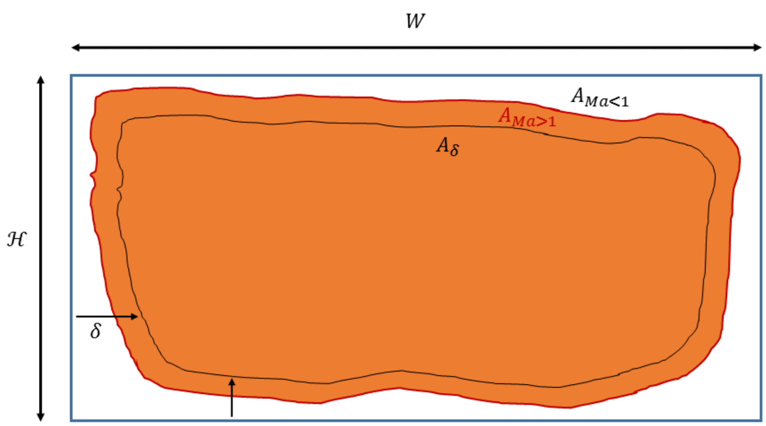

Figure 5.11: Isolator duct cross-section sketch of subsonic ($A_{Ma<1}$), supersonic ($A_{Ma>1}$), and boundary layer confinement (A_δ) areas.

$$C_\delta = \frac{2\delta}{\mathcal{H}} \tag{5.1}$$

$$C_\delta = \frac{A_\delta}{A_{iso}} \approx 1 - \frac{A_{Ma>1}}{A_{iso}} \tag{5.2}$$

Understanding secondary flow is also particularly important in isolators.[137] Corner flows naturally develop in rectangular ducts,[312] even for 2-D nozzles with high aspect ratios.[313] As shown by Sabnis *et al.*,[314] two vortex structures form in each of the lower corners of a single-sided expansion nozzle, corresponding to side wall and lower wall vortices. To characterize the behavior of corner flow development in this scramjet combustor, the normalized streamwise vorticity ($\hat{\omega}_x = \omega_x \mathcal{H}/U_\infty$) on several constant x planes, shown schematically in Figure 5.13, are analyzed.

Near the nozzle exhaust (Figure 5.14 (a)) a single corner vortex is observed near the lower corner. This appears in contrast to experiments[314] which indicate two corner vortices. This may be attributable to the turbulence model. Linear RANS models,

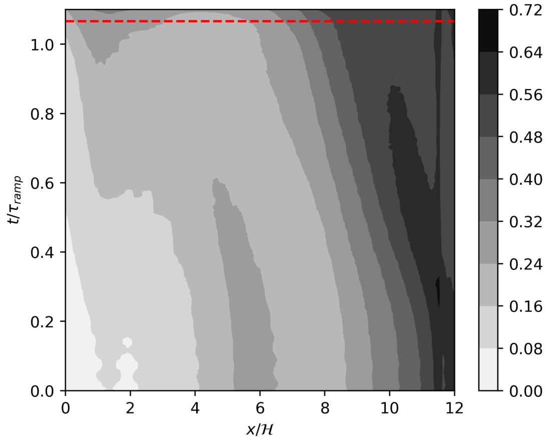

(a) $C_\delta(\hat{x}, \hat{t})$

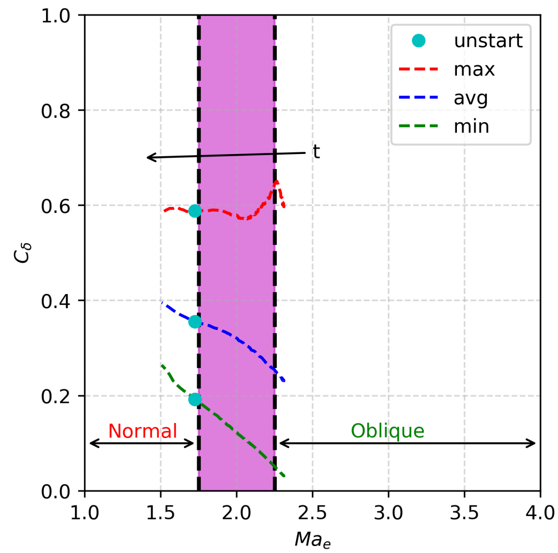

(b) $C_\delta(Ma(t))$

Figure 5.12: Isolator confinement effects for $0 \leq \hat{x} \leq 12$ during fuel-staging transient: (a) space-time diagram of local confinement effects; (b) confinment limits versus inflow Mach number.

for example, are known[315–317] to have difficulties capturing secondary duct flow. In particular, these models require additional corrections† to the Reynolds stresses to capture corner vorticies. Contrarily, the non-linear model employed here appears to capture at least some of the expected naturally developing secondary flow upstream of the isolator, but it does not appear to capture *both* the side wall and lower wall vortices described in other work.[314] However, the secondary flow is also affected by geometry and flow complexity by way of the DG and combustion-induced side wall separation.

As the flow develops downstream of the nozzle (Figure 5.14 (b)-(f)), a shift of the vortex-like signature from the side wall to the cowl wall is observed. This is

†The Quadratic Constitutive Relation (QCR) is a common correction for linear models but may only qualitatively[315] capture secondary flow structure and skin-friction.

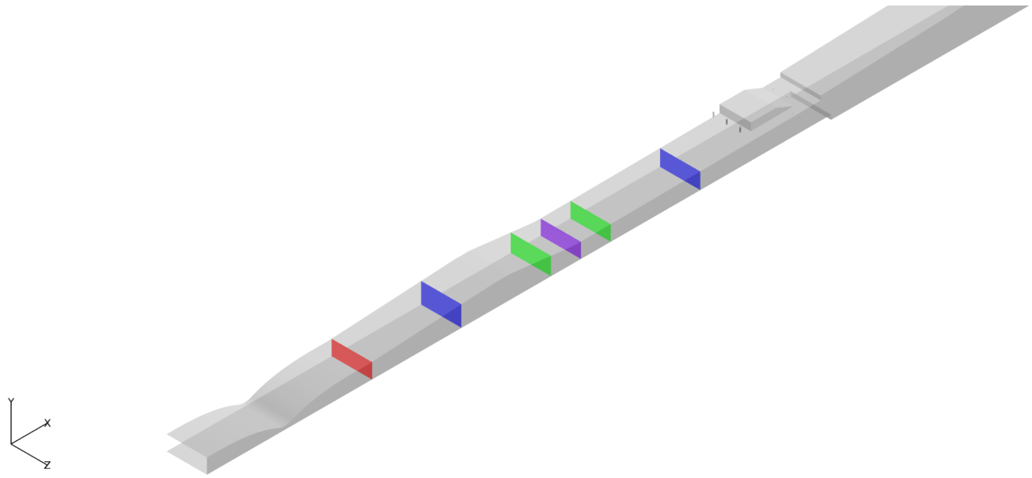

Figure 5.13: Plane for analyzing the development of secondary flow in the isolator: *red* - nozzle exit $\hat{x} = -14$, *blue* - $\hat{x} = \pm 8$, *green* - $\hat{x} = \pm 2$, and *purple* - isolator entrance $\hat{x} = 0$.

partly attributable to flow expansion and contraction through the DG section, which may further distort secondary structures by decreasing and increasing the streamwise pressure gradient. Additional influence on secondary flow may be attributable to side wall separation near the isolator entrance as a consequence of DG-induced flow curvature (Figure 5.8), as well as the pressure gradient from the outboard B2 injectors where vorticity in the lower corner spreads across the span as indicated by Figure 5.14 (e). Only at $\hat{x} = 2$ do the streamlines close, otherwise, the 3-D signature of nozzle secondary-flow is seen for the upstream region $\hat{x} < 0$, DG-separation at $\hat{x} = 0$, and the reaction-induced separation near $\hat{x} = 8$, as suggested by the singularity in the streamlines indicative of the out-of-plane velocity component.

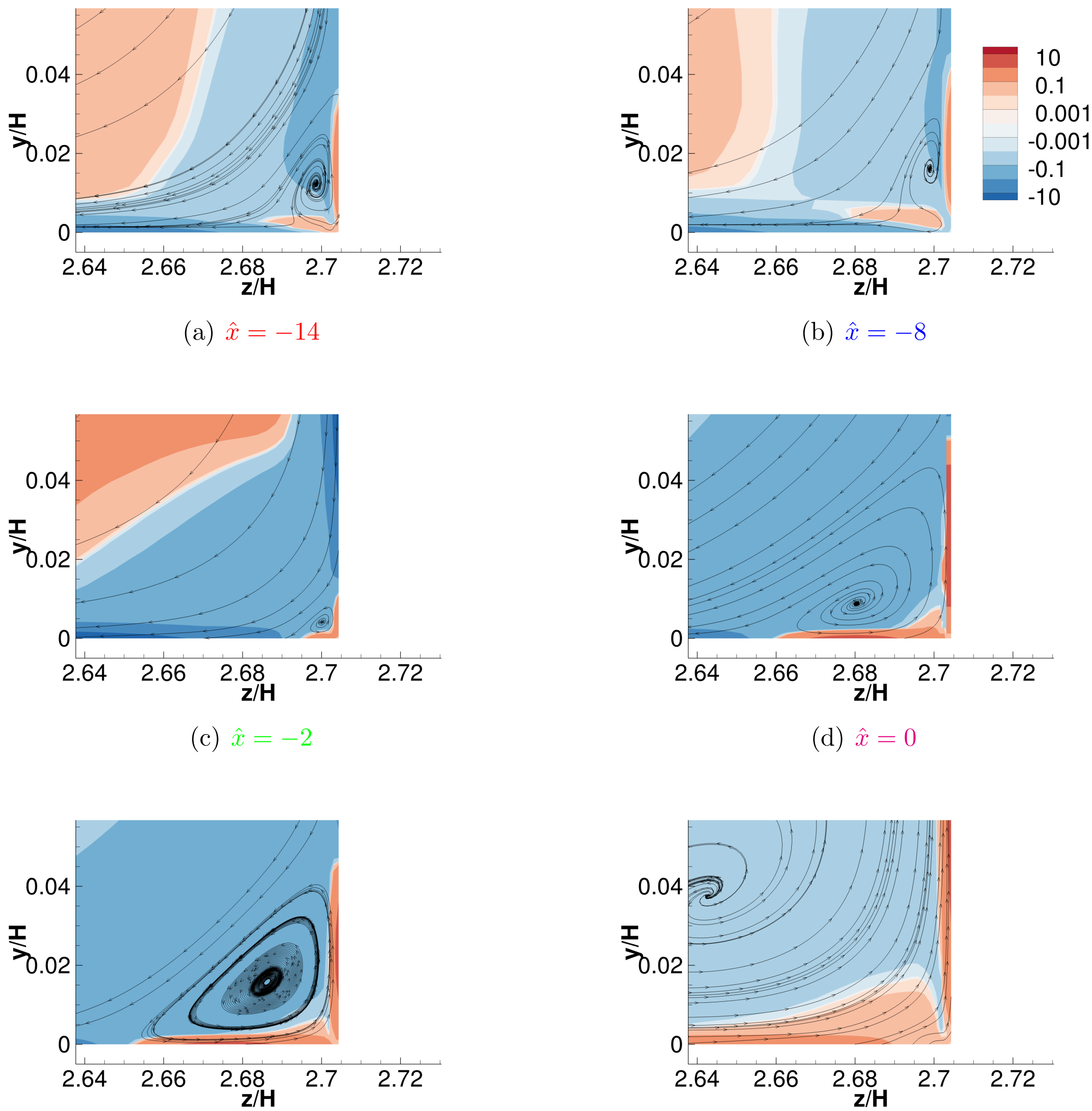

(a) $\hat{x} = -14$ (b) $\hat{x} = -8$

(c) $\hat{x} = -2$ (d) $\hat{x} = 0$

(e) $\hat{x} = 2$ (f) $\hat{x} = 8$

Figure 5.14: Combustor secondary flow development at $\hat{t} = 0$. Contours of normalized streamwise vorticity component: $\hat{\omega}_x = \omega_x \mathcal{H}/U_\infty$. Streamlines of in-plane velocity.

5.2.4 Isolator Unstart and Inlet Ejection Phase

Based on the computed centerline, cowl-side wall pressures, the PCST (x_s) exits the isolator at $\hat{t}_{uns} = 1.066$. The flowfield state at $x_s = 0$ (Figure 5.15) features additional vortical structures near the combustor ($v_{bsw,pri}$) and the isolator entrance ($v_{bsw,sec}$). The latter structure is identified from the node on the body-side wall and is attributable to distortion-induced curvature (Figure 5.15 (a)). The two vortical structures previously observed on the side wall (Figure 5.7 (b)) are replaced by a single structure, as indicated by Figure 5.15 (b).

During the unstart phase, a shift in the footprint of the weakly supersonic core (*e.g.* lines of coalescence in Figure 5.15 (a) and (c)) from cowl-side to body-side is seen during $1.042 \leq \hat{t} \leq 1.093$ as the PCST moves upstream of isolator entrance. However, the ultimate ejection of the shock-train upstream of the inlet shock is slightly delayed until $\hat{t} \approx 1.113$, which is inferred from the dilatation field on the symmetry plane (not shown) when the incident shock from the DG detaches from the cowl-side wall. This ejection phase lasts an additional 2 ms after the PCST leaves the isolator, giving an approximate upper bound on time in which to enact control of 3.6 ms: on the order of 10 percent of the imposed fuel transient timescale.

The predicted unstart shock speeds are similar to other experiments in the literature. Comparison of unstart shock speeds in terms of flow conditions (Ma and Re') and geometry parameters ($\mathcal{H}$, $\mathcal{L}$, and $AR \equiv \mathcal{W}/\mathcal{H}$) are provided in Table 5.1, for both cold and reacting flow experiments. Unit Reynolds numbers (Re') are estimated for each case from isentropic expansion using the reported nozzle stagnation

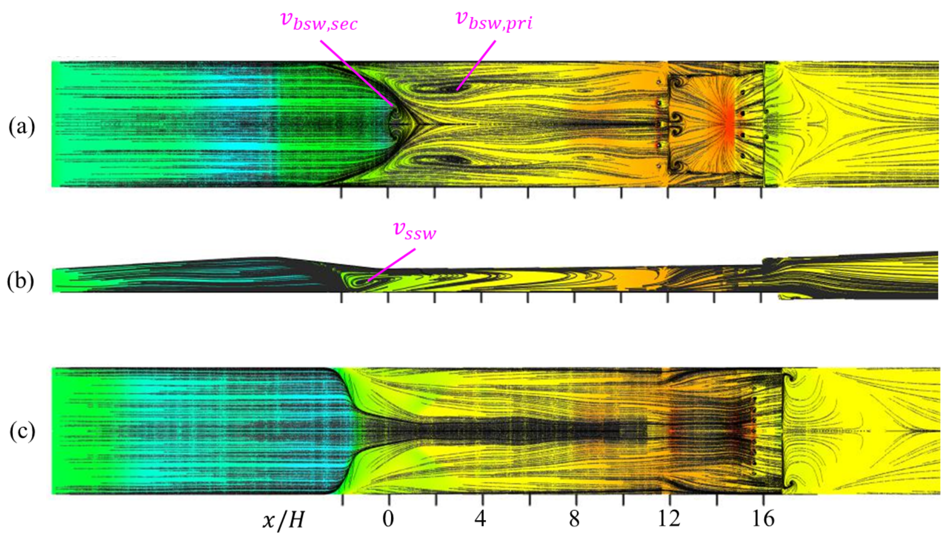

Figure 5.15: Flowfield state at the instant of unstart ($\hat{t}$ = 1.066): Instantaneous streamlines with contours of log pressure for (a) body-, (b) south-, and (c) cowl-side walls.

conditions.[†] The results suggest that unstart shock speed is proportional to Reynolds number. Assuming similar inflow Mach number and isolator geometry, increasing the freestream Reynolds number may be thought of as increasing the dynamic pressure of the incoming flow which would therefore require a greater back-pressure to initiate unstart.

[†]The Do *et al.* shock-speed results are estimated from the reported time-to-unstart and isolator length.

Table 5.1: Comparison of unstart shock speeds for rectangular combustors at similar free-stream Mach numbers.

Ref.	Type	$\mathcal{H}$ $[mm]$	AR $[-]$	$\mathcal{L}$ $[mm]$	Ma_{nozz} $[-]$	$Re' \times 10^{-6}$ $[m^{-1}]$	u_s $[m\ s^{-1}]$
Rodi *et al.*[119]	Cold	25.4	2.03	33.0	4.0	67.0	55-70
Wagner *et al.*[128]	Cold	25.4	2.0	242.3	4.9	29.5	20-74
Wieting[116]	Cold	38.1	0.8	177.8	5.3	$0.6 - 1.2$	10-27
Mashio *et al.*[159]	Fueled, H_2	32.6	0.92	37.1	2	3.56	50
Parrott *et al.*[153]	Fueled, H_2	203.2	0.75	436.9	3.5	0.8	2
O'Byrne *et al.*[160]	Fueled, C_2H_4	24.0	0.20	400.0	3.8	41.0	75-90
This work	Fueled, C_2H_4	42.3	5.40	507.2	2.84	18.4	30
Do *et al.*[179]	Fueled, C_2H_4	15.0	0.27	200.0	4.5	0.2	4

5.2.5 Global and Local Heat Release Analysis

Although the observed importance of separation is similar to previous unstart studies, localized heat release is identified as a primary driver of side wall flow separation. Other studies, including Nordin-Bates *et al.*,[172] also show the influence of spatially localized heat release on shock-train structure. The strong spanwise gradient in pressure, as indicated by the 2-D cowl-wall pressure field analysis, suggests heat-release variation across the combustor span. In particular, relatively stronger heat-release near the upstream injector side wall region is observed as shown in Figure 5.6. Concerning experiments, the regions of greatest heat release and temperature are possible locations for the placement of heat flux or temperature instrumentation, which facilitate measurements of thermal choking. However, it is necessary to distinguish between the apparent global (line-of-sight or spatially integrated) measures of heat release in the combustor versus local effects. This is important in the context of new, laser-based, measurement methods, such as Tunable-Diode Laser Absorption Spectroscopy (TDLAS)[318] and Tunable-Diode

Laser Absorption Tomography (TDLAT),[319] which provide line-of-sight (integrated) measurements of the flowfield. However, caution is necessary when comparing with line-of-sight measurements. As shown by Gruber *et al.*,[320] consistently applying data-reduction methodology to both experimental measurements and CFD predictions improves comparison.

For a potential comparison with path-integrated experimental measurements or 1-D analysis approaches, the area-integrated heat release along the streamwise direction is computed to quantify changes in the field as a result of modulation of the fuel input. In Figure 5.16, non-dimensional heat release $\widehat{HR}$ is shown in the space-time diagram ($\hat{x}$-$\hat{t}$ plane). The normalized cross-sectional area of the flowpath is shown for reference above the heat release map. To the right of the contour map, the temporal variation of the integrated heat release is plotted for the B2 injector ($\hat{x}$ = 11.57) and mid-cavity ($\hat{x}$ = 13.42) planes. The maximum of the area-integrated heat release along $\hat{x}$ is also shown for each temporal snapshot. At the start of the simulation, higher normalized heat release is present downstream of the cavity, corresponding to the two backward-facing steps on the body-side and cowl-side walls. As fuel flow rates are increased at the B2 injectors, a shift in the maximum heat release from the backward-facing steps towards the combustor cavity is observed, commensurate with the change in local fuel equivalence ratio. Heat release at the B2 injector plane decreases with increasing fuel flow rate, while mixing shifts to the cavity for the inboard B2 injectors and downstream along the side wall for the outboard B2 injectors. The normalized maximum heat release rate remains approximately constant across time ($\widehat{HR} \approx 8$), consistent with the fixed total fuel equivalence ratio ($\phi_{tot} = 0.9$). Prior to unstart ($\hat{t} = 0.89$), the heat release reaches a maximum in the cavity; thereafter, a sudden drop in heat release occurs as flame anchoring is lost. An increase in $\widehat{HR}$ at these stations is observed after unstart ($\hat{t} = 1.066$), as the mixing and reaction zones re-establish near the side wall. This observation may parallel experiments in an ethylene-fueled facility by Liu *et al.*,[181] which indicated a unstart transient featuring a sudden drop in measured wall pressure and heat flux corresponding to upstream flame propagation. However, this integrated view obfuscates the spanwise heat-release gradients.

To examine the near-wall (local) mixing region surrounding the outboard B2 injectors, the iso-surface of stoichiometric mixture fraction Z_{st} is computed and shown in Figure 5.17 as an indicator of the reaction zones. The mixture fraction (eqn. 5.4) is defined using the mass of atomic carbon as a conserved scalar, β (eqn. 5.3), this gives a local measure of mixing based on the relative concentration of ethylene (C_2H_4), carbon dioxide (CO_2), and carbon monoxide (CO). The iso-surface ($Z_{st} \approx 0.0637$) is colored by non-dimensional height above the cowl-side wall ($\hat{y}$). As indicated by the contours, the penetration of the outboard B2 injector increases with increasing fuel flow rate, consistent with previous mixing observations of steady-fueled cases in Figure 5.5. As in § 5.1.2, this side wall bias appears similar to laser-based TDLAS measurements[12,320] in this combustor under similar, but not identical, operating conditions. Measurements[12] of hydroxyl (OH) radical flouresence downstream of the cavity are shown in Figure 5.18 (a), which indicate higher PLIF intensity near the side, lower, and upper walls. The simulation prediction of mixture fraction at $\hat{x} \approx 19$, rendered in Figure 5.18 (b), compares well with the experimental measurements at similar operating conditions. In particular, stoichiometrically mixed

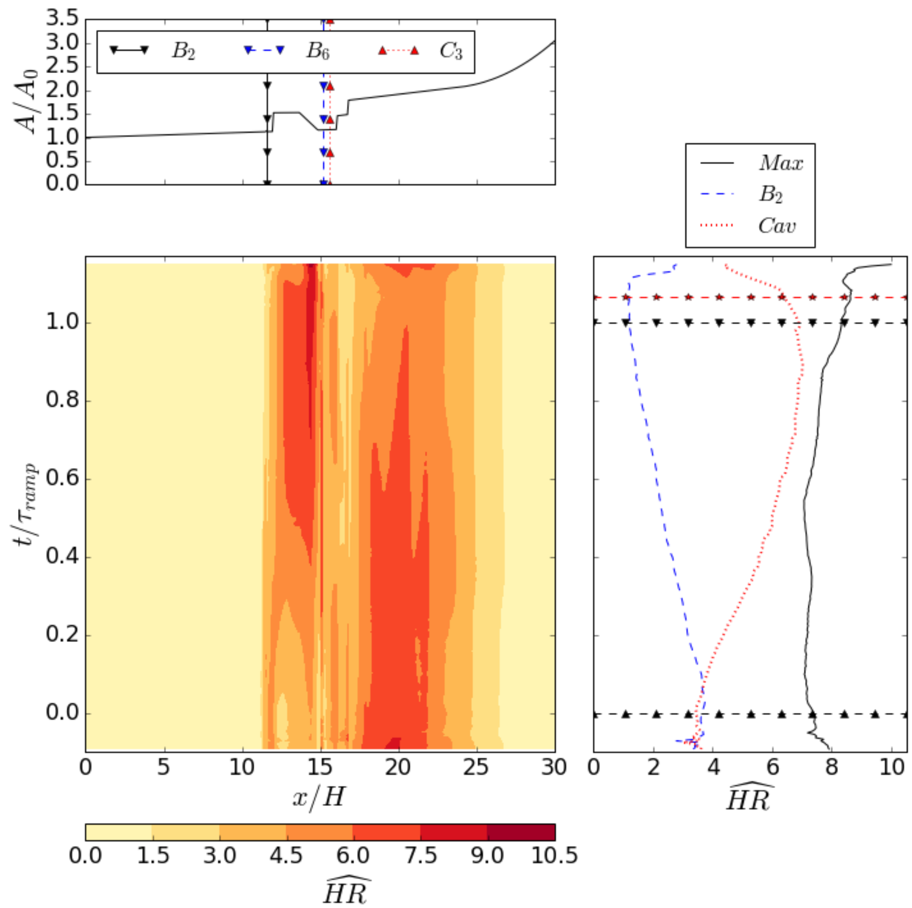

Figure 5.16: Global (spatially integrated) heat release distribution. Non-dimensional, density-weighted, heat release variation along combustor. *Lower left*: contour map $\widehat{HR}(\hat{x}, \hat{t})$. *Top*: Normalized cross-sectional area. *Lower Right*: maximum heat release along flowpath; heat release at cavity plane $\hat{x} = 13.42$; heat release at $B2$ injector plane $\hat{x} = 11.57$; start (▲-▲) and end (▼-▼) of fuel transient, unstart (*red* ⋆-⋆).

regions (purple contour line), as indicators of active reaction zones, coincide with maximum measurement intensity.

In agreement with the analysis of Fotia and Driscoll,[184] increased fuel penetration distance near the side wall presents a mechanical blockage (additional fuel mass flow or momentum change), in addition to the chemical-based obstruction from heat release. For this cavity configuration, changing the upstream fuel injector angle to alter the fuel penetration behavior or modifying the spanwise fuel flow rate distribution for the upstream injectors may be worth exploring as a means to mitigate unstart by adjusting the extent of side wall separation. Gruber *et al.*,[321] for example show that the penetration and mixing are a function of the jet-in-crossflow injection angle. Additionally, a full span cavity might limit local heat release effects by providing area relief near the outboard injectors.

$$\beta = \frac{mass\ C}{mass\ mixture} \tag{5.3}$$

$$Z = \frac{\beta - \beta_{ox}}{\beta_f - \beta_{ox}} \tag{5.4}$$

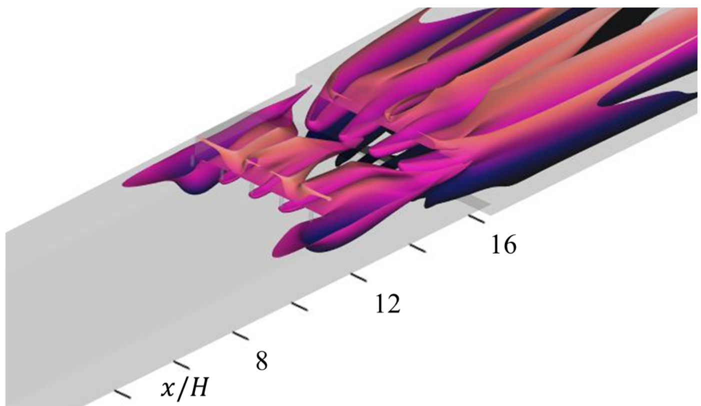

(a) $\hat{t} = 0.00$

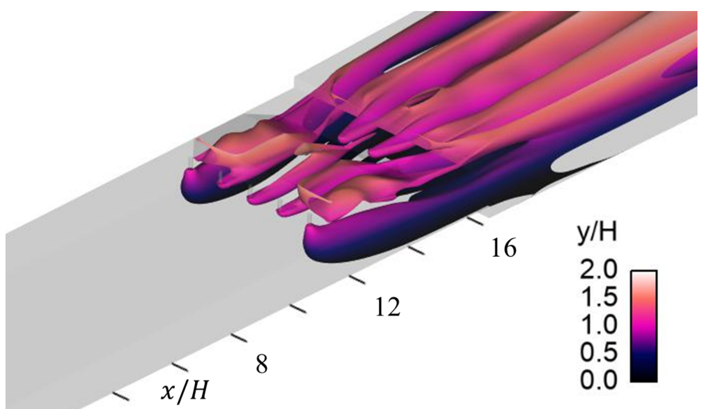

(b) $\hat{t} = 1.00$

Figure 5.17: Fuel injection and mixing as inferred from iso-surface of stoichiometric mixture fraction Z_{st}. Iso-surface colored by height above cowl-side wall $\hat{y}$.

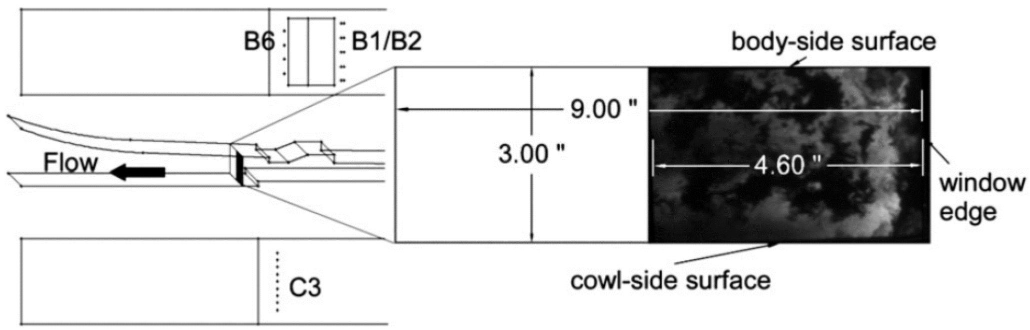

(a) Experimental setup[12]

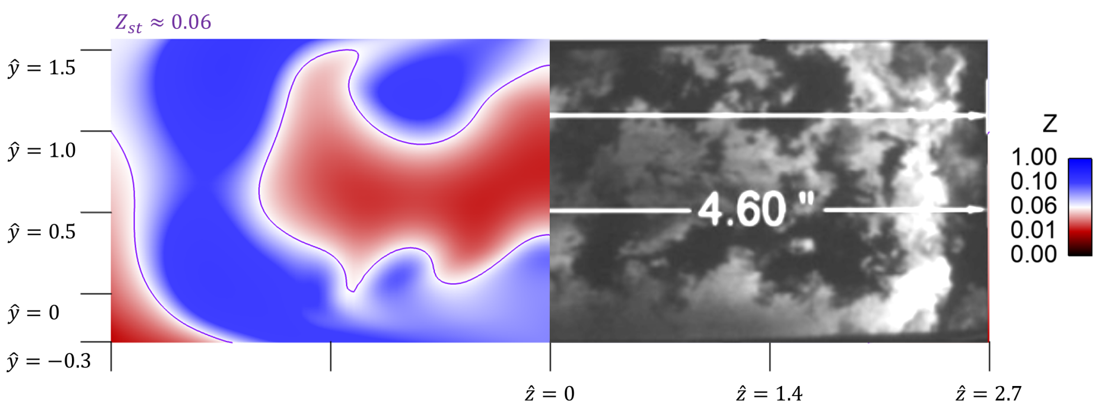

(b) Comparison

Figure 5.18: Reaction zone comparison downstream of cavity: (a) Experimental setup for instantaneous Hydroxyl (OH) radical PLIF measurements downstream of the cavity, reproduced from Ryan *et al.*[12] (Case A with $\phi_{tot} = 0.8$); (b) CFD solution (left) on $\hat{x} = 19$ plane at $\hat{t} = 0$: mixture fraction contours (Z) with *red* - lean, *white* - near stoichiometric, *blue* (rich) mixture, and *purple* - stoichiometric condition (Z_{st}), and experimental measurements (right).

5.3 Summary

- Reference fueling states are characterized to provide a reference for the transient fuel-staging computations:
  - Tare (un-fueled) mode operation features an oblique shock-train which persists throughout the cavity region.
  - Steady-state operation shows jet-like behavior downstream of the cavity.
  - Shock-train length decreases for steady-state reacting flows due to increased reaction-zone back-pressure.
  - Heat release zones are biased near the side wall.
- Transient fueling staging dynamics of the three-dimensional flowfield are characterized with respect to wall pressure sensors.
- Two distinct phases of PCST motion are observed for the imposed fuel-staging transient.
  - The pre-unstart phase features relatively low ($\mathcal{O}(1)$ m/s) upstream PCST speed.
  - The isolator unstart phase shows a much higher PCST speed ($\mathcal{O}(30)$ m/s).
  - The unstart shock speed is comparable to values in the literature for similar Mach numbers and isolator geometries.
- Corner flow effects are examined to understand the unstart initiation process:
  - The pressure-based PCST detector is extended to 2-D, and the wall field highlights side wall separation from the spanwise pressure gradient.

- From the 2-D PCST detector analysis, the incipient unstart condition corresponds to when the pressure rise at the side wall moves upstream of the isolator entrance. The side wall pressure rise precedes the centerline location by several duct heights.
- Separation effects are quantified in terms of the viscous confinement parameter, which suggests that a shift occurs from an oblique to a normal shock-train structure, consistent with 3-D flow observations.
- Secondary flow is captured from the vorticity field which evolves along the lower isolator corner.

* Local versus spatially integrated views of heat release are used to understand unstart initiation:
  - The spatially integrated (global) heat release, analogous to typical laser-based measurements, shows a shift from the back-facing steps to the cavity region consistent with the imposed fuel-staging transient.
  - The integrated view, although consistent with experimental measurement techniques, does not capture the critical spanwise gradient in the reaction zones, however.
  - The mixture fraction and heat release show mechanical and chemical blockage effects from the fuel injections near the side wall consistent with observations in the literature.

Chapter 6

Structure Identification and Model Order Reduction

The development of sophisticated fluid control systems for mixing enhancement[322] or cavity resonance mitigation[323] for high speed propulsion systems motivates the need to understand the behavior of coherent structures within the flowfield. Specifically, a systematic method to quantify dynamics and isolate spatially or temporally correlated features (coherent structures)[324] is necessary to control unsteady flowfields. Understanding these structures facilitates sensor (and actuator) placement. A fundamental challenge that arises is where to *optimally* place a limited number of sensors to characterize the system dynamics so as to provide input for feedback control.[218] In a control-system or linear-stability framework, the gain (sensitivity) of the system is needed to quantify the dynamic response to a given input. In the context of the present analysis, the input is the transient fuel flow rate and the system is the combustor flowfield. However, statistical quantities based on the Reynolds-decomposition, including the time-mean and variance, are only appropriate to quantify flow dynamics when they are not dependent on the time window.[325] The subsequent discussion in § 6.1 introduces a metric to quantify the dynamics of the statistically *unsteady* scramjet flowfield as a first step toward sensor selection and control system design.

A second related issue to sensor placement is how to manage the problem of 'big data'. The 'curse of dimensionality'[326] in CFD computations, which have billions of degrees-of-freedom, makes brute force optimization of sensor placement intractable and motivates development of Reduced Order Modeling (ROM) techniques. Methods to filter dynamically significant features from and reduce the order of (compress) large datasets are important to facilitate sensor placement, Reduced Order Modeling, and control system development. To achieve transient feature extraction and dimension reduction, a data-driven[326] approach is selected for the current analysis. Two popular[222] Model Order Reduction (MOR) methods are Proper Orthogonal Decomposition (POD) and Dynamic Mode Decomposition (DMD), as explored in § 6.2. These data-driven methods, reviewed by Taira *et al.*,[222] are both related to Principal Components Analysis (PCA) (§ 6.2.1), which serves to generate a set of linearly independent basis functions (principal components) to both extract important flow structures (§ 6.2.2) and for compression (order-reduction) of the computational dataset. Because the flowfield in the current problem is non-stationary, the physical significance of the modes must be established with care. Contrarily, for statistically steady flows, POD and DMD modes provide a measure of energy and amplification, respectively. Therefore, the presented analysis compares these MOR modes to physical features such as side wall separation and PCST unsteadiness previously explored (Ch. 5). Additionally, the statistically unsteady flowfield presents a challenge to conventional order-reduction methods of POD and DMD with respect to reconstruction error. Specifically, errors arise due to short-time transients.[327] To mitigate this, the Multi-Resolution DMD (mrDMD)[13] method is employed to capture the *time-local* dynamics, (§ 6.2.3). Critically, the MOR reconstruction errors are leveraged to infer and isolate dynamically significant flowfield regions.

6.1 Dynamical Structure Identification

Optimal sensor placement allows the global system behavior to be approximated or inferred by a limited number (sparse) of spatially local observations.[218] However, optimizing for a large-scale system, such as wind farm sensor placement,[328] or where there are millions of degrees of freedom as in the present work, is computationally intractible for high-dimensional problems. To address this, compressed techniques[329,330] map the problem into a different sparse subspace (*e.g.* the Fourier domain) to select a smaller subset of probe locations before applying the MOR decompositions. However, such an approach is not strictly suitable for the present problem, because of the time-local dynamics. As a computationally efficient estimate of the strongest flowfield dynamics, a new metric is adapted to quantify spatially local flow dynamics and serve as verification for the extracted dynamical features from the MOR filters. The metric characterizes the combustor dynamics and isolates regions within the combustor that are most sensitive to the change in fuel input.

For the current non-stationary flowfield, typical statistical analyses of statistically steady turbulent flows, including time-mean, root-mean-square, and higher-order central moments[325] (*i.e.* Reynolds decomposition), are not appropriate. Instead, the total variation (TV) is adapted as an estimate of the system dynamics across time for each degree-of-freedom (DOF) within the computational domain. As a conservative measure of the dynamics, the total variation (eqn. 6.1) functions as an L_1 norm of the temporal gradients.[331] The L_1 norm is defined in (eqn. 6.2) as a measure of the length of vector ϕ with n elements. In this way, TV also serves as an approximate measure of the average dynamics $\overline{\Delta q}$ (eqn. 6.3) at each DOF. As will be shown, adjusting the time window bounds (t_1 and t_2) can isolate particular dynamics during different phases of transient fuel-staging. Ultimately, the interest is to differentiate between dynamics prior to and during the unstart phase of PCST motion to identify dynamically responsive regions of the flow or flow structures that contribute to the unstart process and might be targeted with control.

$$TV(q)|_{t_1}^{t_2} = \sum_{n=n_1}^{n_2} |q_n - q_{n-1}| \propto \left|\left|\frac{\Delta q}{\Delta t}\right|\right|_1 \tag{6.1}$$

$$L_1(\phi) = ||\phi||_1 = \sum_{i=1}^{n} |\phi_i| \tag{6.2}$$

$$\overline{\frac{\Delta q}{\Delta t}} \approx \frac{1}{t_2 - t_1} TV(q) \tag{6.3}$$

As a test of this metric, the heat release dynamics are computed on two different analysis planes: the symmetry ($\hat{z} = 0$) and horizontal cross section ($\hat{y} = 0.5$) planes of the isolator, as indicated on Figure 6.1 (a) and (b), respectively. The computed heat release field over period $0 \leq \hat{t} \leq \hat{t}_{uns}$ is normalized by $\dot{H}R_x(t = 0)$. On the symmetry plane (Figure 6.2 (a)), local extrema of around 100 times $\dot{H}R_x(t = 0)$ are observed in the cavity flameholder. Bias of the reaction zones toward the side wall is evident from Figure 6.2 (b), where the local maxima ($\widehat{\dot{H}R_{TV}} \approx \mathcal{O}(100)$) are found near the outboard B2 fuel injector. Downstream of the B2 injectors, the fuel plume features relatively lower dynamics ($\widehat{\dot{H}R_{TV}} \approx \mathcal{O}(10)$). These dynamics are attributable to the change in fuel penetration (Figure 5.17) across the isolator duct height. Downstream

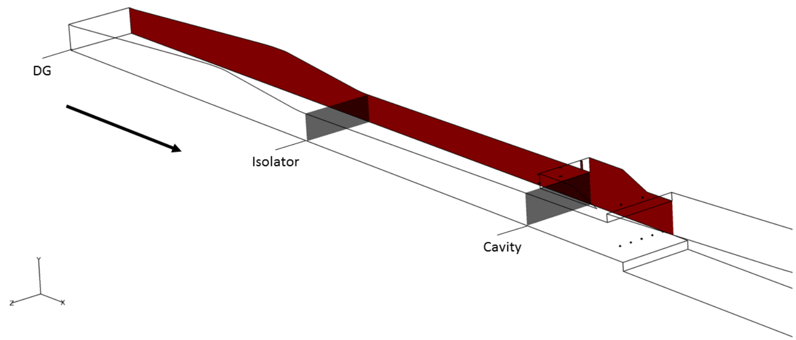

(a) $z/\mathcal{H} = 0$

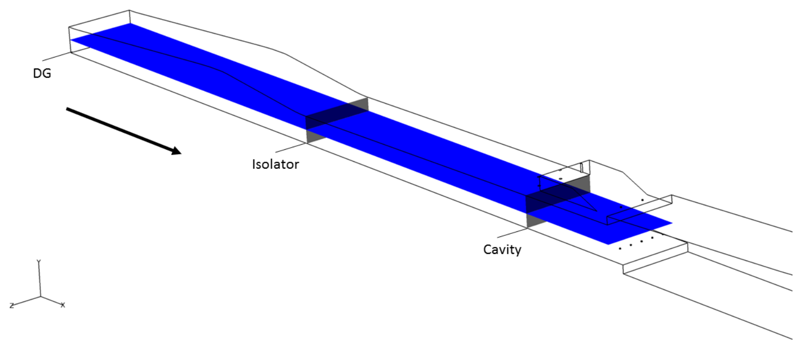

(b) $y/\mathcal{H} = 0.5$

Figure 6.1: Flowfield dynamics analysis plane details: (a) symmetry plane, (b) horizontal cross-section plane.

of the injector in the cavity region ($13 \leq \hat{x} \leq 16$), the fuel-air mixing is more diffuse with relatively lower dynamics as inferred from the magnitude of the heat release TV field. This metric is consistent with previous qualitative description (§ 5.2) and is therefore applied to other observables of interest to identify regions with relatively higher dynamics related to flow separation and PCST motion.

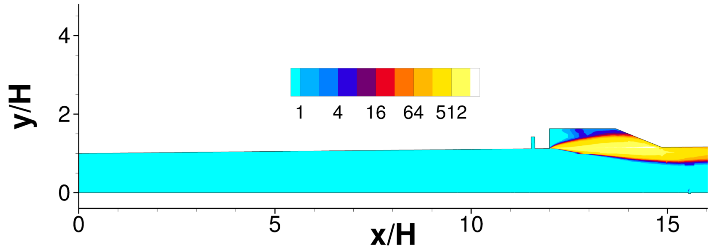

(a) $\hat{z} = 0$

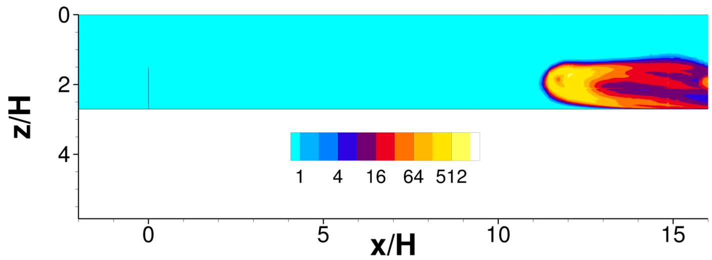

(b) $\hat{y} = 0.5$

Figure 6.2: Heat release dynamics quantification via $TV(\widehat{\dot{H}R})$ on (a) symmetry $(\hat{z} = 0)$ and (b) horizontal $(\hat{y} = 0.5)$ analysis planes .

6.1.1 Side Wall Separation

As previously discussed, formation of the separated flow regions plays an important role in inception of the unstart transient. To understand these dynamics, the velocity field is selected as the observable of interest for the analysis. For convenience, the field is normalized by a mass-flux-weighted average of the streamwise velocity on the isolator entrance plane $u_e(x = 0, t = 0) \equiv 840\ m/s$.

The analysis first isolates the combustor symmetry plane to identify body-side (upper) wall separation features present during the fuel-staging transient (§ 5.2.2). Figure 6.3 (a) shows the computed TV field which highlights several distinct regions of relatively high dynamic importance. As expected, the cavity shear layer region is highlighted similar to the heat release TV field previously discussed. However, higher TV magnitude ($\hat{u}_{TV} \approx 2$) is observed (Figure 6.3 (b)) near the upper wall ($0 \leq \hat{x} \leq 3$) corresponding to the separation region identified in Figure 5.9. Small regions of relatively larger TV on the lower wall at $\hat{x} \approx 3, 7, 10, 15$ are attributable to the impingement locations of the reflected oblique shocks. This is further explored in § 6.1.2. Next, the TV ratio ($\mathfrak{R}_{TV}$) (eqn. 6.4) is introduced to compare dynamics within the unstart window ($1 \leq \hat{t} \leq t_{uns}$) to that over the entire fuel-staging event. From this second metric, regions which respond most strongly during the unstart phase of the fuel-staging transient are inferred. This field, rendered in Figure 6.3 (c), indicates relatively stronger dynamics at the isolator entrance $\hat{x} = 0$ during the unstart phase.

$$\mathfrak{R}_{TV} = \frac{TV|_1^{t_{uns}}}{TV|_0^1} \tag{6.4}$$

Applying the TV metric analysis to the horizontal reference plane ($\hat{y} = 0.5$), provides a measure of side wall dynamics. Unlike the symmetry cross-section, a relatively constant TV magnitude is observed throughout the combustor as shown in Figure 6.4 (a). However, a signature of the inception of DG-induced flow curvature and separation is indicated by a lobe from $-2 \leq \hat{x} \leq 4$, previously observed in Figure 5.7. Windowing the data to isolate the unstart phase via $\mathfrak{R}$, identifies two regions of interest. The first region corresponds to the side-wall separation, indicated by the TV field. The second region corresponds to the oblique DG shock, which is turned toward the centerline. This signature is indicated by the reduction in Mach number magnitude shown in Figure 6.4 (a) which reduces from $Ma \approx 2.8$ to $Ma \approx 2$ near $\hat{x} = 0$.

(a) $\nabla \cdot \mathbf{U}$ at $\hat{t} = 1$

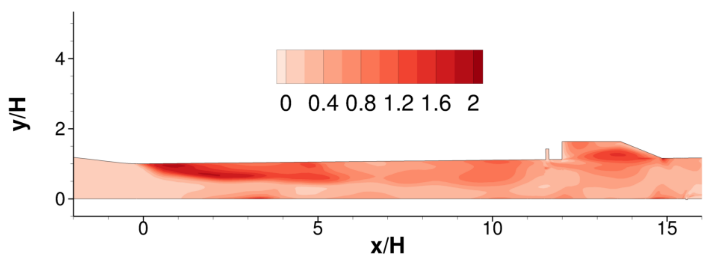

(b) $TV(\hat{u})$

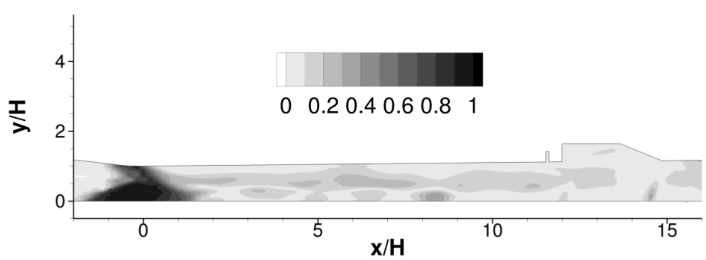

(c) $\mathfrak{R}_{TV}(\hat{u})$

Figure 6.3: Upper wall separation dynamics on symmetry $\hat{z} = 0$ plane: (a) dilatation field, (b) total variation of streamwise velocity, and (c) TV ratio.

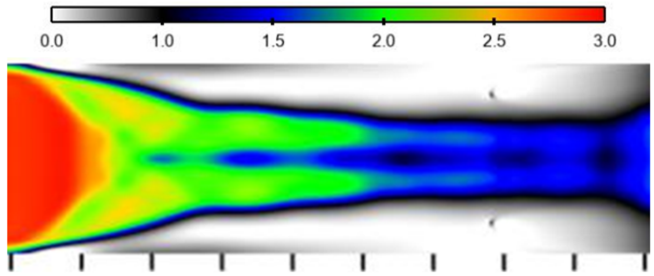

(a) Ma at $\hat{t} = 1$ (symmetry shown)

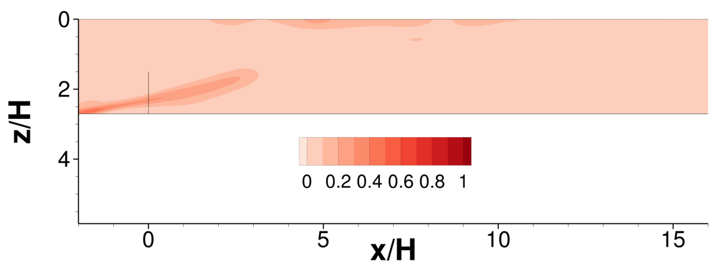

(b) $TV(\hat{u})$

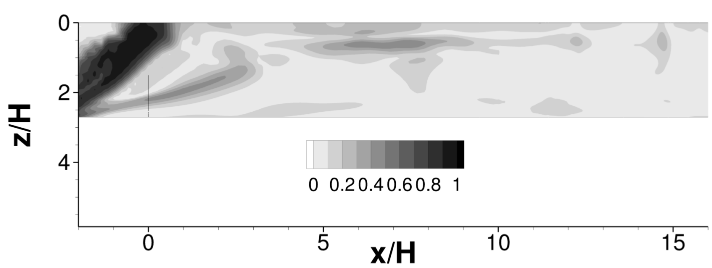

(c) $\mathfrak{R}_{TV}(\hat{u})$

Figure 6.4: Side wall separation dynamics on $\hat{y} = 0.5$ plane: (a) Mach contours at $\hat{t} = 1$, (b) total variation of streamwise velocity, and (c) TV ratio.

6.1.2 Pre-Combustion Shock-Train

The vertical velocity component (v) serves as a better indicator of oblique shock waves within the isolator than the u-velocity component. Like the upper wall separation feature, attention is drawn to a spatial window of the symmetry plane. Here, the vertical velocity normalization is scaled like the streamwise component as $\hat{v} \equiv v/u_e$. For the following, the shock-train dynamics are compared during the pre-unstart and unstart time windows.

The TV metric of $\hat{v}$ in Figure 6.5 (a) highlights reflecting oblique shock waves downstream of isolator entrance ($0 \leq \hat{x} \leq 5$). Unsteadiness of the oblique shocks at the isolator entrance is a consequence of supersonic core flow modulation, which is identified from the unsteady subsonic separated zone discussed in the prior discussion (Figure 5.9). Additional dynamics observed in the cavity downstream of the B2 injectors are attributable to: (1) increased fuel penetration because of increasing B2 injector fuel flow rates with time and (2) heat release modifying the cavity shear layer attachment location at the aft-end of the cavity ramp. Like the upper wall separation, unsteadiness in the reflected shock waves downstream of the isolator entrance *prior* to the unstart phase is inferred from the percentage of TV during unstart (Figure 6.5 (b)).

Connecting this observation to the previous wall pressure signatures, the TV of the cowl-wall pressure field is analyzed on the $\hat{y} = 0$ plane as shown in Figure 6.6 (a). The scaled pressure field (p_{TV}/p_∞) is subsequently shown in Figure 6.6 (b). Notably, high TV ($\hat{p}_{TV} \geq 2$) is identified near the centerline ($\hat{z} = 0$). These spatially periodic signatures (about every $2\mathcal{H}$) are associated with the reflecting oblique shock waves within the isolator, which shift during the fuel-staging transient. However, the region

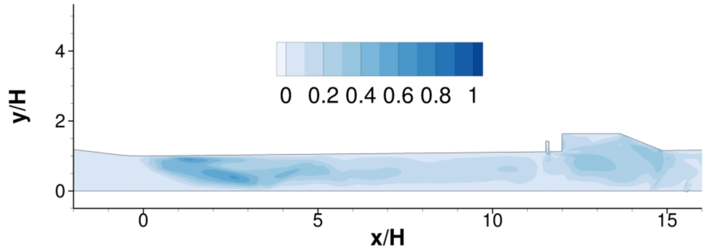

(a) $\hat{v}_{TV}$

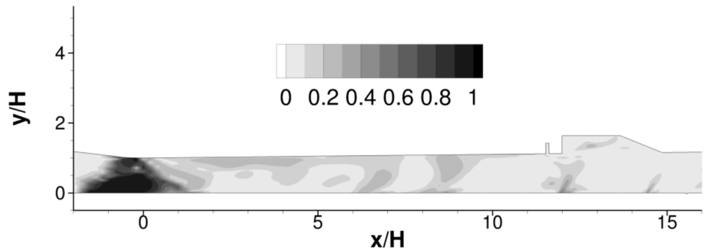

(b) $\mathfrak{R}_{TV}$

Figure 6.5: PCST dynamics on symmetry plane ($\hat{z} = 0$): (a) time-mean field, (b) total variation field $\hat{v}_{TV}$, and (c) TV ratio.

near the side wall $\hat{z} \approx 2.7$ shows relatively constant magnitude. The side wall separation zone, which is driven by the corner heat release, leads to saturation of TV levels along the isolator duct. A small local peak in the TV field near the side wall upstream of the isolator entrance ($\hat{x} = -1$) may indicate dynamics associated with the unstart phase when the PCST moves upstream of the isolator entrance.

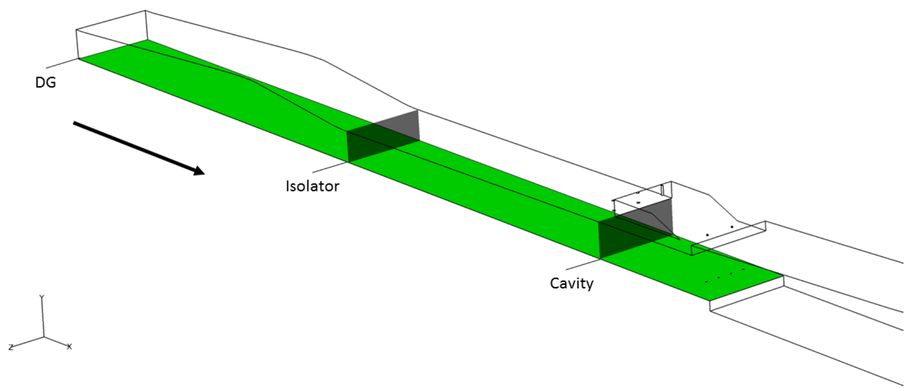

(a) $y/\mathcal{H} = 0$

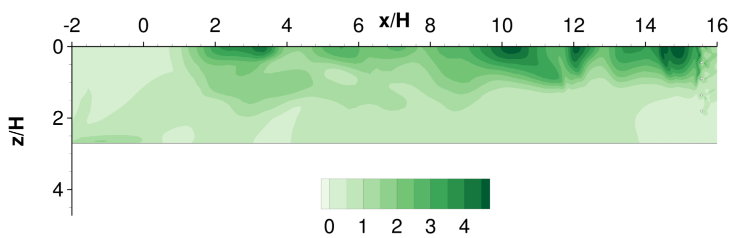

(b) p_{TV}/p_∞

Figure 6.6: PCST wall pressure dynamics on (a) cowl-wall plane and (b) scaling wall pressure field.

6.1.3 Spanwise Flow Gradients

The previous analysis of the streamwise velocity component on the 2-D cross-section plane isolated the near-wall separation regions. While not obvious from these 2-D views, a 3-D perspective reveals some contribution to this separated zone by a vortical-like structure that extends along the isolator duct length. This view further highlights the strong spanwise gradients observed in the discussion of side wall separation.

Qualitative inspection of the flowfield reveals this feature in the isolator duct corner near the upper wall. Reversed flow regions are highlighted by an iso-surface of $\hat{u} = -0.05$ in Figure 6.7. The iso-surface is colored by distance above the cowl-side wall ($\hat{y}$), and the upper corners of the isolator duct are shown in orange. An iso-surface of the dilation field, rendered in teal, identifies the isolator compression waves.

The TV metric is employed to study the relative dynamics over the entire, 3-D velocity field and isolate spanwise gradients. The total variation of each of the three velocity components is computed. Isosurfaces at twenty percent of the global maximum for each velocity component are rendered. For the streamwise velocity ($\hat{u}$), this is equivalent to $0.2||u_{tv}||_\infty$ where $||.||_\infty$ is the infinity norm. In the streamwise direction (Figure 6.8 (a)), several distinct regions are identified. Consistent with previous 2-D analysis, the body-side separation region is highlighted near $\hat{x} = \hat{z} = 0$. Near the isolator entrance ($\hat{x} = 0$) at the side wall $\hat{z} \approx 2.7$, the region affected by flow curvature and separation is identified consistent with Figure 5.7. A final region of prominent dynamics is evident behind the cowl-side step shear layer at $\hat{x} \approx 18$.

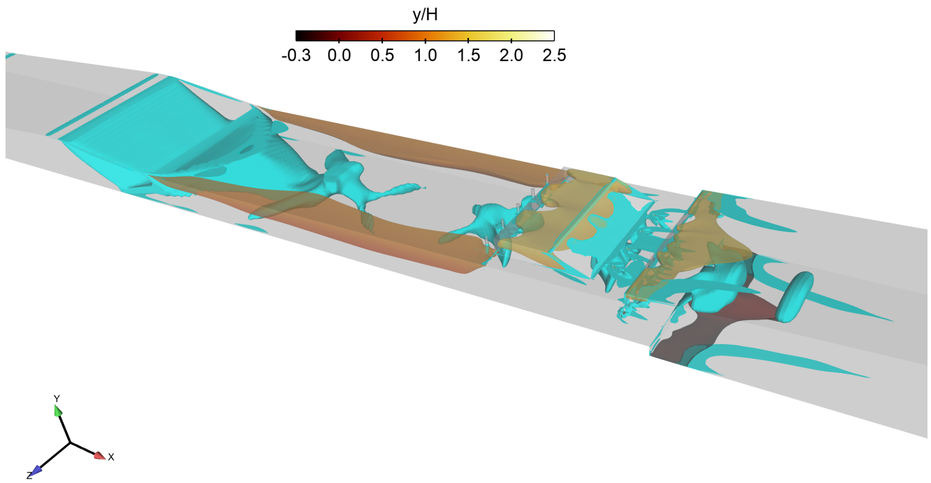

Figure 6.7: Spanwise flowfield variations (flow is left to right): Vortical features in isolator at $\hat{t} = 0$. Iso-surface of dilatation field illustrating compression regions such as inlet oblique shocks (*teal*) and iso-surface of reversed flow regions ($\hat{u} = -0.05$) colored by height above cowl-side wall ($\hat{y}$); reversed flow regions in orange.

Similar to $\hat{u}_{TV}$, the vertical velocity component $\hat{v}_{TV}$ iso-surface highlights the body-side wall separation, isolator corner effects, and the cowl-side-step shear layer as shown in Figure 6.8 (b). Unlike the streamwise and vertical velocity components, the spanwise velocity $\hat{w}_{TV}$ (Figure 6.8 (c)) primarily shows the signature of the cowl-side-step region. However, like the other velocity components, spanwise gradients are evident from the iso-surface in the cowl-step region for each component.

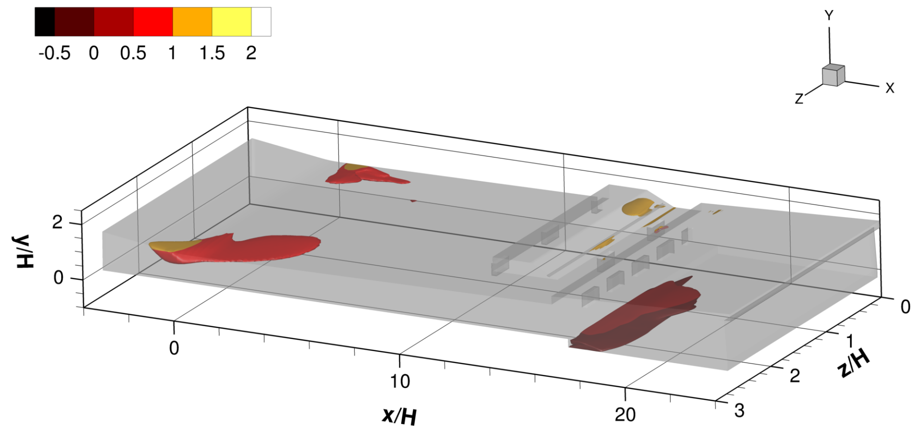

(a) $0.2||u_{tv}||_\infty$

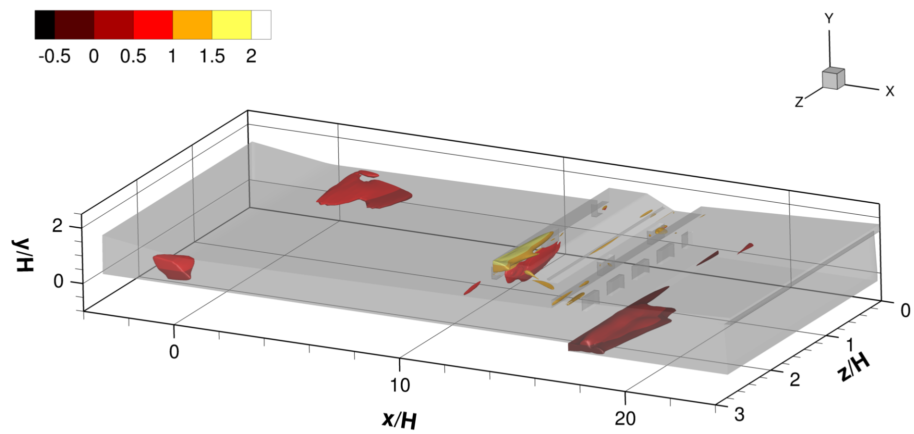

(b) $0.2||v_{tv}||_\infty$

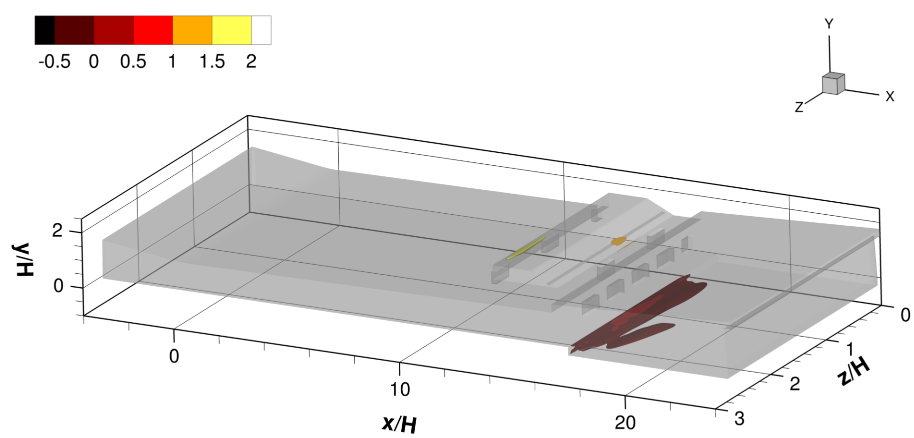

(c) $0.2||w_{tv}||_\infty$

Figure 6.8: Spanwise flowfield gradients. Iso-surfaces of (a) $\hat{u}_{TV}$, (b) $\hat{v}_{TV}$, and (c) $\hat{w}_{TV}$ at 20 percent of the global maximum for each velocity component.

6.2 Model Order Reduction

MOR serves as a step toward reduced order representation of dynamical systems. Such data-driven methods provide a basis for sensing, reduced-order modeling, and design optimization[332] through a low-dimensional representation of unsteady systems.[326] These methods are useful in the development of Reduced Order Models (ROMs), which retain most of the key features of the original data, but with significantly reduced dimensionality relative to the original physical system.[333] POD, for example, in conjunction with Galerkin-based methods,[334–336] provides the basis for ROMs of many turbulent flows. ROMs are further useful for stability analysis[337] and the placement of sensors for control systems.[338] Methods such as compressed-sensing,[330] sparse coding,[339] and optimized Dynamic Mode Decomposition (DMD)[340] while attractive, involve a non-trivial optimization problem to find a sparse basis of much lower dimension than the original dataset.

In contrast, two straight-forward data-driven Model Order Reduction (MOR) methods include snapshot-based Proper Orthogonal Decomposition (POD)[219,341,342] and Dynamic Mode Decomposition (DMD).[220,221,343] For the MOR methods considered, each method generates a new mathematical basis for the input data, assuming a separation of variables (eqn. 6.5), such that the state of system q is approximated by a summation over modes M with time-varying coefficients $a(t)$ and spatial modes $\phi(x)$.

$$q(\mathbf{x}, t) \approx \sum_{m}^{M} a_m(t)\phi_m(\mathbf{x}) \tag{6.5}$$

6.2.1 Methods

The POD and DMD methods are dependent on the Singular Value Decomposition (SVD) and are closely related† to the statistical Principal Component Analysis (PCA)[344] which constructs a basis to filter out noise and reveal hidden structure through a linear combination of basis functions.[345] For these methods, the snapshots from CFD are written in matrix form Q, with dimensions k by n, where k is the spatial dimension and n is the time dimension. PCA decomposes the set of m, k-dimensional observations into a set of linearly independent principal components (basis vectors) in order to reduce the dimensionality of system[344] from dimension m to dimension r for $r < m$.

Snapshot Proper Orthogonal Decomposition

The snapshot-based or space-only[346] Proper Orthogonal Decomposition (POD), derived[347] from the original work of Lumley[219,341] in the context of turbulent flows, is suitable for snapshots gathered from experimental or computational data. This approach assumes a decomposition of the data in which instantaneous fluctuations (q') about the time-mean state ($\bar{q}$) at time (n) (eqns. 6.6-6.7) are separated into the time coefficients ($a_m(t)$) and orthogonal spatial basis vectors ($\phi_m(x)$) for the modes ($1 \leq m \leq M$) (eqn. 6.8) from N collected snapshots.

$$\bar{q} = \frac{1}{N}\sum_{n=1}^{N} q_n \tag{6.6}$$

$$q'_n = q_n - \bar{q} \tag{6.7}$$

$$q'(\mathbf{x}, t) = \sum_{m}^{M} a_m(t)\phi_m(\mathbf{x}) \tag{6.8}$$

†PCA and snapshot-based POD are equivalent.[324]

First, a correlation matrix (eqn. 6.9) is computed from the inner product (eqn. 6.10). Spatial weights are neglected for these computations since they do not qualitatively affect the mode structures,† consistent with observations of Mohan *et al.*[348,349]

$$R_{ij} = \frac{1}{N} < q_i', q_j' > \tag{6.9}$$

$$< f, g > = \int_\Omega f(\mathbf{x}) g(\mathbf{x}) d\mathbf{x} \tag{6.10}$$

An eigenvalue decomposition of the correlation matrix yields eigenvectors (w_m) which form the POD basis. The spatial modes (eqn. 6.12) are computed by projecting the eigenvectors onto the fluctuating snapshots. For convenience, the $(\cdot)$ operator is adopted to simplify the inner product notation.

$$R w_m = \lambda_m w_m \tag{6.11}$$

$$\phi_m = \frac{w_m \cdot q_n'}{||w_m \cdot q_n'||_2} \tag{6.12}$$

Temporal coefficients are subsequently computed from eqn. 6.13. Using a subset of the basis modes ($M \leq N$), the field is reconstructed from eqn. 6.14.

$$a_{m,n} = \phi_m \cdot q_n' \tag{6.13}$$

$$q_n' \approx \sum_{m=1}^{M} a_{m,n} \phi_m \tag{6.14}$$

The eigenvalues (λ) represent the contribution of a given mode to the total system energy.‡ When applied to the full state vector, a different inner product is more

†In the case of a uniform grid, the spatial weights are identical at each point in the domain and uniformly scale the elements in the correlation matrix.

‡The amount of order reduction is typically controlled by retaining modes that contribute to a selected energy (correlation) threshold. *e.g.* Huang *et al.*[350]

suitable for compressible flows to maintain consistency between units for an energy-based norm.[324] For the present work, observables are normalized such that all units cancel.

Dynamic Mode Decomposition

Dynamic Mode Decomposition (DMD) (Schmid[221] and Rowley *et al.*[220]) assumes that the action of a system may be approximated by the linear operator (A) to map the system from state q_n to q_{n+1} (eqn. 6.15).[†] The method is attractive because it can extract low-energy, dynamically relevant features that POD may otherwise overlook.[343] DMD is used to extract coherent structures in a Hydrogen scramjet model by Li *et al.*,[351] for example.

$$q_{n+1} \approx A q_n \tag{6.15}$$

In the SVD-based approach,[221] DMD approximates this A operator from two matrices Q_1^{N-1} and Q_2^N (eqns. 6.16-6.17) using the collected snapshots.

$$Q_1^{N-1} = \{q_1, q_2, ..., q_{N-2}, q_{N-1}\} \tag{6.16}$$

$$Q_2^{N} = \{q_2, q_3, ..., q_{N-1}, q_{N}\} \tag{6.17}$$

The SVD operator is applied to Q_1^{N-1} to yield the approximate operator $\tilde{A}$ (eqns. 6.18-6.20) from the left singular vectors (U), singular values (Σ), and right singular vectors (V). At this stage, rank reduction may be applied to select a reduced basis for $\tilde{A}$ with rank $\tilde{r} \leq r$ where r is the full rank of U.[‡] For this analysis, it is assumed $\tilde{r} = r$;

[†] For statistically stationary, zero-mean snapshots, the DMD operator is equivalent to the Discrete Fourier Transform (DFT).[346]

[‡] The rank r measures the number of linearly-independent basis vectors in U which is at most $m = N - 1$ for DMD.

however, a more optimal *a priori* selection for $\tilde{r} < r$ in the context of order reduction has been proposed for matrices with specific statistical properties.[352]

$$AQ_1^{N-1} = Q_2^N \tag{6.18}$$

$$Q_1^{N-1} = U\Sigma V^* \tag{6.19}$$

$$\tilde{A} \equiv U^* A U = U^* Q_2^N V \Sigma^{-1} \tag{6.20}$$

The eigenvectors of $\tilde{A}$ (w_m) form the POD-projected DMD modes ϕ_m (eqn. 6.21) using U. The eigenvalues of $\tilde{A}$ (μ_m) approximate those of A (λ_m) via eqn. 6.22, in which the real and imaginary components provide mode growth rates (σ_m) and frequencies (ω_m), respectively.

$$\phi_m = U w_m \tag{6.21}$$

$$\lambda_m \approx \frac{\log \mu_m}{\Delta t} = \sigma_m + i\omega_m \tag{6.22}$$

The DMD mode amplitudes (d) are determined by a least-squares projection (eqn. 6.23) of the modes onto the first snapshot (q_1). Reduced-order reconstruction of the data follows[220] (eqn. 6.24) for a subset of the modes ($1 \leq M \leq N-1$).

$$\Phi d = q_1 \tag{6.23}$$

$$q_n \approx \sum_{m=1}^{M} d_m e^{\lambda_m t_n} \phi_m \tag{6.24}$$

Multi-Resolution Dynamic Mode Decomposition

Multi-Resolution DMD (mrDMD)[13] is attractive for analysis of unsteady systems with multiple time scales, because it utilizes a 'hierarchical' application of DMD to extract time-local dynamic content from snapshots, as represented by different bins b in the time-frequency domain illustrated by Figure 6.9. This method is similar

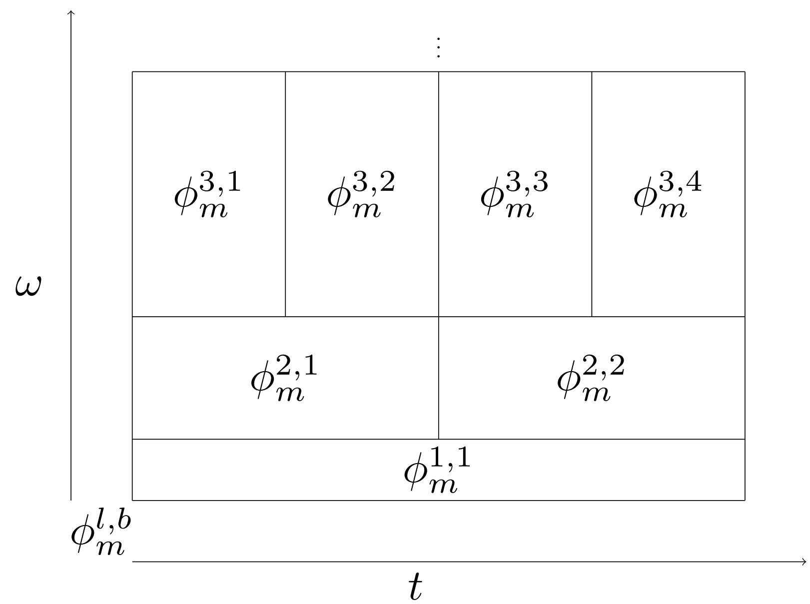

Figure 6.9: Schematic of Multi-Resolution DMD filtering hierarchy for modes (ϕ_m) at level (l) and time bin (b). Adapted from Kutz *et al.*[13]

to wavelet analysis because it seeks to capture time-local dynamic content.[327] The method may also capture translational and rotational structures in snapshots that are difficult to capture with the standard snapshot POD and DMD approaches.[13]

The algorithm described below is based on the implementations of Kutz *et al.*[327] and Taylor.[353] There are several free parameters in the approach which include the maximum number of levels (L), the maximum cycles per bin (max_{cyc}), and the cut-off frequency ($\underline{\rho}$) (eqn. 6.25), which is itself a function of sampling rate. Following Kutz *et al.*,[327] the limit n_{nyq} (eqn. 6.25) is specified as four times the Nyquist rate to resolve the specified number of cycles per bin. A maximum of two cycles are sought within each sampling window. At the first level of application ($l = 1$), DMD operates on $\mathcal{B} = N$ snapshots. Because only the 'slowest' (lowest frequency) modes are of interest in the current bin, the snapshots are sampled with stride ($\Delta\mathcal{B}$) (eqn. 6.27).

After sub-sampling the data, DMD modes and eigenvalues are computed following the standard DMD approach.

$$\underline{\rho} = \frac{max_{cyc}}{\mathcal{B}_{l,b}} \tag{6.25}$$

$$n_{nyq} = 4 \cdot (2 \cdot max_{cyc}) \tag{6.26}$$

$$\Delta\mathcal{B} = \frac{\mathcal{B}_{l,b}}{n_{nyq}} \tag{6.27}$$

Subsequently, 'slow' low-frequency modes with eigenvalues ($|\lambda| < \underline{\rho}$) are identified. For these slow modes, mode amplitudes are computed and stored as before. With these slow modes, a partial reconstruction of the system is computed and subtracted from the original signal ($q^{l,b}$) in the current bin level. Finally, the remaining signal is windowed into bins of size ($\mathcal{B}_{l,b} = N/2^l$) for the next level ($l$) and DMD is applied recursively to each window.

Final reconstruction of the system by the reduced hierarchical basis follows by summing over all modes ($\phi_m^{(l,b)}$) in each bin (b) at each level (l) with eqn. 6.28.[13] The reconstruction relies on a filter function ($f^{l,b}$) taken as eqn. 6.29. This filtering in time and frequency is equivalent to that illustrated in Figure 6.9.

$$q(\mathbf{x}, t) \approx \sum_{l=1}^{L} \sum_{b=1}^{B_l} \sum_{m=1}^{M_{l,b}} f^{l,b} d_m^{l,b} e^{(\lambda_m^{l,b} t)} \phi_m^{l,b}(\mathbf{x}) \tag{6.28}$$

$$f^{l,b}(t) = \begin{cases} 1, & t \in [t_b, t_{b+1}], b \in 1, 2, \cdots, B_l \\ 0, & \text{otherwise} \end{cases} \tag{6.29}$$

6.2.2 Feature Extraction

A focus of statistical and unsupervised learning, such as Principal Component analysis, is to extract low dimensional features[354] from a high-dimensional system. This feature-extraction perspective is adopted for the subsequent analysis.

Specifically, gradients in the spatial modes are examined for indicators of the primary dynamic flow structures (features) related to side wall separation and the isolator shock-train. These modes are compared against previous qualitative and quantitative measures of the flow structures to provide a physical interpretation of the modes.

Side Wall Separation

First, POD and DMD modes are computed and examined for indicators of coherent flow structures related to upper wall separation. To analyze this feature using the data-driven MOR-methods, the streamwise velocity component (u) is scaled by spatially averaged isolator entrance velocity (u_e), as before, to give $\hat{u} \equiv u/u_e$. Other velocity components are similarly scaled. This MOR-analysis considers snapshots over the full transient period ($0 \leq \hat{t} \leq t_{uns}$).

To isolate the modes of interest, metrics of the relative information content in each mode are computed. The modes are assigned weights and ranked to select the modes which best capture the flowfield dynamics. The POD eigenvalues, which serve as a measure of the system energy, and the L_2 norm of the real part of each scaled DMD mode ($||\mathbb{R}(d_m \phi_m)||_2$) are selected as representative measures of relative information content. The DMD weight is computed consistent with the approach of Mohan *et al.*[348,349] The POD and DMD metrics are plotted in Figure 6.10 and indicate a relatively rapid drop off in normalized POD mode amplitude with increasing mode number, consistent with the expectation that POD provides for an optimal basis in terms of energy (L_2 norm). After the first dozen modes however, the amplitude drop-off becomes asymptotic across all modes; this is consistent with the expectation that most of the information is encoded in lower-numbered modes.[355] Because the mode

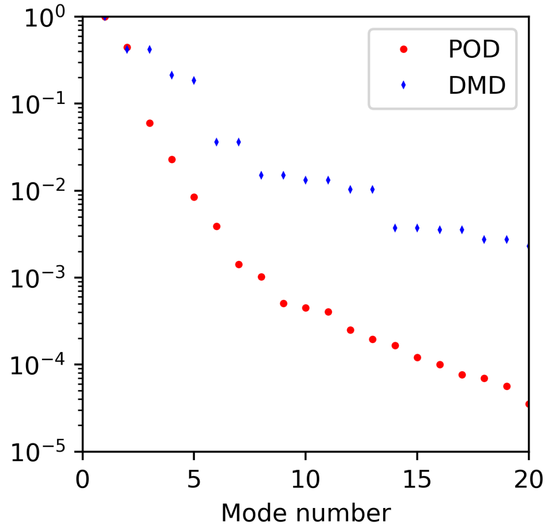

Figure 6.10: Upper wall separation dynamics: POD and DMD mode information-content for first 20 modes.

amplitudes rapidly decrease with mode number, the first mode ($m = 1$) of each basis is representative of the dominant flow features.

Since the system is not statistically steady, additional dynamic flow structures are observed in the dominant modes. This contrasts with statistically steady flowfields where the first computed POD or DMD mode represent the time-mean field when applied to the raw snapshots.[346] The first ($m = 1$) POD and DMD modes are shown in Figure 6.11 (a,b) where the real part of the DMD modes is plotted for comparison ($\mathbb{R}e(\hat{\phi})$). Relatively large, positive magnitudes in the first POD mode highlight the cavity shear layer region and upper wall separated region. For this non-stationary system, the dominant DMD mode contains not only features of the time-averaged field (Figure 6.11 (c)) but also the signature of the upper-wall separation zone. The first

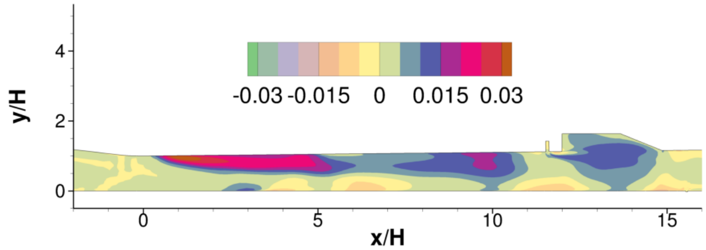

(a) POD $m = 1$

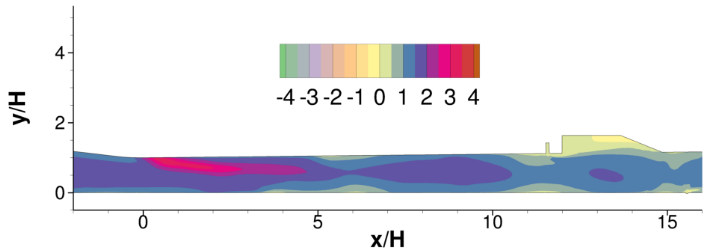

(b) DMD $m = 1$

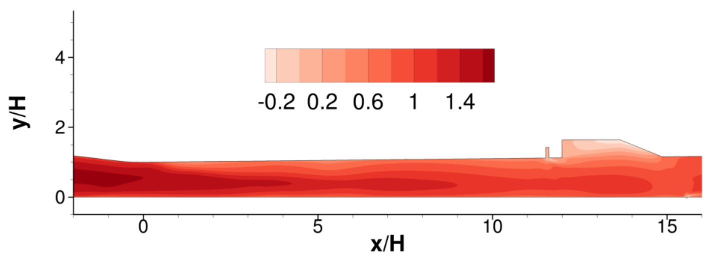

(c) $\bar{\hat{u}}$

Figure 6.11: Upper wall separation dynamics: (a) POD $m = 1$ mode, (b) real part of DMD $m = 1$ mode, and (c) time-mean of streamwise velocity field ($\bar{\hat{u}}$).

POD mode similarly features spatial gradients representing the upper wall separation zone.

Multiple zero-frequency modes appear with different growth rates. Stationary modes for the upper wall separation analysis are compared in Figure 6.12. Despite having zero frequency, the stationary mode growth rates (σ) vary by several orders of magnitude. The growth rates are scaled as $\hat{\sigma}_e = \sigma\mathcal{H}/u_e$. Crucially, each of these

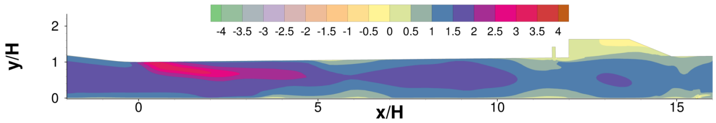

(a) $m = 1$, $\hat{\sigma}_e = 1.5 \times 10^{-4}$

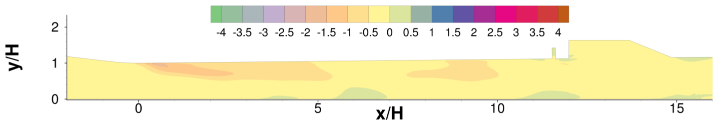

(b) $m = 4$, $\hat{\sigma}_e = 1.0 \times 10^{-3}$

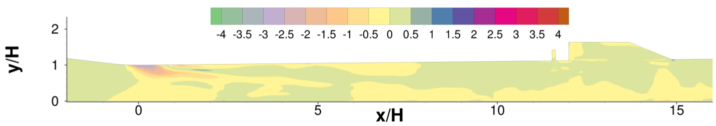

(c) $m = 5$, $\hat{\sigma}_e = -5 \times 10^{-2}$

Figure 6.12: Upper wall separation dynamics: DMD stationary modes.

stationary modes contains spatial content indicative of the upper wall separation, demonstrating the relative dynamic importance of this feature during the transient fuel-staging event; *i.e.*, the dynamics are spread across multiple frequencies.

Like the symmetry plane, evidence of side wall separation structures are found through examination of the horizontal plane located at $\hat{y} = 0.5$ above the lower wall. In this region of interest, the dilatation field (Figure 6.4 (a)) highlights strong flow curvature at the isolator entrance ($\hat{x} = 0$) with dark contours indicative of the compression waves turning the flow. The subsonic separated region is indicated from the sonic condition shown by the red contour line. The dynamics of the separation zone are corroborated by the total variation of the streamwise velocity field (Figure 6.4 (b)), which highlights two dynamic regions of interest. One region associated with DG-initiated oblique shock is located near the isolator entrance at

$\hat{x} = \hat{z} = 0$, the dynamics of which are prominent during the unstart phase as indicated by the $R_{TV}(\hat{u})$ field in Figure 6.4 (c).

A secondary lobe structure is found nearer the side wall and at a more acute angle (relative to the side wall) whose corresponding TV magnitude suggests that its dynamics are mixed between pre-unstart and unstart phases. This latter feature is an indicator of flow curvature at the inception of side wall flow separation due to upstream propagation of the pressure rise associated with combustion. While both dominant POD (Figure 6.13 (a)) and DMD (Figure 6.13 (b)) modes capture regions of strongest dynamics associated with sidewall separation, only DMD captures the signature of DG shock near the isolator midspan ($\hat{z} = 0$). These compression waves are shown in Figure 6.13 (c).

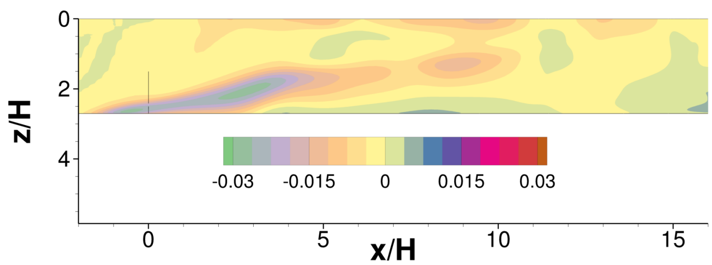

(a) POD $m = 1$

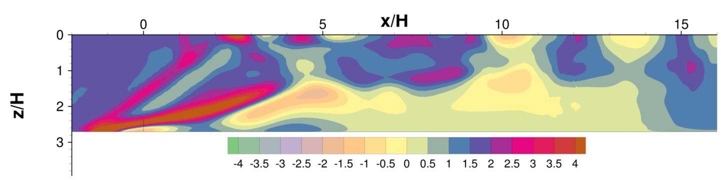

(b) DMD $m = 1$

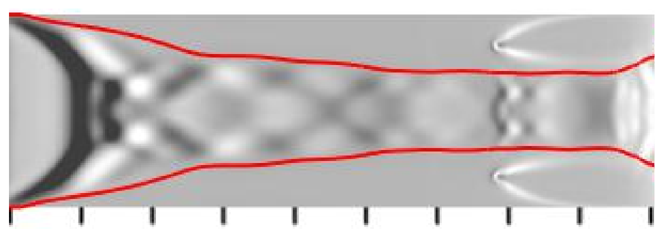

(c) $\nabla \cdot \mathbf{U}$ at $\hat{t} = 1$

Figure 6.13: Side wall separation dynamics: (a) POD $m = 1$ mode and (b) real part of DMD $m = 1$ mode, and (c) snapshot at $\hat{t} = 1$: *greyscale* - dilatation, *red* sonic line.

Pre-Combustion Shock-Train

Like the TV analysis, the vertical velocity component ($\hat{v}$) is analyzed with the MOR techniques to distinguish PCST at different phases of the fuel-staging transient. SBLI structures are identified from the dominant modes for several time-windowed MOR-decompositions. Dominant POD and DMD modes from the analysis of the full simulation window ($0 \leq \hat{t} \leq t_{uns}$) are shown in Figure 6.14 (a) and Figure 6.14 (b), respectively. Time-windowing of the data also isolates the change in SBLI behavior between the two phases of PCST motion. The first mode for the POD-analysis of the pre-unstart (slowly varying) phase (Figure 6.14 (c)), although qualitatively similar to POD of the full transient sequence, is quantitatively closer to the time-mean flowfield during the quasi-steady phase. Caution is warranted because POD assumes ergodicity, which may make the physical interpretation of the modes less straight-forward for the current dataset. DMD, which does not assume a statistically steady system, is therefore better-suited to the statistically non-stationary flow. Consequently, DMD is applied to the unstart phase window. The DMD mode (Figure 6.14 (d)) highlights the incident oblique shock generated by the DG as the dominant dynamic feature, the signature of which is shifted upstream of the isolator entrance ($\hat{x} = 0$), consistent with the upstream motion of the PCST.

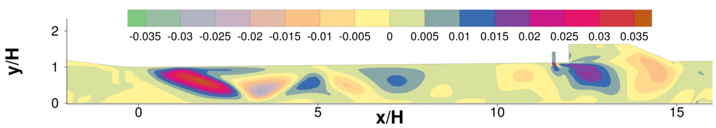

(a) Full sequence, POD

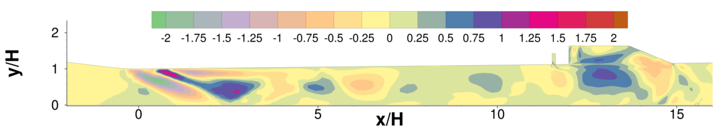

(b) Full sequence, DMD

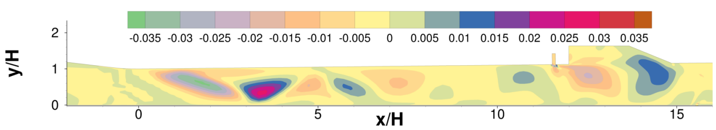

(c) Pre-unstart, POD

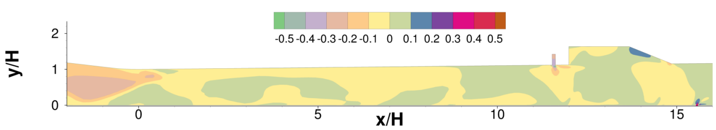

(d) Unstart phase, DMD

Figure 6.14: PCST structures from MOR modes subject to specified time-windows: (a) POD on $0 \leq \hat{t} \leq \hat{t}_{uns}$, (b) DMD on $0 \leq \hat{t} \leq \hat{t}_{uns}$, (c) POD on $0 \leq \hat{t} \leq 1$, and (d) DMD on $1 \leq \hat{t} \leq \hat{t}_{uns}$.

6.2.3 Inference of Dynamics and Data Compression

In addition to isolating the dynamic features within the flowfield, it is desirable to produce reduced-order representations, which maximize order reduction (minimize basis size), while minimizing reconstruction error, to facilitate reduced-order modeling. To assess the effectiveness of the MOR decompositions (*i.e.* as a measure of data compression) the error between the reconstructed flowfield and the original CFD dataset is computed as a function of basis size. For this evaluation, the absolute error field (eqn. 6.30) is used to infer strongly transient regions which are not as well captured by the MOR methods. Subsequently, the relative reconstruction error (eqn. 6.31) is computed from the L_2 norm.

$$E(\mathbf{x}, t_n) = q_{mor}(\mathbf{x}, t_n) - q_{cfd}(\mathbf{x}, t_n) \tag{6.30}$$

$$E_2(t_n) = \frac{||E(\mathbf{x}, t_n)||_2}{||q_{cfd}(\mathbf{x}, t_n)||_2} \tag{6.31}$$

Dynamics

Reconstruction error magnitudes vary for the different MOR methods used. However, these errors facilitate identification of strongly transient regions. In this approach, higher-order dynamics are assumed to require a larger basis size. Therefore, regions with relatively higher reconstruction errors are indicative of non-linear dynamics which are not well represented for a given basis size.

As an example, the average of absolute error is computed for the streamwise velocity field on the symmetry plane. Figure 6.15 shows the time-average of the absolute error magnitude field ($\overline{|E(t)|}$) for POD and DMD with a $M = 20$ basis size. The largest error regions are near the upper wall separation and cavity shear layer

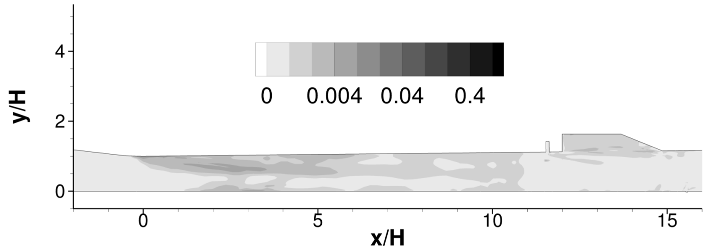

(a) POD

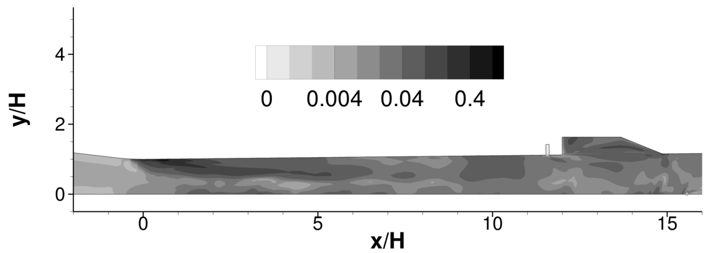

(b) DMD

Figure 6.15: Comparison of average of absolute reconstruction error ($\overline{|E(t)|}$) for (a) POD and (b) DMD using $M = 20$ for streamwise velocity on symmetry ($\hat{z} = 0$) plane.

zones, consistent with previous qualitative and quantitative analysis. This suggests that the error is a suitable analog for the most significant dynamics that are least well-captured for the assumed basis size. POD errors are lower than DMD, which is expected by definition of error in the L_2 norm and the PCA least squares minimization problem.

Next, this error analog is extended to flow dynamics of the full 3-D domain. Previously, the reconstruction error was computed directly. This requires selecting a basis size (M) and reconstructing the signal to evaluate the error. For high-dimensional systems, it is costly to determine a suitable M required to achieve a desired reconstruction error.

To facilitate 3-D analysis, we return to an observation from the feature-extraction discussion. For simplicity, only data within the pre-unstart time window are analyzed. As previously noted, the first DMD mode contains signatures of the time-mean field. However, the first mode also encodes the structure of the non-stationary dynamics. Consequently, the difference between the first DMD mode and the time-mean field is expected to isolate higher-order dynamics, which are also encoded in the higher modes.

The velocity field is also selected for the 3-D MOR-based decomposition. Because of the domain size and corresponding memory requirements, each velocity component is decomposed independently.† A question arises, however, as to whether this separation of the DMD filter is reasonable in terms of consistency between computed dynamics.

As before, the normalized mode amplitudes are computed to characterize relative mode information content. The normalized mode amplitudes for the first 40 DMD modes are shown in Figure 6.16. Here, the amplitude drop-off varies with the relative magnitude of the velocity components where, generally, $|\hat{u}| > |\hat{v}| > |\hat{w}|$. To compare the three DMD computations, the eigenvalues are computed as a measure of the system dynamics. The eigenvalues (μ_m) computed from DMD are used to approximate the frequency and growth rate information of the modes (λ_m). The eigenvalue spectra for each of the velocity components ($\hat{u}$, $\hat{v}$, and $\hat{w}$) are shown in Figure 6.17. Qualitatively, the eigenvalues show some differences in the different velocity eigenspectra. Mezić[355] notes that although any observable selected for

†While previous MOR computations rely on Python-based codes implemented by the author, the memory requirements mandate a more computationally efficient version of DMD, using the Fortran LAPACK[356] library, as implemented by collaborators previously acknowledged.

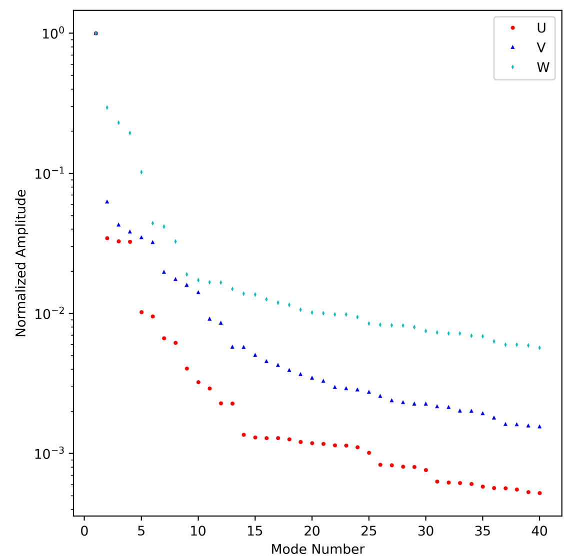

Figure 6.16: Spanwise dynamics variations: DMD mode amplitudes for individual velocity components for $1 \leq M \leq 40$.

analysis with DMD will contain some of the underlying global system dynamics, the choice of observable can lead to differences in the computed spectra. Although the flow is not strictly stationary during the pre-unstart phase, the eigenvalue corresponding to the dominant mode $m = 1$ of each velocity component has zero frequency ($\mathbb{I}m(\lambda) = 0$) and small, but finite, growth rate ($|\mathbb{R}e(\lambda)| > 0$). Interestingly, while the streamwise ($\hat{u}$) and spanwise ($\hat{w}$) components have near-identical growth rates, the vertical velocity component ($\hat{v}$) is lower in magnitude, closer to zero growth rate. Similarity between each of the separate DMD calculations for lower-numbered modes suggests that each DMD calculation captures a similar portion of the system dynamics.

Having established that the independent application of DMD to each of the velocity components yields reasonably-consistent dynamics, the 3-D mode structures are analyzed. Since the flow is not statistically steady, the dominant DMD mode,

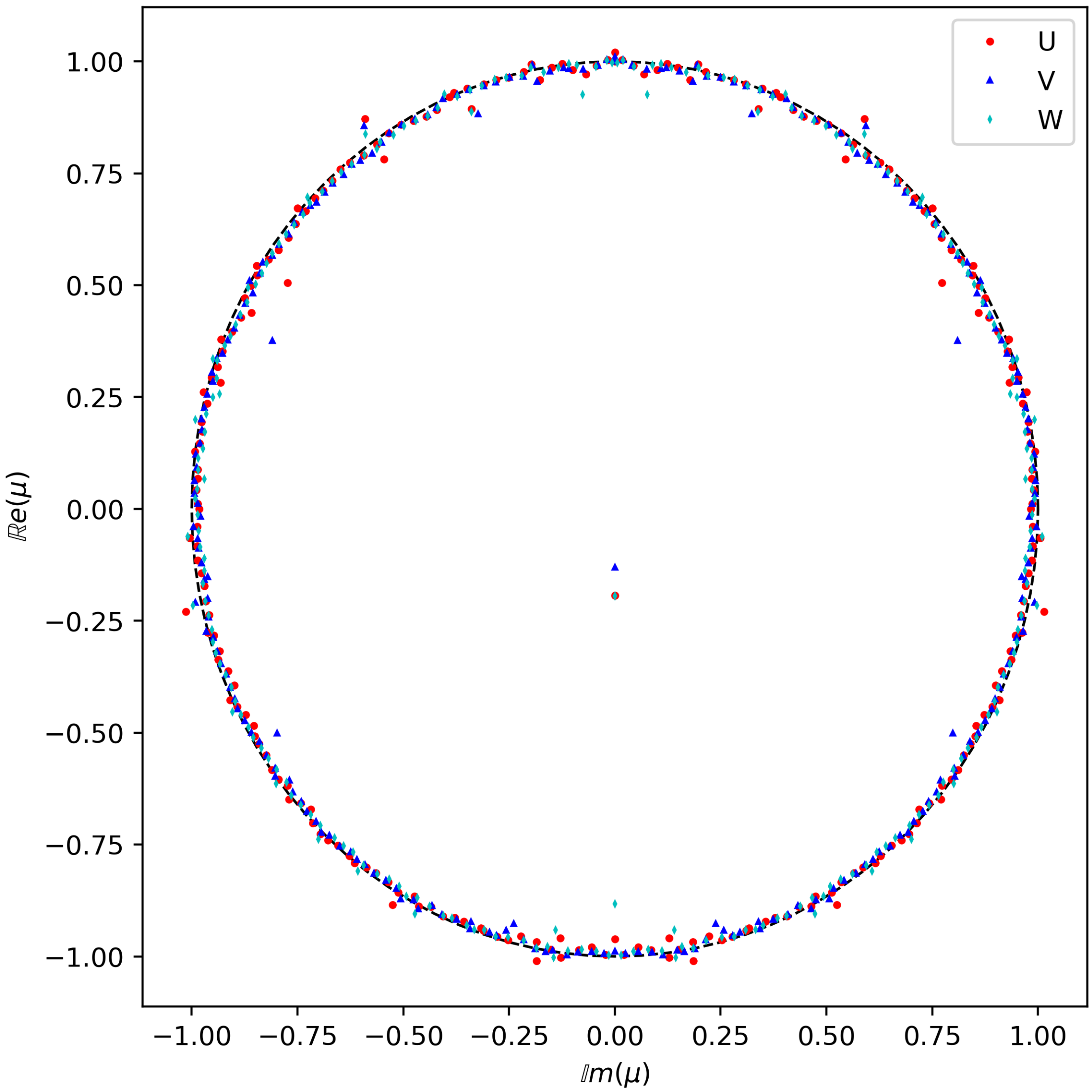

Figure 6.17: Spanwise dynamics variations: Comparison of DMD eigenspectra (μ_m) for $\hat{u}$, $\hat{v}$, and $\hat{w}$ velocity components.

which is scaled relative to the initial state, will contrast with the time-averaged field. The most transiently-responsive regions are inferred from the magnitude of this difference. Contours of this difference in velocity between the first mode and time-mean field ($\delta\hat{u}_i$) are shown in Figure 6.18 (a) for the symmetry plane and several constant $\hat{x}$ planes in the isolator spaced every $\Delta\hat{x} = 2$. The streamwise velocity component, for example, captures the upper wall separation previously discussed (§ 6.1.1) as well as the cavity shear layer, as indicated by the contours on the symmetry plane ($\hat{z} = 0$). The upper corner of the isolator at the side wall is also identified in the region of vortical-like flow previously shown in Figure 6.7.

The vertical velocity component (Figure 6.18 (b)), previously used to characterize the PCST structure, isolates the oblique shock generated by the distortion generator on the symmetry plane, as highlighted by the red band upstream of isolator entrance ($\hat{x} = 0$). Larger magnitudes on the constant $\hat{x}$ planes near the isolator entrance are associated with the modulation of the oblique shock structures by the upper wall separation region, as observed in § 5.9.

However, the spanwise velocity component (Figure 6.18 (c)) contour levels are saturated near the isolator corner. These relatively constant levels are attributable to upstream PCST motion. Similarly, higher-magnitude dynamics are inferred in the cowl-step region downstream of the cavity. This methodology suggests that the difference between the non-zero time-mean and the first DMD mode for statistically unsteady flowfields may provide an economical approach to infer the most dynamically responsive regions within the flowfield.

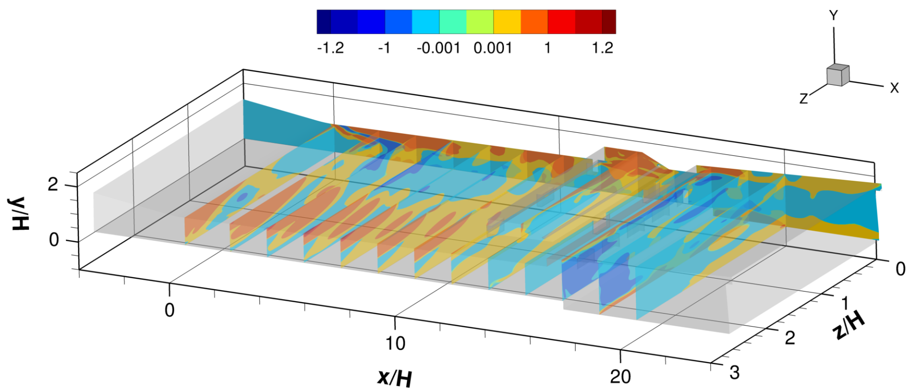

(a) $\delta\hat{u} = \hat{u}_{m=1} - \bar{\hat{u}}$

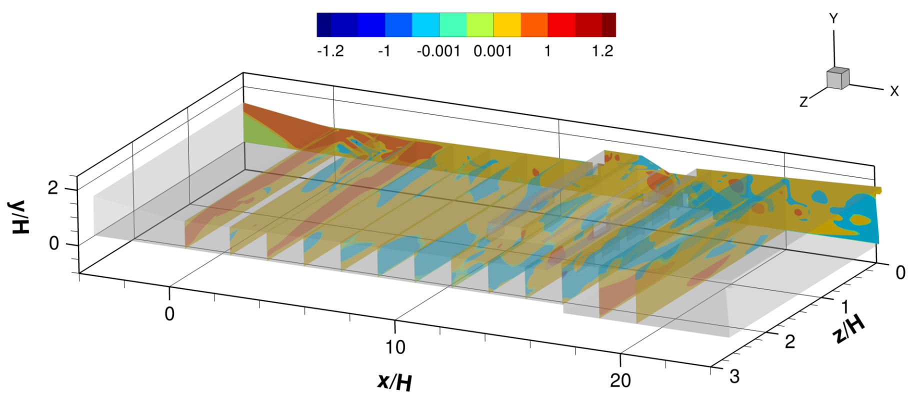

(b) $\delta\hat{v} = \hat{v}_{m=1} - \bar{\hat{v}}$

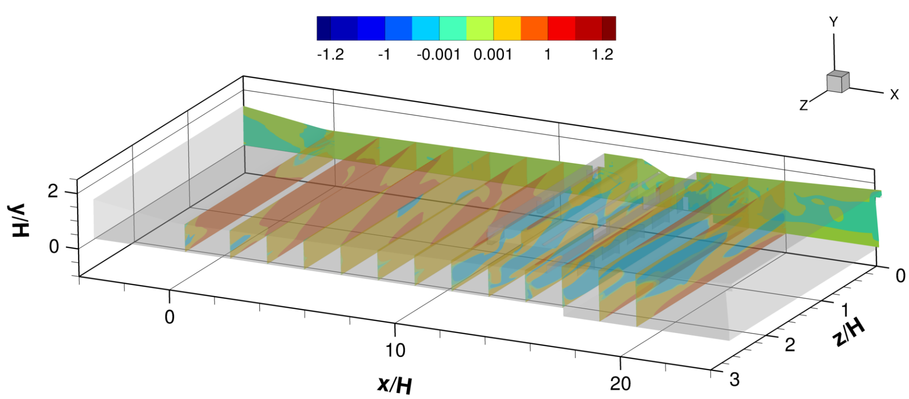

(c) $\delta\hat{w} = \hat{w}_{m=1} - \bar{\hat{w}}$

Figure 6.18: Spanwise flow variations: Inference of dynamic regions from the difference between DMD $m = 1$ mode and time mean for (a) streamwise, (b) vertical, and (c) spanwise velocity components.

Reconstruction Efficiency

A final component of the MOR-based analysis considers the degree of data-compression (order reduction) achievable for a particular reconstruction error magnitude. Understanding error scaling with basis size is important for the efficient construction of reduced-order models. First, the efficiency of POD and DMD to capture flowfield dynamics for a given basis size is assessed. Second, time-windowing of the data is shown to reduce reconstruction errors. However, the time-local nature of unstart unsteadiness motivates the application of the multi-resolution DMD method. Consequently, the multi-resolution method reduces errors associated with non-linear unstart PCST motion compared with the standard DMD and compares favorably with the L_2-optimal POD.

The scaled streamwise velocity on the symmetry plane is used as representative example for the MOR reconstruction behavior. From the previous mode amplitude scaling (*e.g.* Figure 6.10), a $M = 20$ basis size is selected for the initial flowfield reconstruction, corresponding to 10 percent of the computational dataset. The POD and DMD reconstruction errors are illustrated in Figure 6.19. During the pre-unstart phase, DMD exhibits lower errors. As time advances toward the unstart phase, DMD errors increase rapidly, attributable to non-linear PCST transients. POD, however, exhibits relatively constant error during the first half of the fuel-staging transient. Although several higher peaks are observed in the latter half of the fuel-staging transient, the errors during the unstart phase are an order of magnitude lower than DMD.

The number of modes retained for reconstruction is varied to determine the scaling of relative error across time for a specified level of order reduction. Order

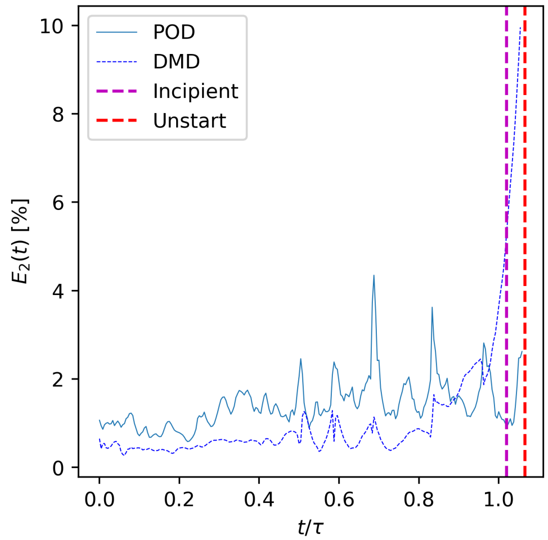

Figure 6.19: Reconstruction error comparison for streamwise velocity field ($\hat{u}$) on symmetry ($\hat{z} = 0$) plane for $M = 20$ basis size.

reduction is defined as the ratio of total snapshots to number of modes retained in the reconstruction. Order reduction (O_r) factors between 1.5 and 50 are imposed, requiring between $M = 160$ and $M = 5$ modes, respectively. Increasing the number of modes used in the reconstruction reduces errors prior to the unstart phase for both POD and DMD. POD errors decrease for each subsequent increase in basis size (M) used for reconstruction (Figure 6.20 (a)). However, by $M = 20$, diminishing returns are observed in the reduction of DMD $E_2(t)$ during the unstart phase (Figure 6.20 (b)). These trends are summarized in Table 6.1, which compares basis size (M_i), order reduction (N/M_i), and reduction in normed relative error ($|E_2|_{M=5}/|E_2|_{M_i}$). Still, prior to unstart, both POD and DMD yield relatively small reconstruction errors ($E_2(t) \leq 10\%$ for $M = 20$), making it attractive for data

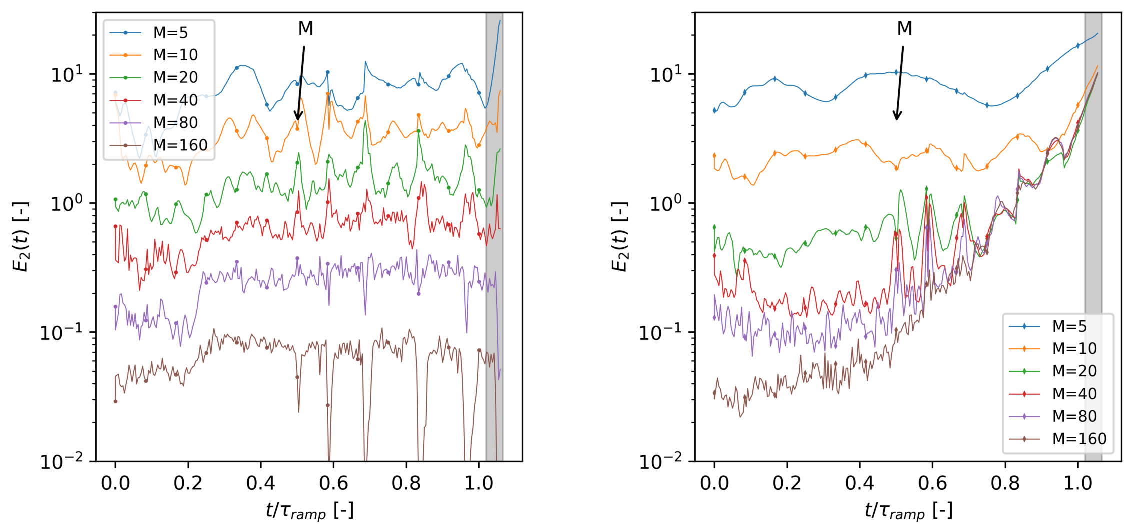

(a) full sequence, POD

(b) full sequence, DMD

Figure 6.20: Reconstruction error scaling with modal basis size: (a) POD and (b) DMD.

compression to facilitate control system development relying on a lower-dimensional representation of the unsteady flowfield.

Next, time-windowing is used to control reconstruction errors by better aligning the stationarity and linearity assumptions of POD and DMD, respectively. Figure 6.21 (a) compares reconstruction errors for POD and DMD during the pre-unstart phase. POD reconstruction errors are smaller, indicative of better compression for the given error level. This suggests that the slowly varing pre-unstart phase is more amenable to statistically steady POD. Conversely, the short-time unstart-phase is better approximated by the DMD filter, because although non-stationary, the linear approximation provides a lower error in DMD reconstruction than POD as shown in Figure 6.21 (b).

Table 6.1: POD and DMD reconstruction error and order reduction scaling with basis size M.

Basis Size M_i	Order Reduction $\frac{N}{M_i}$	Error Reduction $\lvert E_2\rvert_{M=5}/\lvert E_2\rvert_{M_i}$ POD	DMD
5	51.0	1.0	1.0
10	25.5	2.3	3.0
20	12.8	5.4	5.1
40	6.4	12.0	5.0
80	3.2	31.7	5.0
160	1.6	121.6	5.0

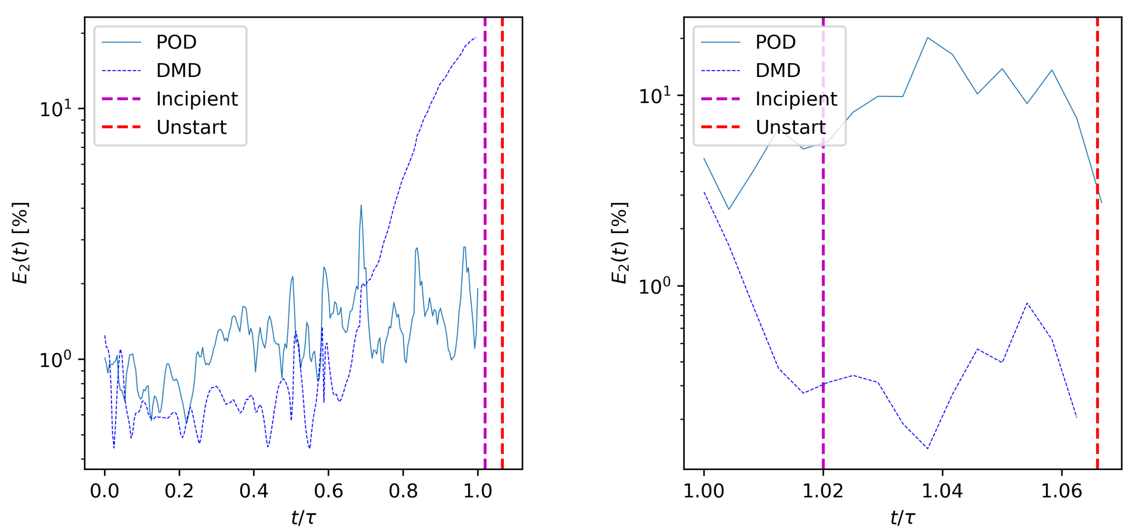

(a) Pre-unstart phase

(b) Unstart phase

Figure 6.21: Reconstruction error sensitivity to time-windowing: (a) pre-unstart time window and (b) unstart time window.

Time-Local Decomposition

Although the dataset violates the statistically steady assumption, the POD basis still provides better compression scaling with basis size. Additionally, the non-linearity of the flowfield reveals the limitations of the DMD approach to capture both pre-unstart and unstart phases of shock-train dynamics. Manually time-windowing the data helps reduce reconstruction errors for a given level of order reduction with both POD and DMD, but this approach requires *a priori* knowledge of the dynamics. Consequently, the multi-resolution DMD is employed as a way to generate a reduced-order representation of the flowfield using a hierarchy of *time-local* DMD bases without manual intervention in windowing of the data.

Given the assumption of cut-off frequency ($\underline{\rho}$) previously described and the snapshots in the range of $0 \leq \hat{t} \leq t_{uns}$, mrDMD selects four levels during the mrDMD sifting process. At each level, the algorithm selects the number of 'slow' modes (M_l). Sample mode shapes at each level are shown in Figure 6.22 and highlight spatial gradients associated with the upper wall separation and cavity shear layer zones, similar to previous MOR decompositions. The separation of dynamic scales is shown for each level and time window from the mrDMD amplitudes shown in Figure 6.23.

Reconstruction error scales with the number of mrDMD mode levels retained in the computation. These errors are shown in Figure 6.24 for the number of levels retained. The error reduction ratio is similarly summarized in Table 6.2. As expected, increasing the number of levels retained for reconstruction reduces the errors associated with higher-order dynamics.

To understand the effectiveness of time-local data compression and reconstruction, the mrDMD results are compared against the POD and DMD results. Reconstruction

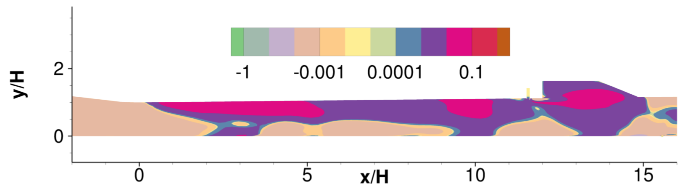

(a) $(l, m) = (1, 2)$

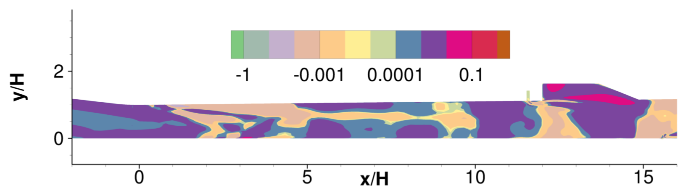

(b) $(l, m) = (2, 1)$

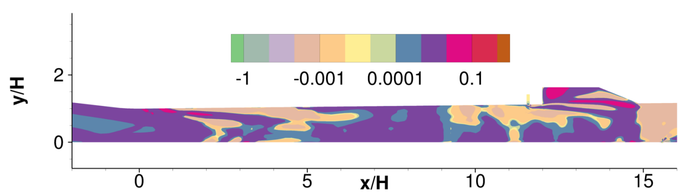

(c) $(l, m) = (3, 1)$

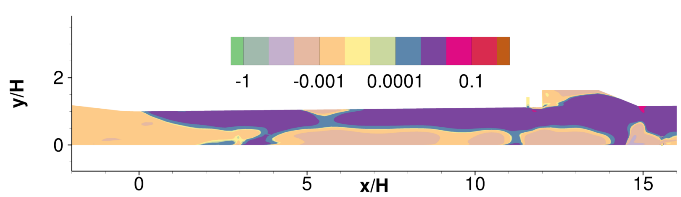

(d) $(l, m) = (4, 1)$

Figure 6.22: Features of mrDMD basis functions ($\mathbb{R}e(\phi)$) for several levels (l) and modes (m).

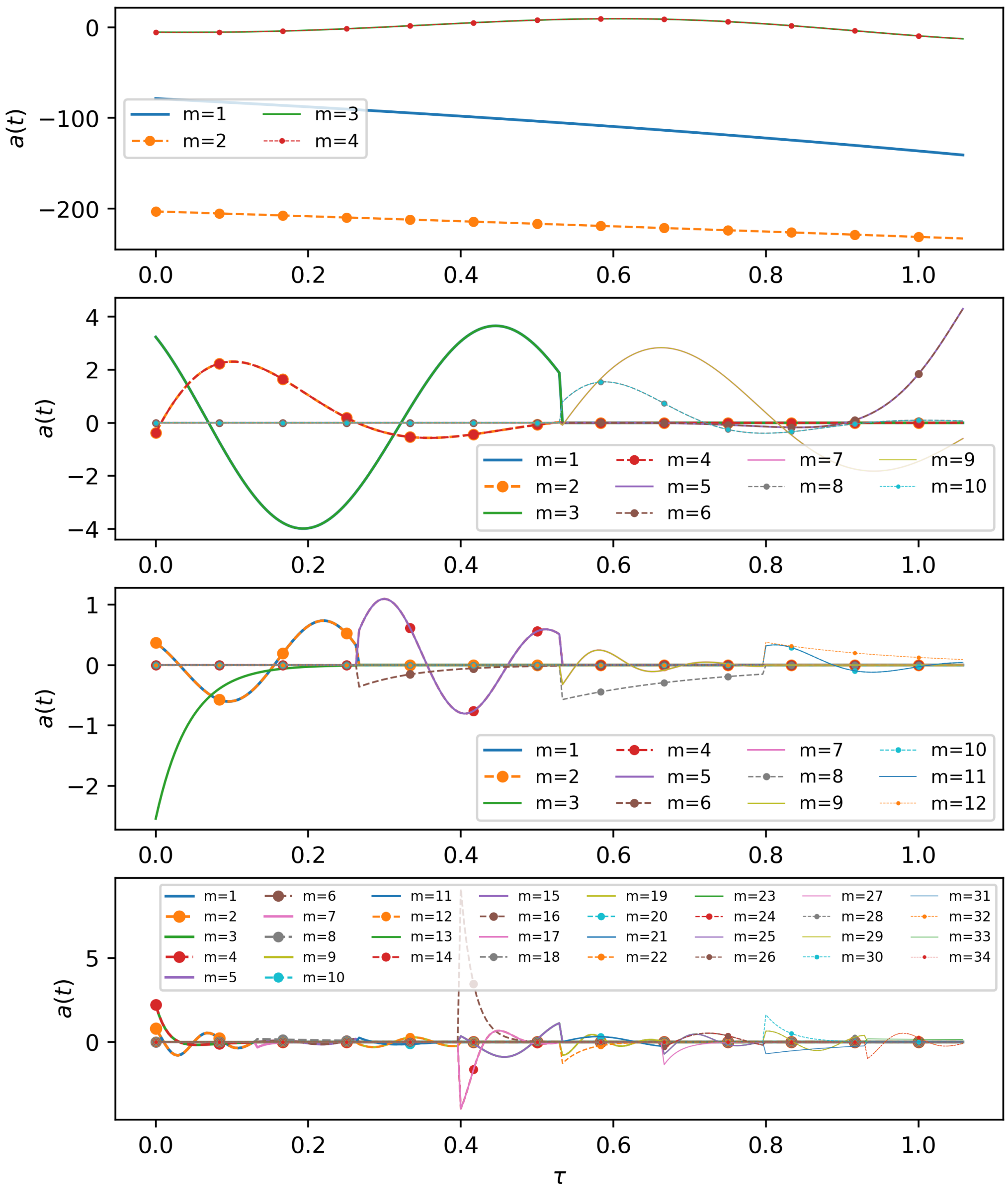

Figure 6.23: Comparison of mrDMD temporal coefficients with level (l) and mode (m).

Table 6.2: mrDMD reconstruction error and order reduction scaling with hierarchy level (L).

Level l	Modes/Level M_l	Order Reduction $\frac{N}{\sum_l M_l}$	Error Reduction $\lvert E_2\rvert_{l=1}/\lvert E_2\rvert_{l_i}$
1	5	51.0	1.0
2	8	19.6	3.7
3	16	8.8	4.9
4	28	4.5	8.8

errors for DMD, POD, and mrDMD decompositions are shown in Figure 6.25. Multi-resolution DMD with all levels is compared to the optimal POD basis for a similar level of order reduction, $O_r \approx 4.5$, corresponding to $M = 57$ POD modes. Hence, mrDMD is comparable to (or better) than POD and DMD in terms of reconstruction error, suggesting the method is a suitable data-driven approach for order reduction of this statistically unsteady flowfield. Moreover, mrDMD automatically selects the number of modes per level and number of levels based on the data and frequency sampling, providing a potentially more robust data-driven selection of modes for model order reduction.

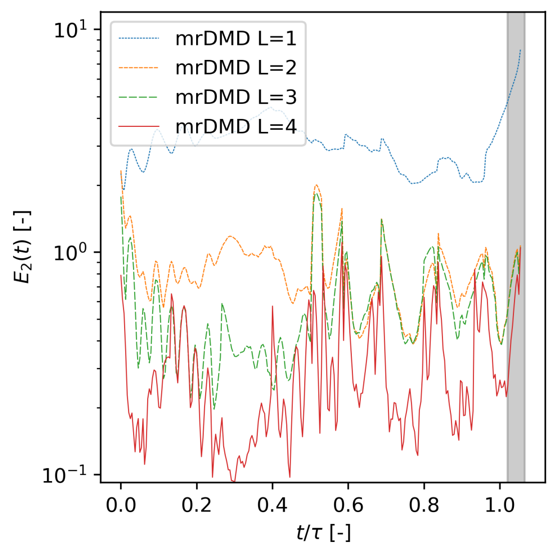

Figure 6.24: Reconstruction error scaling for varying mrDMD levels.

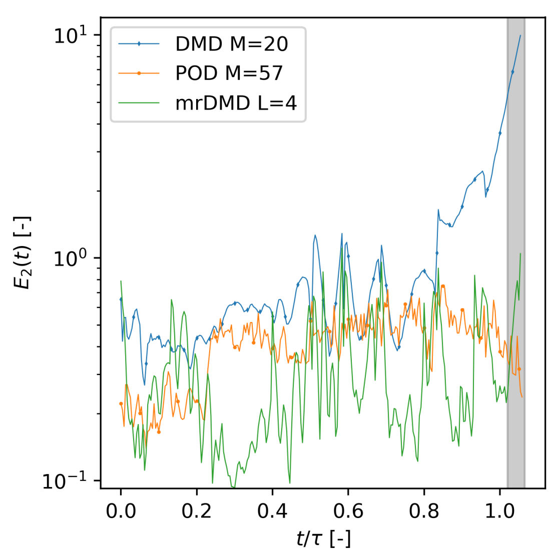

Figure 6.25: Comparison of minimum reconstruction errors for POD, DMD, and mrDMD.

6.3 Summary

- The Total Variation (TV) metric is adapted to quantify the statistically unsteady, dynamic response of the combustor fueling transient.
- The choice of observable for TV-based analysis highlights different combustor dynamics:
  - The heat release TV field reveals the side wall separation bias and cavity shear layer reaction zones.
  - The streamwise velocity TV field highlights the upper wall separation zone from the symmetry plane.
  - Side wall separation is identified from the streamwise velocity TV field on the horizontal analysis plane.
  - The PCST structure is isolated using the vertical velocity component on the symmetry plane.
  - Application of the TV metric on the 3-D field highlights the spanwise gradients associated with the isolator corner, cavity, and backward-facing step regions.
- The data-driven Model Order Reduction (MOR) methods are employed to extract combustor dynamics:
  - The dominant POD and DMD modes, as ranked by amplitude, identify similar dynamic features consistent with the quantitative TV analysis.
  - DMD produces several stationary (zero-frequency) modes for the statistically unsteady system.

  - The high-dimensional, 3-D dataset necessitates parallel decomposition of the velocity field because of the computational scaling cost.
  - The choice of DMD observable affects the predicted eigenspectra, however, similarity between the spectra for each velocity component suggests that such a splitting approach may be suitable for high degree-of-freedom flowfields.

- The order reduction effectiveness of each MOR method is assessed with respect to reconstruction error:

  - For the non-stationary flowfield, subtracting the time-mean field from the first DMD mode filters regions featuring non-linear dynamics.
  - POD produces optimal reconstruction error in terms of the L_2 error norm.
  - Time-windowing the data helps minimize reconstruction errors for the POD and DMD methods. POD reduces errors for the slowly varying, pre-unstart phase. DMD reduces errors for the isolator unstart phase.
  - The multi-resolution DMD method captures time-local effects without manual selection of time-windows in order to filter the flowfield dynamics.
  - The mrDMD method reduces reconstruction error during the unstart phase compared to the standard DMD algorithm and produces errors comparable to the POD reconstruction.

Chapter 7

Conclusions

The development of hypersonic air-breathing propulsion systems for the next generation of access-to-space, high-speed transport, and defense aerospace systems continues to drive significant research into the physics of scramjet engine systems. Despite the geometrical simplicity of scramjet engines, the intensity and coupling of physics, including heat-transfer, laminar-turbulent transition, chemistry, and the range of time scales, make routine hypersonic-powered flight challenging. In particular, the flowfield dynamics within scramjet isolators and the senstivity of the isolator to combustor disturbances motivates continuing research activities.

A crucial large-scale event, with potentially catastrophic consequences, is unstart, where the isolator shock-train is ejected from the combustor adversely affecting structural integrity and propulsion performance. While many unstart studies have considered isolator dynamics under statistically steady conditions, relatively few consider the effect of combustion-induced, rather than mechanically-induced, unstart events. This work has qualitatively described and quantified the dynamics of isolator response to a fuel-staging-induced unstart event in a hydrocarbon-fueled, rectangular combustor at a representative flight Reynolds number. Importantly, a unique feature of the combustor is the distortion generator (DG), which models effects of inlet flow distortion on the isolator flowfield. The model-based computational approach builds on an experimental campaign, to explore the influence of corner flow interactions, heat release, and shock train motion. Unstart is induced by linearly varying the fuel injector flow rates between two reference conditions, representing aft- and forward-fuel-biased operation. The most significant conclusions of the work and an outline of areas for future research focus are subsequently summarized.

7.1 Summary of Findings

Because of the high-Reynolds number and complexity of flowpath, a model-based approach is employed to compute the turbulent reacting flowfield. Sensitivities to the model parameters and assumptions are first quantified. Numerical predictions are compared against the time-mean wall-pressure data obtained from experiments at steady-state fueling conditions. Grid and temporal resolution effects are quantified through the Grid Convergence Index and heat release rates. The influence of inflow turbulence and wall heat-flux boundary conditions is also examined. The predictions are insensitive to inflow turbulence. However, wall-heat flux, in the case of adiabatic walls, increases shock-induced separation compared to the idealized 1-D thermal resistance model. Like other numerical scramjet studies, the turbulent Schmidt number is observed to have the largest first-order effect on steady-state flowfield predictions. Additionally, different Schmidt numbers are found to be optimal for different fueling conditions. Ranges of turbulent and chemical scales are evaluated, demonstrating an increase in the fluid timescales, with increasing forward fuel bias. Additionally, the range of turbulent Mach numbers in the combustor remains high

($Ma_t \geq 0.3$), even during the forward-fueled condition, in which the combustor flow velocity is reduced near the cavity flame holder.

Pre-Combustion Shock-Train (PCST) dynamics are quantified in terms of a wall-pressure-based sensor adapted from experiments. Consequently, distinct phases of PCST motion are identified during the fuel-staging transient. A relatively slow PCST speed ($\mathcal{O}(1)$ m/s) is observed in the first, pre-unstart phase. As fuel input increases at the upstream injectors, outboard fuel injection drives corner and side wall separation. By extending the wall-pressure-based shock sensor from a 1-D centerline to a 2-D wall field measurement, the incipient unstart condition is demonstrated to correspond to the combustion-induced pressure rise advancing upstream of the isolator entrance along the sidewall in advance of the centerline location. A rapid acceleration of the shock-train to $\mathcal{O}(30)$ m/s is estimated during the unstart phase of the fuel-staging transient. A final, short phase of PCST motion comprises the upstream propagation from the isolator entrance to the DG-induced 'inlet' shock. The final isolator and inlet unstart events take place within an approximate three millisecond window during which control must be successfully implemented to eliminate unstart.

Despite the relatively high aspect ratio ($AR = 5.4$) of the isolator duct, corner effects are identified as a primary contributor to isolator unstart. As quantified by the viscous confinement parameter, which compares the ratio of viscous to geometric duct areas, a shift from an oblique to normal shock-train is identified, consistent with the qualitative description of the PSCT from the dilatation field. Secondary corner flow is also quantified from streamwise vorticity and velocity streamlines in the context of the literature. This strong corner flow interaction suggests that the side wall may provide a more conservative estimate of the unstart margin relative to typical wall-pressure-based centerline measurements.

To quantify flowfield dynamics, a dynamical-systems-like perspective is employed, which characterize combustor sensitivity to the imposed fuel transient in order to inform control methodology and sensor placement. The Total Variation (TV) metric is adopted as an estimate of the average change in state for a single timestep at each degree of freedom within the domain. The metric captures the dynamics qualitatively described. Primarily, side wall separation is demonstrated to be the dominant (highest variation) feature from the streamwise velocity component. Similarly, PCST dynamics are identified from the vertical velocity component near the isolator entrance. Spanwise gradients are also identified from the heat release TV field.

A second component of the flowfield dynamics quantification comprises application of data-driven methods to filter the high-dimensional simulation dataset and extract the underlying phenomena. Model Order Reduction (MOR) methods provide a data-driven approach for identifying low-dimensional features from high-dimensional data. For this work, the snapshot-based Proper Orthogonal Decomposition (POD) and Dynamic Mode Decomposition (DMD) methods are used to separate the transient dataset into spatial modes (basis functions or features) and time-varying amplitudes. MOR modes, ranked by amplitude, compare well with the qualitative and quantitative description of combustor dynamic features. Considering the streamwise velocity, for example, the spatial gradients in the first several DMD modes contain signatures of the time-mean as well as the upper wall dynamics. The shock-train structure is also isolated from the MOR analysis of the vertical velocity component. Time windowing is employed to isolate the PCST structure at different phases of the fuel-staging transient.

Given the linearity assumption of DMD and the non-linearity of the combustor flowfield, two methods are proposed to estimate the non-linear dynamics. In the first approach, reconstruction error is directly used to infer which regions are most dynamically responsive: *i.e.* least well-approximated by the linear modal bases. However, for the full 3-D flowfield, computing the error becomes intractable when the degree-of-order reduction is not known *a priori*. Therefore, a second method is proposed for DMD, which relies on the first DMD mode and the time-averaged field. The first DMD mode contains the signatures of the time-mean and higher-order dynamics; consequently, the difference between this mode and the time-mean is employed as an approximate metric to identify the principal dynamic regions of the statistically unsteady flowfield. This velocity-difference metric identifies spanwise gradients and agrees with quantitative and qualitative description of the isolator dynamics.

The final component of the MOR-based combustor analysis considers the scaling of reconstruction error with the level of data compression or order-reduction. POD error decreases with increasing modal basis size. In contrast, DMD errors exhibit diminishing returns after including only 10 percent of the total basis size. DMD is also shown to poorly capture non-linearity of the unstart phase dynamics. To address this limitation of the standard DMD, multi-resolution DMD (mrDMD) is employed to provide a time-local MOR decomposition. This hierarchical approach provides better reconstruction quality compared to standard DMD with comparable error levels to snapshot POD, suggesting that mrDMD provides a better reduced-order representation of the higher-order non-linear dynamics. In the context of reduced-order modeling, separate ROMs might be generated within different time windows to resolve short-time combustor dynamics. Alternatively, MOR bases may provide a compressed computational database for efficient design optimization at significantly lower dimensionality than the original computational dataset.

7.2 Outlook and Future Work

The rich physics and separation of scales present in scramjet flowpaths provide multiple opportunities for future research. First, for model-based approaches, such as those employed in this work, additional sensitivities need to be characterized. For fuel-staging transients, one-to-one comparisons of experimental and computational fuel-staging transients are needed. Work involving an axisymmetric scramjet combustor,[135,199] for example, examined various fuel-transients including the impulse, linear ramp, and sinusoidal fuel flow rate variations and might provide a basis to *directly* quantify model uncertainty with the imposed computational fueling timescale. If time-resolved wall-heat-flux measurements are available, model errors for constant and variable Prandtl number heat-flux models would address model uncertainties for heat-flux predictions, which are often significant.[357,358]

An additional area for study concerns atmospheric flow physics. Resurgence[359] of interest in a long-standing[360–363] problem involves inlet sensitivity to "potholes in the sky,"[14] *i.e.* atmospheric turbulence. One potential path for characterizing the flowfield sensitivity to inflow disturbances is the linear stability framework of Mean Flow Perturbation (MFP).[364] This approach, originally proposed[365] for shock/boundary-layer interactions, has been extended to other free-shear[364] and wall-bounded[366,367] flows relevant to scramjet combustors. This method has the benefit of being applicable to RANS-generated base flows. This implicit, linear perturbation method provides an estimate of unsteady scales from the superposition of a base flow and small perturbations. This approach might facilitate a sensitivity study of isolator unstart as a function of the side-slip angle or angle-of-attack in the presence of inflow turbulence. Extension of this technique might be further adapted to chemically reacting flows to examine thermal-acoustic coupling in combustor cavities. Moreover, the combination of DMD with control (DMDc)[368] methods might be used for flow control optimization.

Fine scale isolator dynamics are also critical. However, the computational cost of scale-resolving simulations of the full vehicle configuration is still significant[194,369] even before including multiphysics phenomena such as combustion. Emerging methods such as Wall-Modeled LES (WMLES)[370] may mitigate some of the computational cost associated with near-wall grid resolution requirements. Additionally, efficient methods for inflow turbulence generation techniques[371] will facilitate accurate simulation of the upstream turbulent perturbations. In this vein, a hybrid LES/RANS approach, such as the Dynamic Hybrid RANS/LES (DHRL) methodology,[372,373] might be employed. This method has been successfully leveraged[374] to study shock-train development and unsteadiness in a rectangular cross section for $Ma_e = 2$ flow with fixed back-pressure, and it might be leveraged for analyzing combustor systems at representative Reynolds numbers.

A final, critical, physics-related issue concerns scale separation. While the timescale of the fuel-staging transient considered in this work is longer than the fine-scale turbulence and combustion scales, a question arises as to what happens if the large-scale disturbances are of the same order of magnitude as the fine-scale and coherent unsteadiness within the combustor. Timescales of interest are associated with both the recirculation and separation zones in the cavity resulting from shock-turbulence interactions, for example. Cavity unsteadiness, in the form of Rossiter[66] or thermo-acoustic[163] resonance, are also important. A related question arises when disturbances are introduced for flow control, or from natural fluctuations, at a different phase relative to the fundamental coherent processes. That is, to what degree is isolator unstart margin affected by the phase offset between fundamental coherent processes and combustor disturbances?

Appendix A

Chemical Kinetics Analysis

A.1 Comparison of Adiabatic Flame Temperature

In Ch. 3, solution sensitivity to different reaction mechanisms are examined. Higher heat release magnitudes are anticipated from the simple quasi-global mechanism compared to the more detailed mechanism. As a validation of this behavior, the adiabatic flame temperature is computed for the quasi-global mechanism and compared against the detailed GRI 3.0[375] mechanism using the Cantera 2.4.0 library.[294]

The adiabatic flame temperature is computed for different fuel equivalence ratios ϕ assuming complete combustion for premixed fuel-air constituents at constant pressure. The reference pressure is specified as $p/p_0 = 0.1$ representative of the combustor flowfield at aft-fueled condition. The initial temperature of the reactants is specified from the nozzle exit condition estimated from the isentropic relations ($T \approx 500\ K$). Similar to other kinetics studies of scramjet combustors[8] the simplified mechanism predicts higher adiabatic flame temperature since there are fewer intermediate species. At $\phi = 0.9$, the total equivalence ratio for the present combustor, a 35 degree

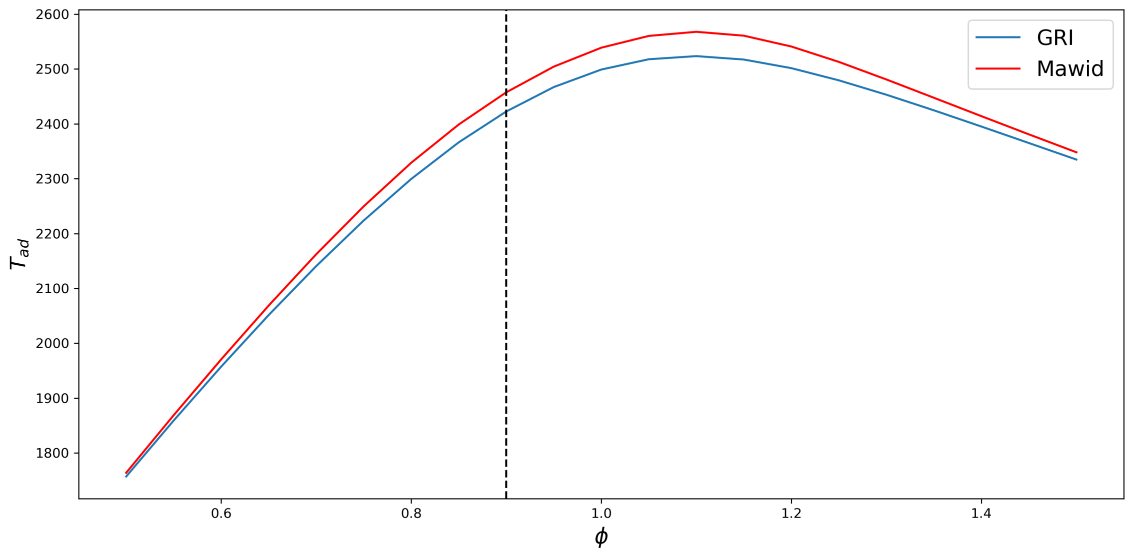

Figure A.1: Comparison of predicted adiabatic flame temperature for Quasi-Global and GRI kinetics mechanisms.

difference is observed between the two mechanisms. This represents an approximately seven percent difference in adiabatic flame temperature.

A.2 Solution of a Freely Propagating Flame

In discussion of turbulent and chemical timescales in Ch 4, estimates of the laminar flame scales are computed. For this purpose, a 1-D model of a freely propagating, laminar, premixed flame is applied to estimate laminar flame speed s_L and flame thickness l_F. Like the adiabatic flame calculation, the Cantera 2.4.0 library[294] is used.

The 1-D flame is a boundary-value problem which assumes constant area, steady-state reaction using 1-D conservation equations for mass, species transport, energy, and the ideal gas state relation, similar to eqns. 3.1-3.4 used in the CFD modeling.

Table A.1: Laminar premixed flame boundary-conditions.

	$z \to -\infty$	$z \to +\infty$
ϕ	0.9	$\frac{\partial Y}{\partial z} = 0$
T	$T_u = 500K$	$\frac{\partial T}{\partial z} = 0$
p	$p_{ref} = 1.66\ atm$	

The laminar GRI kinetics mechanism is used to close system for species production rates $\dot{\omega}_s$. The model further assumes Fourier heat conduction and Fickian diffusion.

The problem domain is sketched in Figure A.2. From the left, unburned gas at initial temperature T_u with fuel (Y_{fuel}) and oxidizer (Y_{ox}) mass fractions are specified. A zero-gradient boundary is assumed for temperature T and species mass fractions Y_i. Assuming a thermal description of the flame, the reaction zone is preceded by the pre-heat zone. Boundary conditions for left (reactants) at $z \to -\infty$ and right (products) $z \to \infty$ boundaries are summarized in Table A.1.

A finite-difference solution is computed on a non-uniform grid using 156 grid points automatically generated to resolve spatial gradients. Grid points are added if: the spacing ratio exceeds 4, the slope (gradient) in values between subsequent points exceeds 0.1 of the global maximum, or the difference in slope between adjacent intervals exceeds 0.1 of the maximum difference. A Newton iteration scheme is used to compute the solution.

The solution provides mass fractions Y_i, temperature T, and heat release $\dot{HR}$ across the flame shown in Figure A.3. The temperature is normalized by the unburned (T_u) and burned (T_b) conditions. The maximum heat release rate is scaled to unity. The mass fractions of the ethylene C_2H_4 and oxygen O_2 reactants, in addition

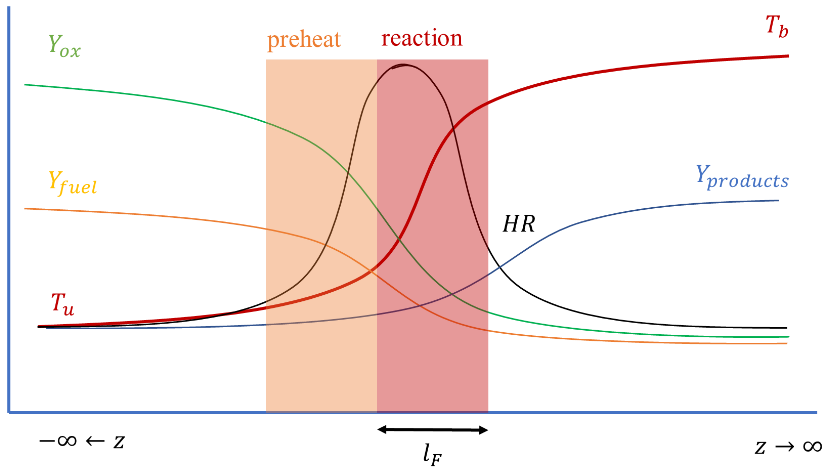

Figure A.2: Schematic of freely propagating laminar premixed flame system.

to water vapor H_2O, are also plotted. From the computation, a laminar flame speed $s_L = 161\ cm/s$ is predicted. From 1-D analytic solutions and curve fits provided by Göttgens,[376] an estimated flame speed of 134 cm/s is computed which is in reasonable agreement with the previous result. The laminar flame thickness is estimated using a simple thermal model[291] from (eqn. A.1) with resulting thickness $l_F = 0.2\ mm$. Finally, the approximate flame timescale is $\tau_F \equiv l_F/s_L \approx 9.7 \times 10^{-5}\ sec$.

$$l_F = \frac{T_b - T_u}{max(|\frac{\partial T}{\partial z}|)} \tag{A.1}$$

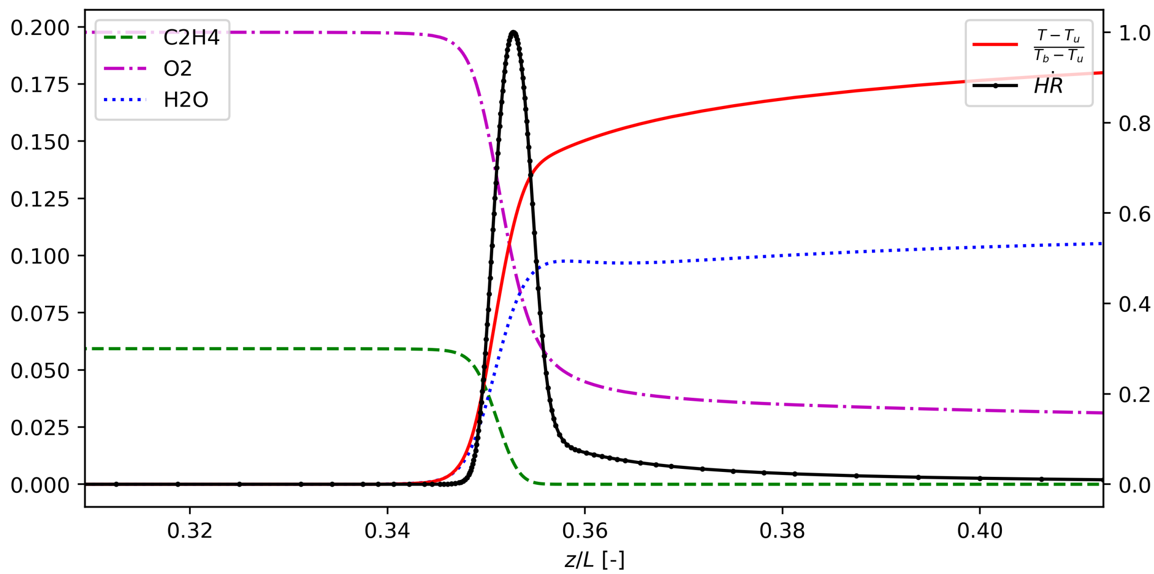

Figure A.3: Computed laminar premixed flame solution: mass fractions of C_2H_4, O_2, and H_2O; non-dimensional temperature $\frac{T-T_u}{T_b-T_u}$; and normalized heat release rate $\dot{HR}$.

Bibliography

[1] "Ohio Supercomputer Center," `http://osc.edu/ark:/19495/f5s1ph73`, 1987.

[2] Tange, O., "GNU Parallel - The Command-Line Power Tool," *;login: The USENIX Magazine*, Vol. 36, No. 1, 2011, pp. 42–47. doi:10.5281/zenodo.1146014.

[3] Python Software Foundation, "The Python Programming Language," , 2017, Accessed: 2017-05-17, `https://www.python.org`.

[4] Pérez, F. and Granger, B. E., "IPython: a System for Interactive Scientific Computing," *Computing in Science and Engineering*, Vol. 9, No. 3, 2007, pp. 21–29. doi:10.1109/MCSE.2007.53.

[5] The NumPy Community, *NumPy Reference*, 1st ed., 2015.

[6] Hunter, J. D., "Matplotlib: A 2D graphics environment," *Computing In Science & Engineering*, Vol. 9, No. 3, 2007, pp. 90–95. doi:10.1109/MCSE.2007.55.

[7] Kennel, M. B., "KDTREE 2: Fortran 95 and C++ software to efficiently search for near neighbors in a multi-dimensional Euclidean space," 2004, *arXiv*, 0408067.

[8] Baurle, R. A. and Eklund, D. R., "Analysis of Dual-Mode Hydrocarbon Scramjet Operation at Mach 4-6.5," *Journal of Propulsion and Power*, Vol. 18, No. 5, 2002, pp. 990–1002. doi:10.2514/2.6047.

[9] Matsuo, K., Miyazato, Y., and Kim, H. D., "Shock Train And Pseudo-shock Phenomena In Internal Gas Flows," *Progress in Aerospace Sciences*, Vol. 35, 1999, pp. 33–100. doi:10.1016/S0376-0421(98)00011-6.

[10] Donbar, J. M., Linn, G. J., Srikant, S., and Akella, M. R., "High-Frequency Pressure Measurements for Unstart Detection in Scramjet Isolators," in "46th AIAA/ASME/SAE/ASEE Joint Propulsion Conference & Exhibit," Nashville, Tennessee, 2010, AIAA Paper 2010-6557, doi:10.2514/6.2010-6557.

[11] Gruber, M. R., Hagenmaier, M. A., and Mathur, T., “Simulating Inlet Distortion Effects in a Direct-Connect Scramjet Combustor,” in “42nd AIAA/ASME/SAE/ASEE Joint Propulsion Conference & Exhibit,” Sacramento, CA, 2006, AIAA Paper 2006-4680, doi:10.2514/6.2006-4680.

[12] Ryan, M., Gruber, M., Carter, C., and Mathur, T., “Planar laser-induced fluorescence imaging of OH in a supersonic combustor fueled with ethylene and methane,” *Proceedings of the Combustion Institute*, Vol. 32, 2009, pp. 2429–2436. doi:10.1016/j.proci.2008.06.209.

[13] Kutz, J. N., Fu, X., and Brunton, S. L., “Multiresolution Dynamic Mode Decomposition,” *SIAM Journal on Applied Dynamical Systems*, Vol. 15, No. 2, 2016, pp. 713–735. doi:10.1137/15M1023543.

[14] Heiser, W. H. and Pratt, D. T., *Hypersonic Airbreathing Propulsion*, American Institute of Aeronautics and Astronautics, 1994.

[15] Buckmaster, J., Jackson, T. L., and Kumar, A., eds., *Combustion in High-Speed Flows (ICASE LaRC Interdisciplinary Series in Science and Engineering)*, Springer Netherlands, 1994, doi:10.1007/978-94-011-1050-1.

[16] Drummond, J. P., Cockrell Jr., C. E., Pellet, G. L., Diskin, G. S., Auslender, A. H., Exton, R. J., Guy, R. W., Hoppe, J. C., Puster, R. L., Rogers, R. C., Trexler, C. A., and Voland, R. T., “Hypersonic Airbreathing Propulsion - An Aerodynamics, Aerothermodynamics, and Acoustics Competency White Paper,” Tech. rep., NASA Langley Research Center, Hampton, Virginia, 2002. NASA TM 2002-211951.

[17] Curran, E. T. and Stull, F. D., “The Utilization of Supersonic Combustion Ramjet Systems at Low Mach Numbers,” Tech. rep., AF Aero Propulsion Laboratory, Wright-Patterson Air Force Base, Ohio, 1964. RTD-TDR-63-4097.

[18] Curran, E. T., Heiser, W. H., and Pratt, D. T., “Fluid Phenomena in Scramjet Combustion Systems,” *Annual Review of Fluid Mechanics*, Vol. 28, 1996, pp. 323–360. doi:10.1146/annurev.fl.28.010196.001543.

[19] Urzay, J., “Supersonic Combustion in Air-Breathing Propulsion Systems for Hypersonic Flight,” *Annual Review of Fluid Mechanics*, Vol. 50, No. 1, 2018, pp. 593–627. doi:10.1146/annurev-fluid-122316-045217.

[20] Smart, M. K., *Scramjet Inlets*, NATO, Brisbane, Aulstralia, chap. 9, p. 24, 2010. NATO RTO-EN-AVT-185.

[21] Ikui, T., Matsuo, K., and Nagai, M., “The Mechanism of Pseudo-Shock Waves,” *Bulletin of the JSME*, Vol. 17, No. 108, 1974, pp. 731–739. doi:10.1299/jsme1958.17.731.

[22] Gnani, F., Zare-Behtash, H., and Kontis, K., "Pseudo-shock waves and their interactions in high-speed intakes," *Progress in Aerospace Sciences*, Vol. 82, 2016, pp. 36–56. doi:10.1016/j.paerosci.2016.02.001.

[23] Mathur, T., Gruber, M., Jackson, K., Donbar, J. M., Donaldson, W., Jackson, T., and Billig, F. S., "Supersonic Combustion Experiments with a Cavity-Based Fuel Injector," *Journal of Propulsion and Power*, Vol. 17, No. 6, 2001, pp. 1305–1312. doi:10.2514/2.5879.

[24] Gruber, M., Baurle, R. A., Mathur, T., and Hsu, K.-Y., "Fundamental Studies of Cavity-Based Flameholder Concepts for Supersonic Combustors," *Journal of Propulsion and Power*, Vol. 17, No. 1, 2001, pp. 146–153. doi:10.254/2.5720.

[25] Ben-Yakar, A. and Hanson, R. K., "Cavity Flame-Holders for Ignition and Flame Stabilization in Scramjets: An Overview," *Journal of Propulsion and Power*, Vol. 17, No. 4, 2001, pp. 869–877. doi:10.2514/2.5818.

[26] Curran, E. T., "Scramjet Engines: The First Forty Years," *Journal of Propulsion and Power*, Vol. 17, No. 6, 2001, pp. 1138–1148. doi:10.2514/2.5875.

[27] Fry, R. S., "A Century of Ramjet Propulsion Technology Evolution," *Journal of Propulsion and Power*, Vol. 20, No. 1, 2004, pp. 27–58. doi:10.2514/1.9178.

[28] Waltrup, P. J., White, M. E., Zarlingo, F., and Gravlin, E. S., "History of Ramjet and Scramjet Propulsion Development for U.S. Navy Missiles," *Johns Hopkins APL Technical Digest*, Vol. 18, No. 2, 1997, pp. 234–243.

[29] Waltrup, P. J., White, M. E., Zarlingo, F., and Gravlin, E. S., "History of U.S. Navy Ramjet, Scramjet, and Mixed-Cycle Propulsion Development," *Journal of Propulsion and Power*, Vol. 18, No. 1, 2002, pp. 14–27. doi:10.2514/2.5928.

[30] Fetterhoff, T., Kraft, E., Laster, M. L., and Cookson, W., "High-Speed/Hypersonic Test and Evaluation Infrastructure Capabilities Study," in "14th AIAA/AHI Space Planes and Hypersonic Systems and Technologies Conference," , 2006, AIAA Paper 2006-8043, doi:10.2514/6.2006-8043.

[31] Gregory, T. J., Petersen, R. H., and Wyss, J. A., "Performance tradeoffs and research problems for hypersonic transports," *Journal of Aircraft*, Vol. 2, No. 4, 1965, pp. 266–271. doi:10.2514/3.43651.

[32] Swithenbank, J., "Hypersonic Air-Breathing Propulsion," *Progress in Aerospace Sciences*, Vol. 8, 1967, pp. 229–294. doi:10.1016/0376-0421(67)90005-X.

[33] Cockrell Jr., C. E., Auslender, A. H., Guy, R. W., McClinton, C. R., and Welch, S. S., "Technology Roadmap for Dual-Mode Scramjet Propulsion to

Support Space-Access Vision Vehicle Development," in "AIAA/AAAF 11th International Space Planes and Hypersonic Systems and Technology," Orleans, France, 2002, AIAA Paper 2002-5188, doi:10.2514/6.2002-5188.

[34] Van Wie, D. M., D'Alessio, S. M., and White, M. E., "Hypersonic Airbreathing Propulsion," *Johns Hopkins APL Technical Digest,*, Vol. 26, No. 4, 2005, pp. 431–437.

[35] Preller, D. and Smart, M. K., "Reusable Launch of Small Satellites Using Scramjets," *Journal of Spacecraft and Rockets*, Vol. 54, No. 6, 2017, pp. 1317–1329. doi:10.2514/1.A33610.

[36] Ferri, A. and Nucci, L. M., "Theoretical and Experimental Analysis of Low-Drag Supersonic Inlets Having a Circular Cross Section and a Central Body at Mach Numbers of 3.30, 2.75, and 2.45," Tech. rep., Langley Aeronautical Laboratory, 1948. NACA RM-L8H13.

[37] Ferri, A. and Nucci, L. M., "The Origin of Aerodynamic Instability of Supersonic Inlets at Subcritical Conditions," Tech. rep., Langley Aeronautical Laboratory, 1951. NACA TM-L50K30.

[38] Ferri, A. and Nucci, L. M., "Preliminary Investigation of a New Type of Supersonic Inlet," Tech. rep., Langley Aeronautical Laboratory, 1952. NACA Report 1104.

[39] Ferri, A., "Mixing-Controlled Supersonic Combustion," *Annual Review of Fluid Mechanics*, Vol. 5, 1973, pp. 301–338. doi:10.1146/annurev.fl.05.010173.001505.

[40] Erdos, J. I. and Nucci, L. M., "Pioneering Scramjet Developments by Antonio Ferri," in "NASA. Lewis Research Center, Rocket-Based Combined-Cycle (RBCC) Propulsion Technology Workshop," , 1992, N92-21519.

[41] Billig, F. S., "Combustion Processes in Supersonic Flow," *Journal of Propulsion and Power*, Vol. 4, No. 3, 1988, pp. 209–216. doi:10.2514/3.23050.

[42] Billig, F. S., "Research on Supersonic Combustion," *Journal of Propulsion and Power*, Vol. 9, No. 4, 1993, pp. 499–514. doi:10.2514/3.23652. Dryden Lectureship on Research.

[43] Freeman Jr., D. C., Reubush, D. E., McClinton, C. R., Rausch, V. L., and Crawford, J. L., "The NASA Hyper-X Program," Tech. rep., NASA, 1997. NASA/TM-1997-207243.

[44] McClinton, C. R., Rausch, V. L., Nguyen, L. T., and Sitz, J. R., "Preliminary X-43 Flight Test Results," *Acta Astronautica*, Vol. 57, No. 2-8, 2005, pp. 266–276. doi:10.1016/j.actaastro.2005.03.060.

[45] McClinton, C. R., "X-43–Scramjet Power Breaks the Hypersonic Barrier Dryden Lectureship in Research for 2006," in "44th AIAA Aerospace Sciences Meeting and Exhibit," Reno, NV, 2006, AIAA Paper 2006-0001, doi:10.2514/6.2006-1.

[46] Smart, M. K., Hass, N. E., and Paull, A., "Flight Data Analysis of the HyShot 2 Scramjet Flight Experiment," *AIAA Journal*, Vol. 44, No. 10, 2006, pp. 2366–2375. doi:10.2514/1.20661.

[47] Jackson, K. R., Gruber, M. R., and Buccellato, S., "Mach 6-8+ Hydrocarbon-Fueled Scramjet Flight Experiment: The HIFiRE Flight 2 Project," *Journal of Propulsion and Power*, Vol. 31, No. 1, 2015, pp. 36–53. doi:10.2514/1.B35350.

[48] Hank, J. M., "Air Force Research Laboratory Hypersonic Propulsion Research Programs," in "43rd AIAA/ASME/SAE/ASEE Joint Propulsion Conference & Exhibit," Cincinnait, Ohio, 2007, AIAA Paper 2007-5371, doi:10.2514/6.2007-5371.

[49] Hank, J. M., Murphy, J. S., and Mutzman, R. C., "The X-51A Scramjet Engine Flight Demonstration Program," in "15th AIAA International Space Planes and Hypersonic Systems and Technologies Conference," Dayton, OH, 2008, AIAA Paper 2008-2540, doi:10.2514/6.2008-2540.

[50] Norris, G., "X-51A Waverider Achieves Goal On Final Flight," , Aviation Week Network, 2013, Accessed: 2014-12-01, `http://aviationweek.com/defense/x-51a-waverider-achieves-goal-final-flight`.

[51] Rondeau, C. M. and Jorris, T. R., "X-51A Scramjet Demonstrator Program: Waverider Ground and Flight Test," in "SFTE 44th International / SETP Southwest Flight Test Symposium," Ft Worth, Texas, 2013.

[52] Townend, L. H., "Domain of the Scramjet," *Journal of Propulsion and Power*, Vol. 17, No. 6, 2001, pp. 1205–1213. doi:10.2514/2.5865.

[53] Colville, J. R., Starkey, R. P., and Lewis, M. J., "Axisymmetric Inlet Design for Combined-Cycle Engines," *Journal of Propulsion and Power*, Vol. 22, No. 5, 2006, pp. 1049–1058. doi:10.2514/1.18063.

[54] Hellman, B. M., Bradford, J., St. Germain, B., Feld, K., and Schaffer, M., "Two Stage to Orbit Conceptual Vehicle Designs using the SABRE Engine," in "AIAA SPACE Forum," Long Beach, California, 2016, AIAA Paper 2016-5320, doi:10.2514/6.2016-5320.

[55] Mehta, U., Aftosmis, M., Bowles, J., and Pandya, S., "Skylon Aerospace Plane and Its Aerodynamics and Plumes," *Journal of Spacecraft and Rockets*, Vol. 53, No. 2, 2016, pp. 340–353. doi:10.2514/1.A33408.

[56] Norris, G., "Skunk Works Reveals SR-71 Successor Plan," , 2013, Accessed: 2018-02-09, http://aviationweek.com/technology/skunk-works-reveals-sr-71-successor-plan.

[57] Norris, G., "Boeing's Hyper Hope," Aviation Week & Space Technology, 2018. pp. 20-22.

[58] Muylaert, J., "Technologies for Propelled Hypersonic Flight," Tech. rep., NATO Resarch and Technology Organization, 2006. TR-AVT-007-V2.

[59] Bertin, J. J. and Cummings, R. M., "CRITICAL HYPERSONIC AEROTHERMODYNAMIC PHENOMENA," *Annual Review of Fluid Mechanics*, Vol. 38, No. 1, 2006, pp. 129–157. doi:10.1146/annurev.fluid.38.050304.092041.

[60] Sziroczak, D. and Smith, H., "A review of design issues specific to hypersonic flight vehicles," *Progress in Aerospace Sciences*, Vol. 84, 2016, pp. 1–28. doi:10.1016/j.paerosci.2016.04.001.

[61] Van Wie, D. M., Drewry Jr., D. G., King, D. E., and Hudson, C. M., "The hypersonic environment: Required operating conditions and design challenges," *Journal of Materials Science*, Vol. 39, 2004, pp. 5915–5924. doi:10.1023/B:JMSC.0000041688.68135.8b.

[62] Borg, M. P., *Laminar Instability and Transition on the X-51A*, Ph.D. thesis, Purdue University, West Lafayette, Indiana, 2009.

[63] Gaitonde, D. V., "Progress in shockwave/boundary layer interactions," *Progress in Aerospace Sciences*, Vol. 72, 2015, pp. 80–99. doi:10.1016/j.paerosci.2014.09.002.

[64] Dolling, D. S., "Fifty Years of Shock-Wave/Boundary-Layer Interaction Research: What Next?" *AIAA Journal*, Vol. 39, No. 8, 2001, pp. 1517–1531. doi:10.2514/2.1476.

[65] Clemens, N. T. and Narayanaswamy, V., "Low-Frequency Unsteadiness of Shock Wave/Turbulent Boundary Layer Interactions," *Annual Review of Fluid Mechanics*, Vol. 46, 2014, pp. 469–92. doi:10.1146/annurev-fluid-010313-141346.

[66] Ünalmis, O. H., Clemens, N. T., and Dolling, D. S., "Cavity Oscillation Mechanisms in High-Speed Flows," *AIAA Journal*, Vol. 42, No. 10, 2004, pp. 2035–2041. doi:10.2514/1.1000.

[67] Cousteix, J., Arnal, D., Aupoix, B., Brazier, J. P., and Lafon, A., "Shock Layers and Boundary Layers in Hypersonic Flows," *Progress in Aerospace Sciences*, Vol. 30, 1994, pp. 95–212. doi:10.1016/0376-0421(94)90006-X.

[68] Anderson, J. D., *Hypersonic and High-Temperature Gas Dynamics*, AIAA Educational Series, American Institute of Aeronautics and Astronautics, Inc., 1801 Alexander Bell Drive, Reston, Virginia 20191-4344, 2nd ed., 2006.

[69] Li, J., Ma, F., Yang, V., Lin, K.-C., and Jackson, T. A., "Control and Optimization of Ignition Transient in Scramjet Engine Using Air Throttling," in "44th AIAA Aerospace Sciences Meeting and Exhibit," Reno, NV, 2006, AIAA Paper 2006-1028, doi:10.2514/6.2006-1028.

[70] Li, J., Ma, F., Yang, V., Lin, K. C., and Jackson, T. A., "A Comprehensive Study of Ignition Transient in an Ethylene-Fueled Scramjet Combustor," in "43rd AIAA/ASME/SAE/ASEE Joint Propulsion Conference & Exhibit," Cincinnati, Ohio, 2007, AIAA Paper 2007-5025, doi:10.2514/6.2007-5025.

[71] Li, X., Liu, W., Pan, Y., Yang, L., An, B., and Zhu, J., "Characterization of ignition transient processes in kerosene-fueled model scramjet engine by dual-pulse laser-induced plasma," *Acta Astronautica*, Vol. 144, 2018, pp. 23–29. doi:10.1016/j.actaastro.2017.12.018.

[72] Shimura, T., Mitani, T., Sakuranka, N., and Izumikawa, M., "Load Oscillations Caused by Unstart of Hypersonic Wind Tunnels and Engines," *Journal of Propulsion and Power*, Vol. 14, No. 3, 1998, pp. 348–353. doi:10.2514/2.5287.

[73] Sajben, M., Bogar, T. J., and Kroutil, J. C., "Forced Oscillation Experiments in Supercritical Diffuser Flows," *AIAA Journal*, Vol. 22, No. 4, 1984, pp. 465–474. doi:10.2514/3.8423.

[74] Bogar, T. J., Sajben, M., and Kroutil, J. C., "Response of a Supersonic Inlet to Downstream Perturbation," *Journal of Propulsion and Power*, Vol. 1, No. 2, 1985, pp. 118–125. doi:10.2514/3.22768.

[75] Pham, H. S., Myokan, M., Tamba, T., Iwakawa, A., and Sasoh, A., "Effects of Repetitive Laser Energy Deposition on Supersonic Duct Flows," *AIAA Journal*, Vol. 56, No. 2, 2017, pp. 542–553. doi:10.2514/1.J056190.

[76] 95th Air Base Wing Public Affairs, "Second Hypersonic Flight Ends Prematurely, Brings New Flight Test Data," , Air Force Print News Today, 2011, Accessed: 2015-02-16, `http://www.afmc.af.mil/news/story_print.asp?id=123260080`.

[77] Hutzel, J. R., *Scramjet Isolator Modeling and Control*, Ph.D. thesis, Air Force Institute of Technology, Wright-Patterson Air Force Base, Ohio, 2011.

[78] Vanstone, L., Hashemi, K. E., Lingren, J., Akella, M. R., Clemens, N. T., Donbar, J., and Gogineni, S., "Closed-Loop Control of Shock-Train Location

in a Combusting Scramjet," *Journal of Propulsion and Power*, Vol. 34, No. 3, 2018, pp. 660–667. doi:10.2514/1.B36743. Article in Advance.

[79] Im, S.-K. and Do, H., "Unstart phenomena induced by flow choking in scramjet inlet-isolators," *Progress in Aerospace Sciences*, Vol. 97, 2018, pp. 1–21. doi:10.1016/j.paerosci.2017.12.001.

[80] Kantrowitz, A. and Donaldson, C. d. P., "Preliminary Investigation of Supersonic Diffusers," Tech. rep., Langley Memorial Aeronautical Laboratory, Langley Field, Virginia, 1945. NACA ACR L5D20.

[81] Waltrup, P. J. and Billig, F. S., "Prediction of Precombustion Wall Pressure Distributions in Scramjet Engines," *Journal of Spacecraft and Rockets*, Vol. 10, No. 9, 1973, pp. 620–622. doi:10.2514/3.27782.

[82] Smart, M. K., "Flow Modeling of Pseudoshocks in Backpressured Ducts," *AIAA Journal*, Vol. 53, No. 12, 2015, pp. 3577–3588. doi:10.2514/1.J054021.

[83] Sullins, G. A. and Waltrup, P. J., "A Comparison of Scramjet Integral Analysis Techniques," *Journal of Propulsion and Power*, Vol. 1, No. 2, 1985, pp. 156–158. doi:10.2514/3.22774.

[84] Pratt, D. T. and Heiser, W. H., "Isolator-Combustor Interaction in a Dual-Mode Scramjet Engine," in "31st Aerospace Sciences Meeting and Exhibit," Reno, Nevada, 1993, AIAA Paper 1993-0358, doi:10.2514/6.1993-0358.

[85] Fiévet, R., Raman, V., and Auslender, A. H., "Data-Driven One-Dimensional Modeling of Pseudoshocks," *Journal of Propulsion and Power*, Vol. 35, No. 2, 2019, pp. 313–327. doi:10.2514/1.B37175.

[86] Xiong, B., qiang Fan, X., guo Wang, Z., and Tao, Y., "Analysis and modelling of unsteady shock train motions," *Journal of Fluid Mechanics*, Vol. 846, 2018, pp. 240–262. doi:10.1017/jfm.2018.209.

[87] Veillard, X., Tahir, R., Timofeev, E., and Molder, S., "Limiting Contractions for Starting Simple Ramp Scramjet Intake with Overboard Spillage," *Journal of Propulsion and Power*, Vol. 24, No. 5, 2008, pp. 1042–1049. doi:10.2514/1.34547.

[88] Dalle, D. J., Driscoll, J. F., and Torrez, S. M., "Ascent Trajectories of Hypersonic Aircraft: Operability Limits Due to Engine Unstart," *Journal of Aircraft*, Vol. 52, No. 4, 2015, pp. 1345–1354. doi:10.2514/1.C032801.

[89] Sullins, G. A. and McLafferty, G., "Experimental Results of Shock Trains in Rectangular Ducts," in "AIAA Fourth International Aerospace Planes Conference," Orlando, FL, 1992, AIAA Paper 1992-5103, doi:10.2514/6.1992-5103.

[90] Sullins, G. A., "Demonstration of Mode Transition in a Scramjet Combustor," *Journal of Propulsion and Power*, Vol. 9, No. 4, 1993, pp. 515–520. doi:10.2514/3.23653.

[91] Bachchan, N. and Hillier, R., "Effects of Hypersonic Inlet Flow Non-Uniformities on Stabilising Isolator Shock Systems," in "AIAA Atmospheric Flight Mechanics Conference and Exhibit," Providence, Rhode Island, 2004, AIAA Paper 2004-4716, doi:10.2514/6.2004-4716.

[92] Hoeger, T. C., King, P. I., Donbar, J. M., and Cox-Stouffer, S., "2-D Transient CFD Model of an Isolator Shock Train," in "17th AIAA International Space Planes and Hypersonic Systems and Technologies Conference," San Francisco, California, 2011, AIAA Paper 2011-2221, doi:10.2514/6.2011-2221.

[93] Hoeger, T. C., *CFD Transient Simulation of an Isolator Shock Train in a Scramjet Engine*, Ph.D. thesis, Air Force Institute of Technology, Wright-Patterson Air Force Base, Ohio, 2012.

[94] Fotia, M. L. and Driscoll, J. F., "Isolator-Combustor Interactions in a Direct-Connect Ramjet-Scramjet Experiment," *Journal of Propulsion and Power*, Vol. 28, No. 1, 2012, pp. 83–95. doi:10.2514/1.B34367.

[95] Aguilera, C., Ghosh, A., Shin, K.-H., and Yu, K. H., "Dynamic Pressure Characterization of a Dual-Mode Scramjet," in "26th International Colloquium on the Dynamics of Explosions and Reactive Systems (ICDERS)," , 2017.

[96] Culick, F. E. C. and Rogers, T., "The Response of Normal Shocks in Diffusers," *AIAA Journal*, Vol. 21, No. 10, 1983, pp. 1382–1390. doi:10.2514/3.60147.

[97] Bruce, P. J. K. and Babinsky, H., "Unsteady shock wave dynamics," *Journal of Fluid Mechanics*, Vol. 603, 2008, pp. 463–473. doi:10.1017/S0022112008001195.

[98] Carroll, B. F. and Dutton, J. C., "Characteristics of Multiple Shock Wave/Turbulent Boundary-Layer Interactions in Rectangular Ducts," *Journal of Propulsion and Power*, Vol. 6, No. 2, 1990, pp. 186–193. doi:10.2514/3.23243.

[99] Carroll, B. F. and Dutton, J. C., "Multiple Normal Shock Wave/Turbulent Boundary-Layer Interactions," *Journal of Propulsion and Power*, Vol. 8, No. 2, 1992, pp. 441–448. doi:10.2514/3.23497.

[100] Carroll, B. F. and Dutton, J. C., "Turbulence Phenomena in a Multiple Normal Shock Wave/Turbulent Boundary-Layer Interaction," *AIAA Journal*, Vol. 30, No. 1, 1992, pp. 43–48. doi:10.2514/3.10880.

[101] Morgan, B., Duraisamy, K., and Lele, S. K., "Large-Eddy and RANS Simulations of a Normal Shock Train in a Constant-Area Isolator," in "50th AIAA Aerospace Sciences Meeting including the New Horizons Forum and Aerospace Exposition," , 2012, AIAA Paper 2012-1094, doi:10.2514/6.2012-1094.

[102] Sugiyama, H., Tsujiguchi, Y., and Honma, T., "Structure and Oscillation Phenomena of Pseudo-Shock Waves in a Straight Square Duct at Mach 2 and 4," in "15th AIAA International Space Planes and Hypersonic Systems and Technologies Conference," Dayton, Ohio, 2008, AIAA Paper 2008-2646, doi:10.2514/6.2008-2646.

[103] Klomparens, R. L., Driscoll, J. F., and Gamba, M., "Boundary layer separation in a 3D shock train," in "53rd AIAA Aerospace Sciences Meeting," Kissimmee, Florida, 2015, AIAA Paper 2015-1519, doi:10.2514/6.2015-1519.

[104] Klomparens, R. L., Driscoll, J. F., and Gamba, M., "Response of a shock train to downstream back pressure forcing," in "54th AIAA Aerospace Sciences Meeting," San Diego, California, 2016, AIAA Paper 2016-0078, doi:10.2514/6.2016-0078.

[105] Merkli, P. E., "Pressure Recovery in Rectangular Constant Area Supersonic Diffusers," *AIAA Journal*, Vol. 14, 1976, pp. 168–172. doi:10.2514/3.61352.

[106] Hunt, R. L., Driscoll, J. F., and Gamba, M., "Unsteadiness characteristics and three-dimensional leading shock structure of a Mach 2.0 shock train," in "55th AIAA Aerospace Sciences Meeting," Grapevine, Texas, 2017, AIAA Paper 2017-0087, doi:10.2514/6.2017-0087.

[107] Hunt, R. L., Driscoll, J. F., and Gamba, M., "Periodic forcing of a shock train in Mach 2.0 flow," in "55th AIAA Aerospace Sciences Meeting," Grapevine, Texas, 2017, AIAA Paper 2017-0088, doi:10.2514/6.2017-0088.

[108] Hunt, R. L. and Gamba, M., "Shock Train Unsteadiness Characteristics, Oblique-to-Normal Transition, and Three-Dimensional Leading Shock Structure," *AIAA Journal*, Vol. 56, No. 4, 2017, pp. 1569–1587. doi:10.2514/1.J056344.

[109] Hunt, R. L., *Shock Train Structure and Dynamics*, Ph.D. thesis, University of Michigan, 2018.

[110] Lindstrom, C. D., Jackson, K. R., Williams, S., Givens, R., Bailey, W. F., Tam, C.-J., and Terry, W. F., "Shock-Train Structure Resolved with Absorption Spectroscopy Part I: System Design and Validation," *AIAA Journal*, Vol. 47, No. 10, 2009, pp. 2368–2378. doi:10.2514/1.41074.

[111] Lindstrom, C., Davis, D. L., Williams, S., and Tam, C.-J., "Shock-Train Structure Resolved with Absorption Spectroscopy Part 2: Analysis and CFD Comparison," *AIAA Journal*, Vol. 47, No. 10, 2009, pp. 2379–2390. doi:10.2514/1.41077.

[112] Xiong, B., Wang, Z.-G., Fan, X.-Q., and Wang, Y., "Response of Shock Train to High-Frequency Fluctuating Backpressure in an Isolator," *Journal of Propulsion and Power*, Vol. 33, No. 6, 2017, pp. 1520–1528. doi:10.2514/1.B36291.

[113] Hsieh, T., Wardlaw Jr., A. B., Collins, P., and Coakley, T. J., "Numerical Investigation of Unsteady Inlet Flowfields," *AIAA Journal*, Vol. 25, No. 1, 1987, pp. 75–81. doi:10.2514/3.9584.

[114] Su, W.-Y. and Chen, Y., "Effects of Dynamic Backpressure on Pseudoshock Oscillations in Scramjet Inlet-Isolator," *Journal of Propulsion and Power*, Vol. 32, No. 2, 2016, pp. 516–528. doi:10.2514/1.B35898.

[115] Oh, J. Y., Ma, F., Hsieh, S.-Y., and Yang, V., "Interactions Between Shock and Acoustic Waves in a Supersonic Inlet Diffuser," *Journal of Propulsion and Power*, Vol. 21, No. 3, 2005, pp. 486–495. doi:10.2514/1.9671.

[116] Wieting, A. R., "Exploratory Study of Transient Unstart Phenomena in a Three-Dimensional Fixed-Geometry Scramjet Engine," Tech. rep., Langley Research Center, Hampton, Virginia, 1976. NASA TN D-8156.

[117] Sato, T. and Kaji, S., "Study on Steady and Unsteady Unstart Phenomena Due to Compound Choking and/or Fluctuations in Combustor of Scramjet Engines," in "AIAA Fourth International Aerospace Planes Conference," Orlando, Florida, 1992, AIAA Paper 1992-5102, doi:10.2514/6.1992-5102.

[118] Sajben, M., Donovan, J. F., and Morris, M. J., "Experimental Investigation of Terminal Shock Sensors for Mixed-Compression Inlets," *Journal of Propulsion and Power*, Vol. 8, No. 1, 1992, pp. 168–174. doi:10.2514/3.23457.

[119] Rodi, P. E., Emami, S., and Trexler, C. A., "Unsteady Pressure Behavior in a Ramjet/Scramjet Inlet," *Journal of Propulsion and Power*, Vol. 12, No. 3, 1996, pp. 486–493. doi:10.2514/3.24061.

[120] Emami, S., Trexler, C. A., Auslender, A. H., and Weidner, J. P., "Experimental Investigation of Inlet-Combustor Isolators for a Dual-Mode Scramjet at a Mach Number of 4," Tech. rep., Langley Research Center, Hampton, Virginia, 1995. NASA TP-3502.

[121] Neaves, M. D., McRae, D. S., and Edwards, J. R., "High-Speed Inlet Unstart Calculations Using an Implicit Solution Adaptive Mesh Algorithm," in "39th

AIAA Aerospace Sciences Meeting and Exhibit," Reno, Nevada, 2001, AIAA Paper 2001-825, doi:10.2514/6.2001-825.

[122] Deng, R., Jin, Y., and Kim, H. D., "Numerical simulation of the unstart process of dual-mode scramjet," *International Journal of Heat and Mass Transfer*, Vol. 105, 2016, pp. 394–400. doi:10.1016/j.ijheatmasstransfer.2016.10.004.

[123] Benson, R. A. and McRae, D. S., "Numerical Simulations of the Unstart Phenomena in a Supersonic Inlet/Diffuser," in "AIAA/SAE/ASME/ASEE 29th Joint Propulsion Conference and Exhibit," Monterey, California, 1993, AIAA Paper 1993-2239, doi:10.2514/6.1993-2239.

[124] Hutzel, J. R., Decker, D. D., Cobb, R. G., King, P. I., Veth, M. J., and Donbar, J. M., "Scramjet Isolator Shock Train Location Techniques," in "49th AIAA Aerospace Sciences Meeting including the New Horizons Forum and Aerospace Exposition," Orlando, FL, 2011, AIAA Paper 2011-402, doi:10.2514/6.2011-402.

[125] Tan, H.-J., Li, L.-G., Wen, Y.-F., and Zhang, Q.-F., "Experimental Investigation of the Unstart Process of a Generic Hypersonic Inlet," *AIAA Journal*, Vol. 49, No. 2, 2011, pp. 279–288. doi:10.2514/1.J050200.

[126] Zhang, Q. F., Tan, H. J., Sun, S., Bu, X., and Rao, Y., "Unstart of a Hypersonic Inlet with Side Compression Caused by Downstream Choking," *AIAA Journal*, Vol. 54, No. 1, 2016, pp. 28–38. doi:10.2514/1.J054095.

[127] Wagner, J. L., *Experimental Studies of Unstart Dynamics in Inlet / Isolator Configurations in a Mach 5 Flow*, Ph.D. thesis, The University of Texas at Austin, 2009.

[128] Wagner, J. L., Yuceil, K. B., Valdivia, A., Clemens, N. T., and Dolling, D. S., "Experimental Investigation of Unstart in an Inlet/Isolator Model in Mach 5 Flow," *AIAA Journal*, Vol. 47, No. 6, 2009, pp. 1528–1542. doi:10.2514/1.40966.

[129] Wagner, J. L., Yuceil, K. B., and Clemens, N. T., "Velocimetry Measurements of Unstart in an Inlet-Isolator Model in Mach 5 Flow," *AIAA Journal*, Vol. 48, No. 9, 2010, pp. 1875–1888. doi:10.2514/1.J050037.

[130] Lin, P., Rao, G. V. R., and O'Connor, G. M., "Numerical Analysis of Normal Shock Train in a Constant Area Isolator," in "27th AIAA/SAE/ASME/ASEE Joint Propulsion Conference," Sacramento, California, 1991, AIAA Paper 1991-2162, doi:10.2514/6.1991-2162.

[131] Lin, P., Rao, G. V. R., and O'Connor, G. M., "Numerical Investigation on Shock Wave/Boundary-Layer Interactions in a Constant Area Diffuser at Mach

3," in "AIAA 22nd Fluid Dynamics, Plasma Dynamics & Lasers Conference," Honolulu, Hawaii, 1991, AIAA Paper 1991-1766, doi:10.2514/6.1991-1766.

[132] Do, H., Im, S., Mungal, M. G., and Cappelli, M. A., "Unstart of a Supersonic Model Inlet/Isolator Flow Induced by Mass Injection," in "49th AIAA Aerospace Sciences Meeting including the New Horizons Forum and Aerospace Exposition," Orlando, Florida, 2011, AIAA Paper 2011-0068, doi:10.2514/6.2011-68.

[133] Do, H., Im, S., Mungal, M. G., and Cappelli, M. A., "The Influence of Boundary Layers on Supersonic Inlet Unstart," in "17th AIAA International Space Planes and Hypersonic Systems and Technologies Conference," San Francisco, California, 2011, AIAA Paper 2011-2349, doi:10.2514/6.2011-2349.

[134] Fiévet, R., Koo, H., Raman, V., and Auslender, A. H., "Numerical Investigation of Shock-Train Response to Inflow Boundary-Layer Variations," *AIAA Journal*, Vol. 55, No. 9, 2017, pp. 2888–2901. doi:10.2514/1.J055333.

[135] Smith, S., Gruber, M., Steiner, R., Collatz, M., and Mathur, T., "Development and Calibration of an Axisymmetric Direct-Connect Supersonic Combustion Flowpath," in "45th AIAA/ASME/SAE/ASEE Joint Propulsion Conference & Exhibit," Denver, Colorado, 2009, AIAA Paper 2009-5035, doi:10.2514/6.2009-5035.

[136] Lin, K.-C., Tam, C.-J., Jackson, K. R., Eklund, D. R., and Jackson, T. A., "Characterization of Shock Train Structures inside Constant-Area Isolators of Model Scramjet Combustors," in "44th AIAA Aerospace Sciences Meeting and Exhibit," Reno, Nevada, 2006, AIAA Paper 2006-816, doi:10.2514/6.2006-816.

[137] Babinsky, H., Oorebeek, J., and Cottingham, T., "Corner effects in reflecting oblique shock-wave/boundary-layer interactions," in "51st AIAA Aerospace Sciences Meeting including the New Horizons Forum and Aerospace Exposition," Grapevine (Dallas/Ft. Worth Region), Texas, 2013, AIAA Paper 2013-0859, doi:10.2514/6.2013-859.

[138] Xiang, X., *Corner effects for oblique shock wave/turbulent boundary layer interactions in rectangular channels*, Ph.D. thesis, University of Cambridge, 2018.

[139] Morajkar, R. R., Klomparens, R. L., E., E. W., Driscoll, J. F., and Gamba, M., "Flow Separation Associated with 3-D Shock-Boundary Layer Interaction (SBLI)," in "AIAA SciTech 52nd Aerospace Sciences Meeting," National Harbor, Maryland, 2014, AIAA Paper 2014-1138, doi:10.2514/6.2014-1138.

[140] Morajkar, R. R. and Gamba, M., "Swept shock/corner flow interactions," in "54th AIAA Aerospace Sciences Meeting," San Diego, California, 2016, AIAA Paper 2016-1165, doi:10.2514/6.2016-1165.

[141] Morajkar, R. R. and Gamba, M., "Turbulence characteristics of supersonic corner flows in a low aspect ratio rectangular channel," in "54th AIAA Aerospace Sciences Meeting," San Diego, California, 2016, AIAA Paper 2016-1590, doi:10.2514/6.2016-1590.

[142] Funderburk, M. and Narayanaswamy, V., "Experimental investigation of primary and corner shock boundary layer interactions at mild back pressure ratios," *Physics of Fluids*, Vol. 28, No. 8, 2016, p. 086102. doi:10.1063/1.4960963.

[143] Cox-Stouffer, S. K. and Hagenmaier, M. A., "The Effect of Aspect Ratio On Isolator Performance," in "39th AIAA Aerospace Sciences Meeting & Exhibit," Reno, Nevada, 2001, AIAA Paper 2001-519, doi:10.2514/6.2001-519.

[144] Grendell, K. M., "A Comparison Study of Rectangular and Chamfered Isolator Cross-Section Shape with Varied Divergence," in "42nd AIAA Aerospace Sciences Meeting and Exhibit," Reno, Nevada, 2004, AIAA Paper 2004-129, doi:10.2514/6.2004-129.

[145] Geerts, J. S. and Yu, K. H., "Shock Train/Boundary-Layer Interaction in Rectangular Isolators," *AIAA Journal*, Vol. 54, No. 11, 2016, pp. 3450–3464. doi:10.2514/1.J054917.

[146] Pizzella, M., Warning, S., Jennerjohn, M., McQuilling, M., Purkey, A., Scharnhorst, R., and Mani, M., "Shock-Wave/Boundary-Layer Interaction in a Large-Aspect-Ratio Test Section," *AIAA Journal*, Vol. 55, No. 9, 2017, pp. 2919–2928. doi:10.2514/1.J055592.

[147] Gaitonde, D. V., Visbal, M. R., Shang, J. S., Zheltovodov, A. A., and Maksimov, A. I., "Sidewall Interaction in an Asymmetric Simulated Scramjet Inlet Configuration," *Journal of Propulsion and Power*, Vol. 17, No. 3, 2001, pp. 579–584. doi:10.2514/2.5780.

[148] Hohn, O. M. and Gülhan, A., "Experimental Investigation of Sidewall Compression and Internal Contraction in a Scramjet Inlet," *Journal of Propulsion and Power*, Vol. 33, No. 2, 2016, pp. 501–513. doi:10.2514/1.B36054.

[149] Stephen, E. J., Hoenisch, S. R., Riggs, C. J., Waddel, M. L., McLaughlin, T., and Bolender, M. A., "HIFiRE 6 Unstart Conditions at Off-Design Mach Numbers," in "53rd AIAA Aerospace Sciences Meeting," Kissimmee, Florida, 2015, AIAA Paper 2015-0109, doi:10.2514/6.2015-0109.

[150] Bolender, M. A., Staines, J. T., and Dolvin, D. J., "HIFiRE 6: An Adaptive Flight Control Experiment," in "50th AIAA Aerospace Sciences Meeting including the New Horizons Forum and Aerospace Exposition," Nashville, Tennessee, 2012, AIAA Paper 2012-0252, doi:10.2514/6.2012-0252.

[151] Le, D. B., Goyne, C. P., Krauss, R. H., and McDaniel, J. C., "Experimental Study of a Dual-Mode Scramjet Isolator," *Journal of Propulsion and Power*, Vol. 24, No. 5, 2008, pp. 1050–1057. doi:10.2514/1.32591.

[152] Ridings, A. N. and Smart, M. K., "Flow Establishment of Precombustion Shock Trains in a Shock Tunnel," *AIAA Journal*, Vol. 55, No. 9, 2017, pp. 2902–2911. doi:10.2514/1.J055590.

[153] Parrott, T. L., Jones, M. G., and Thurlow, E. M., "Unsteady Pressure Loads in a Generic High-Speed Engine Model," Tech. rep., NASA Langley Research Center, 1992. NASA Technical Paper 3189.

[154] McDaniel, K. S. and Edwards, J. R., "Simulation of Thermal Choking in a Model Scramjet Combustor," in "30th AIAA Fluid Dynamics Conference," Norfolk, Virginia, 1999, AIAA Paper 1999-3411, doi:10.2514/6.1999-3411.

[155] McDaniel, K. S. and Edwards, J. R., "Three-Dimensional Simulation of Thermal Choking in a Model Scramjet Combustor," in "39th AIAA Aerospace Sciences Meeting & Exhibit," Reno, NV, 2001, AIAA Paper 2001-0382, doi:10.2514/6.2001-382.

[156] Lin, K.-C., Tam, C.-J., Eklund, D. R., Jackson, K. R., and Jackson, T. A., "Effects of Temperature and Heat Transfer on Shock Train Structures inside Constant-Area Isolators," in "44th AIAA Aerospace Sciences Meeting and Exhibit," , 2006, AIAA Paper 2006-0817, doi:10.2514/6.2006-0817.

[157] Fischer, C. and Olivier, H., "Experimental Investigation of Wall and Total Temperature Influence on a Shock Train," *AIAA Journal*, Vol. 52, No. 4, 2014, pp. 757–766. doi:10.2514/1.J052599.

[158] Yoon, Y., Donbar, J. M., Huh, H., and Driscoll, J. F., "Measured Supersonic Flame Properties: Heat-Release Patterns, Pressure Losses, Thermal Choking Limits," *Journal of Propulsion and Power*, Vol. 12, No. 4, 1996, pp. 718–723. doi:10.2514/3.24093.

[159] Mashio, S., Kurashina, K., Bamba, T., Okimoto, S., and Kaji, S., "Unstart Phenomenon Due to Thermal Choke in Scramjet Module," in "AIAA/NAL-NASDA-ISAS 10th International Space Planes and Hypersonic Systems and Technologies Conference," Kyoto, Japan, 2001, AIAA Paper 2001-1887, doi:10.2514/6.2001-1887.

[160] O'Byrne, S., Doolan, M., Olsen, S. R., and Houwing, A. F. P., "Analysis of Transient Thermal Choking Processes in a Model Scramjet Engine," *Journal of Propulsion and Power*, Vol. 16, No. 5, 2000, pp. 808–814. doi:10.2514/2.5645.

[161] Abouseif, G. E., Keklak, J. A., and Toong, T. Y., "Ramjet Rumble: The Low-Frequency Instability Mechanism in Coaxial Dump Combustors," *Combustion Science and Technology*, Vol. 36, No. 1-2, 1984, pp. 83–108. doi:10.1080/00102208408923727.

[162] Crump, J. E., Schadow, K. C., Yang, V., and Culick, F. E. C., "Longitudinal combustion Instabilities in ramjet engines: Identification of Acoustic Modes," *Journal of Propulsion and Power*, Vol. 2, No. 2, 1986, pp. 105–109. doi:10.2514/3.22852.

[163] Schadow, K. C., Gutmark, E. J., Parr, T. P., Parr, D. M., Wilson, K. J., and Crump, J. E., "Large-Scale Coherent Structures as Drivers of Combustion Instability," *Combustion Science and Technology*, Vol. 64, 1989, pp. 167–186. doi:10.1080/00102208908924029.

[164] Culick, F. E. C., "Unsteady Motions in Combustion Chambers for Propulsion Systems," Tech. rep., NATO, 2006. AG-AVT-039.

[165] Clark, W. H., "Experimental Investigation of Pressure Oscillations in a Side Dump Ramjet Combustor," *Journal of Spacecraft and Rockets*, Vol. 19, No. 1, 1982, pp. 47–53. doi:10.2514/6.1980-1117.

[166] Kailasanath, K., Gardner, J. H., Boris, J. P., and Oran, E. S., "Numerical Simulations of Acoustic-Vortex Interactions in a Central-Dump Ramjet Combustor," *Journal of Propulsion and Power*, Vol. 3, No. 6, 1987, pp. 525–533. doi:10.2514/3.2302.

[167] Kailasanath, K., Gardner, J. H., Boris, J. P., and Oran, E. S., "Acoustic-Vortex Interactions and Low-Frequency Oscillations in Axisymmetric Combustors," *Journal of Propulsion and Power*, Vol. 5, No. 2, 1989, pp. 165–171. doi:10.2514/3.23132.

[168] Menon, S., "Active Combustion Control in a Ramjet Using Large-Eddy Simulations," *Combustion Science and Technology*, Vol. 84, No. 1-6, 1992, pp. 51–79. doi:10.1080/00102209208951845.

[169] Laurence, S. J., Lieber, D., Schramm, J. M., Hannemann, K., and Larsson, J., "Incipient thermal choking and stable shock-train formation in the heat-release region of a scramjet combustor. Part I: Shock-tunnel experiments," *Combustion and Flame*, Vol. 162, 2015, pp. 921–931. doi:10.1016/j.combustflame.2014.09.016.

[170] Larsson, J., Laurence, D., Bermejo-Moreno, I., Bodart, J., Karl, S., and Vicquelin, R., "Incipient thermal choking and stable shock-train formation in the heat-release region of a scramjet combustor. Part II: Large eddy simulations," *Combustion and Flame*, Vol. 162, 2015, pp. 907–920. doi:10.1016/j.combustflame.2014.09.017.

[171] Laurence, S. J., Karl, S., Schramm, J. M., and Hannemann, K., "Transient fluid-combustion phenomena in a model scramjet," *Journal of Fluid Mechanics*, Vol. 722, 2013, pp. 85–120. doi:10.1017/jfm.2013.56.

[172] Nordin-Bates, K. and Fureby, C., "Understanding Scramjet Combustion using LES of the HyShot II Combustor: Stable Combustion and Incipient Thermal Choking," in "51st AIAA/SAE/ASEE Joint Propulsion Conference," Orlando, Florida, 2015, AIAA Paper 2015-3838, doi:10.2514/6.2015-3838.

[173] Gruber, M. R., Jackson, K., and Jiwen, L., "Hydrocarbon-fueled Scramjet Combustor Flowpath Development for Mach 6-8 HIFiRE Flight Experiments," Tech. rep., AFRL, 2008. Conference Pre-print, AFRL-RZ-WP-TP-2010-2243.

[174] Vaden, S. N., Debes, R. L., Burk, R. S., Boyd, C. M., Wilson, L. G., and Pellet, G. L., "Unsteady Extinction Of Opposed Jet Ethylene / Methane HIFiRE Surrogate Fuel Mixtures vs Air," in "45th AIAA/ASME/SAE/ASEE Joint Propulsion Conference and Exhibit," Denver Colorado, 2009, AIAA Paper 2009-4883, doi:10.2514/6.2009-4883.

[175] Chang, W. K., Park, G., Jin, Y., and Byun, J., "Shock Impinging Effect on Ethylene Flameholding," *Journal of Propulsion and Power*, Vol. 32, No. 5, 2016, pp. 1230–1239. doi:10.2514/1.B36007.

[176] Ma, F., Li, J., Yang, V., Lin, K.-C., and Jackson, T. A., "Thermoacoustic Flow Instability in a Scramjet Combustor," in "41st AIAA/ASME/SAE/ASEE Joint Propulsion Conference & Exhibit," Tucson, Arizona, 2005, AIAA Paper 2005-3824, doi:10.2514/6.2005-3824.

[177] Donbar, J. M., Gruber, M. R., Jackson, T. A., Carter, C. D., and Mathur, T., "OH Planar Laser-Induced Flouresence Imaging in a Hydrocarbon-Fueled Scramjet Combustor," in "Proceedings of the Combustion Institute," Vol. 28, 2000, pp. 679–687, doi:10.1016/S0082-0784(00)80269-6.

[178] Lin, K.-C., Jackson, K., Behdadina, R., Jackson, T. A., Ma, F., and Yang, V., "Acoustic Characterization of an Ethylene-Fueled Scramjet Combustor with a Cavity Flameholder," *Journal of Propulsion and Power*, Vol. 26, No. 6, 2010, pp. 1161–1169. doi:10.2514/1.43338.

[179] Do, H., Passaro, A., and Baccarella, D., "Inlet Unstart of an Ethylene-Fueled Model Scramjet with a Mach 4.5 Freestream Flow," in "18th AIAA/3AF International Space Planes and Hypersonic Systems and Technologies Conference," Tours, France, 2012, AIAA Paper 2012-5929, doi:10.2514/6.2012-5929.

[180] Do, H., Passaro, A., Liu, Q., Lee, T., and Baccarella, D., "Ethylene Flame Dynamics in an Arc-Heated Hypersonic Wind Tunnel," in "51st AIAA Aerospace Sciences Meeting including the New Horizons Forum and Aerospace Exposition," Grapevine (Dallas/Ft. Worth Region), Texas, 2013, AIAA Paper 2013-0700, doi:10.2514/6.2013-70.

[181] Liu, Q., Passaro, A., Baccarella, D., and Do, H., "Ethylene Flame Dynamics and Inlet Unstart in a Model Scramjet," *Journal of Propulsion and Power*, Vol. 30, No. 6, 2014, pp. 1577–1585. doi:10.2514/1.B35214.

[182] Liu, Q., Baccarella, D., Hammack, S., Lee, T., Carter, C. D., and Do, H., "Influences of Freestream Turbulence on Flame Dynamics in a Supersonic Combustor," *AIAA Journal*, Vol. 55, No. 3, 2016, pp. 913–918. doi:10.2514/1.J055271.

[183] Liu, Q., Baccarella, D., Lee, T., Hammack, S., Carter, C. D., and Do, H., "Influences of Inlet Geometry Modification on Scramjet Flow and Combustion Dynamics," *Journal of Propulsion and Power*, Vol. 33, No. 5, 2017, pp. 1179–1186. doi:10.2514/1.B36434.

[184] Fotia, M. L. and Driscoll, J. F., "Ram-Scram Transition and Flame/Shock-Train Interactions in a Model Scramjet Experiment," *Journal of Propulsion and Power*, Vol. 29, No. 1, 2013, pp. 261–273. doi:10.2514/1.B34486.

[185] Fotia, M. L., "Mechanics of Combustion Mode Transition in a Direct-Connect Ramjet-Scramjet Experiment," *Journal of Propulsion and Power*, Vol. 31, No. 1, 2015, pp. 69–78. doi:10.2514/1.B35171.

[186] Hagenmaier, M. A., Tam, C.-J., and Chakravarthy, S., "Study of Moving Start Door Flow Physics for Scramjets," in "9th International Space Planes and Hypersonic Systems and Technologies Conference and 3rd Weakly Ionized Gases Workshop," Norfolk, Virginia, 1999, AIAA Paper 1999-4957, doi:10.2514/6.1999-4957.

[187] Tahir, R. B., Molder, S., and Timofeev, E. V., "Unsteady Starting of High Mach Number Air Inlets - A CFD Study," in "39th AIAA/ASME/SAE/ASEE Joint Propulsion Conference and Exhibit," Huntsville, Alabama, 2003, AIAA Paper 2003-5191, doi:10.2514/6.2003-5191.

[188] Su, W.-Y., Hu, Z., Tang, P.-P., and Chen, Y., "Transient Analysis for Hypersonic Inlet Accelerative Restarting Process," *Journal of Spacecraft and Rockets*, Vol. 54, No. 2, 2017, pp. 376–385. doi:10.2514/1.A33601.

[189] Kirchhartz, R. M., Mee, D. J., Stalker, R. J., Jacobs, P. A., and Smart, M. K., "Supersonic Boundary-Layer Combustion: Effects of Upstream Entropy and Shear-Layer Thickness," *Journal of Propulsion and Power*, Vol. 26, No. 1, 2010, pp. 57–66. doi:10.2514/1.44485.

[190] Ombrello, T., Peltier, S., and Carter, C., "Effects of Inlet Distortion on Cavity Ignition in Supersonic Flow," in "53rd AIAA Aerospace Sciences Meeting," Kissimmee, Florida, 2015, AIAA Paper 2015-0882, doi:10.2514/6.2015-0882.

[191] Huete, C., Sánchez, A. L., and Williams, F. A., "Diffusion-Flame Ignition by Shock-Wave Impingement on a Hydrogen–Air Supersonic Mixing Layer," *Journal of Propulsion and Power*, Vol. 33, No. 1, 2017, pp. 256–263. doi:10.2514/1.B36236.

[192] Yentsch, R. J. and Gaitonde, D. V., "Numerical Investigation of Dual-Mode Operation in a Rectangular Scramjet Flowpath," *Journal of Propulsion and Power*, Vol. 30, No. 2, 2014, pp. 474–489. doi:10.2514/1.B34994.

[193] Choi, H. and Moin, P., "Grid-point requirements for large eddy simulation: Chapman's estimates revisited," *Physics of Fluids*, Vol. 24, No. 1, 2012, p. 011702. doi:10.1063/1.3676783.

[194] Bisek, N. J., "High-Fidelity Simulations of the HIFiRE-6 Flow Path," in "54th AIAA Aerospace Sciences Meeting," San Diego, California, 2016, AIAA Paper 2016-1115, doi:10.2514/6.2016-1115.

[195] Yentsch, R. J., *Three-Dimensional Shock-Boundary Layer Interactions in Simulations of HIFiRE-1 and HIFiRE-2*, Dissertation, The Ohio State University, 2013.

[196] Yentsch, R. J. and Gaitonde, D. V., "Unsteady Three-Dimensional Mode Transition Phenomena in a Scramjet Flowpath," *Journal of Propulsion and Power*, Vol. 31, No. 1, 2015, pp. 104–122. doi:10.2514/1.B35205.

[197] Zhang, L., Yang, V., and Lin, K.-C., "Transient Operation of an Ethylene-Fueled Scramjet Engine with Fuel Staging," in "51st AIAA Aerospace Sciences Meeting including the New Horizons Forum and Aerospace Exposition," , 2013, AIAA Paper 2013-0118, doi:10.2514/6.2013-118.

[198] Hawkins, W. R. and Marquart, E. J., "Two-Dimensional Generic Inlet Unstart Detection at Mach 2.5-5.0," in "6th AIAA International Aerospace Planes and

Hypersonics Technologies Conference," Chattanooga, Tennessee, 1995, AIAA Paper 1995-6019, doi:10.2514/6.1995-6019.

[199] Hutchins, K. E., *Detection and Transient Dynamics Modeling of Experimental Hypersonic Inlet Unstart*, Master's thesis, The University of Texas at Austin, 2011.

[200] Srikant, S., Wagner, J. L., Valdivia, A., Akella, M. R., and Clemens, N. T., "Unstart Detection in a Simplified-Geometry Hypersonic Inlet–Isolator Flow," *Journal of Propulsion and Power*, Vol. 26, 2010, pp. 1059–1071. doi:10.2514/1.46937.

[201] Hutchins, K. E., Akella, M. R., Clemens, N. T., Donbar, J. M., and Gogineni, S., "Experimental Identification of Transient Dynamics for Supersonic Inlet Unstart," *Journal of Propulsion and Power*, Vol. 30, No. 6, 2014, pp. 1605–1612. doi:10.2514/1.B35230.

[202] Le, D. B., Goyne, C. P., and Krauss, R. H., "Shock Train Leading-Edge Detection in a Dual-Mode Scramjet," *Journal of Propulsion and Power*, Vol. 24, No. 5, 2008, pp. 1035–1041. doi:10.2514/1.32592.

[203] Guarnaccio, C. C., Bentley, J. L., and Ombrello, T. M., "Dynamic Response of Supersonic Flow to Short Duration Normal Flow Injection," in "54th AIAA Aerospace Sciences Meeting," San Diego, California, 2016, AIAA Paper 2016-0657, doi:10.2514/6.2016-0657.

[204] Qin, B., Chang, J., Jiao, X., and Bao, W., "Unstart Margin Characterization Method of Scramjet Considering Isolator-Combustor Interactions," *AIAA Journal*, Vol. 53, No. 2, 2015, pp. 493–500. doi:10.2514/1.J053547.

[205] Schultz, I. A., Goldenstein, C. S., Jeffries, J. B., Hanson, R. K., Rockwell, R. D., and Goyne, C. P., "Diode Laser Absorption Sensor for Combustion Progress in a Model Scramjet," *Journal of Propulsion and Power*, Vol. 30, No. 3, 2014, pp. 550–557. doi:10.2514/1.B34905.

[206] Geipel, C. M., Rockwell, R. D., Chelliah, H. K., Cutler, A. D., Spelker, C. A., Hashem, Z., and Danehy, P. M., "High-Spatial-Resolution OH PLIF Visualization in a Cavity-Stabilized Ethylene-Air Turbulent Flame," in "33rd AIAA Aerodynamic Measurement Technology and Ground Testing Conference," , 2017, AIAA Paper 2017-3901, doi:10.2514/6.2017-3901.

[207] Lin, K.-C., Tam, C.-J., Jackson, K., Kennedy, P., and Behdadnia, R., "Experimental Investigations on Simple Variable Geometry for Improving Scramjet Isolator Performance," in "43rd AIAA/ASME/SAE/ASEE Joint

Propulsion Conference & Exhibit," Cincinnati, Ohio, 2007, aIAA 2007-5378, doi:10.2514/6.2007-5378.

[208] Huang, H.-X., Tan, H.-J., Wang, J., Sun, S., and Ning, L., "A Fluidic Control Method of Shock Train in Hypersonic Inlet/Isolator," in "50th AIAA/ASME/SAE/ASEE Joint Propulsion Conference," Cleveland, Ohio, 2014, AIAA Paper 2014-3846, doi:10.2514/6.2014-3846.

[209] Valdivia, A., Yuceil, K. B., Wagner, D. A., Clemens, N. T., and Dolling, D. S., "Control of Supersonic Inlet-Isolator Unstart Using Active and Passive Vortex Generators," *AIAA Journal*, Vol. 52, No. 6, 2014, pp. 1207–1218. doi:10.2514/1.J052214.

[210] Sajben, M., Morris, M. J., Bogar, T. J., and Kroutil, J. C., "The Structure of Normal-Shock/Turbulent-Boundary-Layer Interactions Modified by Mass Removal," Tech. rep., McDonnell Douglas Research Laboratories, 1989. AFOSR TR 89-0650, MDC QAO26.

[211] Kodera, M., Tomioka, S., Kanda, T., Mitani, T., and Kobayashi, K., "Mach 6 Test of a Scramjet Enginer with Boundary-Layer Bleeding and Two-staged Fuel Injection," in "AIAA 12th International Space Plane and Hypersonic Systems and Technologies Conference," Norfolk, Virginia, 2003, AIAA Paper 2003-7049, doi:10.2514/6.2003-7049.

[212] Im, S., Do, H., Mungal, M. G., and Cappelli, M. A., "Experimental Study and Plasma Control of an Unstarting Supersonic Flow," in "6th AIAA Flow Control Conference," New Orleans, Louisiana, 2012, AIAA Paper 2012-2809, doi:10.2514/6.2012-2809.

[213] Webb, N. J., *Control of a Shock Wave-Boundary Layer Interaction using Localized Arc Filament Plasma Actuators*, Ph.D. thesis, The Ohio State University, 2013.

[214] Zhang, Q.-F., Tan, H.-J., Bu, H.-X., and Rao, C., "Investigation of a Movable Slot-Plate Control Method for Hypersonic Inlet Unstart Caused by Downstream Mass-Flow Choking," in "50th AIAA/ASME/SAE/ASEE Joint Propulsion Conference," Cleveland, Ohio, 2014, AIAA Paper 2014-3847, doi:10.2514/6.2014-3847.

[215] Webb, N. and Samimy, M., "Control of Supersonic Cavity Flow Using Plasma Actuators," *AIAA Journal*, Vol. 55, No. 10, 2017, pp. 3346–3355. doi:10.2514/1.J055720.

[216] Kreth, P. A. and Alvi, F. S., "The Effects of High-Frequency, Supersonic Microjet Injection on a High-Speed Cavity Flow," in "55th AIAA Aerospace Sciences Meeting," , 2017, AIAA Paper 2017-1882, doi:10.2514/6.2017-1882.

[217] Su, W.-Y., Chen, Y., Zhang, F.-R., and Tang, P.-P., "Control of pseudo-shock oscillation in scramjet inlet-isolator using periodical excitation," *Acta Astronautica*, Vol. 143, 2018, pp. 147–154. doi:10.1016/j.actaastro.2017.10.040.

[218] Manohar, K., *Data-Driven Sensor Placement Methods*, Ph.D. thesis, University of Washington, 2018.

[219] Lumley, J. L., "Computational Modeling of Turbulent Flows," *Advances in Applied Mechanics*, Vol. 18, 1978, pp. 123–176. doi:10.1016/S0065-2156(08)70266-7.

[220] Rowley, C. W., Mezić, I., Baheri, S., Schlatter, P., and Henningson, D. S., "Spectral analysis of nonlinear flows," *Journal of Fluid Mechanics*, Vol. 641, 2009, pp. 115–127. doi:10.1017/S0022112009992059.

[221] Schmid, P. J., "Dynamic Mode Decomposition of Numerical and Experimental Data," *Journal of Fluid Mechanics*, Vol. 656, 2010, pp. 5–28. doi:10.1017/S0022112010001217.

[222] Taira, K., Brunton, S. L., Dawson, S. T. M., Rowley, C. W., Colonius, T., McKeon, B. J., Schmidt, O. T., Gordeyev, S., Theofilis, V., and Ukeiley, L. S., "Modal Analysis of Fluid Flows: An Overview," *AIAA Journal*, Vol. 55, No. 12, 2017, pp. 4013–4041. doi:10.2514/1.J056060.

[223] Gruber, M., Donbar, J. M., Jackson, K., Mathur, T., Baurle, R. A., Eklund, D., and Smith, C., "A Newly Developed Direct-Connect High-Enthalpy Supersonic Combustion Research Facility," *Journal of Propulsion and Power*, Vol. 17, No. 6, 2001, pp. 1296–1304. doi:10.2514/2.5878.

[224] Hagenmaier, M. A., Eklund, D. R., and Milligan, R. T., "Improved Simulation of Inflow Distortion for Direct-Connect Scramjet Studies," in "49th AIAA Aerospace Sciences Meeting including the New Horizons Forum and Aerospace Exposition," , 2011, AIAA Paper 2011-233, doi:10.2514/6.2011-233.

[225] Metacomp, Inc., *CFD++ Manual*, 2016.

[226] McBride, B. J., Heimel, S., Ehlers, J. G., and Gordon, S., "Thermodynamic Properties to 6000^o K for 210 Substances Involving the First 18 Elements," Tech. rep., NASA Lewis Research Center, Cleveland, Ohio, 1963. NASA SP-3001.

[227] Wilke, C. R., "A Viscosity Equation for Gas Mixtures," *The Journal of Chemical Physics*, Vol. 18, No. 4, 1950, pp. 517–519. doi:10.1063/1.1747673.

[228] Palmer, G. E. and Wright, M. J., "Comparison of Methods to Compute High-Temperature Gas Viscosity," *Journal of Thermophysics and Heat Transfer*, Vol. 17, No. 2, 2003, pp. 232–239. doi:10.2514/2.6756.

[229] Gehre, R. M., Wheatley, V., and Boyce, R. R., "Computational Investigation of Thermal Nonequilibrium Effects in Scramjet Geometries," *Journal of Propulsion and Power*, Vol. 29, No. 3, 2013, pp. 648–660. doi:10.2514/1.B34722.

[230] Fiévet, R., Voelkel, S., Koo, H., Raman, V., and Varghese, P. L., "Effect of thermal nonequilibrium on ignition in scramjet combustors," *Proceedings of the Combustion Insitute*, Vol. 36, 2017, pp. 2901–2910. doi:10.1016/j.proci.2016.08.066.

[231] Magnussen, B. and Hjertager, B., "On mathematical modeling of turbulent combustion with special emphasis on soot formation and combustion," *Symposium (International) on Combustion*, Vol. 16, No. 1, 1977, pp. 719–729. doi:10.1016/S0082-0784(77)80366-4.

[232] Borghi, M. R., Engblom, W. A., and Georgiadis, N. J., "Evaluation of Mixing-Limited Quasi-Global Wind-US Model for HIFiRE 2 Flowpath," in "52nd Aerospace Sciences Meeting," National Harbor, Maryland, 2014, AIAA Paper 2014-1160, doi:10.2514/6.2014-1160.

[233] Storch, A. M., Bynum, M., Liu, J., and Gruber, M., "Combustor Operability and Performance Verification for HIFiRE Flight 2," in "17th AIAA International Space Planes and Hypersonic Systems and Technologies Conference," San Francisco, California, 2011, AIAA Paper 2011-2249, doi:10.2514/6.2011-2249.

[234] Scherrer, D., Dessornes, O., Ferrier, M., Vincent-Randonnier, A., Moule, Y., and Sabel'Nikov, V., "Research on Supersonic Combustion and Scramjet Combustors at ONERA," Tech. Rep. 11, AerospaceLab, 2016, doi:10.12762/2016.AL11-04. TP 2016-553, AL11-04.

[235] Quinlan, J. M. and Zinn, B. T., "Transverse Combustion Instabilities: Modern Experimental Techniques and Analysis," in "50th AIAA/ASME/SAE/ASEE Joint Propulsion Conference," Cleveland, Ohio, 2014, AIAA Paper 2014-3682, doi:10.2514/6.2014-3682.

[236] Liu, J., Tam, C.-J., Lu, T., and Law, C. K., "Simulations of Cavity-stabilized Flames in Supersonic Flows Using Reduced Chemical Kinetic Mechanisms,"

in “42nd AIAA/ASME/SAE/ASEE Joint Propulsion Conference & Exhibit,” Sacramento, California, 2006, AIAA Paper 2006-4862, doi:10.2514/6.2006-4862.

[237] Baurle, R. A., “Modeling of High Speed Reacting Flows: Established Practices and Future Challenges,” in “42nd AIAA Aerospace Sciences Meeting and Exhibit,” Reno, Nevada, 2004, AIAA Paper 2004-267, doi:10.2514/6.2004-267.

[238] Wang, H. and Laskin, A., “Optimization of a Comprehensive Detailed Chemical Kinetic Model for Simulating High-Speed Propulsion,” Tech. rep., Dept. of Mechanical and Aerospace Engineering, Princeton University, 1998.

[239] Luo, Z., Yoo, C. S., Richardson, E. S., Chen, J. H., Law, C. K., and Lu, T., “Chemical explosive mode analysis for a turbulent lifted ethylene jet flame in highly-heated coflow,” *Combustion and Flame*, Vol. 159, 2012, pp. 265–274. doi:10.1016/j.combustflame.2011.05.023.

[240] Milligan, R. T., Liu, J., Tam, C.-J., Eklund, D. R., Hagenmaier, M. A., Davis, D. L., Risha, D. J., Gruber, M., and Mathur, T., “Dual-Mode Scramjet Combustor: Numerical Sensitivity and Evaluation of Experiments,” in “50th AIAA Aerospace Sciences Meeting including the New Horizons Forum and Aerospace Exposition,” , 2012, AIAA Paper 2012-947, doi:10.2514/6.2012-947.

[241] Potturi, A. S. and Edwards, J. R., “Large-Eddy / Reynolds-Averaged Navier-Stokes Simulation of Cavity-Stabilized Ethylene Combustion,” in “44th AIAA Fluid Dynamics Conference,” Atlanta, Georgia, 2014, AIAA Paper 2014-2095, doi:10.2514/6.2014-2095.

[242] Pope, S. B., *Turbulent Flows*, Cambridge University Press, Cambridge, 2000.

[243] Gatski, T. B. and Bonnet, J.-P., *Compressibility, Turbulence, and High Speed Flow*, Elsevier, Oxford, UK, 2009, doi:10.1016/B978-0-08-044565-6.00012-9.

[244] Goldberg, U. C., Palaniswamy, S., Batten, P., and Gupta, V., “Variable Turbulent Schmidt and Prandtl Number Modeling,” *Engineering Applications of Computational Fluid Mechanics*, Vol. 4, No. 4, 2010, pp. 511–520. doi:10.1080/19942060.2010.11015337.

[245] Goldberg, U. C., Peroomian, O., Chakravarthy, S. R., and Sekar, B., “Validation of CFD++ Code Capability for Supersonic Combustor Flowfields,” in “33rd Joint Propulstion Conference and Exhibit,” , 1997, AIAA Paper 1997-3271, doi:10.2514/6.1997-3271.

[246] Burrows, M. C. and Kurkov, A. P., “Analytical and Experimental Study of Supersonic Combustion of Hydrogen in a Vitiated Airstream,” Tech. rep., NASA Lewis Research Center, Cleveland, Ohio, 1973. NASA TM X-2828.

[247] DeBonis, J. R., Oberkampf, W. L., Wolf, R. T., Orkwis, P. D., Turner, M. G., Babinsky, H., and Benek, J. A., "Assessment of Computational Fluid Dynamics and Experimental Data for Shock Boundary-Layer Interactions," *AIAA Journal*, Vol. 50, No. 4, 2012, pp. 891–903. doi:10.2514/1.J051341.

[248] Georgiadis, N. J., Mankbadi, M. R., and Vyas, M. A., "Turbulence Model Effects on RANS Simulations of the HIFiRE Flight 2 Ground Test Configurations," in "AIAA SciTech 52nd Aerospace Sciences Meeting," National Harbor, Maryland, 2014, AIAA Paper 2014-0624, doi:10.2514/6.2014-0624.

[249] Baurle, R. A., "Hybrid Reynolds-Averaged/Large-Eddy Simulation of a Cavity Flameholder: Modeling Sensitivities," *AIAA Journal*, Vol. 55, No. 2, 2016, pp. 524–543. doi:10.2514/1.J055257.

[250] Goldberg, U. C., Batten, P., Palaniswamy, S., Chakravarthy, S. R., and Peroomian, O., "Hypersonic Flow Predictions using Linear and Nonlinear Turbulence Closures," *Journal of Aircraft*, Vol. 37, No. 4, 2000, pp. 671–675. doi:10.2514/2.2650.

[251] Demuren, A. O., "Calculation of Turbulence-Driven Secondary Motion in Ducts with Arbitrary Cross Section," *AIAA Journal*, Vol. 29, No. 4, 1991, pp. 531–537. doi:10.2514/3.10616.

[252] Burton, D. M. F. and Babinsky, H., "Corner separation effects for normal shock wave/turbulent boundary layer interactions in rectangular channels," *Journal of Fluid Mechanics*, Vol. 707, 2012, pp. 287–306. doi:10.1017/jfm.2012.279.

[253] Metacomp, I., "Compressibility Correction," Private Communication, 2017.

[254] Sarkar, S., "The Pressure-Dilatation Correlation in Compressible Flows," *Physics of Fluids A*, Vol. 4, No. 12, 1992, pp. 2674–2682. doi:10.1063/1.858454.

[255] Wilcox, D. C., *Turbulence Modeling for CFD*, DCW Industries, Inc., 3rd ed., 2006.

[256] Palaniswamy, S., Goldberg, U., Peroomian, O., and Chakravarthy, S., "Predictions of Axial and Transverse Injection into Supersonic Flow," *Flow, Turbulence and Combustion*, Vol. 66, 2001, pp. 37–55. doi:10.1023/A:1011479002452.

[257] Goldberg, U., Peroomian, O., and Chakravarthy, S., "A Wall-Distance-Free k-ϵ Model With Enhanced Near-Wall Treatment," *Journal of Fluids Engineering*, Vol. 120, 1998, pp. 457–462. doi:10.1115/1.2820684.

[258] Goldberg, U., "A Realizable Version of the $k - \omega$ Turbulence Model," *Studies in Engineering and Technology*, Vol. 4, No. 1. doi:10.11114/set.v4i1.1989.

[259] Batten, P., Clarke, N., Lambert, C., and Causon, D. M., "On the Choice of Wavespeeds for the HLLC Riemann Solver," *SIAM Journal on Scientific Computing*, Vol. 18, No. 6, 1997, pp. 1553–1570. doi:10.1137/S1064827593260140.

[260] Harten, A., Lax, P. D., and van Leer, B., "On Upstream Differencing and Godunov-Type Schemes for Hyperbolic Conservation Laws," *SIAM Review*, Vol. 25, No. 1, 1983, pp. 35–61. doi:10.1137/1025002.

[261] Toro, E. F., Spruce, M., and Speares, W., "Restoration of the contact surface in the HLL-Riemann solver," *Shock Waves*, Vol. 4, 1994, pp. 25–34. doi:10.1007/BF01414629.

[262] Peroomian, O., Chakravarthy, S., and Goldberg, U. C., "A 'grid-transparent' methodology for CFD," in "35th AIAA Aerospace Sciences Meeting & Exhibit," Reno, Nevada, 1997, AIAA Paper 1997-0724, doi:10.2514/6.1997-724.

[263] Chakravarthy, S., "A Unified-Grid Finite Volume Formulation for Computational Fluid Dynamics," *International Journal for Numerical Methods in Fluids*, Vol. 31, No. 1, 1999, pp. 309–323. doi:10.1002/(SICI)1097-0363(19990915)31:1<309::AID-FLD971>3.0.CO;2-M.

[264] Rodriquez, C. G., "Asymmetry Effects in Numerical Simulation of Supersonic Flows with Upstream Separated Regions," in "39th AIAA Aerospace Sciences Meeting and Exhibit," Reno, Nevada, 2001, AIAA Paper 2001-0084, doi:10.2514/6.2001-84.

[265] Karypis, G. and Schloegel, K., *ParMeTiS: Parallel Graph Partitioning and Sparse Matrix Ordering Library*, University of Minnesota, Dept. of Computer Science and Engineering, Minneapolis, MN 55455, ver 4.0 ed., 2013.

[266] Rollins, A., "World's 14th-fastest supercomputer launches at WPAFB," , 2013, Accessed: 2018-06-24, `https://www.wpafb.af.mil/News/Article-Display/Article/819369/worlds-14th-fastest-supercomputer-launches-at-wpafb/`.

[267] Launder, B. E., "On the Computation of Convective Heat Transfer in Complex Turbulent Flows," *Journal of Heat Transfer*, Vol. 110, 1988, pp. 1112–1128. doi:10.1115/1.3250614.

[268] Grotjans, H. and Menter, F. R., "Wall Functions for General Application CFD Codes," in Papailiou, K. D., Tsahalis, D., Périaux, J., Hirsch, C., and Pandolfi, M., eds., "Computational Fluid Dynamics '98 Fourth European Computational Fluid Dynamics Conference," John Wiley & Sons, Ltd., Athens, Greece, Vol. Vol. 1, Part 2, 1998, pp. 1112–1117.

[269] Crow, A. J., Boyd, I. D., and Terrapon, V. E., "Radiation Modeling of a Hydrogen-Fueled Scramjet," in "42nd AIAA Thermophysics Conference," Honolulu, Hawaii, 2011, AIAA Paper 2011-3769, doi:10.2514/6.2011-3769.

[270] Crow, A. J., Boyd, I. D., Brown, M. S., and Liu, J., "Thermal Radiative Analysis of the HIFiRE-2 Scramjet Engine," in "43rd AIAA Thermophysics Conference," New Orleans, Louisiana, 2012, AIAA Paper 2012-2751, doi:10.2514/6.2012-2751.

[271] Crow, A. J., Boyd, I. D., Brown, M. S., and Liu, J., "Thermal Radiative Simulations and Measurements of a Scramjet Test Rig," *Journal of Propulsion and Power*, Vol. 30, No. 6, 2014, pp. 1543–1550. doi:10.2514/1.B35207.

[272] Incropera, F. P., DeWitt, D. P., Bergman, T. L., and Lavine, A. S., *Introduction to Heat Transfer*, John Wiley & Sons, Inc., 5th ed., 2007.

[273] Donbar, J. M., "Cooling Circuits," Private Communication, 2015.

[274] Donbar, J. M., "Thermal Barrier Coating Estimates," Private Communication, 2015.

[275] Donbar, J. M., "Nozzle Composition Estimates," Private Communication, 2015.

[276] Hagenmaier, M. A., "TP2 Implementation," Private Communication, 2017.

[277] Schneider, S. P., "Effects of High-Speed Tunnel Noise on Laminar-Turbulent Transition," *Journal of Spacecraft and Rockets*, Vol. 38, No. 3, 2001, pp. 323–333. doi:10.2514/2.3705.

[278] Pointwise, Inc., "Equiangle Skewness," , 2018, Accessed: 2017-04-22, `https://www.pointwise.com/doc/user-manual/examine/functions/equiangle-skewness.html`.

[279] Roache, P. J., "Quantification of Uncertainty in Computational Fluid Dynamics," *Annual Review of Fluid Mechanics*, Vol. 29, 1997, pp. 123–160. doi:10.1146/annurev.fluid.29.1.123.

[280] Mitani, T., Hiraiwa, T., Sato, S., Tomioka, S., Kanda, T., and Tani, K., "Comparison of Scramjet Engine Performance in Mach 6 Vitiated and Storage-Heated Air," *Journal of Propulsion and Power*, Vol. 13, No. 5, 1997, pp. 635–642. doi:10.2514/2.5228.

[281] Haw, W. L., Goyne, C. P., Rockwell, R. D., Krauss, R. H., and McDaniel, J. C., "Experimental Study of Vitiation Effects on Scramjet Mode Transition," *Journal of Propulsion and Power*, Vol. 27, No. 2, 2011, pp. 506–508. doi:10.2514/1.49090.

[282] Goyne, C. P., McDaniel, J. C., Krauss, R. H., and Whitehurst, W. B., "Test Gas Vitiation Effects in a Dual-Mode Scramjet Combustor," *Journal of Propulsion and Power*, Vol. 23, No. 3, 2007, pp. 559–565. doi:10.2514/1.24663.

[283] Vyas, M. A., Engblom, W. A., Georgiadis, N. J., Trefny, C. J., and Bhagwandin, V. A., "Numerical Simulation of Vitiation Effects on a Hydrogen-Fueled Dual-Mode Scramjet," in "48th AIAA Aerospace Sciences Meeting Including the New Horizons Forum and Aerospace Exposition," Orlando, Florida, 2010, AIAA Paper 2010-1127, doi:10.2514/6.2010-1127.

[284] Brown, G. L. and Roshko, A., "On Density Effects and Large Structure in Turbulent Mixing Layers," *Journal of Fluid Mechanics*, Vol. 64, 1974, pp. 775–816. doi:10.1017/S002211207400190X.

[285] Dimotakis, P. E., "Turbulent Mixing," *Annual Review of Fluid Mechanics*, Vol. 37, 2005, pp. 329–356. doi:10.1146/annurev.fluid.36.050802.122015.

[286] He, G., Guo, Y., and Hsu, A. T., "The Effect of Schmidt Number on Turbulent Scalar Mixing in a Jet-in-Crossflow," *International Journal of Heat and Mass Transfer*, Vol. 42, 1999, pp. 3727–3738. doi:10.1016/S0017-9310(99)00050-2.

[287] Yoder, D. A., DeBonis, J. R., and Georgiadis, N. J., "Modeling of Turbulent Free Shear Flows," Tech. rep., NASA Glenn Research Center, Cleveland, Ohio, 2013. NASA/TM 2013-218072, AIAA Paper 2013-2721.

[288] Xiao, X., Edwards, J. R., Hassan, H. A., and Culter, A. D., "Variable Turbulent Schmidt-Number Formulation for Scramjet Applications," *AIAA Journal*, Vol. 44, No. 3, 2006, pp. 593–599. doi:10.2514/1.15450.

[289] Xiao, X., Hassan, H. A., and Baurle, R. A., "Modeling Scramjet Flows with Variable Turbulent Prandtl and Schmidt Numbers," *AIAA Journal*, Vol. 45, No. 6, 2007, pp. 1415–1423. doi:10.2514/1.26382.

[290] Yamashita, H., Shimada, M., and Takeno, T., "A numerical study on flame stability at the transition point of jet diffusion flames," *Symposium (International) on Combustion*, Vol. 26, No. 1, 1996, pp. 27–34. doi:10.1016/s0082-0784(96)80196-2.

[291] Poinsot, T. and Veynante, D., *Theoretical and Numerical Combustion*, Aquaprint, 3rd ed., 2011. ISBN 978-2-7466-3990-4.

[292] Quinlan, J. R., McDaniel, J. C., Drozda, T. G., Lacaze, G., and Oefelein, J. C., "A Priori Analysis of Flamelet-Based Modeling for a Dual-Mode Scramjet Combustor," in "50th AIAA/ASME/SAE/ASEE Joint Propulsion Conference," Cleveland, Ohio, 2014, AIAA Paper 2014-3743, doi:10.2514/6.2014-3743.

[293] Klimenko, A. and Bilger, R., "Conditional moment closure for turbulent combustion," *Progress in Energy and Combustion Science*, Vol. 25, No. 6, 1999, pp. 595–687. doi:10.1016/S0360-1285(99)00006-4.

[294] Goodwin, D. G., Moffat, H. K., and Speth, R. L., "Cantera: An Object-oriented Software Toolkit for Chemical Kinetics, Thermodynamics, and Transport Processes," `http://www.cantera.org`, 2017, doi:10.5281/zenodo.170284. Version 2.3.0.

[295] Fureby, C., "On the Supersonic Flame Structure in the HyShot II Scramjet Combustor," in "26th International Colloquium on the Dynamics of Explosions and Reactive Systems (ICDERS)," Boston, Massachusetts, 2017.

[296] Jagannathan, S. and Donzis, D. A., "Reynolds and Mach number scaling in solenoidally-forced compressible turbulence using high-resolution direct numerical simulations," *Journal of Fluid Mechanics*, Vol. 789, 2016, pp. 669–707. doi:10.1017/jfm.2015.754.

[297] Gruber, M., Donbar, J. M., Carter, C. D., and Hsu, K.-Y., "Mixing and Combustion Studies Using Cavity-Based Flameholders in a Supersonic Flow," *Journal of Propulsion and Power*, Vol. 20, No. 5, 2004, pp. 769–778. doi:10.2514/1.5360.

[298] Boles, J. A., Choi, J.-I., Edwards, J. R., and Baurle, R. A., "Simulations of High-Speed Internal Flows using LES/RANS Models," in "47th AIAA Aerospace Sciences Meeting Including The New Horizons Forum and Aerospace Exposition," Orlando, Florida, 2009, AIAA Paper 2009-1324, doi:10.2514/6.2009-1324.

[299] Boles, J. A., *Hybrid Large-Eddy Simulation/Reynolds-Averaged Navier-Stokes Methods and Predictions for Various High-Speed Flows*, Ph.D. thesis, North Carolina State University, 2009.

[300] Koo, H. and Raman, V., "Large-Eddy Simulation of a Supersonic Inlet-Isolator," *AIAA Journal*, Vol. 50, No. 7, 2012, pp. 1596–1613. doi:10.2514/1.J051568.

[301] Jang, I., Pečnik, R., and Moin, P., "A Numerical Study of the Unstart Event in an Inlet/Isolator Model," in "Center for Turbulence Research Annual Briefs," Stanford University, pp. 93–103, 2010.

[302] Yentsch, R. J. and Gaitonde, D. V., "Effect of Initial Conditions on Simulations of a Scramjet Flowpath," *Journal of Propulsion and Power*, Vol. 30, No. 4, 2014, pp. 1107–1112. doi:10.2514/1.B35159.

[303] Seiner, J. M., Dash, S. M., and Kenzakowski, D. C., "Historical Survey on Enhanced Mixing in Scramjet Engines," *Journal of Propulsion and Power*, Vol. 17, No. 6, 2001, pp. 1273–1286. doi:10.2514/2.5876.

[304] Gruber, M. R., Nejad, A. S., Chen, T. H., and Dutton, J. C., "Transverse Injection from Circular and Elliptic Nozzles into a Supersonic Crossflow," *Journal of Propulsion and Power*, Vol. 16, No. 3, 2000, pp. 449–457. doi:10.2514/2.5609.

[305] Gruber, M. R., Carter, C. D., Montes, D. R., Haubelt, L. C., King, P. I., and Hsu, K.-Y., "Experimental Studies of Pylon-Aided Fuel Injection into a Supersonic Crossflow," *Journal of Propulsion and Power*, Vol. 24, No. 3, 2008, pp. 460–470. doi:10.2514/1.32231.

[306] Ebrahimi, H. B., Malo-Molina, F. J., and Gaitonde, D. V., "Numerical Simulation of Injection Strategies in a Cavity-Based Supersonic Combustor," *Journal of Propulsion and Power*, Vol. 28, No. 5, 2012, pp. 991–999. doi:10.2514/1.B34512.

[307] Jones, E., Oliphant, T., Peterson, P., et al., "SciPy: Open source scientific tools for Python," , 2001–.

[308] Barber, C., Dobkin, D., and Huhdanpaa, H., "The Quickhull algorithm for convex hulls," *ACM Transactions on Mathematical Software*, Vol. 22, No. 4, 1996, pp. 469–483. doi:10.1145/235815.235821.

[309] Peterson, P., "F2PY: a tool for connecting Fortran and Python programs," *International Journal of Computational Science and Engineering*, Vol. 4, No. 4, 2009, pp. 296–305. doi:10.1504/IJCSE.2009.029165.

[310] McKinney, W., "Data Structures for Statistical Computing in Python," in van der Walt, S. and Millman, J., eds., "Proceedings of the 9th Python in Science Conference," Austin, Texas, 2010, pp. 51 – 56.

[311] Morajkar, R., *Role of secondary flows on flow separation induced by shock/boundary layer interaction in supersonic inlets*, Ph.D. thesis, University of Michigan, 2017.

[312] Gessner, F. B., "The origin of secondary flow in a turbulent flow along a corner," *Journal of Fluid Mechanics*, Vol. 58, No. 1, 1973, pp. 1–25. doi:10.1017/S0022112073002090.

[313] Rice, T., "High Aspect Ratio Isolator Performance for Access-to-Space Vehicles," in "12th AIAA International Space Planes and Hypersonic Systems and Technologies," Norfolk, Virginia, 2003, AIAA Paper 2003-7041, doi:10.2514/6.2003-7041.

[314] Sabnis, K., Galbraith, D., Babinsky, H., and Benek, J. A., "The Influence of Nozzle Geometry on Corner Flows in Supersonic Wind Tunnels," in "AIAA Scitech 2019 Forum," , 2019, AIAA Paper 2019-1650, doi:10.2514/6.2019-1650.

[315] Bisek, N. J., "High-Fidelity Numerical Modeling of Compressible Flow," Tech. rep., AFRL, 2015. AFRL-RQ-WP-TR-2015-0160.

[316] Benek, J. A., Suchyta III, C. J., and Babinsky, H., "Simulations of Incident Shock Boundary Layer Interactions," in "54th AIAA Aerospace Sciences Meeting," San Diego, California, 2016, AIAA Paper 2016-0352, doi:10.2514/6.2016-0352.

[317] Rice, B. E., Bisek, N. J., Peltier, S. J., and Hofferth, J. W., "Investigation of Secondary Motion in High Speed Flow," in "55th AIAA Aerospace Sciences Meeting," Grapevine, Texas, 2017, AIAA Paper 2017-0526, doi:10.2514/6.2017-0526.

[318] Brown, M. S., Herring, G. C., Cabell, K., Hass, N., Barhorst, T. F., and Gruber, M., "Optical Measurements at the Combustor Exit of the HIFiRE 2 Ground Test Engine," in "50th AIAA Aerospace Sciences Meeting including the New Horizons Forum and Aerospace Exposition," , 2012, AIAA Paper 2012-857, doi:10.2514/6.2012-857.

[319] Busa, K. M., Rice, B. E., McDaniel, D. R., Goyne, C. P., Rockwell, R. D., Fulton, J. A., Edwards, J. R., and Diskin, G. S., "Scramjet Combustion Efficiency Measurement via Tomographic Absorption Spectroscopy and Particle Image Velocimetry," *AIAA Journal*, Vol. 54, No. 8, 2016, pp. 2463–2471. doi:10.2514/1.J054662.

[320] Gruber, M. R., Carter, C., Ryan, M., Rieker, G. B., Jeffries, J. B., Hanson, R. K., Liu, J., and Mathur, T., "Laser-Based Measurements of OH, Temperature, and Water Vapor Concentration in a Hydrocarbon-Fueled Scramjet," in "44th AIAA/ASME/SAE/ASEE Joint Propulsion Conference & Exhibit," Hartford, CT, 2008, AIAA Paper 2008-5070, doi:10.2514/6.2008-5070.

[321] Gruber, M., Nejad, A. S., Chen, T. H., and Dutton, J. C., "Mixing and Penetration Studies of Sonic Jets in a Mach 2 Freestream," *Journal of Propulsion and Power*, Vol. 11, No. 2, 1995, pp. 315–323. doi:10.2514/3.51427.

[322] Gutmark, E. J., Schadow, K. C., and Yu, K. H., "Mixing Enhancement in Supersonic Free Shear Flows," *Annual Review of Fluid Mechanics*, Vol. 27, 1995, pp. 375–417. doi:10.1146/annurev.fl.27.010195.002111.

[323] Cattafesta III, L. N., Williams, D. R., Rowley, C. W., and Alvi, F. S., "Review of Active Control of Flow-Induced Cavity Resonance," in "33rd AIAA

Fluid Dynamics Conference and Exhibit," , 2003, AIAA Paper 2003-3567, doi:10.2514/6.2003-3567.

[324] Holmes, P., Lumley, J. L., and Berkooz, G., *Turbulence, Coherent Structures, Dynamical Systems and Symmetry*, Cambridge Univ Press, 2012.

[325] Tennekes, H. and Lumley, J. L., *A First Course in Turbulence*, MIT Press, 1972.

[326] Proctor, J. L., Brunton, S. L., Brunton, B. W., and Kutz, J. N., "Exploiting sparsity and equation-free architectures in complex systems," *The European Physical Journal Special Topics*, Vol. 223, No. 13, 2014, pp. 2665–2684. doi:10.1140/epjst/e2014-02285-8.

[327] Kutz, J. N., Brunton, S. L., Brunton, B. W., and Proctor, J. L., *Dynamic Mode Decomposition: Data-Driven Modeling of Complex Systems*, SIAM-Society for Industrial and Applied Mathematics, 2016.

[328] Annoni, J., Taylor, T., Bay, C., Johnson, K., Pao, L., Fleming, P., and Dykes, K., "Sparse-Sensor Placement for Wind Farm Control," *Journal of Physics: Conference Series*, Vol. 1037, 2018, p. 032019. doi:10.1088/1742-6596/1037/3/032019.

[329] Guéniat, F., Mathelin, L., and Pastur, L. R., "A dynamic mode decomposition approach for large and arbitrarily sampled systems," *Physics of Fluids*, Vol. 27, No. 2, 2015, p. 025113. doi:10.1063/1.4908073.

[330] Erichson, N. B., Brunton, S. L., and Kutz, J. N., "Compressed dynamic mode decomposition for background modeling," *Journal of Real-Time Image Processing*. doi:10.1007/s11554-016-0655-2.

[331] Rudin, L. I., *Images, Numerical Analysis of Singularities and Shock Filters*, Ph.D. thesis, California Institute of Technology, 1987. 52505:TR:87.

[332] Amsallem, D., Zahr, M., Choi, Y., and Farhat, C., "Design optimization using hyper-reduced-order models," *Structural and Multidisciplinary Optimization*, Vol. 51, No. 4, 2015, pp. 919–940. doi:10.1007/s00158-014-1183-y.

[333] VanderWyst, A. S., Shelton, A. B., Martin, C. L., Neergaard, L. J., and Witeof, Z. D., "Reduced Order Models for Generation of Large, High Speed Aerodynamic Databases with Jet Interactions," in "57th AIAA/ASCE/AHS/ASC Structures, Structural Dynamics, and Materials Conference," San Diego, California, 2016, AIAA Paper 2016-0464, doi:10.2514/6.2016-0464.

[334] Cao, Y., Zhu, J., Navon, I. M., and Luo, Z., "A reduced-order approach to four-dimensional variational data assimilation using proper orthogonal decomposition," *International Journal for Numerical Methods in Fluids*, Vol. 53, No. 10, 2007, pp. 1571–1583. doi:10.1002/fld.1365.

[335] Balajewicz, M. J., Dowell, E. H., and Noack, B. R., "Low-dimensional modelling of high-Reynolds-number shear flows incorporating constraints from the Navier-Stokes equation," *Journal of Fluid Mechanics*, Vol. 729, 2013, pp. 285–308. doi:10.1017/jfm.2013.278.

[336] Deshmukh, R., *Model Order Reduction of Incompressible Turbulent Flows*, Ph.D. thesis, The Ohio State University, 2016.

[337] Huang, C., Anderson, W. E., Merkle, C. L., and Sankaran, V., "Multi-Fidelity Framework for Modeling Combustion Instability," in "52nd AIAA/SAE/ASEE Joint Propulsion Conference," Salt Lake City, Utah, 2016, AIAA Paper 2016-4896, doi:10.2514/6.2016-4896.

[338] Manohar, K., Kaiser, E., Brunton, S. L., and Kutz, J. N., "Optimized Sampling for Multiscale Dynamics," 2017, *arXiv*, 1712.05085v1.

[339] Deshmukh, R., McNamara, J. J., Liang, Z., Kolter, J. Z., and Gogulapati, A., "Model order reduction using sparse coding exemplified for the lid-driven cavity," *Journal of Fluid Mechanics*, Vol. 808, 2016, pp. 189–223. doi:10.1017/jfm.2016.616.

[340] Chen, K. K., Tu, J. H., and Rowley, C. W., "Variants of Dynamic Mode Decomposition: Boundary Condition, Koopman, and Fourier Analyses," *Journal of Nonlinear Science*, Vol. 22, No. 6, 2012, pp. 887–915. doi:10.1007/s00332-012-9130-9.

[341] Berkooz, G., Holmes, P., and Lumley, J. L., "The Proper Orthogonal Decomposition in the Analysis of Turbulent Flows," *Annual Review of Fluid Mechanics*, Vol. 25, 1993, pp. 539–575. doi:10.1146/annurev.fl.25.010193.002543.

[342] Towne, A., Schmidt, O. T., and Colonius, T., "Spectral proper orthogonal decomposition and its relationship to dynamic mode decomposition and resolvent analysis," 2017, *arXiv*, 1708.04393.

[343] Tu, J. H., Rowley, C. W., Lucthenburg, D. M., Brunton, S. L., and Kutz, J. N., "On dynamic mode decomposition: Theory and Applications," *Journal of Computational Dynamics*, Vol. 1, No. 2, 2014, pp. 391–421. doi:10.3934/jcd.2014.1.391.

[344] Jolliffe, I. T., *Principal Component Analysis*, Springer New York, 2006.

[345] Schlens, J., "A Tutorial on Principal Component Analysis," 2014, *arXiv*, 1404.1100v1.

[346] Towne, A., Schmidt, O. T., and Colonius, T., "Spectral proper orthogonal decomposition and its relationship to dynamic mode decomposition and resolvent analysis," *Journal of Fluid Mechanics*, Vol. 847, 2018, pp. 821–867. doi:10.1017/jfm.2018.283.

[347] Sirovich, L., "Turbulence and Dynamics of Coherent Structures Part II: Symmetries and Transformations," *Quarterly of Applied Mathematics*, Vol. XLV, No. 3, 1987, pp. 573–582.

[348] Mohan, A. T., Gaitonde, D. V., and Visbal, M. R., "Model reduction and analysis of deep dynamic stall on a plunging airfoil," *Computers and Fluids*, Vol. 129, 2016, pp. 1–19. doi:10.1016/j.compfluid.2016.01.017.

[349] Mohan, A. T., *Data-Driven Analysis Methodologies for Unsteady Aerodynamics from High Fidelity Simulations*, Ph.D. thesis, The Ohio State University, 2017.

[350] Huang, C., Duraisamy, K., and Merkle, C., "Challenges in Reduced Order Modeling of Reacting Flows," in "2018 Joint Propulsion Conference," , 2018, AIAA Paper 2018-4675, doi:10.2514/6.2018-4675.

[351] Li, Q. and Wang, Z., "Dynamic Mode Decomposition of Turbulent Combustion Process in DLR Scramjet Combustor," *Journal of Aerospace Engineering*, Vol. 30, No. 5. doi:10.1061/(ASCE)AS.1943-5525.0000747.

[352] Gavish, M. and Donoho, D. L., "The Optimal Hard Threshold for Singular Values is $4/\sqrt{3}$," 2014, *arXiv*, 1305.5870v3.

[353] Taylor, R., "Multi-resolution DMD," , 2016, Accessed: 2018-06-02, `http://www.pyrunner.com/weblog/2016/08/05/mrdmd-python/`.

[354] Mao, J. and Jain, A., "Artificial neural networks for feature extraction and multivariate data projection," *IEEE Transactions on Neural Networks*, Vol. 6, No. 2, 1995, pp. 296–317. doi:10.1109/72.363467.

[355] Mezić, I., "Analysis of Fluid Flows via Spectral Properties of the Koopman Operator," *Annual Review of Fluid Mechanics*, Vol. 45, No. 1, 2013, pp. 357–378. doi:10.1146/annurev-fluid-011212-140652.

[356] Bai, Z., Demmel, J., Dongarra, J., Langou, J., and Wang, J., *LAPACK*, CRC Press, chap. 75, 2006.

[357] Roy, C. J. and Blottner, F. G., "Review and assessment of turbulence models for hypersonic flows," *Progress in Aerospace Sciences*, Vol. 42, 2006, pp. 469–530. doi:10.1016/j.paerosci.2006.12.002.

[358] Brown, J. L., "Hypersonic Shock Wave Impingement on Turbulent Boundary Layers: Computational Analysis and Uncertainty," *Journal of Spacecraft and Rockets*, Vol. 50, No. 1, 2013, pp. 96–123. doi:10.2514/1.A32259.

[359] Argrow, B., Barjatya, A., Chandler, G., Fritts, D., Lawrence, D., Muschinisk, A., and Rieker, G., "The Hypersonic Flight In the Turbulent Stratosphere (HYFLITS) research team," , 2018, Accessed: 2018-12-27, `https://www.colorado.edu/iriss/research/hyflits`.

[360] Cox, R. N., Sears, W. R., Young, A. D., Dobbinga, E., Ginoux, J. J., Trukenbrodt, E., Valensi, J., and Barschner, B. W., "Aerodynamics of Atmospheric Shear Flows," Tech. rep., NATO AGARD, 1970. AD702659, AGARD CP No. 48.

[361] Douglass, A. R., Carroll, M. A., DeMore, W. B., Holton, J. R., Isaksen, I. S. A., Johnston, H. S., and Ko, M. K. W., "The Atmospheric Effects of Stratospheric Aircraft: A Current Consensus," Tech. rep., NASA, 1991. NASA-RP-1251.

[362] Ehernberger, L. J., "Stratospheric Turbulence Measurements and Models for Aerospace Plane Design," Tech. rep., NASA Dryden Flight Research Facility, 1992. NASA-TM-104262.

[363] Tank, W. G., "Atmospheric Disturbance Environment Definition," Tech. rep., Boeing Commercial Airplane Group, 1994. NASA-CR-195315.

[364] Bhaumik, S., Gaitonde, D. V., Unnikrishnan, S., Sinha, A., and Shen, H., "Verification and application of a mean flow perturbation method for jet noise," *Aerospace Science and Technology*, Vol. 80, 2018, pp. 520–540. doi:10.1016/j.ast.2018.06.027.

[365] Touber, E. and Sandham, N. D., "Large-eddy simulation of low-frequency unsteadiness in a turbulent shock-induced separation bubble," *Theoretical and Computational Fluid Dynamics*, Vol. 23, No. 2, 2009, pp. 79–107. doi:10.1007/s00162-009-0103-z.

[366] Waindim, M., Bhaumik, S., and Gaitonde, D. V., "Further Development of the Navier-Stokes Equations-Based Mean Flow Perturbation Technique," in "54th AIAA Aerospace Sciences Meeting," San Diego, California, 2016, AIAA Paper 2016-1816, doi:10.2514/6.2016-1816.

[367] Ranjan, R., Unnikrishnan, S., and Gaitonde, D. V., "On the Use of Mean Flow Perturbation for Global Stability Analysis," in "2018 Fluid Dynamics Conference," Atlanta, Georgia, 2018, AIAA Paper 2018-3378, doi:10.2514/6.2018-3378.

[368] Proctor, J. L., Brunton, S. L., and Kutz, J. N., "Dynamic Mode Decomposition with Control," *SIAM Journal on Applied Dynamical Systems*, Vol. 15, No. 1, 2016, pp. 142–161. doi:10.1137/15M1013857.

[369] Bisek, N. J., "In fluence of the External Aeroshell on the HIFiRE-6 using High-Fidelity Simulations," in "55th AIAA Aerospace Sciences Meeting," Grapevine, Texas, 2017, AIAA Paper 2017-1480, doi:10.2514/6.2017-1480.

[370] Larsson, J., Kawai, S., Bodart, J., and Bermejo-Moreno, I., "Large eddy simulation with modeled wall-stress: recent progress and future directions," *Mechanical Engineering Reviews*. doi:10.1299/mer.15-00418.

[371] Adler, M. C., Gonzalez, D. R., Stack, C. M., and Gaitonde, D. V., "Synthetic generation of equilibrium boundary layer turbulence from modeled statistics," *Computers & Fluids*, Vol. 165, 2018, pp. 127–143. doi:10.1016/j.compfluid.2018.01.003.

[372] Hassan, E., Peterson, D. M., Walters, K., and Luke, A., "Dynamic Hybrid Reynolds-Averaged Navier-Stokes/Large-Eddy Simulation of a Supersonic Cavity," *Journal of Propulsion and Power*, Vol. 32, No. 6, 2016, pp. 1343–1352. doi:10.2514/1.B36132.

[373] Hassan, E., Peterson, D. M., Walters, K., and Luke, E. A., "Crossflow turbulent production using hybrid Reynolds-averaged Navier–Stokes/large-eddy simulation approaches," *International Journal of Heat and Fluid Flow*, Vol. 70, 2018, pp. 15–27. doi:10.1016/j.ijheatfluidflow.2018.01.008.

[374] Hagenmaier, M. A. and Hassan, E. A., "Computational Analysis of Flow Phenomena in a Back-Pressured Supersonic Isolator," in "52nd AIAA/SAE/ASEE Joint Propulsion Conference," Salt Lake City, Utah, 2016, AIAA Paper 2016-4762, doi:10.2514/6.2016-4762.

[375] Smith, G. P., Golden, D. M., Frenklach, M., Moriarty, N. W., Eiteneer, B., Goldenberg, M., Bowman, C. T., Hanson, R. K., Song, S., Gardiner, W. C., Lissianski, V. V., and Qin, Z., "GRI-Mech," , Accessed: 2015-05-23, `http://www.me.berkeley.edu/gri_mech/`.

[376] Göttgens, J., Mauss, F., and Peters, N., "Analytic approximations of burning velocities and flame thicknesses of lean hydrogen, methane, ethylene, ethane,

acetylene, and propane flames," *Symposium (International) on Combustion*, Vol. 24, No. 1, 1992, pp. 129–135. doi:10.1016/s0082-0784(06)80020-2.